LOS ANGELES PUBLIC LIBRARY

FEB 21 1961

SCIENCE & TECHNOLOGY

ARS JOURNAL

A PUBLICATION OF THE AMERICAN ROCKET SOCIETY

VOLUME 31 NUMBER 1 JANUARY 1961

Sci R v.31 1961

BIND

EDITORIAL

ARS Does It Again . . . . . Martin Summerfield 3

SURVEY ARTICLE

Recent Advances in Electric Arc Plasma Generation Technology . . . . . Richard R. John and William L. Bade 4

CONTRIBUTED ARTICLES

Performance of Plug-Type Rocket Exhaust Nozzles . . . . . K. Bernaus and F. W. Crimp Jr. 18
Low Acceleration Takeoff From a Satellite Orbit . . . . . H. Lass and J. Lorell 24
Powered Trajectory Studies for Low Thrust Space Vehicles . . . . . Robert H. Fox 28
Complete Elementary Solution to Some Optimum Trajectory Problems . . . . . Frank D. Faulkner 33
Experimental Method of Measuring Intensity of Turbulence in a Rocket Chamber . . . . . Martin Hersch 39
Prediction of Composition Limits for Detonation of Hydrogen–Oxygen–Diluent Mixtures . . . . . Richard W. Patch 46
Calibrations of the Card-Gap Test . . . . . Melvin A. Cook and Lee L. Udy 52
Experimental Results With a Collinear Electrode Plasma Accelerator and a Comparison With Ion Accelerators . . . . . W. L. Starr and S. W. Kash 58
Dissociation Effects Upon Compressible Turbulent Boundary Layer Skin Friction and Heat Transfer . . . . . William H. Dorrance 61
Measured Pressure Distribution and Local Heat Transfer Rates for Flow Over Concave Hemispheres . . . . . J. C. Y. Koh and J. P. Hartnett 71

TECHNICAL NOTES

Differentiating Gas Jet for Space Attitude Control . . . . . Robert S. Gaylord 75
Instrument for Measuring Total Incident Radiant Heat Transfer to a Jet Engine Surface . . . . . R. E. Walker and S. E. Gronseski Jr. 77
Heat Transfer Gage for Use in Highly Ionized Gases . . . . . Richard W. Ziemer 78
Optimum Radiant Straight Fin With Exponential Sides . Irving Granet and William Mellroy 80
Shock Tunnel Experimental Techniques for Force and Moment and Surface Flow Direction Measurements . . . . . W. R. Warren, E. M. Kaegi and R. E. Geiger 82
Thrust Termination in Solid Rocket Motors—Evaluation of Ballistic Test Data . . . . . Sherwin Kalt 84
Comparison of Theoretical and Experimental Film Thickness . . . . . A. E. Dukler 86
Meteoritic Impact . . . . . David B. Beard 87
Formulation of the Optimum Rocket Trajectory . . . . . Y. C. Shen 89
Useful Correlation of Interior Ballistic Theory and Experimental Data . . . . . Harold D. Black and Raimond A. Struble 90
Effect of Electrical Augmentation on Nuclear Rocket Flight Performance . Edwin R. Berry 92
Nonequilibrium Ionization in a Shock Tunnel Flow . . . . . Alan Q. Eschenroeder and John W. Daiber 94
Particle Impaction Efficiencies for Bodies in a Free Molecule Flow . . . . . S. K. Friedlander 96
Theory of Motion of a Near Earth Satellite . . Raimond A. Struble and William F. Campbell 154
Densities of the Upper Atmosphere Derived From Discoverer Satellites . Stanley H. Landberg 155
Solid Propellant Sources of Cesium Plasma . . . . Lawrence W. Fagg and Raymond Friedman 157
Location of Focal Points of Ellipses . . . . . Roy C. Spencer 158
Aerodynamic Heating of Plane Bodies of Low Thermal Diffusivity . . . . . Gerald R. Guinn 159

DEPARTMENTS

New Patents 162
Technical Literature Digest 163

RUSSIAN SUPPLEMENT . . . 97–152

JAN 30 1963

ELECTRICITY FROM NUCLEAR HEAT

For employment write to:
Personnel Director
Division 61-1

los Alamos
scientific laboratory

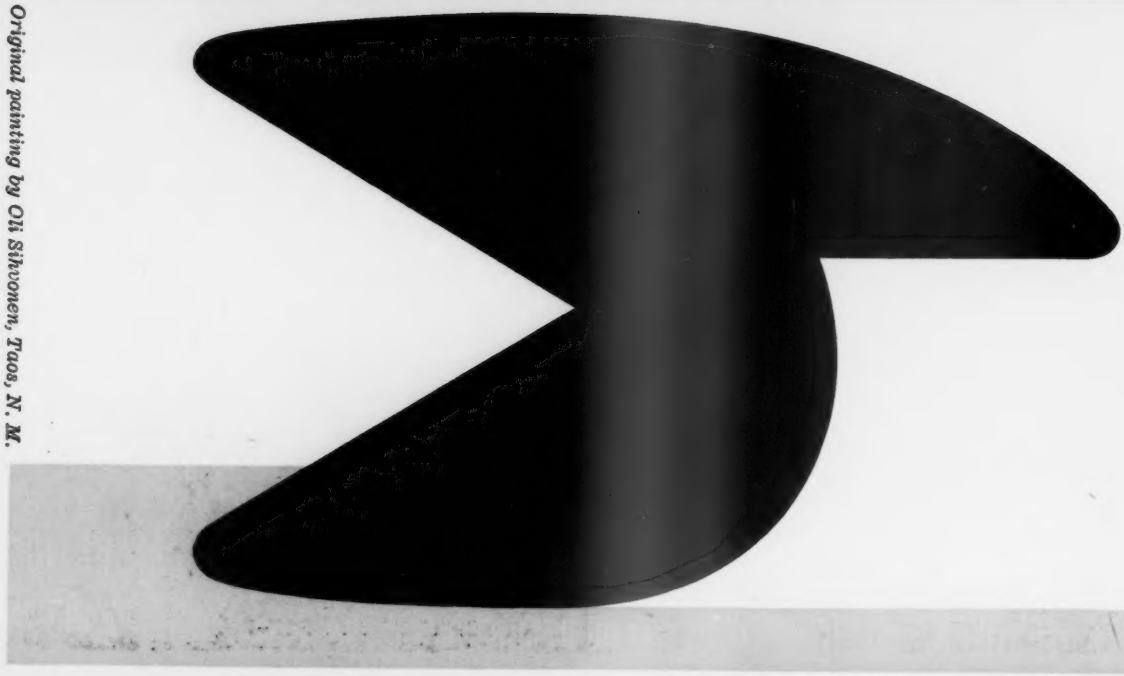

Original painting by Oli Sihvonen, Taos, N. M.

Inventiveness: indispensable ingredient of **S**pace **T**echnology **L**eadership

In the achievement of Space Technology Leadership, on-the-shelf hardware and the existing state-of-the-art are not always equal to the requirements of advanced missile and space systems. In such challenging situations Space Technology Laboratories responds with the full breadth of its resources • In response to the need for time compression, STL inventiveness produced devices answering urgent requirements of advanced space programs conducted for the Air Force Ballistic Missile Division, National Aeronautics and Space Administration, and Advanced Research Projects Agency. Among these: Telebit, first digital computer to enter space; the first multi-million-mile space communications system of Pioneer V; a continuous-wave radio guidance system and lightweight autopilots for Able-series space vehicles; and a low-thrust multi-start space engine for maneuverable satellites • On this foundation of inventiveness STL continues to broaden in scope, translating creative concept into accomplishment for Space Technology Leadership • Outstanding scientists and engineers seeking such an environment are invited to investigate opportunities available at STL. Resumes and inquiries will receive meticulous attention.

SPACE TECHNOLOGY LABORATORIES, INC. P.O. BOX 95005C LOS ANGELES 45, CALIFORNIA

a subsidiary of Thompson Ramo Wooldridge Inc.

El Segundo • Santa Maria • Edwards Rocket Base • Canoga Park STL Cape Canaveral • Manchester, England • Singapore • Hawaii

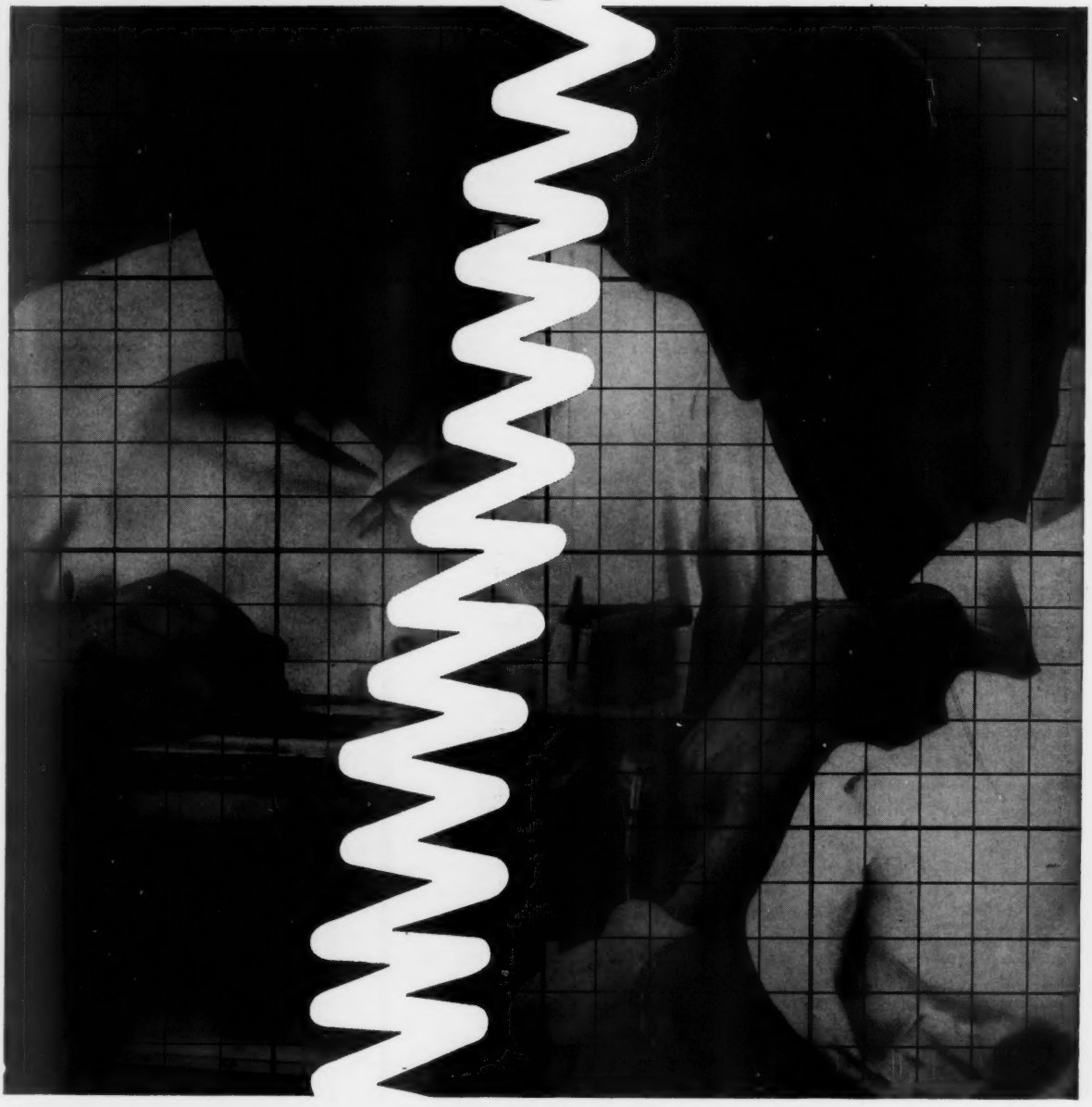

ARS JOURNAL

A PUBLICATION OF THE AMERICAN ROCKET SOCIETY

EDITOR **Martin Summerfield**

ASSOCIATE TECHNICAL EDITOR **Irvin Glassman**

MANAGING EDITOR **Barbara Nowak**

ART EDITOR **John Culin**

ASSOCIATE EDITORS

Igor Jurkevich, *G. E. Space Sciences Laboratory, Russian Supplement;* **George F. McLaughlin,** *Patents;* **Charles J. Mundo Jr.,** *Raytheon Co., Guidance;* **Bernard H. Paiewonsky,** *Aeronautical Research Associates of Princeton, Flight Mechanics;* **M. H. Smith,** *Princeton University, Technical Literature Digest*

ASSISTANT EDITORS

Julie Hight, Carol Rubenstein, Estelle Viertel

DIRECTOR OF MARKETING

Owen Kean

ADVERTISING PROMOTION MANAGER

Robert M. Lamb

ADVERTISING PRODUCTION MANAGER

Walter Brunke

ADVERTISING REPRESENTATIVES

New York
D. C. Emery and Associates
400 Madison Ave., New York, N. Y.
Telephone: Plaza 9-7460

Los Angeles
James C. Galloway and Co.
6535 Wilshire Blvd., Los Angeles, Calif.
Telephone: Olive 3-3223

Chicago
Jim Summers and Associates
35 E. Wacker Dr., Chicago, Ill.
Telephone: Andover 3-1154

Detroit
R. F. Pickrell and Vincent Purcell
318 Stephenson Bldg., Detroit, Mich.
Telephone: Trinity 1-0790

Atlanta
Joe H. Howell
1776 Peachtree Bldg., Atlanta 9, Ga.
Telephone: 873-2136

American Rocket Society

500 Fifth Avenue, New York 36, N. Y.

Founded 1930

OFFICERS

President	Harold W. Ritchey
Vice-President	William H. Pickering
Executive Secretary	James J. Harford
Treasurer	Robert M. Lawrence
General Counsel	Andrew G. Haley
Director of Publications	Irwin Hersey

BOARD OF DIRECTORS

Terms expiring on dates indicated

Ali B. Cambel	1962	Samuel Herrick	1963
Richard B. Canright	1962	Arthur Kantrowitz	1963
William J. Cecka Jr.	1963	A. K. Oppenheim	1961
J. R. Dempsey	1961	Simon Ramo	1963
Herbert Friedman	1962	David G. Simons	1961
George Gerard	1961	John L. Sloop	1961
Robert A. Gross	1962	Martin Summerfield	1962

A. M. Zarem 1963

TECHNICAL COMMITTEE CHAIRMEN

William H. Avery, Ramjets
R. M. L. Baker Jr., Astrodynamics
G. Daniel Brewer, Solid Rockets
Robert W. Bussard, Nuclear Propulsion
Bernhardt L. Dorman, Test, Operations and Support
William H. Dorrance, Hypersonics
James S. Farrior, Guidance and Navigation
Herbert Friedman, Physics of the Atmosphere and Space
George Gerard, Structures and Materials
Martin Goldsmith, Liquid Rockets
Andrew G. Haley, Space Law and Sociology
John H. Huth, Power Systems
Eugene Konecci, Human Factors and Bioastronautics
Frank Lehan, Communications and Instrumentation
Peter L. Nichols Jr., Propellants and Combustion
Milton W. Slawsky, Magnetohydrodynamics
Herman E. Sheets, Underwater Propulsion
Ernst Stuhlinger, Electric Propulsion

Scope of ARS JOURNAL

This Journal is devoted to the advancement of astronautics through the dissemination of original papers disclosing new scientific knowledge and basic applications of such knowledge. The sciences of astronautics are understood here to embrace selected aspects of jet and rocket propulsion, spaceflight mechanics, high speed aerodynamics, flight guidance, space communications, atmospheric and outer space physics, materials and structures, human engineering, overall system analysis, and possibly certain other scientific areas. The selection of papers to be printed will be governed by the pertinence of the topic to the field of astronautics, by the current or probable future significance of the research, and by the importance of distributing the information to the members of the Society and to the profession at large.

Information for Authors

Manuscripts must be as brief as the proper presentation of the ideas will allow. Exclusion of dispensable material and conciseness of expression will influence the Editors' acceptance of a manuscript. In terms of standard-size double-spaced typed pages, a typical maximum length is 22 pages of text (including equations), 1 page of references, 1 page of abstract and 12 illustrations. Fewer illustrations permit more text, and vice versa. Greater length will be acceptable only in exceptional cases.

Short manuscripts, not more than one quarter of the maximum length stated for full articles, may qualify for publication as Technical Notes or Technical Comments. They may be devoted to new developments requiring prompt disclosure or to comments on previously published papers. Such manuscripts are published within a few months of the date of receipt.

Sponsored manuscripts are published occasionally as an ARS service to the industry. A manuscript that does not qualify for publication, according to the above-stated requirements as to subject, scope or length, but which nevertheless deserves widespread distribution among jet propulsion engineers, may be printed as an extra part of the Journal or as a special supplement, if the author or his sponsor will reimburse the Society for actual publication costs. Estimates are available on request. Acknowledgment of such financial sponsorship appears as a footnote on the first page of the article. Publication is prompt since such papers are not in the ordinary backlog.

Manuscripts must be double spaced on one side of paper only with wide margins to allow for instructions to printer. Include a 100 to 200 word abstract. State the authors' positions and affiliations in a footnote on the first page. Equations and symbols may be handwritten or typewritten; clarity for the printer is essential. Greek letters and unusual symbols should be identified in the margin. If handwritten, distinguish between capital and lower case letters, and indicate subscripts and superscripts. References are to be grouped at the end of the manuscript and are to be given as follows. For journal articles: Authors first, then title, journal, volume, year, page numbers; for books: Authors first, then title, publisher, city, edition and page or chapter numbers. Line drawings must be clear and sharp to make clear engravings. Use black ink on white paper or tracing cloth. Lettering should be large enough to be legible after reduction. Photographs should be glossy prints, not matte or semi-matte. Each illustration must have a legend; legends should be listed in order on a separate sheet.

Manuscripts must be accompanied by written assurance as to security clearance in the event the subject matter lies in a classified area or if the paper originates under government sponsorship. Full responsibility rests with the author.

Preprints of papers presented at ARS meetings are automatically considered for publication.

Submit manuscripts in duplicate (original plus first carbon, with two sets of illustrations) to the Managing Editor, ARS JOURNAL, 500 Fifth Avenue, New York 36, N. Y.

ARS JOURNAL is published monthly by the American Rocket Society, Inc. and the American Interplanetary Society at 20th & Northampton Sts., Easton, Pa., U. S. A. Editorial offices: 500 Fifth Ave., New York 36, N. Y. Price: $18.00 per year, $3.00 per single copy. Second-class postage paid at Easton, Pa., with additional entry at New York, N. Y. This publication is authorized to be mailed at the special rates of postage prescribed by Section 132.122. Notice of change of address should be sent to the Secretary, ARS, at least 30 days prior to publication. Opinions expressed herein are the authors' and do not necessarily reflect the views of the Editors or of the Society.

© Copyright 1961 by the American Rocket Society, Inc.

ARS Does It Again

It has been our obligation at various times in the past to write an editorial for the ARS JOURNAL. Generally, the purpose has been to communicate to our readers and authors some new development in our publishing activity on which they should be informed.

These editorials have been appearing at rather frequent intervals in the last two years. In January 1959, for example, we took a page to inform the Society and the Journal readers of the expansion of the Journal that took place at that time and of its broadened policies with respect to scope of subject matter. In October of that same year, we took the occasion to announce the inauguration of the new Russian Supplement as an addition to the Journal, now appearing for the second year; not long afterward, in July 1960, we wrote two pages to inform our readers and especially the members of our Society's Technical Committees of the launching of the new companion to ARS JOURNAL, a series of technical books under the title of "Progress in Astronautics and Rocketry." Two of these volumes have already appeared, three are in the publishing stage, and five more are on the calendar for 1961. And now, we again have a report to make to the Society and to the readers of the Journal concerning an important expansion step.

The theme of our report is expressed by the title above—ARS Does It Again. Starting with this issue, the ARS JOURNAL will contain about 50% more pages per month than in 1960, and all of this increase will be allocated to the publishing of technical papers. Impressive as this figure is, it is even more impressive when it is realized that this expansion comes close to doubling the number of pages that can be devoted to technical articles—that is, the actual percentage is about 80%, after the pages occupied by advertising, Book Notes, Patents, Technical Literature Digest and Russian Supplement are removed from the calculation.

This sharp upward step in the capacity of the Journal, coupled with the capacity of the new ARS Progress Series, should come close to solving the very embarassing backlog problem that has dogged the Society for the past year or two. The impact of this enlarged capacity should become noticeable to our authors and readers in a few months.

Many members of the Society have spoken to us at various times, wondering whether there is not some upper limit to the number of papers the Society should publish or, putting the question differently, are not our scientific people writing too many papers? Allow us to reply by saying first that, as editors, we do not write these papers, for the main part we do not solicit them, we follow strict but impartial reviewing procedures to make sure that only competent papers are published, and we do everything possible to compel our authors to be concise. But, in spite of all this, the stream of acceptable material being offered to us seems to flow in ever-increasing volume. As observers of the current scene, we can spot the reasons for this increase quite easily: Science as a whole is growing exponentially, and so is the number of productive scientists; our field of astronautics is accounting for an ever larger share of this scientific growth; ARS JOURNAL is being selected preferentially by many more members for the dissemination of their research findings because of its large, effective circulation and its world-wide reach; and the need for open publication of such research findings becomes greater as the growth in the scientific population makes it less and less feasible to intercommunicate effectively by means of private mailings of individually printed reports.

Strong as these forces are in compelling the Society to expand its publication program, the strongest force by far in our particular situation is the growing vigor and competence of our Technical Committees. In its Technical Committee structure, the Society has identified itself with 20 different subject areas of research and development, all characterized by rapid progress. It is not surprising that there is a lot to report in each of these areas, and under the guidance of our Committee members, the Society is receiving a steadily larger number of worthy papers for presentation at meetings and for publication in its periodicals.

The Society's Board of Directors has always considered that the primary function of ARS is to facilitate the exchange of technical information. Faced with the growing backlog of worthy papers, the Board recognized the urgency of the need, and authorized this expansion. So, to our friends who asked whether we see an eventual upper limit to our publishing program, we can only give the answer that, if the need for additional publishing space continues to grow—and we personally believe it will—the Board will search for ways to accommodate it.

The cost of this expansion, in editorial salaries, office expenses and printing bills, was the main hurdle that had to be surmounted. In this case, the National Science Foundation, perceiving the importance of the service we were proposing to render to the astronautical sciences, came to the assistance of the Society financially, and guaranteed to meet the cost of the expansion immediately for a limited period with the understanding that the Society would find other sources of revenue to supplant NSF support after this period. The Board of Directors and the Officers of the Society have soberly accepted the responsibility and the challenge implied in this agreement, and are now engaged in searching out and developing the necessary new sources. At the same time, a careful review has been started of our editorial procedures and all of the steps of the publishing process, with the object of reducing the cost per printed page to the lowest possible level.

We believe we will be successful in both directions—in finding the needed sources of income and in keeping our costs down to the bare minimum. In this way, the Society expects to continue its publishing service for our profession with ever-increasing strength.

Martin Summerfield
Editor, ARS JOURNAL

Recent Advances in Electric Arc Plasma Generation Technology[1]

RICHARD R. JOHN
and
WILLIAM L. BADE

Avco Research and
Advanced Development Div.
Wilmington, Mass.

THE ENGINEERING use of electric arcs for heating gases to high temperatures extends back at least to the beginning of the present century. Within the last 5 years, however, activity in this field has increased enormously owing to the development of new applications in aerodynamic simulation and space propulsion. Because arc plasma generation[2] equipment often has a considerable proprietary interest, the technical literature pertaining to this subject is unusually guarded and incomplete. Little information with regard to either engineering design or performance capabilities appears in technical journals. Descriptions of existing units often are found only in trade magazines and in patents. For some equipment, only word-of-mouth information is available. Because of the peculiar character of the technical literature in this field, the current review article does not claim to provide a complete listing of all past and present types of plasma generators. It does attempt, however, to present a clear definition of the current state of the art, with particular attention to arc heated wind tunnels and space engines.

Received Nov. 25, 1960.
[1] Based upon work carried out under Contract no. AF 33(616)-7578 with Wright Air Development Div., Air Research and Development Command, United States Air Force.
[2] In this paper, the term "plasma generator" denotes any electric arc device for sustained heating of gases to high temperatures. The word "plasma," as defined by Langmuir, strictly denotes an electrically neutral gas containing a high concentration of electrons and heavy ions. In many existing arc gas heating units, however, the temperature of the emergent gas stream is not sufficiently high to provide an appreciable amount of ionization. When applied to such units, the term "plasma generator" is a misnomer, but its use as a generic designation for arc gas heating equipment is in common usage.

Plasma Generator Applications

The ability of electric arcs to produce high temperatures has often been exploited in gas heating applications. The many possible uses of electric arc plasma generators include: Chemical synthesis; melting, spraying and cutting of refractory materials; high temperature research; laboratory simulation of re-entry and other thermally severe environments; and space propulsion.

Chemical Synthesis

At the beginning of the present century, Birkeland and Eyde (1)[3] developed an industrial process for the synthesis of nitric oxide from air using an electric arc. Their type of unit had two water-cooled metal electrodes supplied with 5000 v a-c and operated in a d-c magnetic field at a power level of several hundred kilowatts. A number of these units were operated profitably in Norway until the process was superceded by the more economical Haber-Fink method, which produced nitric acid directly by the oxidation of ammonia (2). Schönherr (3) in 1909 described another nitrogen-fixation process, in which air was passed through a long (up to 23 ft!) vortex-stabilized a-c arc operated at 7200 v. Continuous operation for 3 months was reported for these units. More recently, in 1948, Baumann (4) of the Chemische Werke Hüls reported the development of a process for synthesizing acetylene from saturated hydrocarbons, using a 3-ft long d-c arc operated at 7 megawatts between a water-cooled copper cathode and an iron anode. A key requirement for efficient

[3] Numbers in parentheses indicate References at end of paper.

Dr. John received his Ph.D. in aeronautical engineering from Princeton University in 1957. His thesis was on the mechanism of flame propagation in turbulent gas streams. Since 1958 the author has worked at the Research and Advanced Development Division of Avco and has been a participant in the development of electric arc plasma generators for re-entry simulation and space propulsion. An ARS member, he is currently head of the Arc Sciences Section of the Avco RAD Physics Research Department.

Dr. Bade received his Ph.D. in physics from the University of Nebraska in 1954. He was a National Science Foundation post-doctoral fellow at Yale University from 1956 to 1957. Since joining Avco in 1957 the author has done research on various aspects of the physics of fluids including stagnation point heat transfer, transport properties of high temperature gas mixtures, intermolecular forces, electric arcs, plasma jets and unsteady gasdynamics. He is presently Principal Scientist at Avco, RAD, and is an ARS member.

utilization of the input energy in any electric arc gas phase chemical reactor is rapid cooling or quenching of the heated gas to "freeze in" the high temperature equilibrium concentrations of the desired products. In the Hüls process (4), this quenching was accomplished by passing the emergent gas stream through a water spray.

Currently, a number of organizations are conducting research on the application of arc heaters to chemical synthesis (2). Stokes and Knipe of Temple University (5) are utilizing a nitrogen plasma generator for preparation of endothermic nitrogen compounds. Synthesis of titanium nitride, magnesium nitride, cyanogen and nitrogen dioxide from the elements was accomplished in preliminary experiments. Similar research is being carried out with plasma jets by Phillips and Ferguson at Stanford Research Institute (2). A research objective of this program is the direct synthesis of organimetallics by contact between an organic liquid and a metal which has been previously vaporized in a plasma jet.

Utilized as a gas phase chemical reactor, a plasma generator typically yields products whose formation is thermodynamically favored at a temperature of several thousand degrees Kelvin, i.e., at the temperature of the arc or a somewhat lower temperature experienced by the gas during quenching. Such products are usually high energy compounds of relatively simple molecular structure and low molecular weight. Examples are nitric oxide (NO, Birkeland-Eyde and Schönherr processes) and acetylene (C_2H_2, Hüls process). Other compounds which might be formed under suitable conditions include hydrogen peroxide (H_2O_2), hydrazine (N_2H_4) and cyanogen (C_2N_2). In nearly all cases, other processes are available for synthesizing such compounds on an industrial scale, and the future use of electric arc plasma generators for this purpose will depend upon competitive cost factors.

Refractory Processing

The applications discussed in the foregoing concern the use of arcs to bring about high temperature chemical reactions in gases. In another type of application, the arc heater is used merely as a source of hot gas for welding or other fabrication processes. Utilization of plasma generators for such purposes goes back at least to 1910, the year in which Mathers (6) patented a unit designed for heating high temperature furnaces. This device had consumable carbon electrodes and used compressed air as a working fluid.

Numerous subsequent patents describe arc devices for cutting, welding and spraying high temperature materials. The patents (7–9) of Rava, an independent inventor of the 1930's, hold considerable interest in that they describe a series of plasma generators which have both refractory and water-cooled electrodes, make use of swirl injection to confine the discharge, can be operated on either a-c or d-c power, and utilize mognetic fields to control arc motion. In 1956, Briggs of Amalgamated Growth Industries, the firm which presently owns the Rava patents, obtained two patents (10,11) for improvements on the original Rava configuration (9).

The basic Union Carbide patent (12) in the arc gas heater field appears to have been granted to Gage in 1957. This patent primarily involves the use of an arc torch for metal cutting, and features confinement of the arc discharge by means of a cooled metal wall. Gage and others at Union Carbide have subsequently been issued a number of patents pertaining to improvements and extensions of the original device. These later patents typically relate to transferred arc techniques (13,14), arc operation with reactive gases (15), improved welding and cutting methods (16–18), arc starting procedures (19), liquid vortex arc (20), and arc operation with uncooled electrodes (21).

During 1960, Giannini, Ducati and Blackman of Plasmadyne Corp. have received a number of patents in this field. Patents have been issued to Giannini and Ducati (22) and Ducati and Blackman (23) for a high current, low voltage vortex-stabilized plasma generator; to Giannini and Ducati (24) for a plasma generator light source; and to Giannini and Blackman (25) and to Blackman (26) for a plasma generator incorporating a magnetic nozzle.

Opinions as to the validity of the many claims and counterclaims in the foregoing patents are outside the scope of the present paper. However, on the basis of an examination of patents going back to 1911, it is apparent that a great many of the concepts and techniques associated with electric arc gas heaters are, at present, in the public domain.

The chief advantages of arc plasma generators over combustion torches in the material processing field are the extremely high temperatures produced and the capability of operation in completely inert atmospheres. As a consequence of these advantages, it appears certain that arc-jet devices will receive increasingly widespread use in cutting, welding and spraying materials which are either too refractory or too reactive to permit processing by means of chemical flames.

High Temperature Research

Independently of the forementioned American work directed toward the development of arc units for materials processing and fabrication, a considerable body of research was carried out in Germany on arc devices for high temperature research. Until recently, most of this German work dealt with two special types of carbon arc. The unconfined high current carbon arc, which produces a jet of incandescent carbon vapor known as the anode tail flame, was studied extensively by Finkelnburg and his co-workers (27–29). Another group including Maecker (30), Weiss (31) and Peters (32) concentrated its efforts on different versions of the water-stabilized arc originally proposed by Gerdien and Lotz (33) in 1922. In Weiss's (31) version of this apparatus, the arc burns between a carbon rod (anode) and a carbon annulus (cathode), within the hollow of a water vortex. The spinning water column confines the arc discharge and, by evaporation, supplies material to it. A jet consisting of vaporized carbon and water products emerges through the cathode orifice. By pressurizing the chamber containing the water column and the arc, Peters (32) was apparently the first to obtain a supersonic jet with this type of device.

Plasma generator research in Germany has been oriented principally toward the scientific investigation of arc phenomena per se. A major fraction of the effort was expended on measurement of the physical properties and behavior of the arc plasma, and on attempts to obtain a quantitative theoretical understanding of the arc mechanism. The chief value of this German work thus lies more in its contributions to scientific knowledge about arcs than in its development of specific types of arc devices. English-language surveys of this German work have been prepared by Lochte-Holtgreven (34) and Finkelnburg (35). The comprehensive Finkelnburg-Maecker "Handbuch" article (36), which reviews the sum of knowledge about arcs as of 1954, contains descriptions of a wide variety of arc configurations including the ones mentioned here.

Re-Entry Simulation

The extraordinarily rapid development of arc plasma generation technology since 1955 has been motivated principally by the urgent need for facilities capable of evaluating ablative materials under simulated re-entry conditions. This need first arose in the ballistic missile program, but increasingly diversified and severe requirements for sustained simulation of high enthalpy flight are now emerging from programs for the development of recoverable satellites, boost-glide vehicles, lunar probes and other advanced space systems.

The conditions experienced by any given vehicle during entry into a planetary atmosphere are calculable from the atmospheric structure and the aerodynamic properties of the vehicle. Detailed analytical estimates of characteristic hy-

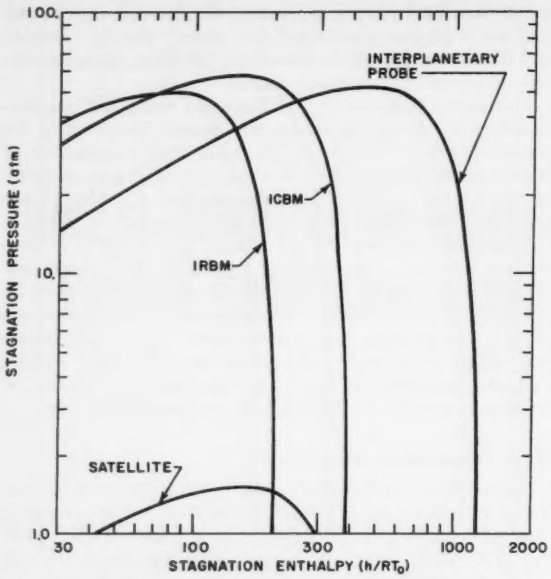

Fig. 1 Stagnation conditions during atmospheric re-entry; $RT_0 = 33.86$ Btu/lb

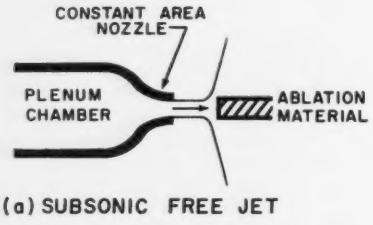

(a) SUBSONIC FREE JET

(b) SUPERSONIC JET

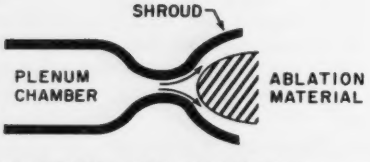

(c) SHROUD CONFIGURATION

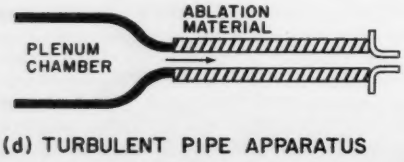

(d) TURBULENT PIPE APPARATUS

Figs. 2 Methods of re-entry simulation

perthermal re-entry environments have been made by a number of investigators including Allen and Eggers (37), Chapman (38) and, most recently, Stalder (39). Fig. 1 summarizes the stagnation pressure and enthalpy conditions experienced by several types of vehicle during re-entry into Earth's atmosphere. The trajectories shown are for relatively severe rather than typical cases. From a materials evaluation viewpoint, the conditions which are most important to simulate are those in the neighborhood of peak pressure, where the aerodynamic heat transfer and shear stress are high.

Assuming that a suitable source of heated gas is available, the problem of re-entry simulation can be approached in a number of different ways (40,41), as illustrated in Figs. 2. The subsonic free jet (Fig. 2a) has the advantage that only a small stagnation pressure loss occurs between the arc chamber and the model, and is particularly useful for simulating laminar ablation in the relatively high pressure ballistic missile environment (42). The supersonic jet (Fig. 2b) is suitable for testing relatively large models and is appropriate for matching satellite (43,44) and glide vehicle re-entry environments. The shroud technique (Fig. 2c), originally suggested by Ferri (45), has the advantage that a large fraction of the heated gas comes into contact with the model, and again there is very little stagnation pressure loss between arc chamber and model surface. Also, the shroud can be contoured to give a prescribed pressure distribution over the model face. Finally, the pipe apparatus (Fig. 2d) is useful for simulating turbulent flow conditions along the sides of a re-entering vehicle (46) or, when operated with different gases, for simulating a rocket nozzle environment (47). Achievement of turbulent boundary layer flow in a pipe configuration requires a relatively high mass flow and, hence, at the enthalpy values illustrated in Fig. 1, a relatively high power input to the gas stream (40,46).

At the time of the ballistic missile program's inception in 1954, the basic experimental equipment for the study of high speed flow and hyperthermal environments included the continuous flow hypersonic tunnel, the rocket engine exhaust and the shock tube. Because of inherent limitations, none of these types of facility was fully suitable for simulation of the IRBM and ICBM re-entry conditions indicated in Fig. 1. The hypersonic tunnel (48) was capable of achieving Mach numbers up to 15, but its stagnation enthalpy was too low to permit investigation of re-entry heating and ablation. The blast from a rocket motor (49) produced high heat transfer rates, but was subject to limitations of temperature, enthalpy and chemical composition. Finally, the shock tube (50) was capable of producing an air stream with the full stagnation enthalpy characteristic of ICBM re-entry, but only on an intermittent basis for periods of the order of 100 microsec. The study of ablation (51) requires the simulation of high aerodynamic shear stress and heat transfer on a sustained basis, for time periods of many seconds.

The need for improved high enthalpy aerodynamic simulation facilities led to the development of several new types of test equipment (52). The "Hotshot"-type blowdown tunnel (53), driven by a condenser discharge, achieved hypersonic Mach numbers together with the stagnation enthalpies characteristic of ballistic missile re-entry, but again the available running time was only a fraction of a second. To meet the need for a laboratory facility capable of continuously supplying heated gases at enthalpies and pressures at least approaching the values illustrated in Fig. 1, a number of organizations directly or indirectly involved in the ballistic missile program turned to the plasma generator.

Early efforts were directed toward use of the unconfined high current carbon arc and the water-stabilized arc described previously. Investigators at Vitro Laboratories (54,55) took up the study of the anode tail flame and explored its applications to the testing of materials under conditions of high aerodynamic heat flux. Water-stabilized arcs were constructed and applied to materials studies at General Electric

(56–58), Chicago Midway Laboratories (59), Avco (60), the Royal Aircraft Establishment (61), and elsewhere. Although these devices provided high heat fluxes, they were not satisfactory for re-entry simulation because the chemical compositions of the exit jets were radically different from that of air. For this reason, efforts were turned toward the development of arc heaters in which the exit gas stream would consist of air with only a minimum of foreign contamination.

Initial studies on plasma generators using air as a working fluid were performed with configurations employing carbon for both the anode and the cathode. The work was carried out at a number of laboratories including NASA-Langley (62–64), ABMA (65,66), General Electric (67,68) and Chicago Midway (69). The observation that the anode in these all-carbon arcs usually lost more material than the cathode, suggested that the contamination level of the heated jet might be considerably reduced by using some material other than carbon for the anode. In 1957 Brogan at Avco (70), and at about the same time Lai and others (71) at the University of California, built and operated plasma generators with carbon cathodes and cooled copper anodes. Subsequently, many groups have used this electrode combination in extensive material study programs.

Even before the development of the carbon-copper configuration, Plasmadyne (72,73) had built and operated plasma generators employing thoriated tungsten cathodes and cooled metal anodes. Subsequently, many other groups have used this combination (74–77). The use of thoriated tungsten in place of carbon as the cathode material results in sharply reduced contamination when the unit is operated with non-oxidizing gases, such as argon, helium and nitrogen. In operation with air, however, the susceptibility of tungsten to oxidation results in a considerable loss of cathode material. Recently, as part of the continuing effort to reduce exit jet contamination, several organizations including NASA-Ames (78), NASA-Langley (79), Vidya (80) and Westinghouse (81) have initiated development programs on arc configurations employing cooled copper for both electrodes, and utilizing a magnetic field to keep the arc in motion. Early results of these programs appear promising.

It is generally agreed (39,41,52) that, because of throat erosion problems and arc chamber pressure limitations, arc heated wind tunnels are limited to operating Mach numbers of less than 7 or 8. However, such facilities are well suited for material studies, since they are capable of sustained production of heat flux, pressure and enthalpy conditions similar to those characteristic of re-entry.

Space Propulsion

At an early stage in the development of the plasma generator as a re-entry simulator, it became apparent that the device was also attractive as a low thrust space engine (82–86). A variety of mission studies suggested that a thermal arc-jet rocket operating in the specific impulse range from 1000 to 2000 sec would be capable of carrying out a number of interesting space missions in the region between Earth and the moon (87–91).

Early exploratory work on use of the plasma generator as a propulsive device was carried out by Cann et al. of Plasmadyne (82,92). Argon was used as a working fluid, yielding a specific impulse of the order of a few hundred seconds. More recently, engines have been operated with hydrogen and helium by Ducati and Cann (93), and by Brogan (85) and John (94) of Avco. With these lower molecular weight gases, specific impulses in the range from 1000 to 1500 sec have been obtained.

A critical factor in evaluating the plasma generator as a propulsive device is the extent to which energy absorbed in ionizing and dissociating the propellant fluid is converted into kinetic energy during the nozzle expansion process (94–99). The "frozen" flow losses in electrothermal engines are similar in character to the dissociation losses which occur in chemical rocket engines. However, since arc units are operated at higher chamber temperatures than chemical rockets, more energy is absorbed in dissociation and ionization, and the frozen flow losses may be larger. Table 1 shows calculated values of arc engine specific impulse for hydrogen as a function of gas enthalpy, assuming complete conversion of available gas enthalpy to kinetic energy, for the two limiting cases of equilibrium and frozen flow. The enthalpies shown are within the performance capabilities of existing equipment. It is clear from Table 1 that engine performance depends substantially upon the extent to which atoms recombine in the nozzle. One-dimensional analysis of the nozzle flow, based upon recent information on atom-atom recombination rates, strongly suggests that the flow is frozen (98,99). However, attempts are being made to realize the potentially large performance gains associated with equilibrium flow by means of catalytic agents for increasing atom-atom and ion-electron recombination rates and nozzle contours for postponing the point of transition from equilibrium to frozen flow.

Work on the plasma generator for space propulsion is currently being pursued vigorously at a number of laboratories. Particular emphasis is being placed on the extension of electrode life and the development of regenerative, transpiration and radiative cooling techniques to reduce the size of the required external cooling system and radiator to a minimum. It is generally agreed that, of the various proposed electric propulsion devices, the thermal arc-jet engine is closest to hardware realization.

Table 1 Hydrogen arc engine performance, equilibrium vs. frozen flow

Gas enthalpy, Btu/lb	Equilibrium specific impulse, sec	Frozen specific impulse, sec
50,000	1560	1090
100,000	2200	1270
150,000	2700	1590

Design and Operating Characteristics

Plasma Generator Configurations

In spite of the apparent diversity of the many types of plasma generator developed during recent years, nearly all of these units have two features in common:

1 Approximate rotational symmetry about a central axis.

2 Coaxial electrodes separated by an annular gap, across which the arc current passes, and through which the gas flows.

The topology provided by these features guarantees that at least part of the gas passing through the unit will flow through the current carrying region (arc column), where the heating occurs.

Figs. 3 illustrate schematically the three principal types of configuration currently receiving widespread use in plasma generators for re-entry simulation and space propulsion. The simplest is the cylindrical configuration (Fig. 3a), consisting of a refractory (carbon or tungsten) central cathode and a surrounding water-cooled metal anode (100,101). Motion of the arc column and of its termini upon the electrode surfaces (electrode spots) is an important factor affecting electrode life and the contamination level of the emergent heated gas. In cylindrical configuration plasma generators, self-induced or natural motion of the arc column and the electrode spots is adequate to prevent anode burnout at relatively low pressures and arc input powers (102). For operation at high power and pressure levels, anode spot motion can be increased by aerodynamic means (e.g., vortex flow within the arc chamber) or by application of a magnetic field with a component normal to the current flow (101).

In the toroidal configuration (Fig. 3b), the electrodes are

two water-cooled copper rings. The arc column, which strikes across the annular gap separating the rings, is forced to revolve about the axis of the unit by application of an external magnetic field (78–81). Absence of the field results in immediate electrode burnout. The mechanical design of the device requires considerable ingenuity on the part of the designer to minimize the total area of cooled metal surface exposed to the hot gas.

In the constricted configuration (Fig. 3c), the flow in the region of the arc column is accelerated by forming the chamber as a converging duct. A refractory material is generally used for the inner electrode, whereas both refractory materials and water-cooled copper have been used for the outer one. Units have been operated with the inner electrode as cathode and the outer as anode, as well as with the reversed polarity. By varying the mass flow of gas, the inlet flow pattern (axial or swirl injection) and the geometry (length/diameter ratio for the electrode throat), the arc column can be caused to terminate upstream (70), within (75) or downstream (12,71,-72) of the constriction in the electrode. In the last case, where the arc column strikes through the throat to the diverging section of the nozzle electrode, a phenomenon known as column confinement occurs in the throat region if this passage has a sufficiently small cross section in relation to the arc current. Column confinement is known empirically to have several important effects upon arc behavior, including increase of column voltage gradient, current density and arc temperature. Column confinement also tends to suppress column motion, a significant source of electrical and aerodynamic fluctuations. Possible additional advantages include more uniform heating of the entire gas stream, increased efficiency and reduced contamination. The extent to which these advantages of confinement are actually realized in existing units is difficult to gage, because little effort has been expended on comparison of the performances of different types of configuration.

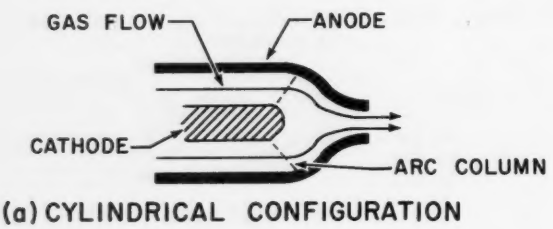

(a) CYLINDRICAL CONFIGURATION

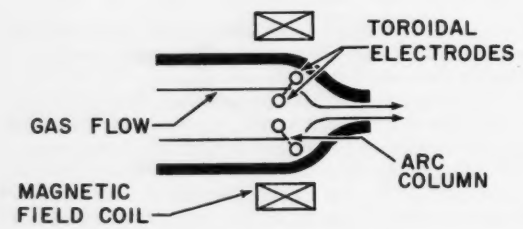

(b) TOROIDAL CONFIGURATION

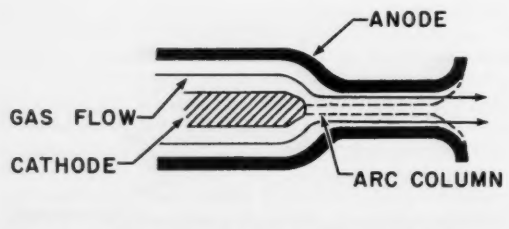

(c) CONSTRICTED CONFIGURATION

Figs. 3 Plasma generator configurations

Voltage-Current Characteristics

Plasma generators, like ordinary electric arcs without forced convection, have definite intrinsic electrical properties. However, the mass flow of gas through the arc chamber represents a new, independent parameter not present in ordinary arcs with natural convection.

Typical voltage-current characteristics for a cylindrical configuration plasma generator (Fig. 3a) with a central carbon cathode and a surrounding water-cooled copper anode are presented in Fig. 4 (103). The working fluid is air. At fixed mass flow, the arc voltage is relatively insensitive to arc current. However, at fixed current and essentially constant chamber pressure, the arc voltage increases significantly with air mass flow. At fixed mass flow, the arc voltage is observed to increased in proportion to a fractional ($\frac{1}{4}$ to $\frac{1}{2}$) power of the arc chamber pressure (46,69,104). The value of the pressure exponent is an empirical function of the arc configuration and operating conditions.

In Fig. 5, arc voltage-current characteristics are presented for operation of a constricted configuration plasma generator (Fig. 3c) with argon, helium, nitrogen and hydrogen (102). The arc unit to which these data pertain uses a thoriated tungsten cathode and a water-cooled copper nozzle-anode, and in these experiments was operated with the anode spot in the throat region. Fig. 5 shows that, at currents greater than 350 amp, the arc voltage becomes relatively insensitive to the current. The striking variation in arc voltage with gas type is well known from studies on arcs without forced convection, and is attributed to the corresponding variation in thermal conductivity (105,106).

Calibration Procedures

The simplest method conceptually for determining the properties of a gas stream issuing from a plasma generator is to assume that the exit flow is one-dimensional, steady and in equilibrium. Estimates of the average free stream thermodynamic and gasdynamic properties may then be obtained from measurements either of total mass flow and net power to the gas (103,107), or of the mass flow and arc chamber pressure (108). The main shortcoming of these approaches is that the exit flow from existing plasma generators deviates substantially from one dimensionality.

Probably the simplest calibration technique for determining the *local* enthalpy of the emergent gas is that proposed by Brogan (70). This method is based upon measurements of the stagnation pressure and the stagnation point heat flux at the center of a supersonic jet of arc heated air. On the assumption that the stagnation point heat transfer results obtained in the shock tube (50) are applicable to the exit stream of a plasma generator, these data are sufficient to determine the local stagnation enthalpy at the center of the jet. For plasma generators with plenum chambers, the local enthalpy determined using Brogan's technique agrees crudely with the average gas enthalpy determined from measurements of arc chamber pressure, mass flow and power to the gas, but the occurrence of substantial deviations indicates the presence of residual nonuniformities in the emergent flow (102).

More advanced techniques have been developed recently for measuring the local thermodynamic and gasdynamic properties of arc heated gases. The apparatus used includes conventional static and stagnation pressure probes and newly developed probes for measuring local stagnation en-

thalpy (109–111) and local mass flow (110,111). Measurements obtained using these instruments can be combined to yield estimates of the local flow state in terms of velocity, density, pressure and enthalpy, without recourse to the assumption of equilibrium (110,111). This type of calibration procedure makes it possible to assess the effectiveness of a plasma generator plenum chamber in smoothing out spatial flow nonuniformities, and is well suited for determining the characteristics of the environment to which test materials and structures are subjected.

The preceding types of measurement pertain to local continuum properties of the flow. Other procedures, such as spectroscopic techniques and methods for determining the electron concentration (34,112–116), yield information about the local gas kinetic properties, e.g., concentrations of individual molecular, atomic or ionic species, and the "temperatures" associated with the translational, rotational, vibrational and electronic motions. If the plasma generator effluent gases are in equilibrium, the species concentrations and temperatures can be calculated from thermodynamic considerations. However, the assumption of equilibrium is not invariably valid. For example, preliminary experiments by Blackman using both induction coil and Langmuir probe techniques suggest that arc heated argon has an abnormally high electron temperature and concentration (117). Evidence for excessive ionization in argon, based upon a simple arc energy balance, has also been reported by Cann and Ducati (118).

Operating Limits

Table 2 shows estimated performance limits for a continuous 1-megawatt plasma generator operated with air for re-entry simulation. The tabulated values of maximum enthalpy and energy conversion efficiency are based upon rough interpolations and extrapolations of available data (46,78,80,81,104), so that Table 2 should be considered only semiquantitative. It is generally recognized that air enthalpies substantially in excess of 350 RT_0 can be obtained at 1 atm by reducing the size of the plasma generator plenum chamber. However, this increase in mean enthalpy is achieved at the expense of flow steadiness and uniformity. The effect of these changes upon the validity of material studies has not yet been established.

Table 2 Operating limits, 1-megawatt plasma generator

Arc chamber pressure, atm	Maximum enthalpy, h/RT_0	Energy conversion efficiency, %
1	250–350	50–75
25	150–200	40–60
50	70–150	20–40
100	30–90	10–20

Perhaps the most significant feature of the operating limits shown in Table 2 is the progressive reduction in arc efficiency and maximum obtainable gas enthalpy with increasing pressure. The same trend appears at all power levels. This effect may prove to represent a fundamental limitation upon the production of high pressure, high temperature gases using plasma generators.

Considerable effort has also been expended on the operation of plasma generators with gases other than air. Table 3 presents experimental values of the maximum specific enthalpy obtained in a 50-kw constricted configuration plasma generator (thoriated tungsten cathode, copper anode) operated at chamber pressures between 1 and 5 atm in four different gases (102). Similar results have been reported by Browning (75). It is seen that the maximum specific enthalpy varies with gas type over a wide range. Table 3 also gives the maximum enthalpy in units of the RT_0 for each gas. This nondimensional

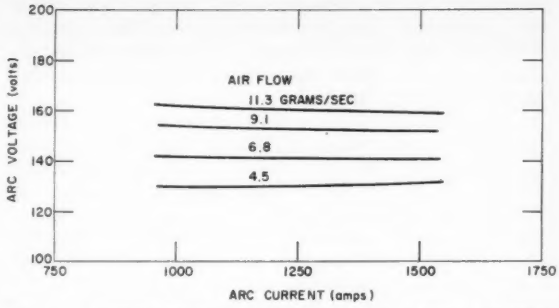

Fig. 4 Current-voltage characteristics for plasma generator operation in air

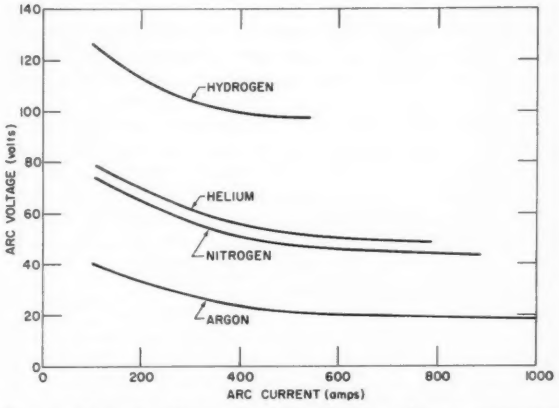

Fig. 5 Current-voltage characteristics for plasma generator operation in argon, nitrogen, helium and hydrogen; chamber pressure 1 atm, mass flow 0.50 gm per sec

enthalpy is, in marked contrast to the specific enthalpy, relatively insensitive to gas type. The present level of theoretical understanding of arcs and plasma generators is not adequate to permit quantitative explanation of this interesting and useful empirical generalization. However, since h/RT_0 is proportional to the *molar* enthalpy, this experimental result implies crudely that the plasma generator imparts approximately the same amount of energy to each gas particle passing through it, regardless of type.

Contamination

The requirements on a plasma generator for re-entry simulation include, in addition to high pressure, enthalpy and power, a demand for high purity of the heated air stream. The principal source of contamination in an arc tunnel is loss of material from the electrodes, and in most existing units these are constructed of carbon, tungsten and copper.

Table 3 Maximum enthalpy in various gases

Gas	Molecular weight	RT_0, Btu/lb	Maximum enthalpy, Btu/lb	Maximum enthalpy, h_{max}/RT_0
hydrogen	2	488	140,000	290
helium	4	244	70,000	290
nitrogen	28	34.8	15,000	430
argon	40	24.4	8,000	330

The seriousness of a given weight percentage of contamination depends upon both the nature of the contaminant and the type of test being conducted. The following are the principal possible effects of contamination in experiments designed to evaluate ablative materials:

1 Gross change in the chemical composition of the boundary layer over the surface of the ablation specimen. For example, a given amount of carbon contaminant will combine with 2.7 times its own weight of oxygen, so that 4 weight per cent of carbon will reduce the free oxygen concentration in the boundary layer by a factor of 2. The significance of such a change depends upon the type of ablative material being studied. For ceramic oxides, the effect is negligible. For plastics which undergo surface combustion, a major change in the concentration of available oxygen might tend to invalidate the experimental results. However, even in this case, Georgiev and Rose (119) suggest that a few per cent of carbon contamination may not be seriously detrimental. From this standpoint of gross change in composition, a given weight percentage of tungsten or copper contamination is considerably less serious than the same percentage of carbon, since, because of their high atomic weights, these metals combine with only a fraction of their own weight of oxygen.

2 Direct interaction of the contaminant with the ablative material. Contaminants may, for example, deposit upon the ablating surface, react chemically with it or dissolve in it. In the case of glassy-type ablative materials (51) which rely upon maintenance of a high viscosity in the molten layer, dissolution of comparatively small amounts of contaminants, such as tungsten trioxide and cupric oxide, could have a major effect upon material performance.

3 Change of gas properties which depend sensitively upon gas composition. Such properties include electrical conductivity and radiative emissivity, and are chiefly of interest in experiments simulating space probe re-entry.

Typical observed percentages of contamination for 1-megawatt d-c plasma generators operated at chamber pressures in the 1- to 5-atm range and air stagnation enthalpies up to 300 RT_0 are given in Table 4. The data refer to units utilizing central cathodes of carbon (102,119), thoriated tungsten (120) and water-cooled copper (81). In all cases, the anode is water-cooled copper.

As a general rule, the contamination level appears to rise with increasing arc current and with increasing pressure. In chemically inert gases (e.g., helium) and in reducing ones (e.g., hydrogen), the amount of contamination is considerably reduced, particularly in the cases of carbon and thoriated tungsten. For example, a thoriated tungsten cathode operated continuously at a current of 600 amp for 37 hr in helium showed a weight loss of less than 0.1 gm (102), a value lying far below the theoretical lower limit suggested by Pearce (121).

A number of schemes have been proposed and investigated for reducing the contamination level in plasma generators. Probably the most successful of these techniques is to operate a plasma generator with a thoriated tungsten cathode using nitrogen, with cold oxygen added downstream in order to simulate the composition of air (122). Work on use of porous transpiration-cooled electrodes has been carried out at NASA-Ames (78), General Electric (97) and Vitro (123). Results obtained at NASA-Ames indicate that this approach leads to a low maximum gas enthalpy. Another contamination reducing technique is to suck away the gas surrounding the electrodes, to remove contaminants from the main gas stream. Investigation has shown that this approach does reduce the contamination level, but only at a sacrifice in efficiency and gas enthalpy. A fourth method involves surrounding a thoriated tungsten cathode with a layer of argon to protect it from oxidation. The difficulty with this scheme is simply the relatively large quantity of argon required, e.g., 10 or 20 weight per cent of the main gas flow. The question then is whether 20 per cent argon contamination is more or less significant than 5 per cent carbon contamination. The answer would depend upon the particular application intended.

Table 4 Contamination level as a function of cathode material

Cathode material	Contamination level, %
carbon (102,119)	~5
thoriated tungsten (120)	~0.5
cooled copper (81)	~0.2

Alternating Current Operation

The relatively high cost of a-c/d-c power conversion equipment makes alternating current plasma generators attractive, especially for large chemical processing or re-entry simulation facilities operating at multimegawatt power levels. Recent effort on large-scale a-c arcs in this country has been concentrated at NASA-Langley (62–64,79) and at General Electric MSVD in Philadelphia (67,68). The earliest units utilized four carbon electrodes and operated successfully on three-phase alternating current. However, the contamination level was 10 per cent or higher, and the enthalpy level of the exhaust stream was relatively low.

Recently, the trend in three-phase alternating current plasma generator design has turned to "cold" water-cooled electrodes instead of the original "hot" refractory electrodes. The electrodes are co-planar concentric rings, and the arcs are made to revolve about the unit's axis by means of an external magnetic field transverse to the arc path (79). The water-cooled copper electrodes give very low contamination in the exhaust stream when operated in low pressure air. However, the highest enthalpy values obtained so far appear to be considerably below those obtained in direct current plasma generators. The reason for the characteristically lower enthalpies of existing a-c plasma generators in comparison with d-c generators is probably the larger volume and greater area of electrode surface inherent in the a-c designs.

Radio-Frequency Heating

Smith and Early (124), some years ago, attempted to develop a system for heating a low density, supersonic gas stream using an arc discharge. The motivation for this work was the elimination of the throat cooling problems encountered in high enthalpy test facilities in which the energy is added to the gas upstream of the throat. Smith and Early's experiments were conducted in a Mach 4 air stream at static pressures of the order of 1 mm Hg. The arc was stabilized transverse to the stream by means of a magnetic field. However, even at the low pressures used, the arc tended to constrict into a narrow column and localize in the boundary layer. This approach toward uniform heating of a supersonic gas stream, therefore, did not appear promising (124, 125). Subsequently, Early and Miller (125) also studied heating by means of a pulsed corona discharge.

A new method for achieving relatively uniform energy addition to a supersonic gas stream, radio-frequency heating, was investigated by Chuan (126,127). In these experiments, air was expanded through a glass nozzle to Mach 3.5, then partially ionized by an RF discharge at a frequency of 10 mc. Recombination downstream transformed the added ionization energy to thermal form. The highest downstream stagnation temperature achieved was 1200 K at a static pressure of 0.40 mm of mercury. Williams (128) and Romig (129) have carried out theoretical analyses to determine the time and length required for the recombination processes.

Recently, Reed (130) at MIT Lincoln Laboratory has successfully operated a radio-frequency (4 mc) plasma generator

in argon at atmospheric pressure. Measured peak temperatures ranged from 14,000 to 19,000 K. The total power transferred to the gas ranged from 1.5 to 3.0 kw. The results suggested that equilibrium was closely approached in the heated gas.

(Operation of RF electrodeless discharges in air at atmospheric pressure was previously reported by G. I. Babat, in "Electrodeless Discharges and Some Allied Problems," J. Institution of Electrical Engineers, pt. III, vol. 94, 1947, pp. 27-37.)

Radio-frequency or induction heating is an attractive method for adding energy to gas streams, because it does away with the use of electrodes and thus eliminates what, in plasma generators of a more conventional type, is usually the major source of contamination. In wind tunnel applications, the possibility of adding heat downstream of the throat, to avoid throat cooling problems and reduce energy losses from the gas, is a further advantage. Even though the use of radio-frequency power imposes a severe penalty in power supply cost, the potential advantages of this gas heating technique are of sufficient importance to insure its continued study and eventual utilization in specialized applications.

Factors Affecting Plasma Generator Performance

Existing plasma generators fall short of meeting the pressure, enthalpy, gas purity and electrode life requirements for re-entry simulation and space propulsion. In order to understand and overcome the observed performance limitations, it is necessary to examine the principal factors limiting or otherwise influencing plasma generator performance. These include heat losses from the gas, electrode phenomena, arc column behavior and interactions between arcs and magnetic fields.

Convective and Radiative Heat Losses

The advance of plasma generation technology into the high temperature, high pressure region may ultimately be limited by heat transfer problems. As operating pressure is increased at a given enthalpy level, both convective and radiative heat transfer rates rise, imposing more and more severe requirements upon cooling systems and power supplies, and making the attainment of high gas enthalpy in the test section increasingly difficult.

The convective heat flux from a heated gas stream to a wall may be represented by the formula

$$q_c = C_H \rho U \ (h_s - h_w) \qquad [1]$$

where

q_c = convective heat flux
C_H = Stanton number
ρU = streamwise mass flux

The Stanton number in turbulent flow is given by the empirical expression (131)

$$C_H = 0.023/N_{Pr}^{0.60} \ N_{Re}^{0.20} \qquad [2]$$

where N_{Pr} and N_{Re} are the Prandtl and Reynolds numbers, respectively. It is evident from Equations [1 and 2] and the continuity relation ρUA = constant, that the highest convective heat transfer rate is encountered where the flow has its smallest cross-sectional area, and where the mass flux ρU consequently has its maximum value. Normally, this condition occurs at the throat of the plasma generator exit nozzle.

Fig. 6 shows lines of constant throat heat flux in a plot of plasma generator chamber pressure vs. stagnation enthalpy, assuming sonic flow of air in a throat of ~0.5-in. diameter. The heat flux values are relatively insensitive to throat diameter at fixed enthalpy and pressure, so that the throat heating rates in Fig. 6 can be considered typical of those in nearly any laboratory-size arc tunnel facility operated with air.

Within the present state of the art, it is possible, by water cooling, to prevent major loss of material from copper surfaces exposed to steady heat fluxes of 5 to 10 kw per cm² (46,132,-133). Throat heat fluxes of about 20 kw per cm² are implied (Fig. 6) by some of the more severe re-entry simulation requirements illustrated in Fig. 1. Improvement of the high pressure, high enthalpy capabilities of plasma generators is thus dependent upon the development of improved forced convection cooling techniques.

The radiative power loss from an optically thin[4] sample of heated air is shown as a function of enthalpy and pressure in Fig. 7. The values plotted are based upon work of Kivel and Bailey (134) and are estimated to be accurate to within a factor of 2 or 3. The rapid increase of radiated power with pressure and enthalpy illustrated in Fig. 7 poses three interrelated problems in the design of high pressure plasma generating units:

1 The radiative loss must be supplied by the plasma generator power source, and may multiply the power supply requirement of a unit by a substantial factor. For example, Fig. 7 shows that a unit with a 3-in. diameter spherical chamber, operating at a pressure of 100 atm and an enthalpy of 300 RT_0, would have a radiative power loss of over 2 megawatts.

2 The energy radiated from the gas is absorbed by the walls of the arc chamber, and imposes a relatively severe requirement upon the chamber cooling system. The general

[4] The values of radiated power and reradiation time plotted in Figs. 7 and 8 are calculated on the assumption that the gas is optically thin. If the linear dimensions of the gas are comparable with or larger than the absorption length, the cooling of the central part of the sample is retarded by the shielding effect of the surrounding gas. The effect of opacity is negligible at pressures of 40 atm and lower (39). At 100 atm and h/RT_0 = 300, however, the absorption length is 4 in., and under these conditions absorption effects would be significant for units with chamber diameters in excess of an inch or two. Therefore, at the highest pressures and enthalpies, the results shown in Figs. 7 and 8 must be modified to take optical absorption effects into account.

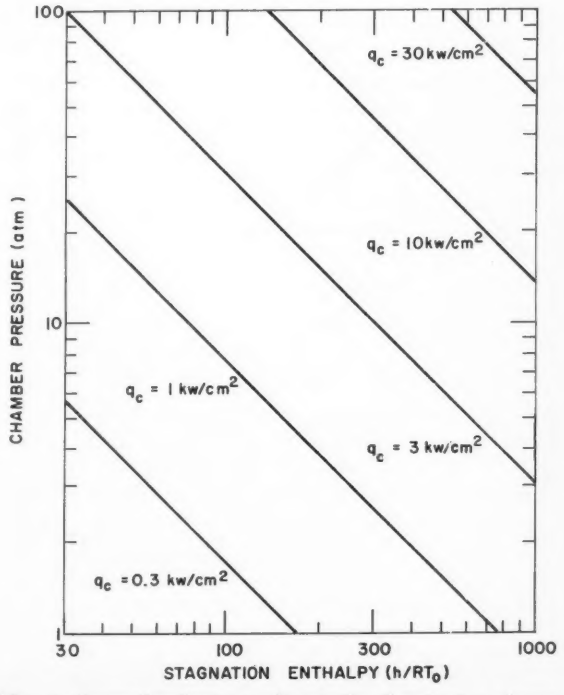

Fig. 6 Convective heat transfer at the throat of a plasma generator

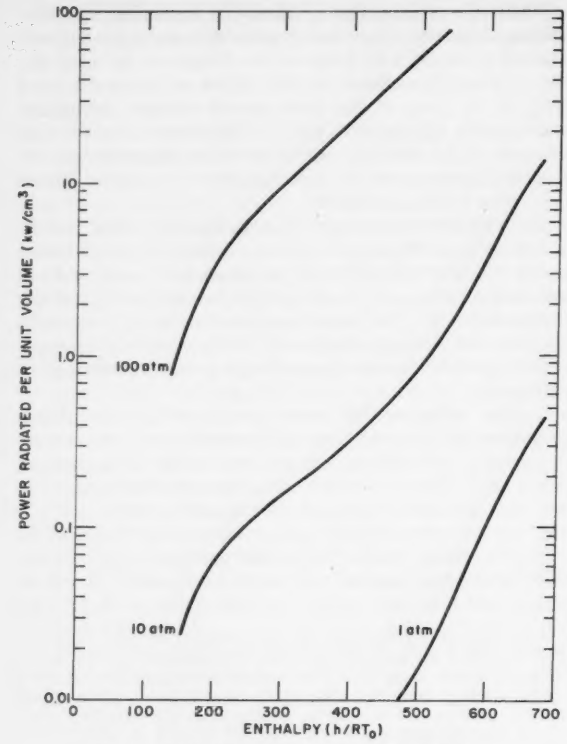

Fig. 7 Radiative power loss from heated air

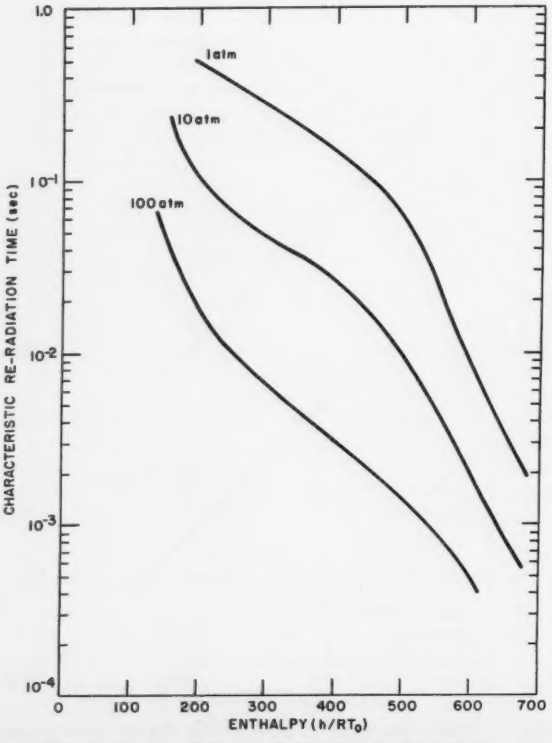

Fig. 8 Characteristic reradiation time for heated air

magnitude of the radiative heat flux to the wall is given by

$$q_r = rP_o/3 \qquad [3]$$

where r is the spherical chamber radius. For the case of a 3-in. sphere containing air at 100 atm and 300 RT_0, the heat flux is about 10 kw per cm².

3 As a result of radiation, air at high pressures and temperatures loses its energy content quite quickly. Fig. 8, also based upon the work of Kivel and Bailey (134), gives the time required for a sample of air at given enthalpy and pressure to radiate away all of its enthalpy, based upon the initial instantaneous cooling rate. The cooling rate, of course, changes continually as the gas temperature falls. However, Fig. 8 indicates the importance of reducing chamber and nozzle length in the direction of the gas flow, to cut down the time during which the gas can cool off.

The rapid increase in radiated power and decrease in reradiation time with increasing pressure and enthalpy, as shown in Figs. 7 and 8, is presumably one of the principal causes of the empirically observed decrease in gas enthalpy with increasing arc chamber pressure (see Table 2). Detailed theoretical and especially experimental studies are needed to determine whether this "radiation barrier" can be circumvented by ingenious design, or whether it sets an unavoidable limit to the advance of plasma generator technology into the high pressure, high temperature regime.

Electrode Processes

An electric arc discharge consists of three relatively distinct regions: The arc column and the cathode and anode fall zones. The column normally occupies most of the volume of the discharge and, although it is characterized by a relatively low potential gradient, accounts for most of the observed voltage drop between the electrodes. The conversion of electrical to thermal energy in the gas thus occurs mainly in the arc column. The anode and cathode fall zones are very thin but contain high potential gradients. Processes occurring at and near the surfaces of the electrodes determine in large part the loss of material from the electrodes and the contamination level of the final heated gas stream.

Surveys of theories and experimental data on arc electrode phenomena have been presented by Cobine (135), von Engel (136), Brown (137), Somerville (138), and Finkelnburg and Maecker (139). The available information may be summarized from the viewpoint of plasma generation technology as follows.

Arc cathodes may be classified into two types, cold cathodes and refractory cathodes. Both types have fall voltages of about 5 v when operated at high currents. The term "cold cathode" is applied to metals which exhibit negligible thermionic emission at temperatures up to their boiling points, e.g., copper. Cold cathodes are characterized by extremely high current densities ($\sim 10^6$ amp per cm²), irregular motion of the cathode spot over the surface, and often by the existence of several cathode spots (138). The physical process by which the cold cathode emits electrons is a subject of considerable controversy and not yet resolved (140–144).

Refractory cathodes (e.g., tungsten and carbon) can, in principle, supply a substantial fraction of the cathode current by thermionic emission at temperatures below the boiling point. This indeed happens in some cases, and the resulting cathode current density is of the order of 10^3 amp per cm². However, under other arc conditions, refractory cathodes (in particular, tungsten) exhibit current densities of 10^4 to 10^5 amp per cm²(145), which are too high to be explained by a purely thermionic processs. The cause of the transition from the thermionic to the "burning-spot" mechanism, and the process by which electrons are emitted from the concentrated cathode spot are not clearly understood (145). One key question appears to be the partition of the cathode current between electrons and positive ions.

In the case of the anode, the current through the fall zone is carried entirely by electrons (146). The anode fall potential serves to accelerate these electrons toward the anode surface. Part of the energy thus added to the electrons is transferred to the anode surface, and part is expended in ionizing gas molecules in the fall zone. This latter process is described as "field ionization" if the electrons experience, on the average, only a single heavy particle collision in traversing the fall zone, and as "thermal ionization" if the electrons experience many such collisions (146). The ions produced in the fall zone are drawn into the arc column by the electric field, and serve to replace the ions withdrawn from the column by collection to the cathode. At low currents, the fall potential for metal anodes is of the order of 10 v, indicating that field ionization may play an important role. At high currents, however, the fall potential is much lower, often of the order of 1 or 2 v, and presumably thermal production of ions in the anode fall region is the dominant process (146).

Current densities on metal anodes at high currents are of the order of 10^2 to 10^4 amp per cm^2 (114,146). In some cases, the anode spot tends to "stick" to its position on the surface, and skips if forced to move by application of a magnetic field (146).

The existence of electrode fall potentials of several volts together with relatively high current densities implies that the electrode fall zones are regions of intense energy dissipation. Because of the thinness of the zones, a substantial fraction of the heat generated within them must be transferred to the electrode surfaces. The resulting heat flux should be in each case of the same order of magnitude as the electrode fall power dissipation per unit area, given by

$$q_f = j_e V_e \qquad [4]$$

where

j_e = electrode spot current density
V_e = electrode fall potential

Table 5 presents estimated values of the current density and fall potential for several types of electrodes, together with corresponding values of the electrode spot energy flux calculated using Equation [4]. The values given in this table should only be considered semiquantitative, because the current density and fall potential vary with gas type, pressure, current level and arc geometry, and data in the literature are often in wide disagreement with one another. In addition to these uncertainties, the values of energy flux given in the last column provide, in any event, only a crude estimate of the net heat flux to the electrode surface, since only a fraction of the power dissipated in the fall zone is transferred to the surface, and since other effects, such as absorption and release of electron work-function energy, have not been considered.

All of the energy flux values given in Table 5 are high by ordinary heat transfer standards, but the values nevertheless cover a range of more than three orders of magnitude. The flux of ~6 kw per cm^2 to a carbon cathode is partially reradiated (~1 kw per cm^2), but presumably is absorbed mainly by vaporization. A heat flux of the order of ~2 kw per cm^2 to a copper anode can be handled easily by water cooling (114). The flux of ~200 kw per cm^2 to the spot on a thoriated tungsten cathode is very high, but such cathodes are generally observed to survive without serious loss of material in nonoxidizing gases, at least at current up to about 1000 amp. It is speculated that three-dimensional heat conduction within the cathode provides sufficiently intense local cooling to limit the molten region (if any) to a size which can be retained in its position on the electrode by surface tension. In the case of a copper cathode, the estimated local heat flux of ~7000 kw per cm^2 is so high that catastrophic failure of the electrode occurs almost instantaneously, unless the cathode spot is forced to move rapidly over the surface. Such motion of the cathode spot can be provided by aerodynamic means (vortex flow within the arc chamber), but is perhaps best accomplished by application of a magnetic field as discussed in the following.

From the standpoint of plasma generation technology, electrode phenomena are chiefly of interest in connection with the loss of material from the electrode surfaces, which affects electrode life and gas purity. It is known empirically that well-cooled metal anodes can be operated without gross melting or vaporization. Pearce (121) has suggested that the loss of material from the cathode has a lower limit, which might be approached by strong cooling and rapid forced motion of the cathode spot, and that this limit is determined by the sputtering loss. He estimates, on the basis of data published by Holm (147), that this sputtering loss is 2×10^{-6} gm per coulomb for tungsten, 1.0×10^{-5} gm per coulomb for copper, and 1.1×10^{-5} gm per coulomb for carbon. However, as mentioned previously in the section on contamination, material loss rates several orders of magnitude lower than Pearce's estimate have been observed in the case of tungsten. Thus, at present, it is not definitely known whether, even in principle, electrode material loss is required for operation of an arc.

Table 5 Electrode phenomena, high current arc

Material	Electrode	Fall potential V_e, v	Current density j_e, amp/cm^2	Energy flux q_f, kw/cm^2
carbon	cathode	3[a]	2×10^3 [b]	6
copper	anode	4[b]	5×10^2 [c]	2
copper	cathode	7[d]	10^6 [e]	7000
tungsten (thoriated)	cathode	7[b]	3×10^4 [a,b,e]	200

Note: 1 kw/cm^2 = 881 Btu/ft^2sec = 239 cal/cm^2 sec.
[a]Reference (36), pp. 406–407.
[b]C. Sherman, Avco RAD, unpublished data.
[c]Reference (114).
[d]Estimated.
[e]Reference (141).

Arc Column Behavior

Energy addition to the gas heated in a plasma generator occurs mainly in the arc column, the partially ionized path along which the arc current flows. The electric field accelerates electrons in the column toward the anode, and the kinetic energy thus imparted to the electrons is transferred to the ions, atoms and molecules and distributed over the various degrees of freedom by means of collisions.

From a macroscopic point of view, the details of these collision processes can be ignored, and the density U_c of power dissipation in the arc column can be calculated using

$$U_c = j_c X_c \qquad [5]$$

where

j_c = current density
X_c = voltage gradient or electric field strength in the column

Energy is removed from the column by the usual mechanisms: Radiation, conduction or aerodynamic heat transfer, and convection or transport of sensible heat by flow of the heated gas.

Numerous attempts have been made to develop theories of the arc column based in part upon a balance of these energy production and removal processes. The earlier work in this area was concerned principally with the classical unconfined arc subject to natural convection. Examples include investigations by Suits and Poritsky (148) and by Champion (149). These theories (148,149) are fairly successful in predicting the experimentally observed form of the variation of column voltage gradient with total current, pressure, column diameter

Table 6 Effects of confinement upon the arc column in nitrogen at 1 atm

	Column diameter, cm	Current, amp	Voltage gradient, v/cm	Mean current density, amp/cm²	Mean conductivity, mho/cm	Mean temperature, K	Mean power density, kw/cm³	Radiative power loss, kw/cm³
Unconfined arc (157)	1.6	20	13	10	0.8	7,000	0.13	...
Confined arc (154)	0.50	20	30	100	3.3	8,000	3	...
	0.50	100	22	500	23	9,500	11	0.5
	0.50	300	29	1500	52	13,000	44	1.9

and gas type for low current arcs ($\lesssim$10 amp). In the low current region, for arcs subject to free convection, the column gradient is found to decrease with increasing current, to increase with pressure, and to be higher for low molecular weight gases (150). For the high current region ($\gtrsim$100 amp), accurate and systematic measurements of the behavior of the unconfined arc column as a function of pressure, current and gas type do not appear to be available. For plasma generator design, arcs with forced convection are of more interest than those with natural convection. Again, however, very little information on the characteristics of the unconfined arc column with forced convection is present in the literature. Qualitatively, forced convection causes a rise in column voltage gradient, and has been observed (151) to produce constriction of the arc column.

The confined arc column[5] is more attractive for both experimental and theoretical study than the unconfined arc, because its boundary conditions are more clear cut, and because it can be forced to possess axial symmetry. Maecker (152–154) and Schmitz and Uhlenbusch (155) have investigated the cylindrically symmetrical confined arc without gas flow, and Emmons (156) is studying the case with laminar flow along the arc column. Confinement has the effect of increasing the current density, the voltage gradient and the column temperature, as illustrated in Table 6 in which data of Maecker (154) and Foitzik (157) for nitrogen arcs at 1 atm are used. The current densities shown are simply mean values based upon the total current and cross-sectional area. The conductivity, in turn, is calculated using $\sigma = j_c/X_c$ with the mean current density. The temperature is estimated from this mean conductivity using the theoretical relation between σ and T (158). Actually, none of these quantities is constant over the cross section of the arc column, but the mean values nevertheless give an indication of their general magnitudes and trends.

The power density values shown in Table 6 are roughly of the same order of magnitude as those ($\sim$10 kw per cm³) observed in high performance chemical rocket engines (159). With stronger confinement, the power density in an arc column can be raised to much higher values, e.g., 1000 to 10,000 kw per cm³.

The last column of Table 6 gives the mean radiative power loss per unit volume from the arc column, based upon Maecker's (154) measurements. In nitrogen at 1 atm, this loss is only of the order of 5 per cent of the input power density. However, Fig. 7 shows that the radiative power loss per unit volume rises very steeply with increasing pressure. Radiation from the arc column may therefore exert a major influence upon plasma generator operation at high pressures. The progressive reduction in efficiency and enthalpy observed at pressures in the 10- to 100-atm range (Table 2) may be, in large part, a consequence of this effect.

Magnetic Field Effects

Because of the very high current densities and local heating rates on low melting point cathodes, such as copper, electrodes of this type can be operated at high current levels only if the cathode spot is forced to move rapidly over the surface. At very high current levels, forced anode spot motion is also required to prevent excessive contamination of the heated gas.

Arc column and electrode spot motion can be induced by the imposition of a magnetic field perpendicular to the direction of current flow in the arc. A rather natural approach to the prediction of such motion is to regard the arc column as a conductor carrying a current, acted upon by the usual electromagnetic driving force and by aerodynamic drag forces. However, the phenomena produced by operation of an arc in a magnetic field are considerably more complicated than this simple model would suggest, as illustrated by the following experimental observations:

1 Application of a magnetic field at right angles to the direction of current flow in the neighborhood of a cathode spot very often causes the arc spot to move in a direction opposite to that predicted by the ponderomotive force law or "right-hand rule" (160). This so-called "retrograde" motion has been observed both on mercury and on solid metal cathodes, and its occurrence depends upon several variables including pressure and electrode separation. Theories to explain it have been put forward by Robson and von Engel (161,162) and Smith (163), among others. However, the various theories appear to be in contradiction, and none has gained general acceptance.

2 The velocity of arc motion in weak fields has been reported by Guile et al. (164–166) to be determined principally by processes occurring in the cathode spot region. Use of a ferromagnetic material for the cathode leads to a marked increase in cathode spot velocity. In the case of a permanently magnetized cathode, the spot moves in such a way as to suggest that the direction of motion is determined by the field within the cathode material rather than that outside (165).

3 Application of a strong axial magnetic field to an open cylindrical plasma generator similar to configuration (a) in Fig. 3 has been observed (167) to transform the arc column into a relatively uniform current carrying "disk" possessing approximate circular symmetry.

The utilization of magnetic fields to induce electrode spot motion in plasma generators is, at present, accomplished on a semi-empirical basis. It is found, in practice, that magnetic field configurations designed using the simple Amperian approach usually do reduce electrode erosion, provided that the fields used are made strong enough. It is anticipated that magnetic field-arc interactions will continue to be a fruitful area of investigation, both for their engineering applications in plasma generator design and for their purely scientific interest.

Conclusions

During the next few years, plasma generators will receive increasingly widespread use in high enthalpy simulation, space propulsion and other fields. These applications will generate increasingly severe performance requirements which, in the immediately foreseeable future, will substantially exceed the capabilities of all existing types of arc gas heating

[5] This term is used to denote an arc which burns within a tight-fitting channel with well-cooled walls. Such arcs are sometimes also described as "wall-stabilized."

equipment. The primary requirements will be for operation at high pressure (~100 atm) and enthalpy (300 to 900 RT_0), with very low contamination of the heated gas stream and with long electrode life. Empirical trends observed in performance data for existing units indicate that achievement of these goals will necessitate major advances.

The ultimate limitations on plasma generator performance are, at present, not established. It is not known whether electrode material loss is essential to arc operation, or whether fundamental upper limits on arc enthalpy and operating pressure exist. Thus, present knowledge is even inadequate to establish the feasibility of meeting a given set of performance requirements.

Until recently, the development of new plasma generator configurations has proceeded largely on an empirical basis. This type of approach will doubtlessly continue to achieve some success, but it appears that major improvements in performance will require the expenditure of a great amount of effort on numerous presently unresolved problems of arc phenomenology and mechanism.[6]

Acknowledgments

The authors wish to express their gratitude to the many individuals who have supplied information from their respective laboratories in the form of personal communications. Acknowledgment is made particularly to T. Brogan and P. Rose of the Avco-Everett Research Laboratory, J. R. Jedlicna of NASA-Ames, J. N. Kotanchik of NASA-Langley, C. E. Shepard of NASA-Lewis, Dr. R. Buhler and Mrs. D. Christensen of Plasmadyne Corp., Dr. M. Boobar of Vidya, Inc. and, finally, to H. Marcus and E. Soehngen of Wright Air Development Div., USAF. The information on the plasma generator patent situation was obtained in large part by Avco RAD patent counselors W. Kunz and A. Ogman. Finally, the authors have benefited from numerous discussions and constant support from their associates at Avco RAD, particularly, Dr. J. Yos, Experimental and Theoretical Physics Section; Dr. M. Malin, Manager, Physics Research Department; and Dr. F. deWeiss, Technical Staff Assistant to the Vice President.

References

Chemical Synthesis

1 Edstrom, J. S., "Electrical Extraction of Nitrogen from the Air," *Electrochemical Industry*, vol. 2, 1904, pp. 399–400.

2 Phillips, R. C. and Ferguson, F. A., "High Temperature Chemical Synthesis," in "Proceedings of an International Symposium on High Temperature Technology," McGraw-Hill Book Co., Inc., N. Y., 1960, pp. 192–197.

3 Schönherr, O., "On the Manufacture of Nitric Oxide by the Process of the Badischen Anilin- und Sodafabrik," *Electrotechnische Zeitschrift*, vol. 30, 1909, pp. 365–369, 397–402. (In German.)

4 Baumann, P., "Generation of Acetylene by the Arc Process," *Angewandte Chemie*, vol. B20, 1948, pp. 257–259. (In German.)

5 Stokes, C. S. and Knipe, W. W., "The Use of a Plasma Jet in Chemical Synthesis," Research Institute of Temple University, 1959.

Refractory Processing

6 Mathers, E. A., "Electric Arc Furnace Heater," U. S. Patent no. 1,002,721 (1911).

7 Rava, A., "High Temperature Torch," U. S. Patent no. 2,011,873 (1935).

8 Rava, A., "High Temperature Torch," U. S. Patent no. 2,052,796 (1936).

9 Rava, A., "Electric Arc Torch Apparatus," U. S. Patent no. 2,768,279 (1956).

10 Briggs, R. L., "High-Temperature Electric Torch," U. S. Patent no. 2,769,079 (1956).

11 Briggs, R. L., "Electric Arc Torch," U. S. Patent no. 2,770,708 (1956).

12 Gage, R. M., "Arc Torch and Process," U. S. Patent no. 2,806,124 (1957).

13 Gage, R. M., "Arc Torch and Process," U. S. Patent no. 2,858,411 (1958).

14 Kane, J. S. and Hill, C. W., "Arc Torch," U. S. Patent no. 2,858,412 (1958).

15 Gage, R. M., "Arc Torch Process with Reactive Gases," U. S. Patent no. 2,862,099 (1958).

16 Gage, R. M., "Electric Metal Arc," U. S. Patent no. 2,868,950 (1959).

17 Reed, T., "Non-transferred Arc Torch Process and Apparatus," U. S. Patent no. 2,874,265 (1959).

18 Oyler, G., "Arc Torch and Process," U. S. Patent no. 2,890,322 (1959).

19 Reed, T. R., "Arc Torch Push Starting," U. S. Patent no. 2,898,441 (1959).

20 Morton, H. S., "Liquid Vortex Arc Torch Process," U. S. Patent no. 2,906,858 (1959).

21 Anderson, J. E. and Reed, T., "Arc Torch Application," U. S. Patent no. 2,951,143 (1960).

22 Giannini, G. and Ducati, A., "Plasma Stream Apparatus and Methods," U. S. Patent no. 2,922,869 (1960).

23 Ducati, A. and Blackman, V. H., "Plasma-Jet Torch Apparatus and Method Related to Increasing the Life of the Back Electrode," U. S. Patent no. 2,941,063 (1960).

24 Giannini, G. M. and Ducati, A. C., "Self-Circulating Plasma Device," U. S. Patent no. 2,929,952 (1960).

25 Giannini, G. and Blackman, V., "High-Intensity Electrical Plasma-Jet Torch Incorporating Magnetic Nozzle Means," U. S. Patent no. 2,944,140 (1960).

26 Blackman, V. H., "Stabilized Magnetic Nozzle for Plasma Jets," U. S. Patent no. 2,945,119 (1960).

High Temperature Research

27 Finkelnburg, W., "The High Current Carbon Arc," Office of Military Government for Germany (U. S.), FIAT Final Rep. no. 1052, U. S. Dept. of Commerce, Washington 25, D. C.

28 Finkelnburg, W., "Hochstromkohlebogen, Physik und Technik einer Hochtemperatur-Bogenentladung," Springer-Verlag, Berlin, 1948.

29 Finekelnburg, W., "The High Current Carbon Arc and Its Mechanism," *J. Appl. Phys.*, vol. 20, 1949, pp. 468–474.

30 Maecker, H., "An Arc for High Intensities," *Zeitschrift für Physik*, vol. 129, 1951, pp. 108–122. (In German).

31 Weiss, R., "Investigation of the Plasma Jet Which Issues from a High Intensity Arc," *Zeitschrift für Physik*, vol. 138, 1954, pp. 170–182. (In German.)

32 Peters, T., "Plasma Jets with Supersonic Velocity," *Naturwissenschaften*, vol. 41, 1954, p. 571. (In German.)

33 Gerdien, H. and Lotz, A., "On a Light Source of Very High Surface Brightness," *Wissenschaftliche Veröffentlichungen aus den Siemens-Werken*, vol. 2, 1922, p. 489. (In German.)

34 Lochte-Holtgreven, W., "Ionization Measurements at High Temperatures," in "Temperature, Its Measurement and Control in Science and Industry," Vol. II, H. C. Wolfe, Ed., Reinhold Publishing Co., N. Y., 1955, pp. 413–427.

35 Finkelnburg, W., "The Behavior of Matter at High Temperatures," in "High Temperature—A Tool for the Future," Stanford Research Institute, Menlo Park, Calif., 1956, pp. 39–45.

36 Finkelnburg, W. and Maecker, H., "Electric Arcs and Thermal Plasma," in "Handuch der Physik, Vol. 22," S. Flügge, Ed., Springer-Verlag, Berlin, 1956, pp. 254–444. (In German.)

Re-Entry Simulation

37 Allen, H. J. and Eggers, A. J., "A Study of the Motion and Aerodynamic Heating of Missiles Entering the Earth's Atmosphere at High Supersonic Speeds," NACA TN 4047, 1957.

38 Chapman, D. R., "An Approximate Analytical Method for Studying Entry into Planetary Atmospheres," NACA TN 4276, 1958.

39 Stalder, J. R. et al., "Aerodynamic Applications of Plasma Wind Tunnels," Vidya, Inc., Palo Alto, Calif., Rep. no. 18, Feb. 1960.

40 Offenhartz, E. and Curtiss, H., "Design of Air Arc Experimental Facilities for Simulation of Re-Entry Ablation," Avco RAD, Wilmington, Mass., TR 59–12, March 1959.

41 Warren, W. R., "Laboratory Experimental Studies in Re-entry Aerothermodynamics," Tenth IAF Congress, London, Sept. 1959.

42 John, R. R. and Recesso, J., "Ablation Characteristics of a Subliming Material Using Arc Heated Air," ARS Journal, vol. 29, no. 9, Sept. 1959, pp. 663–665.

43 Warren, W. R. and Diaconis, N. S., "The Performance of Ablation Materials as Heat Protection for Re-Entering Satellites," IAS Paper no. 60–49, 1960.

44 Georgiev, S., Hidalgo, H. and Adams, M., "On Ablation for the Recovery of Satellites," Avco-Everett Research Laboratory, Everett, Mass., Research Rep. 47, March 1959.

45 Ferri, A. and Libby, P. A., "A New Technique for Investigating Heat Transfer and Surface Phenomena Under Hypersonic Flow Conditions," *J. Aeron. Sci.*, vol. 24, 1957, pp. 464–465.

46 Rose, P. H., Powers, W. E. and Hritzay, D., "The Large High Pressure Arc Plasma Generator: A Facility for Simulating Missile and Satellite Re-entry," Avco-Everett Research Laboratory, Everett, Mass., Research Rep. 56, June 1959; *also* ARS preprint 858–59.

47 "Semiannual Report on High Mach Number and Materials Research Program, Vol. II," Space Technology Laboratories, STL/TR-60-V002-09205, AFBMD-TR-60-118, July 1960.

48 Bogdonoff, S. M. and Hammitt, A. G., "The Princeton Helium Hypersonic Tunnel and Preliminary Results Above M = 11," Princeton Univ., Aeron. Engng. Rep. 260, June 1954; *also* WADC TN 54-124.

49 Lucas, W. and Huston, M., "Planning a Re-Entry and Recovery Test Program," Astronautics, vol. 4, 1959, no. 3, pp. 30–31.

50 Rose, P. H. and Stark, W. I., "Stagnation Point Heat Transfer Measurements in Dissociated Air," *J. Aeron. Sci.*, vol. 25, 1958, pp. 86–97.

51 Adams, M. C., "Recent Advances in Ablation," ARS Journal, vol. 29, no. 9, Sept. 1959, pp. 625–632.

52 Henshall, B. D., "A Review of the Development of High Enthalpy Aerodynamic Test Facilities," *Appl. Mech. Rev.*, vol. 13, 1960, pp. 387–390.

53 Perry, R. W. and MacDermott, W. N., "Development of the Spark-Heated, Hypervelocity, Blowdown Tunnel—Hotshot," Arnold Engng. Dev. Center, AEDC-TR-58-6, June 1958.

[6] After this article had been written, the authors' attention was drawn to another, very recent survey of plasma generation technology, prepared by the Materials Advisory Board of the National Academy of Sciences-National Research Council (168). This MAB report provides further information about many of the topics covered in the present review.

54 Rothacker, D., Sheer, C. and Mead, L., "The High Intensity Arc for Materials Evaluation," in "High Intensity Arc Symposium," The Carborundum Co., Niagara Falls, N. Y., 1958, pp. 138–165.

55 Sheer, C., Mead, L. H., Rothacker, D. L. and Johnson, L. H., "Measurement of Thermal Diffusivity of Various Materials by Means of the High Intensity Arc Technique," Vitro Laboratories, WADC TR 57-226, Nov. 1957.

56 McGinn, J. H. and Wachman, H., "Development and Investigation of Fluid Stabilized Arcs," in "High Intensity Arc Symposium," The Carborundum Co., Niagara Falls, N. Y., 1958, pp. 98–115.

57 Gruntfest, I. J. and Shenker, L. H., "Behavior of Reinforced Plastics at Very High Temperature, Part I," *Modern Plastics*, vol. 35, 1958, no. 10, pp. 155–166.

58 Gruntfest, I. J., Shenker L. H. and Saffire, V. N., "Behavior of Reinforced Plastics at Very High Temperature, Part II," *Modern Plastics*, vol. 36, 1959, no. 8, pp. 137–148.

59 Jacobs, K. H., Bonin, J. H. and Dickerman, P. J., "Preliminary Investigation of Fluid-Stabilized Arcs," in "High Intensity Arc Symposium," The Carborundum Co., Niagara Falls, N. Y., 1958, pp. 116–137.

60 Schweiger, R. N., "High-Intensity Arc—I," Avco RAD, Wilmington, Mass., 2-TM-57-52, Aug. 1957.

61 Osborn, A. B., "7 kw Plasma Jet for Laboratory Use," *J. Sci. Instr.*, vol. 36, 1959, pp. 317–319.

62 Kotanchik, J. N., "The Use of High-Intensity Arcs in Arc-Image Furnaces and Electric Arc-Powered Jets," in "High Intensity Arc Symposium," The Carborundum Co., Niagara Falls, N. Y., 1958, pp. 14–28.

63 Heldenfels, R. and Kotanchik, J., "Electric Arc-Powered Air Jets for Materials and Structures Testing at Temperatures to 10,000°R," National Summer Meeting of the IAS, July 1958, Los Angeles, Calif.

64 Gilruth, R. R., Greenshields, D. H., Heldenfels, R. R., Kotanchik, J. N., Ross, R. D. and Wallio, M. A., "Electric Arc Powered Jet," U. S. Patent no. 2,850,662 (1958).

65 Barr, T. A., Hales, L. W., Cason, C. M. and Gibson, J. W., "Design and Construction of High Temperature Tests Facilities," ARGMA, Research Laboratories Quarterly Research Review no. 17, May 1958, pp. 55–58.

66 Hales, W. L., Barr, T. A., Cason, C. M. and Gibson, J. S., "Spectroscopic Studies of an Argon Plasma," ARGMA, Research Laboratories Quarterly Research Review no. 17, May 1958, pp. 59–83.

67 General Electric Co., MSVD, "Air Arc Simulates Re-entry Problems, *Aviation Week*, vol. 69, July 14, 1958, pp. 71–73.

68 Diaconis, N. S. and Foshag, F. C., "The 2500 Kilowatt AC Air Arc," Proc. Soc. Experimental Stress Analysis, May 1959.

69 Hogness, T. R., "Arc-Heated Plasma for Laboratory Hypersonics," Astronautics, vol. 4, no. 3, March, 1959, pp. 40–42.

70 Brogan, T. R., "The Electric Arc Wind Tunnel—A Tool for Atmospheric Re-Entry Research," ARS Journal, vol. 29, no. 9, Sept. 1959, pp. 648–653.

71 Lai, W., Sloan, D. H. and Talbot, L., "Preliminary Design and Tests of a Plasma Jet," Univ. Calif. Inst. Engng. Res., Berkeley, Tech. Rep. HE-150-153, Nov. 1957.

72 Giannini, G. M., "The Plasma Jet," *Scientific American*, vol. 197, 1957, no. 2, pp. 80–88.

73 Giannini, G. M., "The Plasma Jet and Its Application," in "High Intensity Arc Symposium," The Carborundum Co., Niagara Falls, N. Y., 1958, pp. 29–48.

74 Lai, W., Gustavson, J. and Talbot, L., "Design Considerations and Initial Evaluation of Model B Plasma Generator," Univ. Calif. Inst. Engng. Res., Berkeley, Tech. Rep. HE-150-161, Sept. 1958.

75 Browning, J. A., "Techniques for Producing Plasma Jets," in "Dynamics of Conducting Gases," Northwestern University Press, Evanston, Ill., 1960, pp. 126–138.

76 Stokes, C. S., Knipe, W. W. and Streng, L. A., "Heat Transfer Rates of an Argon Plasma Jet," *J. Electrochem. Soc.*, vol. 107, 1960, pp. 35–38.

77 Roberts, T. G. and Hales, W. L., "Spectroscopic Measurements in a Plasma Jet," ARGMA, Research Laboratory Quarterly Research Review no. 26, Sept. 1960, ARGMA TN 2H1N-26, pp. 45–47.

78 Jedlicha, J. R., NASA-Ames, personal communication.

79 Kotanchik, J. N., NASA-Langley, personal communication.

80 Vidya, Inc., "Arc Wind Tunnel Simulates Re-Entry," *Aviation Week*, vol. 73, 1960, no. 13, Sept. 26, 1960, p. 110.

81 Westinghouse Electric Corp., "Electric-Arc Heater," *Mech. Engng.*, vol 82, no. 11, Nov. 1960, p. 85.

Space Propulsion

82 Cann, G., Ducati, A. and Blackman, V., "Experimental Studies on the Thrust from a Continuous Plasma Jet," in "Advanced Propulsion Systems Symposium," M. Alperin and G. P. Sutton, Eds., Pergamon Press, Inc., N. Y., 1959, pp. 33–43.

83 Moeckel, W. E., Baldwin, L. V., English, R. E., Lubarsky, B. and Maslen, S. H., "Satellite and Space Propulsion Systems," NASA TN D-285, June 1960.

84 Malin, M. E., John, R., Bade, W., Schweiger, R. and Yos, J., "Application of Electric-Arc Plasma Generators to Propulsion," Proc. Ninth International Astronautical Congress, Springer-Verlag, Vienna, 1959, pp. 445–455.

85 Brogan, T. R., "Preliminary Evaluation of Helium as an Electric Arc Heated Propellant," ARS Journal, vol. 29, no. 9, Sept. 1959, pp. 662–663.

86 Corliss, W. R., "Propulsion Systems for Space Flight," McGraw-Hill Book Co., Inc., N. Y., 1960, pp. 173–183.

87. Camac, M., "Plasma Propulsion of Spacecraft," Astronautics, vol. 4, no. 10, 1959, p. 31.

88 Camac, M., "Use of Energy Storage in Low Thrust Space Flight," ARS Journal, vol. 30, no. 1, Jan. 1960, pp. 54–63.

89 Evvard, J. C., "Electric Space Propulsion," Amer. Inst. Elec. Engrs., preprint no. 59–1229, 1959.

90 Giannini, G. M., "The Arc Jet," Second Symposium on Advanced Propulsion Concepts, Oct. 1959, Boston, paper no. M-11.

91 Heller, G., "The Plasma Jet as an Electric Propulsion System for Space Application," ARS preprint 1040–59, 1959.

92 Ducati, A. C. and Cann, G. L. "Propulsive Properties of High Intensity Plasma Jets," AFOSR TN 57-748, Feb. 1958; *also* Giannini Research Laboratory TR-9.

93 Ducati, A. C. and Cann, G. L. "Plasma Propulsion," ARS Preprint 1010-59, 1959.

94 John, R., Connors, J. and Mironer, A., "A Working Arc Jet Rocket Engine," Eleventh IAF Congress, Stockholm, 1960.

95 Adams, M. C. and Camac, M., "The Arc Heated Plasma Thrust Chamber," ARS preprint 791–59, 1959.

96 Moeckel, W. E. and Rayle, W. D., "NASA Research on Plasma Accelerators," ARS preprint 1005–59, 1959.

97 Ghai, M. L., "Space Propulsion Engines—A Problem in Production of High Velocity Gases," in "Dynamics of Conducting Gases," Northwestern University Press, Evanston, Ill., 1960, pp. 168–177.

98 Hall, J. G., Eschenroeder, A. Q. and Klein, J. J., "Chemical Non-equilibrium Effects on Hydrogen Rocket Impulse at Low Pressure," ARS Journal, vol. 30, no. 2, Feb. 1960, pp. 188–190.

99 Camac, M., "Plasma Propulsion Devices," in "Advances in Space Science, Vol. 2," F. Ordway III, Ed., Academic Press, Inc., N. Y., 1960, pp. 215–262.

Plasma Generator Configurations

100 Schweiger, R. N., "High-Intensity Arc—2," Avco RAD, Wilmington, Mass., 2-TM-58-81, July 1958.

101 Shepard, C. E. and Boldman, D. R., "Preliminary Development of Electrodes for an Electric-Arc Wind Tunnel," NASA Memo 4-14-59E, March 1959.

102 Avco RAD, Wilmington, Mass., unpublished data.

103 John, R. R. and Bade, W. L., "Testing of Reinforced Plastics Under Simulated Re-entry Conditions. Part I. Plasma-Jet Calibration," in "Symposium on Reinforced Plastics and Thermal Ablation," American Society for Testing Materials (to be published); *also* Avco RAD-TR-9(7)-59-21, Aug. 1959.

104 Eschenbach, R. C. and Skinner, G. M., "Study of Arc Heaters for a Hypersonic Wind Tunnel," Speedway Research Laboratory, Linde Co., Indianapolis, Ind., WADD TR 60-35 1960.

105 von Engel, A., "Ionized Gases," Clarendon Press, Oxford, 1955, p. 233.

106 Somerville, J. M., "The Electric Arc," John Wiley and Sons, Inc., N. Y., 1959, p. 24.

Calibration Procedures

107 John, R. R. and Bade, W. L., "Stagnation Point Heat Transfer in a Subsonic Jet of Arc-Heated Air," ARS Journal, vol. 29, no. 7, July 1959, pp. 523–525.

108 Warren, W. R., "Determination of Air Stagnation Properties in a High-Enthalpy Test Facility," *J. Aeron. Sci.*, vol. 26, 1959, pp. 835–836.

109 Grey, J., "Heat Transfer from an Ionized Gas to a Gaseous Coolant," Princeton Univ., Aeron. Engng. Rep. no. 487-A, Aug. 1959.

110 Giannini, G., Ducati, A., von Jaskowsky, W. and Ragusa, D., "Experiments with High Intensity Electric Discharges," in "Proceedings of an International Symposium on High Temperature Technology," McGraw-Hill Book Co., Inc., N. Y., 1960, pp. 21–32.

111 Christensen, D. and Buhler, R., "Arc Jet Measurements Related to Ablation Test Validity," in "Symposium on Reinforced Plastics and Thermal Ablation," American Society for Testing Materials (to be published); *also* Plasmadyne Corp., Santa Ana, Calif., Rep. no. 45, Oct. 1959.

112 Finkelnburg, W. and Maecker, H. "Handbuch der Physik, vol. 22," S. Flügge, Ed., Springer-Verlag, Berlin, 1956, pp. 369–376. (In German.)

113 Pearce, W. J., "Plasma Jet Temperature Study," WADC TR 59-346, Feb. 1960.

114 Olsen, H. N., "Thermal and Electrical Properties of an Argon Plasma," *Phys. Fluids*, vol. 2, 1959, pp. 614–623.

115 Larenz, W., "Method for Measuring Very High Temperatures in Almost Transparent Arc Columns," *Zeitschrift für Physik*, vol. 129, 1951, pp. 327–342. (In German.)

116 Talbot, L., "Theory of the Stagnation-Point Langmuir Probe," *Phys. Fluids*, vol. 3, 1960, pp. 289–298.

117 Blackman, V. H., "A Continuous High Temperature Gas Flow Facility for Magnetohydrodynamic Studies," Plasmadyne Corp., Santa Ana Calif., Rep. T-1TN069-334; *also* AFOSR TN-59-681, June 1959.

118 Cann, G. L. and Ducati, A. C., "Energy Content and Ionization Level in an Argon Gas Jet Heated by a High Intensity Arc," *J. Fluid Mech.*, vol. 4, 1958, pp. 529–537.

Exit Jet Contamination

119 Georgiev, S. and Rose, P. H., "On Carbon Contamination of Air Arcs and its Effect on Ablation Measurements," Avco-Everett Research Laboratory, Everett, Mass., RN 177, Dec. 1959.

120 Christensen, D., Plasmadyne Corp., Santa Ana, Calif., personal communication.

121 Pearce, W. J., "Calculation of the Contamination Level of Copper from Water-Cooled Copper Electrodes," General Electric Co., MSVD, Aerosciences Laboratory, Phila., Pa., Summary of Technical Rep., Vol. II, 1959.

122 "Effects of Hyperthermal Conditions on Plastic Ablation Materials," Plasmadyne Corp., Santa Ana, Calif., First Quarterly Progress Rep., Contract no. AF33(616)-7110 with WADD, Sept. 1960.

123 Sheer, C., "Development of Nonconsumable Anode for Fluid Transpiration into a High-Intensity Arc," Vitro Laboratories, East Orange, N. J., Dec. 1959.

Radio-Frequency Heating

124 Smith, H. L. and Early, H. C., "Investigation of Heating of Air Stream in a Wind Tunnel by Means of an Electrical Discharge," Univ. Michigan, Engng. Res. Inst., Rep. 2154-3-F, Oct. 1954.

125 Early, H. C. and Miller, D. B., "Heating a Supersonic Air Stream with a Corona Discharge," Univ. Michigan, Engng. Res. Inst., Rep. 2147-16-T, April 1957.

126 Chuan, R. L., "Plasma Heating of Supersonic Airstream," *Phys. Fluids*, vol. 1, 1958, p. 452.

127 Chuan, R. L. and Smetana, F. O., "Experiments on a Radio Frequency Discharge Plasma in Supersonic Flow," 1959 Heat Transfer and Fluid Mechanics Institute, Stanford University Press, 1959, pp. 236–243.
128 Williams, J. C., III, "The Decaying Plasma as a Method of Heating a Supersonic Gas Stream," 1959 Heat Transfer and Fluid Mechanics Institute, Stanford University Press, 1959, pp. 222–235.
129 Romig, M. F., "Steady State Solutions of the Radiofrequency Discharge with Flow," *Phys. Fluids*, vol. 3, 1960, pp. 129–133.
130 Reed, T. B., "The Induction-Coupled Plasma Torch," MIT Lincoln Laboratory, Cambridge, Mass., Rep. no. G-0026, Sept. 1960.

Convective and Radiative Heat Losses

131 McAdams, W. H., "Heat Transmission," McGraw-Hill Book Co., Inc., N.Y ., 1954, pp. 219–220.
132 Gambill, W. R. and Greene, N. D., "A Preliminary Study of Vortex-Boiling Burnout Heat Flux," JET PROPULSION, vol. 28, 1958, pp. 192–194.
133 Smelt, R., "Test Facilities for Ultra-High Speed Aerodynamics," Proc. Conference on High-Speed Aeronautics, Polytechnic Institute of Brooklyn, N. Y., 1955, pp. 311–333.
134 Kivel, B. and Bailey, K., "Tables of Radiation from High Temperature Air," Avco Research Laboratory, Everett, Mass., Res. Rep. 21, Dec. 1957.

Electrode Processes

135 Cobine, J. D., "Gaseous Conductors," Dover Publications, N. Y., 1958, pp. 300–311, 343–344.
136 von Engel, A., "Ionized Gases," Clarendon Press, Oxford, 1955, pp. 242–250.
137 Brown, S. C., "Basic Data on Plasma Physics," The Technology Press, MIT, and John Wiley and Sons, Inc., N. Y., 1959, pp. 321–324.
138 Somerville, J. M., "The Electric Arc," John Wiley and Sons, Inc., N. Y., 1959, chap. 3.
139 Finkelnburg, W. and Maecker, "Handbuch der Physik, vol. 22," S. Flügge, Ed., Springer-Verlag, Berlin, 1956, pp. 403–408, 422–427. (In German.)
140 Robson, A. E. and von Engel, A., "Excitation Processes and the Theory of the Arc Discharge," *Nature* (London), vol. 175, 1955, p. 646.
141 von Engel, A. and Robson, A. E., "The Excitation Theory of Arcs with Evaporating Cathodes," Proc. Royal Soc., vol. A242, 1957, pp. 217–236.
142 von Engel, A. and Robson, A. E., "Mechanism of Electron Emission from the Arc Cathode," *J. Appl. Phys.*, vol. 29, 1958, p. 734.
143 Lee, T. H., "On the Discussion of the T-F Theory by Robson and von Engel," *J. Appl. Phys.*, vol. 29, 1958, pp. 734–735.
144 Lee, T. H., "T-F Theory of Electron Emission in High-Current Arcs," *J. Appl. Phys.*, vol. 30, 1959, pp. 166–171.
145 Somerville, J. M., "The Electric Arc," John Wiley and Sons, Inc., N. Y., 1959, pp. 64–73.
146 *Ibid.*, pp. 85–93.
147 Holm, R., "The Vaporization of the Cathode in the Electric Arc," *J. Appl. Phys.*, vol. 20, 1949, pp. 715–716.

Arc Column Behavior

148 Suits, C. G. and Poritsky, H., "Application of Heat Transfer Data to Arc Characteristics," *Phys. Rev.*, vol. 55, 1939, pp. 1184–1191.
149 Champion, K. S. W., "The Energy Balance Equation for the Positive Columns of High Pressure Arcs," Proc. Physical Soc. (London), vol. B66, 1953, pp. 169–174.
150 Suits, C. G., "High Pressure Arcs in Common Gases in Free Convection," *Phys. Rev.*, vol. 55, 1939, pp. 561–567.
151 Cobine, J. D., "Gaseous Conductors," Dover Publications, N. Y., 1958, pp. 330–331.
152 Maecker, H., "A Cylindrical Arc for High Intensities," *Zeitschrift für Naturforschung*, vol. 11a, 1956, pp. 457–459. (In German.)
153 Maecker, H., "On the Characteristics of Cylindrical Arcs," *Zeitschrift für Physik*, vol. 157, 1959, pp. 1–29. (In German.)
154 Maecker, H., "The Measurement and Interpretation of Arc Characteristics (A, N_2)," *Zeitschrift für Physik*, vol. 158, 1960, pp. 392–404. (In German.)
155 Schmitz, G. and Uhlenbusch, J., "On the Mathematical Description of Cylindrically Symmetrical Arcs," *Zeitschrift für Physik*, vol. 159, 1960, pp. 554–562. (In German.)
156 Emmons, H. W., "The Poiseuille Plasma Experiment," 1960 Annual Meeting, Amer. Phys. Soc., Div. Fluid Dynamics, Baltimore, Nov. 1960.
157 Foitzik, R., "Investigations on the Stabilized Electric Arc (Rotating Arc) in Nitrogen and Carbon Dioxide at Pressures of 1 to 40 Atmospheres," *Wissenschaftliche Veröffentlichungen aus den Siemens-Werken*, vol. 19, 1940, pp. 28–58. (In German.)
158 Finkelburg, W. and Maecker, H., "Handbuch der Physik, vol. 22," S. Flügge, Ed., Springer-Verlag, Berlin, 1956, p. 352. (In German.)
159 Bittker, D. A., and Brokaw, R. S., "Estimate of Chemical Space Heating Rates in Gas-Phase Combustion With Application to Rocket Propellants," ARS JOURNAL, vol. 30, no. 2, Feb. 1960, pp. 179–185.

Magnetic Field Effects

160 Somerville, J. M., "The Electric Arc," John Wiley and Sons, Inc., N. Y., 1959, pp. 80–85.
161 Robson, A. E. and von Engel, A., "Origin of Retrograde Motion of Arc Cathode Spots," *Phys. Rev.*, vol. 93, 1954, p. 1121.
162 Robson, A. E. and von Engel, A., "Motion of a Short Arc in a Magnetic Field," *Phys. Rev.*, vol. 104, 1956, pp. 15–16.
163 Smith, C. G., "Motion of an Arc in a Magnetic Field," *J. Appl. Phys.*, vol. 28, 1957, pp. 1328–1331.
164 Guile, A. E. and Mehta, S. F., "Arc Movement Due to the Magnetic Field of Current Flowing in the Electrodes," Proc. Inst. Elec. Engrs., vol. A104, 1957, pp. 533–540.
165 Guile, A. E., Lewis, T. J. and Mehta, S. F., "Arc Movement and Electrode Magnetism," *Nature* (London), vol. 179, 1957, pp. 1023–1024.
166 Guile, A. E., Lewis, T. J. and Mehta, S. F., "Arc Motion with Magnetized Electrodes," *Brit. J. Appl. Phys.*, vol. 8, 1957, pp. 444–448.
167 DeBolt, H. E., Avco RAD, Wilmington, Mass., unpublished data.
168 Materials Advisory Board, "Development and Possible Applications of Plasma and Related High-Temperature Generating Devices," National Academy of Sciences-National Research Council, Rep. MAB-167-M, Aug. 1960.

1960–61 ARS Meeting Schedule

Date	Meeting	Location	Abstract Deadline
Feb. 1–3	Solid Propellant Rocket Conference	Salt Lake City, Utah	Past
March 13–16	Missile and Space Vehicle Testing Conference	Los Angeles, Calif.	Past
April 4–6	Lifting Re-Entry Vehicles: Structures, Materials, and Design Conference	Palm Springs, Calif.	Past
April 26–28	Propellants, Combustion, and Liquid Rockets Conference	Palm Beach, Fla.	Past
May 3–5	ARS/ORNL Nuclear Applications in Space Conference	Gatlinburg, Tenn.	Past
May 22–24	National Telemetering Conference	Chicago, Ill.	Past
June 13–16	Joint ARS-IAS Mid-Year Meeting	Los Angeles, Calif.	Feb. 1
Aug. 7–9	Guidance and Navigation Conference	Palo Alto, Calif.	March 15
Aug. 16–18	International Hypersonics Conference	Cambridge, Mass.	March 30
Aug. 23–25	Biennial Gas Dynamics Symposium	Evanston, Ill.	Past
Oct. 2–7	XIIth International Astronautical Congress	Washington, D.C.	To be announced
Oct. 9–14	ARS SPACE FLIGHT REPORT TO THE NATION	New York, N.Y.	April 15

Send all abstracts to Meetings Manager, ARS, 500 Fifth Ave., New York 36, N.Y.

Performance of Plug-Type Rocket Exhaust Nozzles

K. BERMAN[1] and
F. W. CRIMP Jr.[2]

General Electric Co.
Schenectady, N. Y.

The physical characteristics of a plug nozzle are described and compared with a conventional converging-diverging nozzle. The mathematical analysis of the aerodynamic performance of a plug nozzle is outlined, including the Prandtl-Meyer corner expansion of the flowing gas. The advantages of the plug nozzle in terms of superior performance at lower than design pressure ratio, smaller physical size and aerodynamic thrust vector control are described. A brief description is given of how these advantages can be utilized in liquid propellant rocket engines. Application of plug nozzles for solid propellant rocket engines is discussed primarily from the viewpoint of using the plug's movement to adjust for chamber pressure variation, to control thrust magnitude and direction and to control total impulse.

WITHIN recent years, the application of plug-type nozzles as rocket propulsion elements has been intensively investigated, since these nozzles have several advantageous design and performance features. The basic concept of a plug nozzle is not new; manufacturers of air-breathing propulsion systems and the Lewis Research Center of NASA have studied their characteristics for many years (1–9).[3] As a matter of fact, the early German turbojets incorporated them to achieve throat area variation.

We shall begin our discussion by reviewing some of the essentials of plug nozzle design and operation. This will be followed by a presentation of some data significant to the application of plug nozzles to rocket propulsion systems.

Characteristics of Plug Nozzles

In a conventional convergent-divergent nozzle, the supersonic expansion occurs within the divergent portion of the unit. Except when flow separation occurs, the walls form a boundary surface or stream surface which contains the flow until a design Mach number or pressure ratio, fixed by the ratio of nozzle exit area to throat area, has been achieved. If the nozzle exit pressure is equal to the ambient pressure, the nozzle is operating at its design point; from the performance standpoint, this represents the ideal condition. If the nozzle exit pressure is lower than the ambient pressure, an external shock wave is required to raise the flow static pressure to ambient conditions; under these conditions of "overexpansion," a considerable entropy increase, resulting in performance loss relative to an "ideal" nozzle, occurs. If the nozzle exit pressure is higher than the ambient pressure, an external expansion to the ambient pressure occurs. Even though this expansion process is isentropic, there occurs a performance decrease relative to the "ideal" nozzle, since the flow deflection associated with the external expansion produces nonaxial velocity components.

A plug nozzle may be looked upon as a modification of a conventional nozzle; the significant point of departure is that the supersonic expansion, which is generally not confined within solid walls, is continuously "re-directed" by the ambient pressure to produce an essentially axial velocity vector. For purposes of classification, one may consider two general types of plug nozzles (illustrated in Figs. 1): One in which all the supersonic expansion occurs externally (Fig. 1a); one in which part of the supersonic expansion occurs externally (Fig. 1b).

A third type (Fig. 1c) in which none of the supersonic expansion occurs externally is essentially a divergent nozzle having performance characteristics similar to the conventional divergent nozzles. This type shall not be considered further in this paper.

As a supersonic flow undergoes an expansion from a given pressure to a lower value, the velocity vector undergoes a change in direction related to the increase in Mach number. The simplest example is a corner expansion in which the flow undergoes a sudden change in flow direction. Although expansion is a continuous process, as an approximation one may consider it as occurring through a series of expansion waves, each of which causes a finite flow deflection as shown in Fig. 2. When the expansion or Mach lines are centered at the corner, one has a simple, centered expansion fan. Such a flow is frequently called a Prandtl-Meyer expansion.[4] The flow deflection occurring as the supersonic flow expands to a given Mach number or pressure ratio is called the Prandtl-Meyer angle. Its value, as a function of the final Mach number, is

$$\omega = \sqrt{\frac{\gamma+1}{\gamma-1}}\arctan\sqrt{\frac{\gamma-1}{\gamma+1}(M^2-1)} - \arctan\sqrt{M^2-1} \quad [1]$$

based upon a value of ω = Mach 1.

The pressure ratio, corresponding to the Mach number, is

$$\frac{P_0}{P} = \left(1+\frac{\gamma-1}{2}M^2\right)^{\frac{\gamma}{\gamma-1}} \quad [2]$$

Values of Prandtl-Meyer angle as a function of Mach number are plotted in Figs. 3a and b. Values of Mach number vs. pressure ratio are plotted in Figs. 3c, d and e.

Presented at the ARS Solid Propellant Rocket Research Conference, Princeton, N. J., Jan. 28–29, 1960.

[1] Manager, Liquid Rocket Sub-Operation, Flight Propulsion Div. Fellow Member ARS.

[2] Manager, Solid Rocket Projects, Flight Propulsion Div. Member ARS.

[3] Numbers in parentheses indicate References at end of paper.

[4] Detailed discussions of Prandtl-Meyer flow can be found in any textbook on supersonic flow. Typical examples are listed in (12–14).

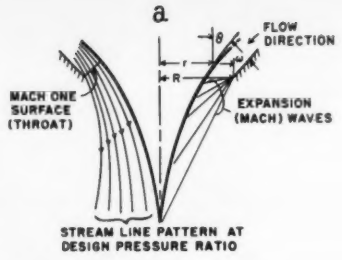

Fig. 1a Plug nozzle with complete external supersonic expansion

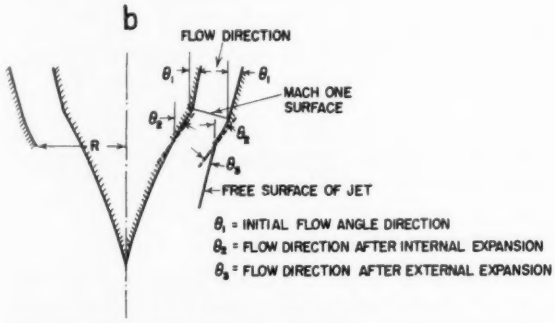
b
FLOW DIRECTION
MACH ONE SURFACE
FREE SURFACE OF JET
θ1 = INITIAL FLOW ANGLE DIRECTION
θ2 = FLOW DIRECTION AFTER INTERNAL EXPANSION
θ3 = FLOW DIRECTION AFTER EXTERNAL EXPANSION

Fig. 1b Plug nozzle with some internal supersonic expansion

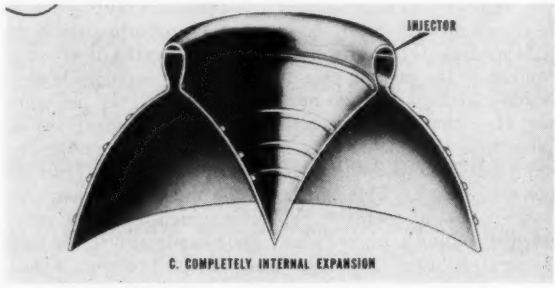

Fig. 1c Plug nozzle with complete internal expansion

Consider now the plug nozzle of Fig. 1a. If the gas stream expanding through the design pressure ratio is to have an axial direction, the initial flow direction at the throat must be inclined at the Prandtl-Meyer angle from the vertical. The throat area becomes

$$A_t = \pi(R^2 - r^2)\,\frac{1}{\cos\,[(\omega + \phi)/2]} \qquad [3]$$

The nozzle exit area is

$$A_e = \pi R^2 \qquad [4]$$

Geometric considerations for the existence of a throat dictate that the following approximate relationship between ω and ϕ exist

$$r \tan \phi = R \tan \omega \qquad [5]$$

Once the thrust level or throat area and the area ratio are specified, the unknowns R, r and ϕ can be determined from the three equations

$$\frac{A_e}{A_t} = \frac{R^2 \cos\,[(\omega + \phi)/2]}{(R^2 - r^2)} \qquad [6a]$$

$$A_t = \frac{T}{C_F P_0} = \pi(R^2 - r^2)\,\frac{1}{\cos\,[(\omega + \phi)/2]} \qquad [6b]$$

$$r \tan \phi = R \tan \omega \qquad [6c]$$

The Prandtl-Meyer angle is, of course, determined as soon as the area ratio is specified.

The plug itself becomes a streamline of the flow. The shape of the axisymmetrical plug can be easily computed by means of the method of characteristics.[5] There exists only one plug contour which causes no disturbance in the flow for the given design condition. We shall designate it as an isentropic plug. In a later section, the effect of plug shape will be discussed.

In the plug nozzle of the type shown in Fig. 1a, all the supersonic expansion occurs externally. It is of course possible, and in many cases advantageous, to portion the total expansion between internal and external expansion. If we assume that the internal expansion is a simple corner expansion, the total expansion angle is the sum of the internal and external expansions

$$\omega = (\theta_2 - \theta_1) + (\theta_2 - \theta_3) \qquad [7]$$

If the jet free boundary is to be axial at the design pressure ratio, then θ_3 is equal to zero. If it should be further desired that $\theta_1 = 0$, it is clear that the jet deflection is split equally between internal and external expansion. It is, of course, required for efficient plug nozzle operation that the lowest operating pressure ratio encountered by the nozzle is high enough so that some external expansion always occurs. That is

$$\omega_{o_{P_L}} > (\theta_2 - \theta_1) \qquad [8]$$

where $\omega_{o_{P_L}}$ is the deflection angle corresponding to the lowest operating pressure ratio encountered (10).

[5] The method of characteristics is discussed in many textbooks on supersonic flow theory. Typical examples are presented in (12–14).

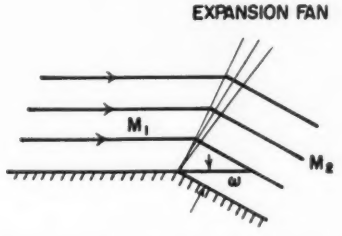

Fig. 2 Mach number M_2 larger than M_1 centered expansion fan

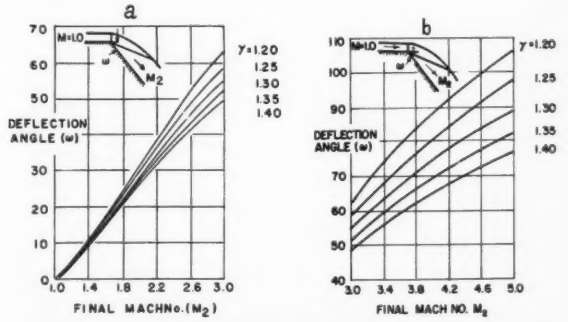

Figs. 3a,b Deflection angle vs. final Mach number for isentropic expansion

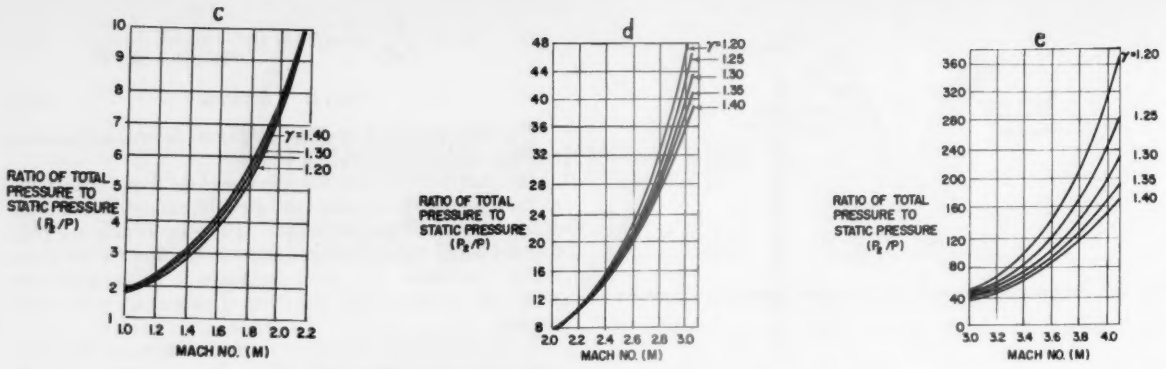

Figs. 3c,d,e Pressure ratio vs. Mach number

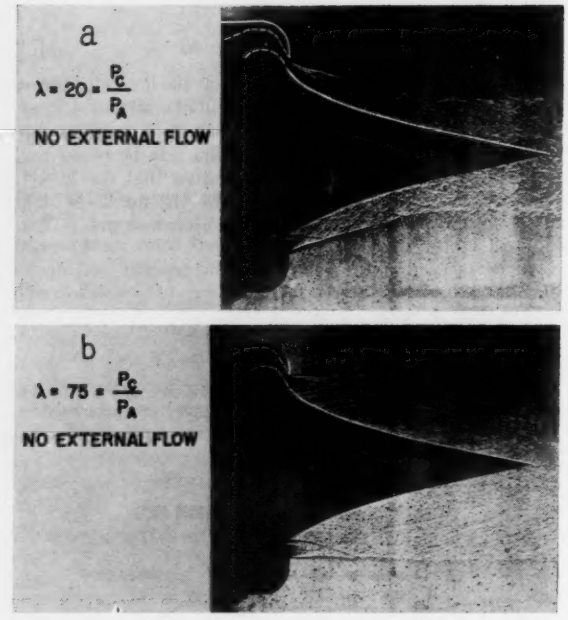

Figs. 4a,b Shadowgraph of plug nozzle flow fields

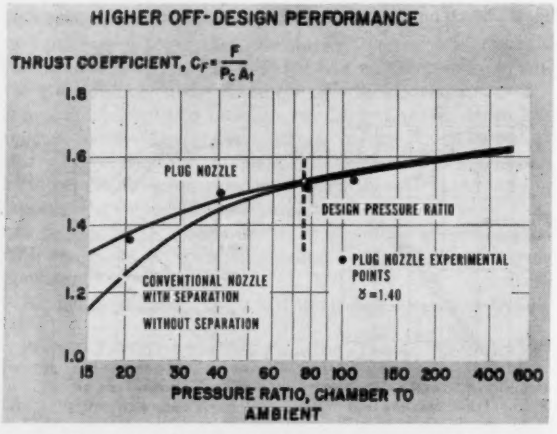

Fig. 5 Comparison of theoretical performances of plug and conventional nozzles

The geometrical dimensions of the type of plug nozzles shown in Fig. 1b can be computed as a function of the desired operating characteristics (11).

Performance of Plug Nozzles

The outer boundary of the jet along a plug nozzle is a free surface which can adjust itself continuously to the existing ambient conditions. Figs. 4a and b show some typical shadowgraphs of the flow field for a given plug nozzle at various pressure ratios. It is significant that the jet cross-sectional area at the plug apex, which is the effective nozzle exit area, adjusts itself as a function of the pressure ratio. Below the design pressure ratio, the variation is approximately such that the exit to throat area ratios correspond to the ideal value required by the existing pressure ratio; i.e., the plug acts as a pseudo-variable area ratio nozzle. As a result, the performance of a plug nozzle operating below the design point is higher than that of the conventional nozzle. Above the design point, the theoretical performances are identical, as shown in Fig. 5. This can be easily understood when one considers that at operation above the design point, the pressure distribution along the plug remains undisturbed, whereas at operation below the design point, the local pressure downstream of the plug location where the ambient pressure level is first reached adjusts itself to ambient conditions by a series of weak compressions and expansion. See Fig. 6.

The discussions so far have considered the application of an isentropic plug shape. Such shapes are fairly long. The effect of the replacement of the lower part of the isentropic plug by a cone, such that there exists a smooth transition into the upper plug portion, has been analytically and experimentally investigated. The effect of such geometrical perturbations on performance is illustrated by the analytical curve of Fig. 7. This figure indicates that even with a 20-deg cone half-angle, the performance loss is relatively small. Experimental data indicate that even up to 30-deg half-angle cones, the performance loss is less than 1 per cent. The plug length is appreciably shortened by using the cone shapes as shown in Fig. 8.

Thrust Vector Control

A significant aspect of the application of plug nozzles is that they provide a relatively simple technique to produce adequate side forces for thrust vector control. If, for example, one divides the annular combustor around the base of the plug into independent units so that the chamber pressure can be raised in one sector and lowered in another, then the gas stream will undergo a rotation and translation with respect to the axis of symmetry of the plug. These effects, as far as

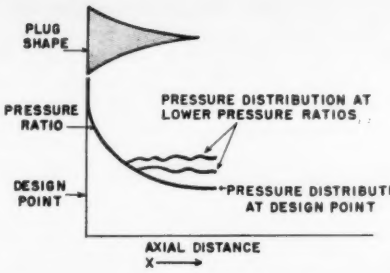

Fig. 6 Schematic illustration of pressure distribution along a fixed plug nozzle at various operating pressure ratios

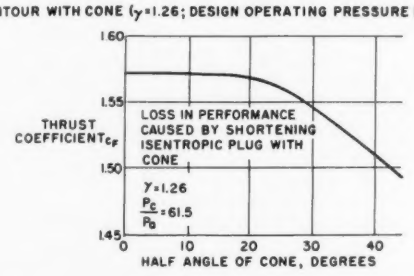
CONTOUR WITH CONE (γ=1.26; DESIGN OPERATING PRESSURE RATIO, Pc/Pa=61.5
THRUST COEFFICIENT CF
LOSS IN PERFORMANCE CAUSED BY SHORTENING ISENTROPIC PLUG WITH CONE
γ=1.26
Pc/Pa=61.5
HALF ANGLE OF CONE, DEGREES

Fig. 7 Theoretical loss in performance caused by replacement of lower plug

thrust vector is concerned, can be shown to be additive. A typical set of data showing the variation of effective thrust vector angle with overpressure in the higher pressure combustor cell is shown in Fig. 9.

Application to Liquid Propellant Engine Design

The plug nozzle can be combined with annular combustors to form attractive liquid propellant propulsion system configurations. Fig. 10 represents an example of a plug-type turbopumped liquid propellant engine. The combustors are located around the base of the nozzle, and, in this particular unit, the turbine exhaust is brought out through the center of the nozzle. Such engines can be designed extremely short and compact to produce a well-packaged propulsion system. In fact, studies indicate that for identical thrust levels, the plug-type engines would be about half the length of conventional configurations as shown in Fig. 11 for a 1,500,000-lb thrust level. This makes them attractive not only for first-stage booster applications, but also for medium thrust size upper-stage propulsion systems. Similarly, the weight of the plug-type engine compares favorably with that of the conventional unit.

Application to Solid Rocket Engines

The problems and advantages of plug nozzle application to solid rocket engines differ considerably from those of liquid engines. Not all of the major advantages of liquid propellant plug nozzle engines such as thrust vector control, scaling, combustion stability and thrust structure simplification can be directly transposed to solid engine application. Gains unique to the application of plug nozzles to solid engines exist, but are generally not as compelling. Consequently, the advisability of converting to the plug from the cluster of four DeLaval nozzles typically employed in modern solid propellant rockets is not particularly clear-cut and depends to a large extent on the specific missile application intended.

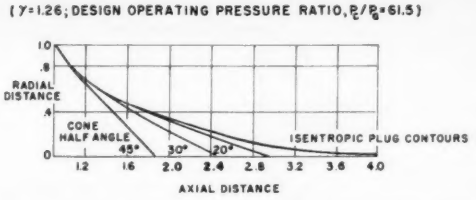

Fig. 8 Plug profiles for isentropic expansion and for shortened versions terminating with conical contours

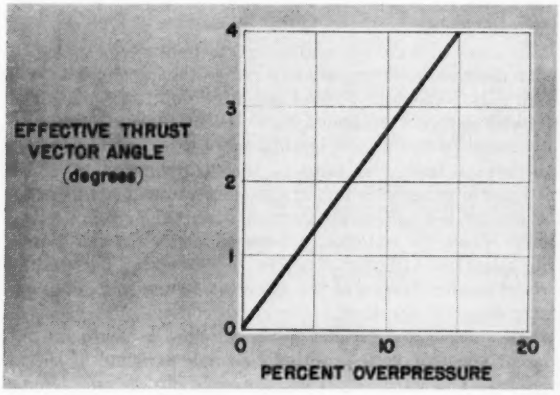

Fig. 9 Effect of per cent overpressure on effective thrust vector angle

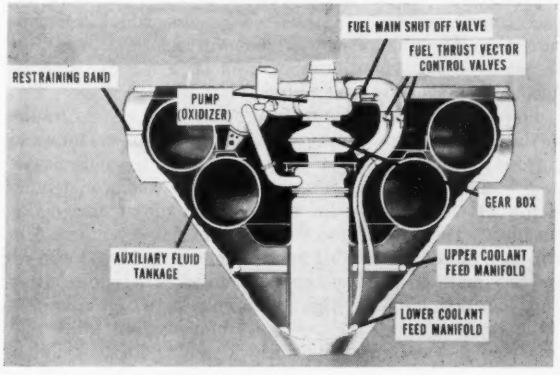

Fig. 10 Plug nozzle engine assembly

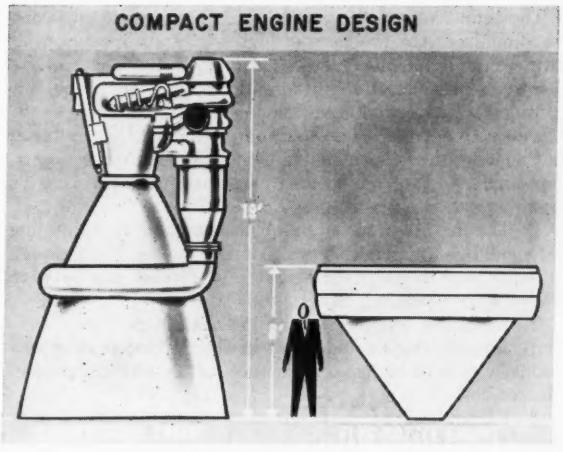

Fig. 11 Size of plug nozzle engine compared with that of conventional engine

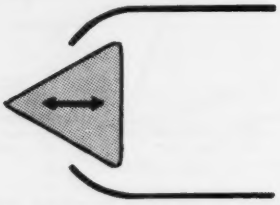

Fig. 12 Schematic illustration of plug nozzle with movable plug insert

Advances in materials and design technology may also be quite decisive in determining whether the plug nozzle will eventually come into general usage on solid engines. The problem of throat erosion is an excellent case in point. In any nozzle system involving ablation of throat materials as a function of time, the ratio of throat perimeter to cross-sectional area becomes important, since the higher this ratio, the greater the percentage increase in throat area in a given time. Thus, for example, a large diameter circular nozzle will maintain a flatter chamber pressure-time curve than several smaller nozzles of the same total cross section. Similarly, since the throat of a plug nozzle consists of two concentric boundaries, the perimeter-area ratio is very high, and the system becomes very sensitive to small amounts of throat erosion. This effect, by itself, has served to discourage plug nozzle use on uncooled solid engines, which, utilizing throats of graphite or similar materials, generally have exhibited an appreciable amount of throat erosion over the required burning time. Recently, however, this potent objection has been largely overcome by the development of high temperature throat configurations which will maintain constant throat areas throughout burning, even when operated with the hottest propellants in general use today.

Projecting this analysis to future solid propellants results in the interesting possibility that, as flame temperature and corrosivity increase from their present level, the plug nozzle may be one of the very few configurations that would function satisfactorily from the standpoint of throat area maintenance. This arises from the fact that flame temperatures will then exceed the melting points of any presently known refractory materials, and successful operation will require either compensation for very high ablation rates or provision for some type of sacrificial cooling. Compensation for throat area changes can be accomplished with a plug nozzle, uniquely and with negligible loss in performance, by movement of the plug insert with respect to its outer shroud as shown schematically in Fig. 12.

The complexity of the variable area plug nozzle must not be minimized; the problems of high temperature supporting struts, high differential pressure loading, thrust vector alignment and plug vibration are formidable and would require a considerable design and development effort. The payoff, however, is not limited to solution of the ablation problem, but includes the following advantages accrued by the concurrent ability of the variable area plug nozzle to control engine chamber pressure and thrust:

1 The effect of propellant ambient temperature on burning rate could be compensated for, reducing the maximum design strength, and therefore the weight, of the rocket case by 10 to 25 per cent depending on the propellant used.

2 Resultant relaxation of propellant temperature sensitivity specifications could result in the development of new propellants with higher performance, better physical properties, or both.

3 Elimination of peak chamber pressures during start could also contribute to case weight reductions.

4 The ability to program thrust as a function of time can both reduce guidance system complexity and result in appreciable range increases. Trajectory studies of several major solid rocket missiles have been performed on an IBM 704 computer and have shown that, particularly in the case of the booster stages, the increased performance of the plug nozzle at low altitude plus an optimized thrust-time curve could produce range or payload increases of a very attractive magnitude.

5 Simplified grain designs and higher loading fractions might be attained.

6 Higher engine total impulse and better thrust termination characteristics could be produced by reduction in the amount of unburned propellant.

7 Grain reliability might be increased if the response of the chamber pressure control could be made sufficiently fast to prevent small grain cracks from causing spiraling increases in burning rate.

The most difficult design problem for either a fixed or variable area solid rocket plug nozzle is thrust vector control. No simple solution, such as valving flow to various segments of the plug as in the liquid application, has yet been determined. At first glance, it would appear that the use of four nozzles each pivoting the plug or part of the plug on a single axis (similar to the usual DeLaval nozzle solid rocket design) would yield the simplest configuration for control of pitch, yaw and roll. The difficulty, however, lies in the fact that, unlike a DeLaval nozzle, the maximum cross-sectional area of each plug nozzle is at the forward end, in the plane of its throat, and therefore flush against the ellipsoidal aft closure of the rocket case. The design and manufacturing problems of the closure, joint, blast tubes, insulation and propellant configuration in this area are quite difficult for a conventional nozzle configuration. When complicated by four plug nozzles—each requiring axially aligned structures with smooth aerodynamics, maximum diameter for equivalent expansion ratio, noneroding throats, actuation devices and means for supporting the central plug against high differential pressures —the solution of complexity, cost, weight and manufacturing difficulties becomes impractical. These considerations alone point strongly toward a single plug as the only logical choice for solid rocket application. The conclusion is further augmented by the fact that a single plug:

1 Can utilize the entire engine cross section for expansion, thereby increasing expansion ratio by approximately 50 per cent over that obtainable within the envelope by four nozzles.

2 Reduces base drag.

3 With only small performance penalty can consist of a shortened cone no longer than a conventional four-nozzle cluster configuration.

Assuming then a single plug, pitch and yaw control can be provided by gimballing all or part of the plug in a manner similar to that used for single liquid propellant thrust chambers. If variable area is to be part of the design, the increased complexity of plug gimballing can be quite nominal. In most applications, however, roll control is also required of the main engine. In the case of the single plug, the use of some form of jet vanes can serve this purpose. If located just below and between segments of a segmented annular throat, drag losses can be minimized and vane sizes can become very reasonable, since they are working primarily in a high Mach region. Design and cost analysis to date suggests that the use of such vanes in conjunction with a fixed plug for pitch, yaw and roll control may be the most practical method for many applications.

The engineer attempting to apply a plug-type nozzle to a solid rocket engine will find a wide range of possible configurations. The plug itself, for instance, may be noncircular, even irregular, in cross section. Two-dimensional nozzles may have design advantages in some cases. Multiple-tip plugs appear practical. The possibility of multiple chambers, clustered and exhausting on one large plug has some interesting ramifications, particularly for applications where very large missile control forces are required.

Conclusions

1 The performance of plug-type rocket exhaust nozzles exceeds that of a conventional converging-diverging nozzle in the overexpanded condition, and equals it under perfect or underexpansion conditions.

2 Reasonable manipulation of pressure on the quadrants of a liquid propellant plug nozzle can produce thrust vectoring forces equivalent to a gimballed nozzle and with considerable decrease in complexity and response time.

3 The use of plug-type configurations on large liquid propellant engines appears to offer distinct advantages in size, weight, cost and performance.

4 Plug nozzle technology has advanced to the point where the plug is becoming competitive with clustered conventional nozzles for some solid rocket applications. Further advances combined with the inherent design flexibility of this nozzle type may result in its eventual widespread use as a solid rocket component. Thrust vector control remains a serious problem.

5 The plug-type nozzle configuration is adaptable for use as a variable throat area device. Its ability to control thrust and chamber pressure offers wide advantages in solid engines which may warrant the increased complexity involved under some conditions.

Nomenclature

A_t = throat area
A_e = nozzle exit area
C_F = thrust coefficient
M = Mach number
P_0 = total or stagnation pressure
P = static pressure
R = radius from plug centerline to outer lip at Mach 1 plane (Fig. 1a)
r = radius from plug centerline to inner lip at Mach 1 plane (Fig. 1a)
T = thrust
γ = ratio of specific heats
ω = Prandtl-Meyer angle
ϕ = angle of inclination of inside wall at Mach 1 plane (Fig. 1a)
θ = flow angle inclination (Fig. 1b)

References

1 Ciepluch, C. C., Krull, H. G. and Steffen, F. W., "Preliminary Investigation of Performance of Variable-Throat Extended Plug Type Nozzles, Over Wide Range of Nozzle Pressure Ratios," NACA RM E53J28, 1954.

2 Hearth, D. P. and Gorton, G. C., "Investigation of Thrust and Drag Characteristics of a Plug-Type Exhaust Nozzle," NACA RM E53L16, 1954.

3 Krull, H. G. and Beale, W. T., "Effect of Plug Design on Performance Characteristics of Convergent-Plug Exhaust Nozzles," NACA RM E54H05, 1954.

4 Krull, H. G. and Beale, W. T., "Effect of Outer-Shell Design on Performance Characteristics of Convergent-Plug Exhaust Nozzles," NACA RM E54K22, 1955.

5 Krull, H. G. and Beale, W. T., "Comparison of Two Methods of Modulating the Throat Area of Convergent Plug Nozzles," NACA E54L08, 1955.

6 Salmi, R. J., "Preliminary Investigation of Methods to Increase Base Pressure of Plug Nozzles at Mach 0.9," NACA RM E56J05, 1956.

7 Smolak, G. R. and Koffel, W. K., "Investigation of an Air-Cooled, Plug-Type, Variable-Area Exhaust Nozzle," NACA RM E57A07, 1957.

8 Connors, J. F. and Meyers, R. C., "Design Criteria for Axisymmetric and Two Dimensional Inlets and Exits," NACA TN 3589, 1956.

9 Krase, W., "Studies of Aerodynamic Performance of Several Types of Rocket Nozzles," General Electric Co., Flight Propulsion Div., Cincinnati, Ohio, Rep. R56 AGT 246, 1956.

10 Barnes, S., "Aerodynamic Analysis of Plug Nozzles," General Electric Co., Flight Propulsion Div., Cincinnati, Ohio, Rep. R58 AGT 780, 1958.

11 Machell, W. and Ellison, T., "Parametric Analysis of Plug Nozzles to Determine Geometric Relationships," General Electric Co., Flight Propulsion Div., Cincinnati, Ohio, Rep. R59 FPD 786, 1959.

12 Edelfelt, I., "Graphical Presentation of Compressible Flow Functions," General Electric Co., General Engineering Laboratory, Schenectady, N. Y., R52 GL 300, 1952.

13 Shapiro, A. H., "The Dynamics and Thermodynamics of Compressible Fluid Flow," The Ronald Press Co., N. Y., 1953, p. 462.

14 Liepman, R. and Puckett, A.,"Aerodynamics of a Compressible Fluid, 1953," John Wiley & Sons, Inc., N. Y., 1947, chaps. 12 and 13.

Low Acceleration Takeoff From a Satellite Orbit[1]

H. LASS[2] and J. LORELL[3]

Jet Propulsion Laboratory,
California Institute of Technology
Pasadena, Calif.

The method of Kryloff and Bogoliuboff for handling problems in nonlinear mechanics is applied to the problem of takeoff from a satellite orbit. The analysis is restricted to low acceleration, and covers these cases: Constant radial thrust, constant tangential thrust and intermittent thrust. The results are compared with those appearing elsewhere in the literature.

IN A 1953 paper (1)[4] titled "Take-Off From a Satellite Orbit," Tsien treated the equations of motion of a powered rocket in a central gravitational field. His method of analysis was direct, and led to elliptic integrals for the radial thrust case and to series approximations for the circumferential thrust case. Most of the subsequent literature on low thrust trajectories continues to use Tsien's results and his direct method of approach.

Thus, Dobrowolski (3) makes use of the elliptic integral solution to get formulas for the rate of precession of the line of apses. Copeland (4) also derives the elliptic integral expressions and in addition exhibits graphs of particular trajectories. Perkins (5), treating the case of low level tangential thrust, uses the method of linear perturbations.

Many of the results obtained by these direct methods can be obtained much more quickly by the nonlinear techniques of Kryloff and Bogoliuboff (2). A brief statement of this method is given herein. For more details, the reader is referred to Minorsky (6).

In the following sections, the Kryloff-Bogoliuboff method is applied to three different examples of low acceleration orbits: Radial thrust, circumferential thrust and intermittent thrust. It is seen that the results agree with those in the literature, and in certain cases are arrived at much more quickly.

The Kryloff-Bogoliuboff Method

An approximate solution to the nonlinear differential equation

$$dx/dt = uf(x, \sin t) \qquad \mu << 1 \qquad [1]$$

can be obtained as follows. Equation [1] yields

$$\frac{x(t + 2\pi) - x(t)}{2\pi} = \frac{\mu}{2\pi}\int_t^{t+2\pi} f(x, \sin \tau)d\tau \qquad [2]$$

Since μ is very small, one may consider that x remains essentially constant during the integration from $\tau = t$ to $\tau = t + 2\pi$. Since $\sin t$ is periodic, Equation [2] becomes

$$\frac{x(t + 2\pi) - x(t)}{2\pi} \sim \frac{\mu}{2\pi}\int_0^{2\pi} f(x, \sin \tau)d\tau = \mu F(x) \qquad [3]$$

Finally, the left side of Equation [3] is replaced by dx/dt, since the slope of the secant line is approximately the slope of the tangent line for $\mu << 1$. Equation [1] is replaced by

$$\frac{dx}{dt} = \mu F(x) = \frac{\mu}{2\pi}\int_0^{2\pi} f(x, \sin \tau)d\tau \qquad [4]$$

and Equation [4] can be integrated by a separation of variables. Equation [4] can be obtained immediately from Equation [1] simply by averaging the right-hand side of Equation [1] over one cycle of the motion in the time domain. This Kryloff-Bogoliuboff method can be applied to a system of differential equations involving slowly varying quantities.

Planetary Motion With a Constant Radial Perturbing Force

Consider the case of a point mass m under the influence of a central, inverse square law force of attraction upon which is superimposed a small constant radial force ϵ. Using polar coordinates (r, θ) with origin at the center of attraction, the equations of motion are

$$\frac{d^2r}{dt^2} - r\left(\frac{d\theta}{dt}\right)^2 = -\frac{GM}{r^2} + \frac{\epsilon}{m} \qquad \epsilon << 1$$

$$\frac{d}{dt}\left(r^2\frac{d\theta}{dt}\right) = 0$$

..... [5]

In the usual way one eliminates dt, using $r^2d\theta = hdt$, and replaces r by $1/u$ to obtain

$$\frac{d^2u}{d\theta^2} + u = \frac{GM}{h^2} - \frac{\epsilon}{mh^2u^2} \qquad [6]$$

or the system

$$\frac{du}{d\theta} = v \qquad \frac{dv}{d\theta} = -u + \frac{GM}{h^2} - \frac{\epsilon}{mh^2u^2} \qquad [7]$$

For $\epsilon = 0$, the solution of Equation [7] is[5]

$$u = s_0 \sin(\theta + \theta_0) + GM/h^2 \qquad v = s_0 \cos(\theta + \theta_0) \qquad [8]$$

with s_0 and θ_0 constants of integration. In order to apply the averaging process of Kryloff-Bogoliuboff, let u be equal to $s \sin(\theta + \phi) + GM/h^2$ and v be equal to $s \cos(\theta + \phi)$, with s

---

Presented at the ARS Semi-Annual Meeting, June 8–11, 1959, San Diego, Calif.

[1] This paper presents results of one phase of research carried out at the Jet Propulsion Laboratory, California Institute of Technology, under Contract no. NASw-6, sponsored by NASA.

[2] Research Specialist, Space Sciences Div.

[3] Research Specialist, Systems Division. Member ARS.

[4] Numbers in parentheses indicate References at end of paper.

[5] The unperturbed solution is restricted to closed (i.e., elliptic) orbits. Hyperbolic orbits, being noncyclic, cannot be handled by the present technique.

and ϕ unknown functions of θ. Thus

$$\frac{du}{d\theta} = \frac{ds}{d\theta}\sin(\theta+\phi) + s\left(1+\frac{d\phi}{d\theta}\right)\cos(\theta+\phi)$$

$$\frac{dv}{d\theta} = \frac{ds}{d\theta}\cos(\theta+\phi) - s\left(1+\frac{d\phi}{d\theta}\right)\sin(\theta+\phi)$$

.....[9]

Equations [7] yield

$$\frac{ds}{d\theta} = -\frac{\epsilon\cos(\theta+\phi)}{mh^2\,[s\sin(\theta+\phi)+GM/h^2]^2}$$

$$\frac{d\phi}{d\theta} = \frac{\epsilon\sin(\theta+\phi)}{mh^2 s\,[s\sin(\theta+\phi)+GM/h^2]^2}$$

.....[10]

Applying the averaging process of Kryloff-Bogoliuboff to Equations [10] yields

$$\frac{ds}{d\theta} = -\frac{\epsilon}{2\pi mh^2}\int_0^{2\pi}\frac{\cos\tau\,d\tau}{(s\sin\tau+GM/h^2)^2} = 0$$

$$\frac{d\phi}{d\theta} = \frac{\epsilon}{2\pi mh^2 s}\int_0^{2\pi}\frac{\sin\tau\,d\tau}{(s\sin\tau+GM/h^2)^2} = -\frac{\epsilon}{mh^2}\left(\frac{G^2M^2}{h^4}-s^2\right)^{-3/2}$$

.....[11]

An integration of Equations [11] yields

$$s = s_0 = \text{constant}$$

$$\phi = -\frac{\epsilon}{mh^2}\left(\frac{G^2M^2}{h^4}-s_0^2\right)^{-3/2}\theta+\phi_0$$

.....[12]

so that

$$u = \frac{1}{r} = \frac{GM}{h^2} + s_0\sin\left\{\left[1-\frac{\epsilon}{mh^2}\left(\frac{G^2M^2}{h^4}-s_0^2\right)^{-3/2}\right]\theta+\phi_0\right\} \quad [13]$$

It is seen that the line of apsides advances by the amount

$$\frac{2\pi\epsilon}{mh^2}\left(\frac{G^2M^2}{h^4}-s_0^2\right)^{-3/2} \text{ radians per revolution}$$

while the apogee and perigee distances remain invariant. In the case of a nearly circular orbit, $s_0 << GM/h^2$, the precession rate is $2\pi\eta$, where η is the ratio of thrust acceleration ϵ/m to the gravitational acceleration GM/r^2.

For small eccentricity, $\mu = s_0h^2/GM << 1$, one can obtain an improved solution of Equation [6] by making use of Equation [13]. Let

$$u = GM/h^2 + s_0\sin[(1-\Gamma)\theta+\phi_0] + \epsilon K(\theta)$$

with $\Gamma = \epsilon h^4/mG^2M^3$; see Equation [13]. Substituting into Equation [6] and neglecting ϵ^2 and $\epsilon\mu$ terms, one obtains

$$K'' + K = -h^2/mG^2M^2$$

which is satisfied by $K = -h^2/mG^2M^2$. Thus

$$u = \frac{GM}{h^2} + s_0\sin[(1-\Gamma)\theta+\phi_0] - \frac{\epsilon h^2}{mG^2M^2} \quad [14]$$

is an improved solution for small eccentricity.

Planetary Motion Under a Constant Transverse Perturbing Force

A properly oriented reflecting sail will experience a small transverse thrust as a result of solar radiation. In the following example, the transverse thrust is assumed to be constant.

The equations of motion are given by

$$\frac{d^2r}{dt^2} - r\left(\frac{d\theta}{dt}\right)^2 = -\frac{GM}{r^2}$$

$$\frac{1}{r}\frac{d}{dt}\left(r^2\frac{d\theta}{dt}\right) = \frac{\epsilon}{m} \qquad \epsilon << 1$$

.....[15]

Let $h = r^2(d\theta/dt)$, so that $dh/dt = (\epsilon/m)r$ and $dt = (r^2/h)d\theta = d\theta/hu^2$ for $u = 1/r$. Then

$$\frac{dh}{d\theta} = \frac{dh}{dt}\frac{dt}{d\theta} = \frac{\epsilon}{mh\,u^3}$$

$$\frac{dr}{dt} = \frac{dr}{d\theta}\frac{d\theta}{dt} = \frac{h}{r^2}\frac{dr}{d\theta} = -h\frac{du}{d\theta}$$

$$\frac{d^2r}{dt^2} = -h^2u^2\frac{d^2u}{d\theta^2} - \frac{\epsilon}{mu}\frac{du}{d\theta}$$

.....[16]

Letting $k = h^2$ and $v = du/d\theta$ yields

$$\frac{dk}{d\theta} = \frac{2\epsilon}{mh^3} \qquad \frac{du}{d\theta} = v$$

$$\frac{dv}{d\theta} = -u + \frac{GM}{k} - \frac{\epsilon v}{mk\,u^3}$$

.....[17]

For $\epsilon = 0$, the solutions of Equations [17] are

$$k = k_0 = \text{constant}$$

$$u = GM/k_0 + s_0\sin(\theta+\theta_0)$$

$$v = s_0\cos(\theta+\theta_0)$$

.....[18]

Now let

$$u = GM/k + s\sin(\theta+\phi) \qquad v = s\cos(\theta+\phi) \quad [19]$$

with s, ϕ and k unknown functions of θ. Equations [17] become

$$\frac{dk}{d\theta} = \frac{2\epsilon}{m}\left[\frac{GM}{k}+s\sin(\theta+\phi)\right]^{-3}$$

$$\frac{ds}{d\theta} = \left[\frac{2\epsilon GM\sin(\theta+\phi)}{mk^2} - \frac{\epsilon s\cos^2(\theta+\phi)}{mk}\right]\left[\frac{GM}{k}+s\sin(\theta+\phi)\right]^{-3}$$

$$\frac{d\phi}{d\theta} = \left[\frac{2\epsilon GM\cos(\theta+\phi)}{mk^2 s} + \frac{\epsilon\cos(\theta+\phi)\sin(\theta+\phi)}{mk}\right]\left[\frac{GM}{k}+s\sin(\theta+\phi)\right]^{-3}$$

.....[20]

Applying the averaging process of Kryloff-Bogoliuboff yields

$$\frac{dk}{d\theta} = \frac{\epsilon}{m}\frac{(2G^2M^2/k^2 + s^2)}{(G^2M^2/k^2 - s^2)^{5/2}}$$

$$\frac{ds}{d\theta} = -\frac{\epsilon}{2mk}\frac{(7G^2M^2/k^2 - s^2)}{(G^2M^2/k^2 - s^2)^{5/2}}$$

$$d\phi/d\theta = 0$$

.....[21]

From Equations [21], it follows that

$$\frac{ds}{dk} = -\frac{s}{2k}\frac{(7G^2M^2/k^2 - s^2)}{(2G^2M^2/k^2 + s^2)} \qquad [22]$$

The substitution $s = w(k)/k$ makes possible the integration of Equation [22], with the result that

$$k = K\{[G^2M^2 - (sk)^2]/(sk)^{4/3}\} \qquad [23]$$

with K a constant of integration which depends on the initial values of s and $k = h^2$. Equation [23] is a cubic equation in $(sk)^2$, and the algebraic solution of this equation yields $s = s(k)$.

From Equations [21] for $\epsilon < 0$, it follows that $dk/d\theta < 0$, so that k tends to zero, and hence $r \to 0$, an expected result. From Equation [23], it is seen that the square of the eccentricity of the orbit $E^2 = s^2k^2/G^2M^2 \to 1$, for $\epsilon < 0$. For $\epsilon > 0$, it can be seen that $k \to \infty$ and $s \to 0$, so that $r \to \infty$.

The apogee distance is given by

$$r_a = \frac{1}{GM/k - s} \qquad s > 0 \qquad [24]$$

so that in one cycle r_a changes by an amount Δr_a, given by

$$\Delta r_a \simeq \frac{2\pi}{(GM/k - s)^2}\left(\frac{GM}{k^2}\frac{dk}{d\theta} + \frac{ds}{d\theta}\right) \simeq$$

$$\frac{\pi\epsilon(4GM + sk)}{mk^2(G^2M^2/k^2 - s^2)^{1/2}} \qquad [25]$$

For a nearly circular orbit, $r_a \simeq k/GM$, $s << 1$, it follows that

$$\Delta r_a \simeq \frac{4\pi\epsilon r_a^3}{GmM} = 4\pi r_a\left[\frac{\epsilon/m}{GM/r_a^2}\right] \qquad [26]$$

Satellite Motion Under an Intermittent Perturbing Force

It is of interest to compute the motion of an Earth satellite acted upon intermittently by a uniform thrust (e.g., an ion motor). The uniform thrust acts upon the satellite for the half range $0 \leqq \theta \leqq \pi$; in the half range $\pi < \theta < 2\pi$, the ion motor is shut off. This periodic thrust program is continued, and the motion of the satellite is compared with the motion of a satellite having no thrust program. The latter satellite is assumed to move in a circular path. The oblateness of Earth is neglected, since the small force field resulting from Earth's oblateness affects the motion of both satellites in much the same fashion.

In polar coordinates the motion of the satellite is given by

$$\frac{d^2r}{dt^2} - r\left(\frac{d\theta}{dt}\right)^2 = -\frac{GM}{r^2} + \mu gF\sin\theta$$

$$\frac{1}{r}\frac{d}{dt}\left(r^2\frac{d\theta}{dt}\right) = \mu gF\cos\theta$$

.....[27]

with $F = 1$ for $0 \leqq \theta \leqq \pi$, $F = 0$ for $\pi < \theta < 2\pi$. The potential per unit mass of the ion thrust motor is given by $\phi = -\mu gFy = -\mu gFr\sin\theta F$, $\mu << 1$; g is the acceleration of gravity at Earth's surface. The loss of mass of the satellite has been neglected.

Let $r^2(d\theta/dt) = h \neq$ constant, $u = 1/r$, so that

$$\frac{dr}{dt} = \frac{dr}{d\theta}\frac{h}{r^2} = -h\frac{du}{d\theta}$$

$$\frac{d^2r}{dt^2} = -h^2u^2\frac{d^2u}{d\theta^2} - \frac{\mu g}{u}\frac{du}{d\theta}F\cos\theta$$

.....[28]

The equations of motion become

$$\frac{du}{d\theta} = v \qquad \frac{dh}{d\theta} = \frac{\mu g}{hu^3}F\cos\theta$$

$$\frac{dv}{d\theta} = -u + \frac{GM}{h^2} - \frac{\mu g}{h^2u^2}F\sin\theta - \frac{\mu gv}{h^2u^3}F\cos\theta$$

.....[29]

The substitution

$$u = GM/h^2 + A\sin\theta + B\cos\theta$$

$$v = A\cos\theta - B\sin\theta$$

.....[30]

with A and B unknown functions of θ, reduces Equations [29] to

$$\frac{dA}{d\theta} =$$

$$\frac{2\mu gGM}{h^4u^3}F\sin\theta\cos\theta - \frac{\mu g}{h^2u^2}F\sin\theta\cos\theta - \frac{\mu gv}{h^2u^3}F\cos^2\theta$$

$$\frac{dB}{d\theta} =$$

$$\frac{2\mu gGM}{h^4u^3}F\cos^2\theta + \frac{\mu g}{h^2u^2}F\sin^2\theta + \frac{\mu gv}{h^2u^3}F\sin\theta\cos\theta$$

$$\frac{dh}{d\theta} = \frac{\mu g}{hu^3}F\cos\theta$$

.....[31]

The instantaneous eccentricity of the orbit is given by

$$\epsilon = (h^2/GM)\sqrt{A^2 + B^2}$$

The ϵ^2 terms, etc., are neglected so that $A^2 + B^2 << G^2M^2/h^4$. Thus

$$u = \frac{GM}{h^2}\left(1 + \frac{Ah^2}{GM}\sin\theta + \frac{Bh^2}{GM}\cos\theta\right)$$

$$u^{-2} \approx \frac{h^4}{G^2M^2}\left(1 - \frac{2Ah^2}{GM}\sin\theta - \frac{2Bh^2}{GM}\cos\theta\right)$$

$$u^{-3} \approx \frac{h^6}{G^3M^3}\left(1 - \frac{3Ah^2}{GM}\sin\theta - \frac{3Bh^2}{GM}\cos\theta\right)$$

.....[32]

Applying the averaging process to Equations [31] by mak-

ing use of Equations [32] yields

$$\left\langle \frac{dA}{d\theta} \right\rangle = -\frac{\mu g h^4}{\pi G^3 M^3} B$$

$$\left\langle \frac{dB}{d\theta} \right\rangle = \frac{3}{4}\frac{\mu g h^2}{G^2 M^2} - \frac{3}{\pi}\frac{\mu g h^4}{G^3 M^3} A$$

$$\left\langle \frac{dh}{d\theta} \right\rangle = -\frac{3}{4}\frac{\mu g h^7}{G^4 M^4} B$$

..... [33]

Next, we remove the averaging symbol $< >$, and integrate the system of equations [33]. Thus

$$\frac{dA}{dh} = \frac{4GM}{3\pi h^3} \qquad A = -\frac{2GM}{3\pi h^3} + K \qquad [34]$$

with K a constant of integration. From Equations [33 and 34] are obtained

$$BdB = -\frac{G^2M^2}{h^5}\left(1 + \frac{8}{3\pi}\right)dh + \frac{4KGM}{\pi h^3}\,dh$$

$$\frac{B^2}{2} = \left(\frac{1}{4} + \frac{2}{3\pi}\right)\frac{G^2M^2}{h^4} - \frac{2KGM}{\pi h^2} + L$$

..... [35]

with L a constant of integration. The assumption $A^2 + B^2 << G^2M^2/h^4$ enables one to deduce that h is a constant whose value can be obtained by setting the right side of Equations [35] equal to zero and solving for h. This result is not surprising for orbits of small eccentricity, since on the average the torque produced by the thrust for the range $0 \leqq \theta \leqq \pi/2$ tends to cancel the torque produced by the thrust for the range $\pi/2 \leqq \theta \leqq \pi$.

Integrating the second equation of [33], with h and A constants of the motion, yields

$$B = \frac{\mu g h^2}{G^2M^2}\left[\left(\frac{3}{4} + \frac{2}{\pi^2}\right) - \frac{3Kh^2}{\pi GM}\right]\theta + B_0 \qquad [36]$$

Thus

$$u = \frac{1}{r} = \frac{GM}{h^2} + \left(K - \frac{2GM}{3\pi h^2}\right)\sin\theta + \left\{\frac{\mu g h^2}{G^2M^2}\left[\left(\frac{3}{4} + \frac{2}{\pi^2}\right) - \frac{3Kh^2}{\pi GM}\right]\theta + B_0\right\}\cos\theta \qquad [37]$$

If the satellite is initially in circular motion, then $r = R$, $GM/h^2 = 1/R$, $u = 1/R$, $\dot{u} = 0$, at $\theta = 0$, $t = 0$, so that

$$K - \frac{2GM}{3\pi h^2} + \frac{\mu g h^2}{G^2M^2}\left[\left(\frac{3}{4} + \frac{2}{\pi^2}\right) - \frac{3Kh^2}{\pi GM}\right] = 0$$

$$B_0 = 0$$

..... [38]

Hence

$$K = \frac{\dfrac{2GM}{3\pi h^2} - \dfrac{\mu g h^2}{G^2M^2}\left(\dfrac{3}{4} + \dfrac{2}{\pi^2}\right)}{1 - 3\,\mu g h^4/\pi G^3 M^3}$$

$$K \approx \frac{2GM}{3\pi h^2}\left(1 - \frac{9\,\pi\mu g h^4}{8G^3M^3}\right)$$

..... [39]

and

$$u = \frac{1}{r} = \frac{GM}{h^2} - \frac{3}{4}\frac{\mu g h^2}{G^2M^2}\sin\theta + \frac{3}{4}\frac{\mu g h^2}{G^2M^2}\theta\cos\theta \qquad [40]$$

neglecting μ^2 terms, so that

$$r \approx R\,[1 + (3\,\mu g R^2/4GM)(\sin\theta - \theta\cos\theta)] \qquad [41]$$

since $h^2 = GMR$. The change in r per revolution is

$$\Delta r = -\,[(3/2)\pi\mu g R^3/GM] \qquad [42]$$

The instantaneous eccentricity is given by

$$\epsilon = \frac{3}{4}\frac{\mu g R^2}{GM}\sqrt{1 + \theta^2} \qquad [43]$$

For $\mu \approx 10^{-5}$, $GM/R^2 \approx g$, one has $\epsilon \approx (3/4)(10^{-5}) \times \sqrt{1 + \theta^2}$, so that the eccentricity will remain small for a considerable number of revolutions. Thus we are justified in omitting ϵ^2 terms, etc.

From $r^2\,(d\theta/dt) = h$, and from Equation [41] one obtains

$$\theta \approx \frac{h}{R^2}\,t + \frac{3\,\mu g R^2}{GM} \times \left[\cos\left(\frac{h}{R^2}t\right) + \frac{ht}{2R^2}\sin\left(\frac{h}{R^2}t\right) - 1\right] \qquad [44]$$

The coordinates of the unperturbed satellite are $r_0 = R$, $\theta_0 = ht/R^2$. The distance ρ between the two satellites is given by

$$\rho = \frac{3\,\mu g R^3}{GM}\left\{\frac{1}{16}\left[\sin\left(\frac{ht}{R^2}\right) - \left(\frac{ht}{R^2}\right)\cos\left(\frac{ht}{R^2}\right)\right]^2 + \cos\left[\left(\frac{ht}{R^2}\right) + \frac{ht}{2R^2}\sin\left(\frac{ht}{R^2}\right) - 1\right]^2\right\}^{1/2} \qquad [45]$$

Comparison With Other Results

It has been shown in the foregoing, in the discussion of a constant radial perturbing force, that for a small radial thrust the trajectory is given by Equation [14] which may be written in the form

$$r = \frac{h^2/GM}{1 + (s_0h^2/GM)\sin[(1 - \Gamma)\theta + \phi_0] - \epsilon h^4/m(GM)^3} \qquad [46]$$

where

$$\Gamma = \frac{\epsilon\, h^4}{mG^3M^3} \qquad [47]$$

Equation [46] is almost in standard form for an ellipse. In fact, by setting $\epsilon = 0$ it is seen that the osculating ellipse has the following parameters: Semilatus rectum, h^2/GM; eccentricity, s_0h^2/GM; angle from pericenter to origin, $\phi_0 - \pi/2$.

In particular, for a near-circular orbit s_0 is small. Therefore, by Equation [46]

$$h^2 \sim GMr_0 \qquad [48]$$

and by Equation [47]

$$\Gamma \sim \frac{\epsilon}{m} \div \frac{GM}{r^2} = \eta \qquad [49]$$

It follows from Equations [46 and 49] that the line of apsides advances by the amount $2\,\pi\eta$ radians per revolution.

Dobrowolski indicates a regression of the line of apses. However, he apparently used an incorrect expansion for his parameter b to substitute in his general solution. Substitution of the correct expansion gives a result in agreement with ours. Copeland's Fig. 2 further confirms the result that the line of apsides advances rather than regresses.

For near-circular motion we can evaluate the constants s_0

and ϕ_0 as follows. Assume that initially $r = r_0$, $\dot{r} = 0$ and $\theta = 0$. Then, by Equation [46]

$$\frac{1}{r_0} = \frac{GM}{h^2} + \varepsilon_0 \sin \phi_0 - \frac{\eta}{r_0} \qquad [50]$$

and, from the first derivative of Equation [46]

$$0 = \varepsilon_0(1 - \Gamma) \cos \phi_0 \qquad [51]$$

It then follows that the initial position is at pericenter with

$$\phi_0 = \pi/2 \qquad [52]$$

$$-\varepsilon_0 = \frac{GM}{h^2} - \frac{1}{r_0} - \frac{\eta}{r_0} \qquad [53]$$

hence, using Equation [48]

$$\varepsilon_0 \sim \eta/r_0 \qquad [54]$$

which in conjunction with Equation [48] implies that η is approximately equal to the eccentricity.

To get the maximum excursion of the radial distance r, it is only necessary to take the difference between r_{max} and r_{min} as obtained from Equation [46] and write

$$\frac{r_{max} - r_{min}}{r_0} = 2r_0\varepsilon_0 = 2\eta \qquad [55]$$

in agreement with Dobrowolski.

In the case of circumferential thrust, the maximum radial distance in each cycle does not remain stationary. Its rate of growth is given by Equation [26] for the nearly circular orbit, i.e., $\Delta r_a/r_a \sim 4\pi\eta$. This result agrees directly with that of Perkins (5) as can be seen by substituting $\Delta\phi = 2\pi$ in Equation [29] of Perkins' paper.

Conclusion

Briefly, application of the nonlinear techniques of Kryloff and Bogoliuboff has been shown to provide concise solutions to the problems of small radial thrust and small circumferential thrust previously discussed in the literature, and to the problem of intermittent thrust, which has not had previously published solutions. It is hoped that this work will inspire more extensive application of the method.

References

1 Tsien, H. S., "Take-Off From Satellite Orbits," JOURNAL OF THE AMERICAN ROCKET SOCIETY, vol. 23, July-Aug. 1953, pp. 233–236.

2 Kryloff, N. and Bogoliuboff, N., "Introduction to Non-Linear Mechanics," Kiev, 1937, chaps. 10–12. Translation edition tr. by Solomon Lefschetz, Princeton University Press, Princeton, 1943. [See (6).]

3 Dobrowolski, A., "Satellite Orbit Perturbations Under a Continuous Radial Thrust of Small Magnitude," JET PROPULSION, vol. 28, no. 10, Oct. 1958, pp. 687–688.

4 Copeland, J., "Interplanetary Trajectories Under Low Thrust Radial Acceleration," ARS JOURNAL, vol. 29, no. 4, April 1959, pp. 267–271.

5 Perkins, F. M., "Flight Mechanics of Low-Thrust Spacecraft," *J. Aero/-Space Sci.*, vol. 26, May 1959, pp. 291–297.

6 Minorsky, N., "Introduction to Non-Linear Mechanics," J. W. Edwards, Ann Arbor, 1947, chap. X, based on cited chapters of reference (2).

Powered Trajectory Studies for Low Thrust Space Vehicles[1]

ROBERT H. FOX[2]

Lawrence Radiation Laboratory,
University of California
Livermore, Calif.

Powered trajectory calculations have been carried out for missions from Earth to Venus, Mars, Jupiter and return. The procedure used was based upon an optimization which minimizes total energy requirements and maximizes payload. Data are presented which relate payload fraction, total mission time, and minimum specific power requirements. It is shown that propulsion plant weight-to-exhaust power ratios of 122 lb/kw and 22 lb/kw are adequate for missions ranging in difficulty from one-way trips to Mars with 10 per cent payload fraction to round trips to Mars with 30 per cent payload, respectively. In both cases the transfer is assumed to be between low altitude satellite orbits about the planets in question.

DURING the last year a study of electrical propulsion has been carried out at the Lawrence Radiation Laboratory. In order to lay a proper foundation for such a study it was necessary to determine the relationship among mission requirements (characteristic velocity), propulsion system specific power, mission time, and payload fraction. Consequently, some theoretical studies of a simple nature were made, supplemented by some powered trajectory calculations on the IBM-704. The results, while certainly not optimal, do provide the desired results in an approximate form with minimum expenditure of effort and computer time.

Presented at the ARS Semi-Annual Meeting, June 8–11, 1959, San Diego, Calif.

[1] This work has been performed under auspices of the U. S. Atomic Energy Commission.

[2] Assistant Division Leader, Nuclear Propulsion Division.

Now, there are many ways to carry out such a calculational program. The procedure adopted here was to minimize (approximately) the energy expenditure for a given mission and to calculate the time requirement. It turned out fortuitously that great economies in digital computer time resulted.

The fundamental equation to be considered for low thrust vehicles is

$$F = 2P/c \qquad [1]$$

where

F = thrust magnitude
P = exhaust power
c = exhaust velocity

If the power is kept constant at its maximum value, then it can be shown that the total energy consumption and hence power-on time τ are minimized when the exhaust velocity is varied in time according to (1,2)[3]

$$c(t) = \frac{V_e}{\mu - 1}\frac{m(0)}{m(t)} \qquad [2]$$

Here

μ = ratio of initial to final mass
$m(t)$ = vehicle mass at time t (we ignore the coasting part of the trip)
V_e = characteristic velocity for the mission

V_e is defined by

$$V_e = \int_0^\tau a(t)dt \qquad [3]$$

where a is the acceleration due to thrust forces [a = thrust/$m(t)$] and t is measured only during the power-on time. Note that a is independent of the vehicle velocity. Since the power is constant, the exhaust velocity program [Eq. 2] yields constant acceleration. Equation [2] may be substituted into Equation [1] and the resulting equation of motion integrated to yield

$$\tau = \frac{V_e^2}{2P_{sp}}\frac{\mu}{\mu - 1}\frac{1}{1 - r\mu} \qquad [4]$$

P_{sp} = specific power of the propulsion plant (P/propulsion plant mass)
r = payload fraction (payload mass/initial total mass)

We may further minimize τ with respect to μ and we find a minimum when

$$\mu^2 = 1/r \qquad [5]$$

Then the correct average exhaust velocity is found to be

$$\bar{c} = V_e r^{1/4}/(1 - r^{1/2}) \qquad [6]$$

This is plotted in Fig. 1. Also

$$\tau_{\min} = (V_e^2/2P_{sp})(1 - r^{1/2})^{-2} \qquad [7]$$

Since the acceleration is constant and given by

$$a = V_e/\tau$$

Equation [7] may be written

$$2P_{sp}(1 - r^{1/2})^2 = aV_e \qquad [8]$$

(Note that the choice for μ given by Equation [5] also maximizes r if τ, V_e, P_{sp} are fixed. The nature of the maximum is shown in Fig. 2 for $r_{\max} = 0.25$.)

Equation [8] is the fundamental relationship which is the basis of the powered trajectory calculations. The idea is as follows: For a vehicle in space under the influence of a gravitational field and acted on by a thrust force **F**, it can be shown that the instantaneous rate of change of the total energy E of the vehicle (kinetic plus potential energy) is maximized by having **F** parallel to the velocity vector. This is a "gravity-turn" thrust program. It does not, however, maximize the total change in E over the powered portion of the flight, and is not much different from the optimum program in this sense. Also, if V_e varies only slowly with acceleration, then the exhaust velocity program [Eq. 2] is nearly optimal for minimum energy trajectories.

It turns out that a gravity-turn thrust program with constant acceleration is particularly easy to calculate, using a digital computer. In fact, the already existing satellite code was immediately applicable to this program. The basic procedure was then the following: Starting from a low altitude orbit about Earth, the equations of motion were integrated for a fixed acceleration with thrust parallel to the instantaneous velocity vector until escape energy relative to Earth was reached. Some initial runs which included the moon's effect on the motion indicated that it is small if the time phasing is properly carried out. Hence, the moon's effect was not included, in general. It was not necessary to repeat these calculations for the other planets, since scaling laws exist which permit Earth escape problems to be transformed

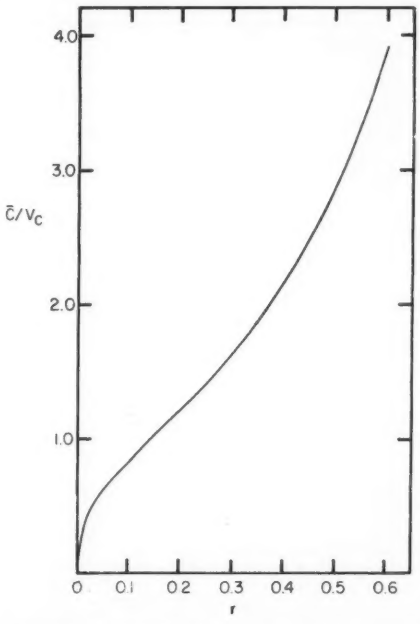

Fig. 1 Dependence of optimum average exhaust velocity upon mission characteristic velocity and vehicle payload fraction

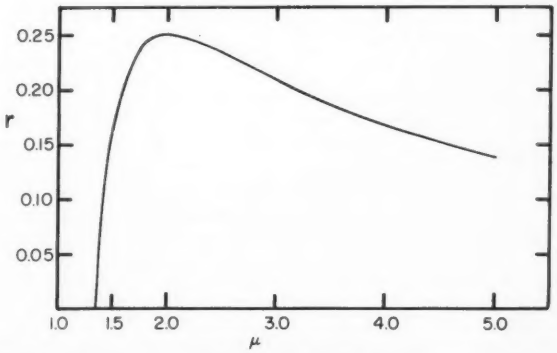

Fig. 2 Nature of dependence of payload fraction on mass ratio for $P_{sp}/a\ V_e = 2.0$

[3] Numbers in parentheses indicate References at end of paper.

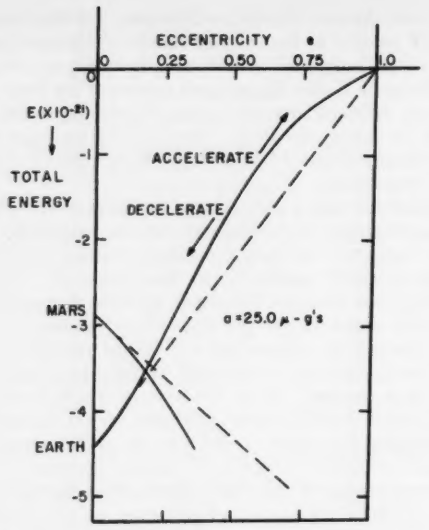

Fig. 3 Locus of osculating orbits for gravity-turn program

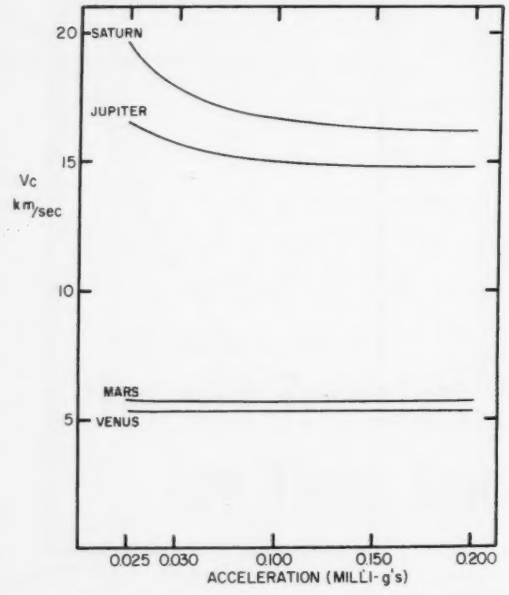

Fig. 4 Variation of V_c with acceleration. One-way trip from Earth solar orbit to planetary solar orbit. Gravity-turn thrust program

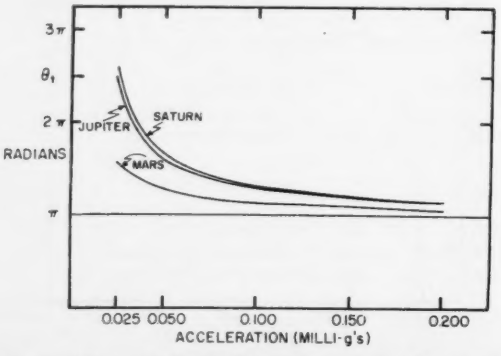

Fig. 5 Variation of interorbit transfer angle θ_t with acceleration. Gravity-turn thrust program

directly into the escape problems from other planetary gravitational fields.

Interorbital transfer calculations were then undertaken using the sun as the only gravity source. Acceleration problems from Venus' and Earth's solar orbits were run, starting with the planet's velocity and accelerating until escape energy from the sun's gravitational field was achieved. Similarly, deceleration problems were run, starting from Jupiter's, Saturn's and Mars' solar orbits, and terminating when the total energy characteristic of Earth's orbit was reached. An additional set of deceleration problems were started from Earth's solar orbit and terminated when the total energy was characteristic of Venus' orbit.

Now, in an actual spaceflight of this type, the vehicle would accelerate only until the proper coasting energy was achieved, coast part of the way to the destination orbit and, at the proper moment, resume acceleration so as to achieve the matching condition on the velocity vector upon arrival at the destination orbit. The problem here is the determination of the proper moments for thrust shutdown and startup. Consider for a moment the osculating orbit at some moment of powered flight. This is the orbit the vehicle would follow if thrust ceased at that moment. The shape of this orbit is characterized by two parameters, the total energy E and the eccentricity e. These parameters are printed out at each integration step. We may now plot the locus of the osculating orbits for our gravity-turn interplanetary powered trajectories in the E, e coordinate system; this is done for a typical Earth-Mars case in Fig. 3. If the vehicle is accelerating, the point representing the osculating orbit moves in the direction of increasing E as indicated. If we decelerate, the same curve is traversed in the opposite direction. We note that an accelerating curve starting from Earth intersects a decelerating one starting from Mars. From symmetry considerations, the locus of osculating orbits for a deceleration trajectory starting from Mars is identical with the locus for an acceleration trajectory which matches the Mars orbit at its terminal point. The intersection in the E, e coordinate system is determined from the code outputs, and thus the positions in space for power shutdown and startup are obtained. This makes possible calculation of the coasting time which is determined by the parameters of the osculating orbit at the intersection point, and the radial distances from the sun at this point as determined from the code output. The power-on transit angles are obtained from the code output. Having determined the total transit time T_t and total transit angle θ_t required to make such a transfer, we can now quickly determine the waiting time in the vicinity of the destination planet before return is possible. We have for the waiting time

$$T_w = bn \pm 2b\frac{T_t}{T_E} \mp \frac{b}{\pi}\theta_t \qquad [9]$$

T_E is the period of revolution of Earth. The total round trip time from Earth's orbit back to Earth's orbit is then

$$T = bn + 2(1 \pm b)\frac{T_t}{T_E} \mp \frac{b}{\pi}\theta_t = T_w + 2T_t \qquad [10]$$

where

b = $2\pi/(\dot{\theta}_i - \dot{\theta}_o)$
$\dot{\theta}_i$ = angular velocity of inner planet
$\dot{\theta}_0$ = angular velocity of outer planet
n = integer = $(n-1)\pi < \pm[2\pi(T_t/T_E) - \theta_t] < n\pi$

In these equations, upper signs apply when destination is an inner planet, lower signs when destination is an outer planet.

When such a calculation has been carried out for a given value of the acceleration a, the characteristic velocity is also obtained, from

$$V_c = a\tau \qquad [11]$$

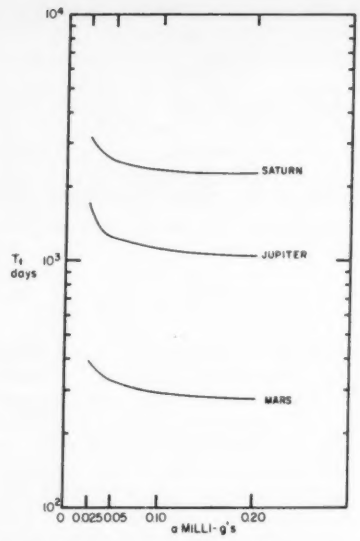

Fig. 6 Variation of one-way interorbit transfer time with acceleration. Gravity-turn thrust program

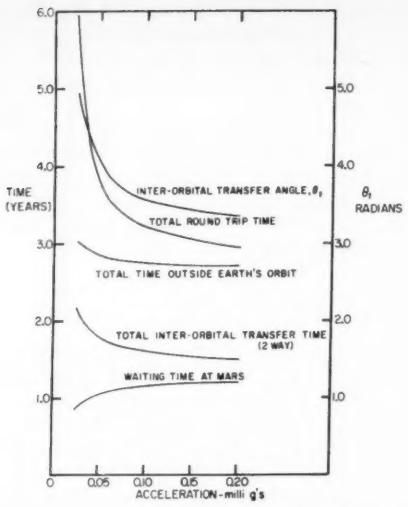

Fig. 7 Total round trip time for Earth-Mars mission. Terminal conditions: 250-mile Earth orbit, 200-mile Martian orbit. The time breakdown and interorbital transfer angles are also shown. Gravity-turn thrust program

Thus, the right side of Equation [8] is known. Since the left side contains two variables, P_{sp} or r, this single machine solution corresponds to a large variety of real solutions, namely, any combination of P_{sp} and r which satisfies Equation [8]. This fact, together with the scaling laws for escape from planetary gravitational fields, has permitted the calculation of all the gravity-turn trajectories at accelerations of 0.2, 0.15, 0.1, 0.05, 0.025 milli-g and for missions from Earth to Venus, Mars, Jupiter and Saturn, with a total expenditure of less than 20 hr of IBM-704 computer time. Since the acceleration problems were carried out to escape energy relative to the sun, we also have the near-Earth part of the solution for transfer to Jupiter or Saturn on a high energy coasting orbit. However, achieving the necessary matching condition at Jupiter's orbit cannot be done by gravity turn, in this case; therefore this has not yet been computed. At sufficiently high accelerations ($\lesssim 0.7$ milli-g) such a transfer could reduce the round trip time by a factor of 2, and the Jupiter trip time would then be comparable to that required for the Martian trip. However, since both a and V_e are considerably greater, the specific power would have to be about a factor of 10 higher in order to achieve the same payload fraction.

In order to indicate the nature of the results, the interorbital characteristic velocity V_e, orbital transfer angle θ_t, and total one-way transit time T_t are plotted vs. the acceleration in Figs. 4, 5 and 6. Clearly, for $a < 0.10$ milli-g, both transit time and transit angle begin to increase as the acceleration decreases. For $a > 0.10$, they are essentially independent of acceleration. Similar behavior for V_e is noted for trips to the outer planets but not for trips to Venus and Mars. In the latter two cases V_e begins to increase when $a < 0.025$ milli-g.

The results of these calculations can be used to determine minimum requirements for P_{sp} as a function of payload for missions to a given planet. In Fig. 7 a plot has been made of total round trip time as a function of the acceleration for the Mars trip. For this trip we assume that the vehicle starts in a 250-statute-mile orbit about Earth, goes to Mars and descends to a 200-mile orbit about Mars, and returns to a 250-mile orbit about Earth. A time breakdown is also indicated. Since the function $P_{sp}(1 - r^{1/2})^2$ is known once a and V_e are known, we can plot minimum P_{sp} vs. desired payload fraction and allowable trip time. This is shown in Fig. 8 for the Martian round trip.

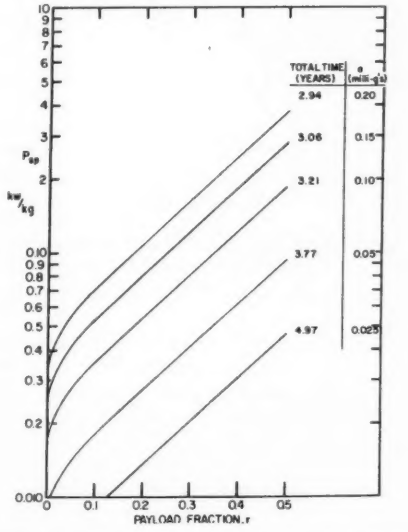

Fig. 8 Specific power requirements for round trip to Mars. Start from 250-mile Earth orbit, descend to 200-mile Martian orbit, and return

From Fig. 8 it is evident that a specific power of about 0.1 kw/kg is required if we want to transport reasonably large payloads ($r \sim 0.3$) round trip in a time of about 3 years. This would be the situation for a manned trip. On the other hand, if we are concerned with an unmanned probe going one way, the situation is considerably different. In this case, a large fraction of the useful payload can be the powerplant, and r merely represents the date-gathering and communication equipment. Thus we may have $r \sim 0.1$ or less. V_e is smaller by a factor of 2, and the time is greatly reduced. The resulting plots of required P_{sp} vs. r is shown in Fig. 9. The results for Venus are quite similar in both cases.

Taking the 409-day curve as a reasonable compromise between time and specific power we see that a payload fraction

of 0.1 requires a specific power value of only 0.018 kw/kg. For $r = 0.025$ this requirement is reduced to only 0.014 kw/kg. Clearly, if reasonably light thrust chambers can be developed with good efficiency these requirements are not too far beyond our present capabilities.

Now the foregoing calculational procedure is not optimal if we consider trip time to be the important parameter rather than energy consumption. For example, Irving and Blum (3) have considered the general variational problem of minimizing the transit from orbit-to-orbit, allowing both specific impulse and thrust angle to vary.

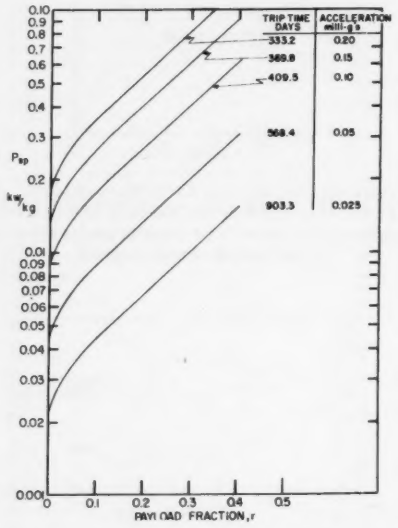

Fig. 9 Specific power requirements for one-way trip to Mars. Start from 250-mile Earth orbit, descend to 200-mile Martian orbit

They were able to obtain a 90-day transit time and $\theta_t = 78.2$ deg with $P_{sp} = 0.10$ kw/kg and $r = 0.182$. Compare this with 270 days and $\theta_t = 190$ deg for the minimum energy case. The transit V_e was a factor of 2 higher for that case and hence the energy expenditure a factor of 4 higher.

Although their procedure does lead to minimization of transit time for one-way trips it does not lead to minimization of round trip time in general. The reason can be seen by referring to Equation [10]. For the round trip case, the waiting time is quite important. Consequently, rather than minimizing T_t, the quantity

$$2(1 - b)\frac{T_t}{T_E} + \frac{b}{\pi}\theta_t$$

should be minimized. This is a completely different variational problem. Note from Equation [10] that if we decrease T_t and keep θ_t constant we actually *increase* the orbit-to-orbit round trip time for missions to the outer planets. In the comparison case cited, the round trip times are 890 days for the time-optimized solution and 975 days for the energy-optimized solution. Since the time-optimized solution led to such interesting results for one-way transits, it is suggested that the corresponding variational problem outlined here might lead to equally interesting results for round trip missions.

Acknowledgment

I would like to express my appreciation to Mr. Nevin Sherman who carried out the computer calculation and analysis of the computer results.

References

1 Seifert, H. S., "The Performance of a Rocket With Tapered Exhaust Velocity," JET PROPULSION, vol. 27, no. 12, 1957, pp. 1264–1266.

2 Fox, R. H., "Optimum Exhaust Velocity Programming and Propulsion Efficiency," Lawrence Radiation Lab., Univ. of California, Livermore, Calif., Rep. UCRL-5135, May 26, 1958.

3 Irving, J. H. and Blum, E. K., "Comparative Performance of Ballistic and Low Thrust Vehicles for Flight to Mars," Space Technology Laboratory, Inc., Los Angeles, Calif.; *also* "Vistas in Astronautics," Vol. II, Pergamon Press, N.Y., 1959, pp. 191–218.

Complete Elementary Solution to Some Optimum Trajectory Problems

FRANK D. FAULKNER[1]

U. S. Naval Postgraduate School
Monterey, Calif.

A complete elementary and direct method is given for solving a class of optimum trajectory and design problems which arise in rocketry. The solution of problems which involve an optimum relation among final fuel consumption, position and time is reduced to elementary algebra. It is assumed that aerodynamic forces are negligible and gravity is constant or can be expressed as a function of time. The problem of intercepting a ballistic missile with minimum fuel consumption is studied in some detail as a typical problem. For this problem a hyperbola can be plotted on a prepared graph and the answers read. Solutions for the lower bound of fuel consumption, corresponding to infinite thrust can be read also. It is assumed that enough of the initial conditions are given so that the problem is properly posed. A more general class including the Mayer reciprocal problems can also be handled, provided the velocity at one end is not involved in the end conditions. The method can be applied to initial design problems wherein it is desired to make an estimate of thrust and fuel requirements for a rocket which is to effect some specified mission, such as to gain a given altitude or intercept a specified type of target.

A COMPLETE and elementary method is given in this paper for solving a class of problems which arises in the study of optimum performance of a rocket and in associated design problems. The method reduces the solution of problems, such as that of intercepting a target following a known path above the atmosphere, in a uniform gravitational field, to elementary algebra. For many problems a prepared graph can be used to reduce the work of solving to the plotting of a simple curve and reading off values associated with the solution.

The method is based on the following simplifying assumptions: The gravitational field is a known function of time, aerodynamic forces are negligible, the rocket is treated as a point mass, and the path of the target point is a known function of time.

The method is carried through in some detail for the case of a rocket whose maximum thrust is constant, and for a ballistic target. The general type of problems which it treats are: Initial conditions are assumed given; it is desired to intercept a target following a known path in minimum time, or with minimum fuel consumption, or to maximize the range attained by a rocket with a given amount of fuel. Most of the problems which are Mayer reciprocal [(1) p. 574][2] can be solved more or less directly, and some problems wherein the initial values are not all given.

It is well known [see (4) or (8) for elementary proofs] that under these assumptions, thrust must be fixed in direction and as large as possible during an initial period for maximum performance. With these assumptions, a single grid for displacement can be drawn up in dimensionless form for all rockets whose thrust is similar (defined in the text) during its period of application. On this graph the displacement of the target point may be plotted in the proper coordinate set, and from the relation between the two curves it can be determined at what times, if any, interception is possible, including the earliest and latest times, and the time which corresponds to minimum fuel consumption. For a ballistic target in a uniform gravitational field the target displacement is a hyperbola.

The essential features of the graphic solution can be extended to several other cases wherein the differential equations of motion are linear and symmetric in the variables. However the construction of the graphs is more tedious and not generally worthwhile.

Features of the graphic solution include:

1 The solution is completely elementary.

2 Every number in the solution can be determined directly.

3 The quantities which enter have physical significance, which reduces the likelihood of gross errors.

4 In many problems involving optima, the interpretation is so straightforward that it is obvious the conditions are both necessary and sufficient, under the given conditions (analytic proofs have also been carried out).

5 Existence or nonexistence of solutions, and their nature, is determined directly.

6 The solution for thrust as an impulse may be obtained directly from the same graph.

Most of this paper is devoted to the simple graphic solution, but it should be pointed out also that the results given in (4 and 8) reduce the solution of a somewhat wider class of problems in optimum trajectories to the solution of finite equations; that is, no differential equations or integrals are involved in the solution. In particular, if the gravitational acceleration can be expressed as a function of time only, if the motion of the final point is a known function of time, if the velocity is not involved at one end, and if the mass is specified at one end; then the solution of the problem is reduced to the solution of finite equations, that is, not involving differential equations or integrals. Somewhat more involved cases will be mentioned.

Construction of the Graph

The equation of motion for a rocket subject to no external forces may be written

$$a = c\dot{m}/(1 - m) \qquad [1]$$

Received Dec. 3, 1959.

[1] Professor of Mathematics and Mechanics; also Consultant, Boeing Airplane Co. Member ARS.

[2] Numbers in parentheses indicate References at end of paper.

where

a = acceleration
c = effective speed of the emitted particles, assumed constant
m = ratio of mass of the fuel which has been consumed to initial gross mass of the rocket including its fuel
$(\dot{})$ = time derivative

This may be integrated for one-dimensional motion to obtain the velocity

$$v = -c \ln(1 - m) \qquad [2]$$

if the initial velocity is zero.

If the rate of burning fuel is constant, $\dot{m} = \dot{m}_0$ during the period of thrust, this may be integrated again to get displacement

$$r = ct[1 + (1/m - 1) \ln (1 - m)] \qquad [3]$$

if $r(0) = 0$. In the following sections $\dot{m}$ is constant during the period of thrust and the subscript will be dropped. If thrust is applied for a time t_1 and the rocket then coasts, the displacement is given by

$$r(t, t_1) = -ct \ln (1 - m_1) + ct_1[1 + (1/m_1) \ln (1 - m_1)] \qquad [4]$$

for $t \geq t_1$; this includes Equation [3] if we set $t = t_1$ during thrust, or the period of burning.

For the dimensionless form, introduce the three dimensionless quantities [(5) p. 10]

$$t^* = \dot{m}t$$
$$v^* = v/c$$
$$r^* = r/(c/\dot{m}) \qquad \ldots\ldots\ldots\ldots\ldots\ldots\ldots\ldots [5]$$

The equations given earlier become

$$v^* = -\ln (1 - t^*) \qquad [6]$$

or

$$v_1^* = -\ln (1 - t_1^*)$$
$$r(t^*) = t^* + (1 - t^*) \ln (1 - t^*) \qquad \ldots\ldots\ldots\ldots\ldots\ldots\ldots\ldots [7]$$

and

$$r^*(t^*, t_1^*) = -t^* \ln (1 - t_1^*) + t_1^* + \ln (1 - t_1^*) \qquad [8]$$

These equations describe the motion owing to thrust for any rocket whose thrust is constant, except for the parameters c and $\dot{m}$ of the rocket and its fuel.

Fig. 1 is a graph of $r^*(t^*, t_1^*)$ vs. t^* with t_1^* as a parameter. It has several interesting properties. For example, if it were possible to burn up the entire rocket with the same equation of motion, the velocity would become infinite, but the distance it would travel in that time would be finite, namely $c/\dot{m}$, which is the unit of distance used in the conversion to dimensionless form. The unit of time $1/\dot{m}$ is the corresponding time it would take to burn up the entire rocket, and is sometimes given the descriptive name "burnup time" [(5) p. 12]. It can be verified by substitution into Equation [8] that

$$r^*(1, t_1^*) = t_1^* \qquad [9]$$

It is desired to determine the point t_1^* of tangency of lines tangent to the curve $r^*(t^*, t_1^*)$. Since the contact of these curves is of first degree, it is not easy to do this accurately by direct means. However the point of intersection of the tangent line with the line $t^* = 1$ can be determined much more accurately, since the lines cross at a finite angle, to yield t_1^*.

Solution of the Interception Problem

The equation for the relative displacement of a ballistic target with respect to a missile, when both are above the sensible atmosphere and near enough together so that the difference of the gravitational acceleration on the two is negligible may be written [(4) chap. III]

$$\varrho = \mathbf{R} - \int_0^t (t - \tau)\mathbf{a}(\tau)d\tau \qquad [10]$$

where $\mathbf{a}$ is the acceleration of the rocket owing to thrust

$$\mathbf{r} = \int_0^t (t - \tau)\mathbf{a}(\tau)d\tau \qquad [11]$$

is the displacement of the rocket starting from rest in an inertial frame, and

$$\mathbf{R} = \mathbf{R}_0 + \dot{\mathbf{R}}_0 t \qquad [12]$$

with $\mathbf{R}_0$ the initial relative position of the target, and $\dot{\mathbf{R}}_0$ its initial relative velocity.

It is fairly well known that for optimum performance in effecting an optimum relation among fuel consumption, time and displacement, two basic principles must be observed.

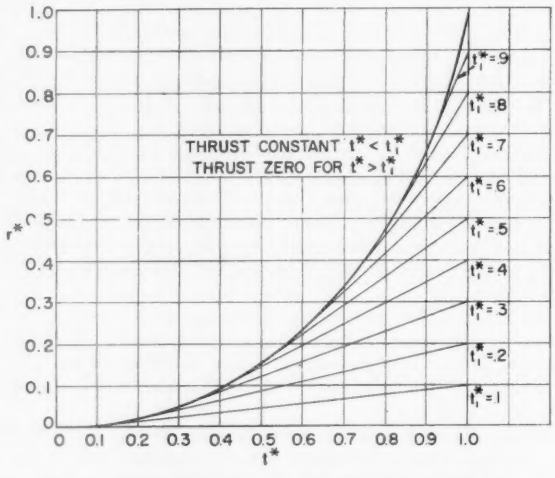

Fig. 1 Displacement vs. time in dimensionless form

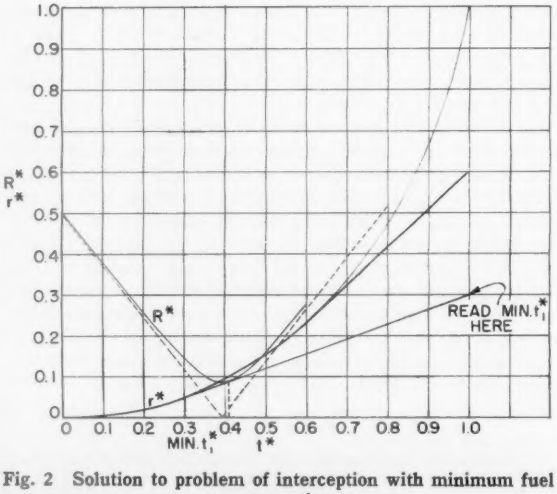

Fig. 2 Solution to problem of interception with minimum fuel consumption

The direction of the thrust must be fixed in the proper direction, and the thrust must be as large as possible during a properly chosen initial period, then zero thereafter [see (4) chaps. IV and V or (8) sections III and IV for elementary proofs].

The graph of Fig. 1 then describes $r = |\mathbf{r}|$ in this case. For interception it is necessary that $\varrho = 0$, hence that

$$r = R = |\mathbf{R}| \qquad [13]$$

But R is a known function of t, when the initial conditions are given. Convert R into a dimensionless form

$$R^* = R/(c/\dot{m}) \qquad [14]$$

and superimpose the graph of R^* vs. t^* on the grid of Fig. 1; see Fig. 2.

The rocket will have available a certain amount of fuel, described by the maximum value of t_1^*, say t_{1m}^*. The graph consisting of

$$r^* = \begin{cases} r^*(t^*),\ 0 < t^* \leq t_{1m}^* \\ r^*(t^*, t_{1m}^*),\ t_{1m}^* \leq t^* \end{cases} \qquad [15]$$

indicated by the heavy curve of Fig. 2, represents a curve of maximum performance, i.e., it represents the maximum possible value of r^* as a function of t^* for that rocket. It will be denoted by $r_m^*(t^*)$ or r_m^* when it is desired to emphasize this property.

Interception is possible for all times t_2^* when the curve for R^* lies on or below this curve for r_m^* and is not possible at any other time. This completely describes the times at which interception can be effected. The maximum and minimum values of interception time may be read directly from the graph.

Interception with minimum fuel consumption corresponds to minimum t_1^*, since $t_1^* = m_1$ under the given conditions. This corresponds to a common tangent to the curve for $r^*(t^*)$ and R^* with $t_2^* > t_1^*$: For any smaller value of t_1^*, the curve for $r^*(t^*, t_1^*)$ lies entirely below the convex curve for R^*.

A path of minimum fuel consumption is possible only for a target which is essentially incoming; the range rate must be negative at $t = 0$. If it is outgoing initially, or if it is incoming too rapidly so that it overshoots, then there is no common tangent. In the former case, when a path of minimum fuel consumption exists, it is found that $\ln(1 - t_1^*) < |\dot{R}_0^*|$. In the latter case, when it does not, $\ln(1 - t_1^*) > |\dot{R}_0^*|$. See (5) section IV.

As an example consider a rocket with an initial gross weight of 3000 lb of which 1800 lb is fuel, thrust 30,000 lb, $c = 8000$ fps. Then $\dot{m}$ is 0.04, and $c/\dot{m}$ is 200,000 ft. Let the initial position of the rocket be (100,000; 0; 300,000) and the target (166,667; 66,667; 333,333), so that $R_0 = 100{,}000$. Let the velocity of the rocket have components (1157; 2157; 3919), and for the target (−5000; −4000; −1000), so that the initial relative speed is 10,000. The value for R is given by $R^2 = (66{,}667 - 6157t)^2 + (66{,}667 - 6157t)^2 + (33{,}333 - 4919t)^2$. This is converted into dimensionless form and plotted in Fig. 2. It may be seen that the initial range becomes 100,000/200,000 = 0.5, and the magnitude of the initial relative velocity is $V^* = 10{,}000/8000 = 1.25$, and $t^* = t/25$. It is seen that interception is possible for $0.39 \leqq t_2^* \leqq 0.49$, and a period of thrust corresponding to $0.3 \leqq t_1^* \leqq 0.49$. For $t_1^* = 0.3$, t_2^* equals 0.41, and t_2 equals 10.25 sec. The corresponding direction of thrust is that of the vector

$$[66{,}667 - 6157(10.25)]\mathbf{i} + [66{,}667 - 6157(10.25)]\mathbf{j} + [33{,}333 - 1919(10.25)]\mathbf{k}$$

The other desired values may be obtained easily.

Solution of Other Problems

The general class of problems that can be solved by using graphs such as Fig. 2 is stated. A displacement vector is represented as the sum of two vectors, one resulting from thrust and one independent of the variations of the thrust. The displacement resulting from thrust has the property that its form is invariant under rotation of coordinates. Some sort of optimum is sought among the terminal values of time, fuel consumption and displacement, as in the following examples.

Attaining a Fixed Point

Suppose we wish to attain a certain point in space, x_2, y_2, z_2, in a constant gravitational field, starting from rest. The relative displacement is given by

$$\varrho = x_2\mathbf{i} + y_2\mathbf{j} + (z_2 + \tfrac{1}{2}gt^2)\mathbf{k} - \int_0^t (t - \tau)\mathbf{a}(\tau)d\tau$$

if the z-axis is positive upward. In this case, set

$$R = \sqrt{x_2^2 + y_2^2 + [z_2 + (1/2)gt^2]^2}$$

Convert this to dimensionless form and draw R^* on the same coordinate set with $r^*(t^*, t_1^*)$. The values associated with minimum fuel consumption are again obtained from the common tangent to the curves for $r^*(t^*)$ and $R^*(t^*)$ at the points t_1^* and t_2^*, respectively. The earliest and latest times when the rocket can reach the point correspond to the two times where the curve for R^* crosses the curve for r_m^*.

If the time of arrival t_2 is specified, then there is a single point $R^*(t_2^*)$. The corresponding line tangent to the curve for $r^*(t^*)$ defines the minimum value for fuel consumption to attain the specified point at the specified time. If the initial velocity and displacement are not zero, they are included in R.

The direction for the thrust is in the direction of

$$x_2\mathbf{i} + y_2\mathbf{j} + [z_2 + (1/2)gt_2^2]\mathbf{k}$$

Maximum Altitude at Specified Range With Fixed Fuel Consumption

Consider the plane problem of attaining a maximum value for y, in the direction of the vertical, with a prescribed final value of x, in a constant gravitational field, starting from rest, with the rocket performance specified for $t < t_1$, thrust constant.

In this case, we may write

$$r^2 = x^2 + [y + (1/2)gt^2]^2$$

where r or r^* is obtained from Fig. 1. Hence, in the equation

$$y^* = \sqrt{r^{*2} - x^{*2}} - g^*t^{*2}/2$$

the right side is a known function of t^*; allowed values of t^* are those for which the radicand is positive. A graph for $y^*(t^*)$ can be constructed and the maximum estimated quickly. Analytic values can be used to improve the estimates, but for most purposes the graphical solution is adequate. Initial conditions which are not zero change only the algebra. The direction of thrust is in the direction of the vector $x_2\mathbf{i} + [y_2 + (1/2)gt_2^2]\mathbf{j}$. If t_2 is prescribed, only the solution of a right triangle is required.

Initial Speed Specified

An interesting variation of the foregoing is one wherein the initial velocity vector has its magnitude specified, but not its direction, as might be the case for a booster rocket whose direction could be controlled. It is found that the initial velocity vector must be parallel to the thrust vector. This

result is similar to that observed in the boost for launching a satellite [(10) p. 13]. In the foregoing, the result follows from the triangle inequality.

Lower Bound to Fuel Consumption

The lower bound to fuel consumption is given by the limit as $\dot{m}$ becomes infinite with m_1 remaining finite. If for example the curve for R^* is given as in Fig. 3 and t_2 is selected, the lower bound to fuel consumption is given, for interception at that time, as follows. Let P_2 denote the point which corresponds to the desired interception time. Draw OP_2 and the line parallel to OP_2 but tangent to the curve for $r^*(t^*)$. The point of tangency t_{10}^* yields the lower bound to fuel consumption for that interception time. The lower bound, for t_2 free, is clearly obtained if the line OP_2 is tangent to the curve for R^* at P_2.

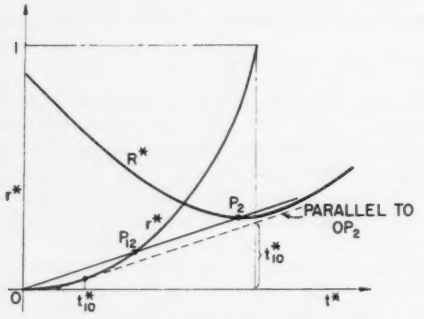

Fig. 3 Solution for very large thrust

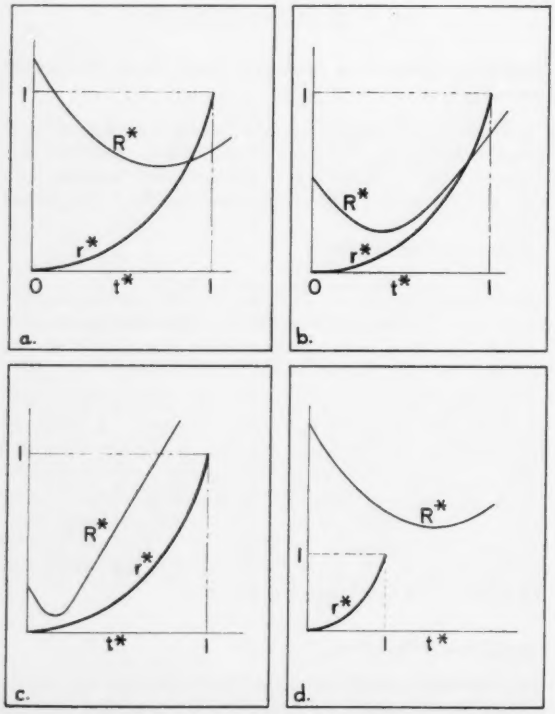

Figs. 4 Relation between curves for various values of thrust: a and b, approximately correct; c, too small; d, unnecessarily large

Estimates in Design

The procedure applies directly to some related problems in design. Fig. 1 can be used to make quick estimates of the thrust and fuel requirements of a rocket which is to perform some task. Suppose one wishes to design a rocket to intercept, with the target conditions given. Then, one may make a guess $\dot{m}_g$ for $\dot{m}$. Then plot the graph of R^* vs. t^*. If the value $\dot{m}_g$ is about right, the curves will look like those in Figs. 4a or 4b. If $\dot{m}_g$ is too small, they will look like those in Fig. 4c, and if it is too large, they will look like those in Fig. 4d.

Since both t^* and R^* have a factor $\dot{m}$, when t and R are given, the effect of increasing $\dot{m}$ by a factor σ is to move each point of the curve σ times as far from the origin; all of the curves for R^* are similar as $\dot{m}$ is varied. The curve for r^* vs. t^* does not change with $\dot{m}$, as may be seen from the formulas. The curves can be sketched in corresponding to different values of $\dot{m}$, and estimates made as to the required values of $\dot{m}$, and m_1. Details and applications to particular problems are given in (5 and 9).

Thrust Constant to Interception

If it is desired to intercept at the time corresponding to P_2 by a constant thrust applied during the entire time interval $(0, t_2)$, the desired burning rate $\dot{\mu}$ may be obtained as follows. In Fig. 3 draw the line OP_2 and observe the point P_{12} where it cuts the curve for $r^*(t^*)$. The desired value s given by

$$\dot{\mu} = \dot{m}\, \overline{OP}_{12}/\overline{OP}_2$$

$\dot{m}$ the value associated with the original graph. This defines the minimum thrust which will effect the desired displacement in the required time.

Remarks

This method was developed in the study of the problem of intercepting a ballistic missile, Project Wizard, beginning 14 years ago, but the method does not seem to be generally known. The associated theory was given in several internal memoranda, principally (2), in an external memorandum (4), and a paper (8). The method of solution was given in various internal memoranda, principally (3), in an external memorandum (5), and not otherwise published except for a brief mention in the paper (8). A complete publication record of the external memoranda is available through ASTIA, in accordance with its policies.

Some of the results have appeared since in fragmentary forms. In a recent report, Miele and Cappelari say that their report is the first to investigate the problem of programming both magnitude and direction of thrust [(7) p. 39]. They study the problems of attaining maximum altitude and maximum range, and conclude by formal methods in the calculus of variations "no variable-thrust sub-arc is present in the extremal of best range." These problems are included in the class which were solved by the procedures given here 9 years earlier (5). A precise statement for the thrust is given in (4), theorem V, for all such problems. Miele and Cappelari devote a chapter [(7) chap. 5] to obtaining conditions on the Lagrange multipliers for this problem, without solving it, though they recommend the use of dynamic programming techniques. These problems are among the simpler problems, since the first involves only a single integral and the second is isoperimetric in type, neither being properly a problem of Bolza. If the Lagrange multipliers are desired, they can be obtained from the equations for the direction of the thrust.

Leitmann (11) in a recent paper, has investigated the general optimization problem for the two-dimensional flight of a rocket above the sensible atmosphere in a constant gravi-

tational field. He has obtained some conditions for a general optimum relation among the terminal values of position, velocity, fuel consumption and time, without any method of solution. All of the problems which he considered which do not involve the terminal velocity can be solved completely by the techniques of this paper. It should be pointed out that other problems which he considered, such as orbital transfer, for example, cannot be handled by the simple techniques of this paper, since neither of the two conditions for the acceleration of the thrust are generally satisfied on an optimum trajectory: The thrust or acceleration is not generally fixed in direction, and the thrust or acceleration is not generally confined to an initial period when it is a maximum but may also have a terminal period when it is also required to be a maximum. Incidentally, it can be shown by direct methods that the case where the acceleration is a maximum in an interior interval occurs only in an indeterminate case when the interval of thrust is not unique.

The solution of other problems can be obtained in a related way. If the approximation used by Foy (6) is used for the differential equations of motion, and if the time of flight is short (less than 21 min in the vicinity of Earth's surface), then it can be shown by direct methods that for an optimum relation among terminal fuel consumption, displacement and time, with initial conditions given, it is required that thrust be fixed in direction, and that thrust must be as high as possible early, then zero. The solution of problems of this type can be reduced to a graphical procedure similar to the one given here. However there is a constant in the differential equations which introduces a new parameter, and it is no longer feasible to consider variations of $\dot{m}$ in a simple fashion.

For the case of the uniform gravitational field, a graph can be drawn in dimensionless form for any class of burning functions where the thrust or the burning rate is similar; two rockets are said to have a similar burning rate if the values of the burned fuel ratios m and μ for the two are connected by a relation of the form

$$\mu(t) = m(kt)$$

during the period of thrust. This is elaborated in (4), section IX.

It is essential for the solution given here that the equation for the motion owing to thrust has a form which is invariant under rotation, and the velocity vector does not enter in the final conditions.

If the final mass M_1, rather than the initial mass M_0 is specified, then a similar graphical solution can be made. In this case two curves must be drawn corresponding to the curve for $r^*(t^*)$. If M_0 is taken as the parameter, the two curves correspond to $r_1 = r[t_1(M_0)]$ and to the envelope $r_e(t)$ of the curves for $r(t, M_0)$. These two curves coincide in the case where M_0 is given and M_1 is the parameter. The solutions are determined by straight lines which are tangent to the curve for $r_e(t)$ at time t_e, and their intersections with the curves for r_1 at time t_1. The relation $t_1 < t_e < t_2$ must hold. The curves may be made dimensionless by introducing the parameters c and $\dot{M}/M_1$ properly. Problems of this class are generally harder to solve than those in which the initial mass is given; they are quite tedious when performed on a desk calculator.

Appendix

This appendix has been added at the request of one reviewer to clarify some underlying theory, whose sources may not be available. The important results are stated as a theorem and corollaries.

Suppose that a problem of the following form is given. A curve is sought, and the endpoints of the curve are required to satisfy several equations of the form

$$m_0 = 0$$

$$\psi_i(x_0, y_0, z_0, \dot{x}_0, \dot{y}_0, \dot{z}_0, t_0, x_2, y_2, z_2, t_2, m_2) = 0$$

$$i = 1, 2, \ldots n \leqq 11 \qquad \text{[A-1]}$$

The quantities involved are as defined earlier. Subscript zero denotes the initial or beginning values, and subscript 2 denotes end or terminal values. A function of the same arguments is to be a maximum

$$f = \text{maximum} \qquad \text{[A-2]}$$

It is assumed that the functions of Equations [A-1 and A-2] are all independent and have continuous derivatives in the region of interest. The curve which connects these two endpoints is to satisfy differential equations

$$\ddot{x} = a \cos \theta_1 + g_x$$
$$\ddot{y} = a \cos \theta_2 + g_y$$
$$\ddot{z} = a \cos \theta_3 + g_z \qquad \text{[A-3]}$$

where

$$a = c\,\dot{m}/(1 - m) \geq 0 \qquad \text{[A-4]}$$

is bounded above by a nondecreasing function which can be expressed as $A_{\max}(t - t_0)$, and

$$\sum \cos^2 \theta_i = 1$$

Theorem

It is necessary for any extremum that

1 θ is always a constant.

2 $a = \begin{cases} A_{\max}, & t_0 < t < t_1 \\ 0, & t_1 < t < t_2 \end{cases}$

Proof

The essential feature in the proof, given earlier in (2, 4 and 8) in particular cases, is to show that if the curve does not satisfy these conditions, then a better one exists.

First it should be observed that [(4) p. 17]

$$\int_{t_0}^{t_2} a\,dt = -c \ln (1 - m_2) \qquad \text{[A-5]}$$

so that problems involving fuel consumption may be rephrased as problems involving the integral, since $-\ln(1 - m) = m + m^2/2 + \ldots$ is a monotonic function of m.

Suppose now that a solution has been obtained for the problem posed. Let the values associated with this solution be denoted by capital letters. If the functions ψ_i, f have continuous derivatives in some neighborhood of the point $(X_0, \ldots M_2)$, they are independent if the Jacobian matrix $\partial(\psi_i, f)/\partial(x_0, \ldots m_2)$ has rank $n + 1$ at the point. Assume this to be the case.

Every solution to [A-3] may be expressed in the form

$$x_2 = x_0 + \dot{x}_0(t_2 - t_0) + G_x(t_0, t_2) + \int_{t_0}^{t_2} (t_2 - t) a \cos \theta_1\,dt$$
$$y_2 = \ldots, \quad z_2 = \ldots \qquad \text{[A-6]}$$

which may be rewritten as

$$\mathbf{r}_2 = \mathbf{r}_0 + \dot{\mathbf{r}}_0(t_2 - t_0) + \mathbf{G}(t_0, t_2) + \int_{t_0}^{t_2} (t_2 - t)\mathbf{a}\,dt$$

which is of the form

$$\boldsymbol{\rho} = \mathbf{r}_2 - \mathbf{r}_0 - (t_2 - t_0)\dot{\mathbf{r}}_0 - \mathbf{G} = \mathbf{P}$$

this defines $\boldsymbol{\rho}$ as the last integral above and the remaining terms define $\mathbf{P}$ as indicated.

Suppose that on the given curve **A** does not satisfy both principles of the theorem. Compare then $\rho = |\boldsymbol{\varrho}|$ with ρ_m to be constructed as followed. First the value T_1 is defined by the relation

$$\int_{T_0}^{T_1} A_{\max}\, dt = \int_{T_0}^{T_2} A\, dt$$

it follows that $T_0 < T_1 \leqq T_2$. Now let

$$\rho_m = \int_{T_0}^{T_1} (T_2 - t) A_{\max} dt$$

this defines the magnitude of a new vector $\boldsymbol{\varrho}_m$

Lemma: $\rho_m > \rho$

Proof of lemma: Let **e** denote the unit vector parallel to $\boldsymbol{\varrho}$ so that $\boldsymbol{\varrho} = \rho\mathbf{e}$. Let

$$B = \int_{T_0}^{T_1} (A_{\max} - A)\, dt = \int_{T_1}^{T_2} A\, dt$$

Then

$$\rho_m - \rho = \int_{T_0}^{T_1} (T_2 - t) A_{\max} dt - \int_{T_0}^{T_2} (T_2 - t)\mathbf{A}\cdot\mathbf{e} dt$$

$$= \int_{T_0}^{T_1} (T_2 - t)(A_{\max} - A) dt - \int_{T_1}^{T_2} (T_2 - t) A\, dt + \int_{T_0}^{T_2} (T_2 - t) A [1 - \cos(\mathbf{A}, \mathbf{e})]\, dt$$

Now the first integral satisfies the inequality

$$\int_{T_0}^{T_1} (T_2 - t)(A_{\max} - A) dt \geqq \int_{T_0}^{T_1} (T_2 - T_1) \times (A_{\max} - A) dt = B(T_2 - T_1)$$

The second integral satisfies the inequality

$$\int_{T_1}^{T_2} (T_2 - t) A\, dt \leqq B(T_2 - T_1)$$

The difference of these two is positive unless A satisfies condition 2 of the theorem.

The third integral is positive unless $A\ [1 - \cos(\mathbf{A},\mathbf{e})] = 0$, except possibly on a set of measure zero.

This establishes the lemma.

Consider now the function

$$\rho_m(t_1 - t_0, t_2 - t_0) = \int_{t_0}^{t_1} (t_2 - t) A_{\max} dt \qquad t_1 \leqq t_2$$

It is a continuous function of its arguments. Also $\rho_m(0, t_2 - t_0) = 0$ and $\rho_m(T_1 - T_0, T_2 - T_0) > |\mathbf{P}|$. Note also that **P** is a continuous function of the arguments $(x_0, y_0, z_0, \dot{x}_0, \dot{y}_0, \dot{z}_0, t_0, x_2, y_2, z_2, t_2)$. If **P** is determined, ρ_m can be determined by setting $\rho_m = |\mathbf{P}|$ and solving for t_1. The direction of $\boldsymbol{\varrho}_m$ is determined by **P**.

From the continuity, it follows that there is an admissible curve from every point in some neighborhood of $(X_0, Y_0, Z_0, \dot{X}_0, \dot{Y}_0, \dot{Z}_0, T_0)$ to every point in some neighborhood of (X_2, Y_2, Z_2, T_2), and on none of these is $M_2 < m_2$.

Now m_2 plays a special role. It may not be possible to increase it, or even to hold it fixed, whenever $t_2 - t_0$ is decreased if $a = A_{\max}$ for all t. The cases where it is to be increased seem to have no practical significance.

From the fact that every point in the neighborhood of the end points can be attained, with the exception of the situation noted, it is refuted that f is a maximum. The theorem is established.

No complete set of sufficient conditions is likely for all sets of functions ψ_i; the problem is too complex. For simple problems, such as maximum range and various interception problems, the special nature of the functions ψ_i allows a complete set of sufficiency conditions which can be checked by the graphic solution very quickly.

Corollary 1

If the function $\rho_m(t_1 - t_0, t_2 - t_0)$ can be obtained in finite form, the determination of optimum trajectories is reduced to that of solving finite equations for the corresponding optima.

The equations

$$x_2 = x_0 + \dot{x}_0(t_2 - t_0) + G_x(t_0, t_2) + \rho\cos\theta_1$$

$$y_2 = \ldots, \quad z_2 = \ldots$$

$$\rho = \rho_m(t_1 - t_0, t_2 - t_0)$$

$$\sum \cos^2\theta_i = 1$$

..... [A-7]

are adjoined to Equations [A-1], and an ordinary maximum for f sought.

If the maximum thrust is constant, then ρ_m is given by Equation [4], modified so that the arguments are $t_1 - t_0$ and $t_2 - t_0$.

Corollary 2

The foregoing results are not changed materially if the roles of m_0 and m_2 are reversed.

In this case the bound on a has a different form; it is a function of $t_1 - t$ rather than $t - t_0$.

Corollary 3

If the velocity is involved at the terminal point, but not at the beginning, then instead of an initial period of maximum thrust, there is a terminal period.

The essential part of establishing this is to replace t by $-t$.

Corollary 4

The impulse solution to the problem is reduced to the solution of finite equations.

For the case where a is not bounded, the limiting value is $(t_2 - t_0)V$ for ρ_m, where V is the magnitude of the initial jump in the velocity, and the corresponding fuel consumption is given by $m_2 = 1 - \exp(-V/c)$.

Comments

1 The principle that thrust be a maximum initially for an optimum relation among terminal position, fuel consumption and time is a very general one. It arises from the transversal conditions. A vector which is defined by the adjoint system of differential equations must vanish at the terminal value of t if the velocity does not enter at that end. The proof is based on the fact that the magnitude of this vector decreases with time.

2 If the terminal velocity enters, no such simple results exist, generally. In the corresponding cases, there is an initial and a terminal period of maximum thrust, and thrust varies in direction for the optima.

3 These arguments can be extended readily provided the form of $\boldsymbol{\varrho}$, the displacement owing to thrust, is invariant under rotation of coordinates.

4 Computations on a limited number of problems suggest that it is essential to use the transversal conditions in determining an optimum trajectory in some cases, specifically in the case of interception with minimum fuel consumption. These conditions are obtained by differentiating Equations [A-1, A-2 and A-7]. In that problem, one form of the transversal conditions is that the direction of **a** be perpendicular to the vector of relative velocity for $t_1 < t$ [see (4) p. 54]. On the other hand, in the problem of interception in minimum time, there seems to be no need to use them.

Acknowledgment

Most of this work was done under AAF contract W33-038 ac-14222. C. M. Fowler, W. J. Nemerever and W. A. Wilson participated in the development, and much of the material taught in a course in guidance at the U. S. Naval Postgraduate School the past 4 years.

References

1 Bolza, O., "Vorlesungen über Variationsrechnung," Teubner, Leipzig, 1909.

2 Faulkner, F. D., "The Problem of Minimum Fuel Consumption in Intercepting a Target in Free Flight above the Earth's Atmosphere," University of Michigan Aeronautical Research Center, IMF-7, 9 Aug. 1946.

3 Faulkner, F. D., Fowler, C. M. and Wilson, W. A., "Graphic Method or Solving the Homing Problem When Thrust Is a Specified Function of Mass During Burning," University of Michigan Aeronautical Research Center, IMF-15, 16 Dec. 1946.

4 Faulkner, F. D., "Homing in a Vacuum with Minimum Fuel Consumption," University of Michigan Aeronautical Research Center, UMM-18, 1 Feb. 1949; *also* ASTIA no. ATI 50732. (Available from the author.)

5 Faulkner, F. D., "Solution to the Problem of Homing in a Vacuum with a Point Mass," University of Michigan Aeronautical Research Center, UMM-19, 1 Feb. 1949. (Available from the author.)

6 Foy, W. H., Jr., "Steering of an Ascent Rocket for Maximum Cutoff Velocity," Paper no. 14, Proc. Fourth Annual Meeting, Amer. Astron. Soc., Jan. 29–31, 1958.

7 Miele, A. and Cappelari, J. O., "Topics in Dynamic Programming for Rockets," Purdue Research Foundation, Rep. no. A58-5, July 1958.

8 Faulkner, F. D., "Some Results from Direct Methods Applied to Optimum Rocket Trajectories," in "Proc. Tenth Int. Astron. Congress, Amsterdam 1958," Springer Verlag, Vienna, 1959, pp. 694–701.

9 Hahn, D. W. and Rounds, J. M., "A Method for Determining Thrust/Weight Ratio and Propellant Loading for Maneuvering the Terminal Stage of an ICBM," Boeing Airplane Co., Seattle, Ref. no. 5-7841-385, March 20, 1959.

10 Okhotsimskii, D. E. and Eneev, T. M., "Certain Variational Problems Associated with the Launching of an Artificial Earth Satellite," in "The Russian Literature of Satellites, Part 1," International Physical Index, Inc., N. Y., 1958.

11 Leitmann, G., "On a Class of Variational Problems in Rocket Flight," *J. Aero/Space Sci.*, vol. 26, 1959, pp. 586–591

Experimental Method of Measuring Intensity of Turbulence in a Rocket Chamber

MARTIN HERSCH[1]

Lewis Research Center,
NASA
Cleveland, Ohio

Experimental values of intensity of turbulence in a two-dimensional hydrogen-liquid oxygen rocket engine were determined from the spread of a gas jet diffusing in the combustion chamber. The diffusion was determined photographically, using sodium *d*-line radiation as a flow tracer. A simplified model of turbulent diffusion was used to estimate the intensity of turbulence from the gas jet spreading. The results indicated that the intensity of turbulence is relatively high near the injector but diminishes downstream. The variation of lateral fluctuating velocity with downstream distance was in agreement with theoretical predictions for decaying turbulence in a cold flow accelerating stream. Changes of several operating parameters had little, if any, effect upon intensity of turbulence.

GAS-PHASE mixing has generally been considered to influence rocket engine performance (17).[2] The rate of gas-phase mixing may be shown to be a function of the level or intensity of turbulence by simplified turbulent flow theory. Turbulence has been observed in rocket combustors (2, 4), but quantitative values of the intensity of turbulence do not exist for rocket engine conditions. The absence of such values has been an impeding factor in the progress of theoretical considerations of mixing in rocket engine combustion (5). The research reported herein was undertaken to develop a method for measuring intensity of turbulence, and to fulfill, in part, the indicated need for quantitative experimental data.

Intensity of turbulence and gas-phase mixing may be measured by hot-wire methods (13,18,19), gas sampling techniques (21) and optical methods (8,11,13). Even for cold flow conditions these methods are difficult, and those which require probes can disturb the flow. A new application of a method previously described (6,18) was used in this study to determine experimentally the intensity of turbulence in a rocket combustor, and some of the results obtained are presented. Since the method was optical, no flow disturbances are introduced. Other optical methods of studying flow in combustion are covered in (1, 12 and 14).

The experimental method consisted of measuring the spread of a hydrogen jet into a burning mixture of hydrogen and oxygen. The hydrogen jet was "seeded" with finely divided sodium chloride, which enabled the spread and concentration profile of the jet to be measured photographically. Simplified turbulent flow theory was used to estimate the intensity of turbulence from the spread of the hydrogen jet as measured from photographs.

Presented at the ARS 14th Annual Meeting, Nov. 16–20, 1959, Washington, D. C.

[1] Aeronautical Powerplant Research Engineer. Member ARS.

[2] Numbers in parentheses indicate References at end of paper.

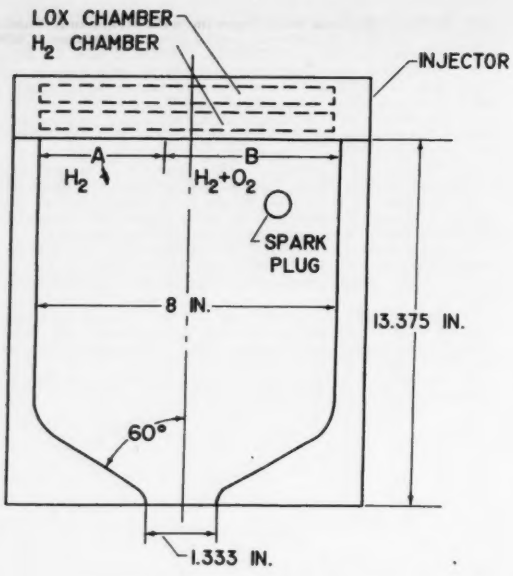

a: Front view

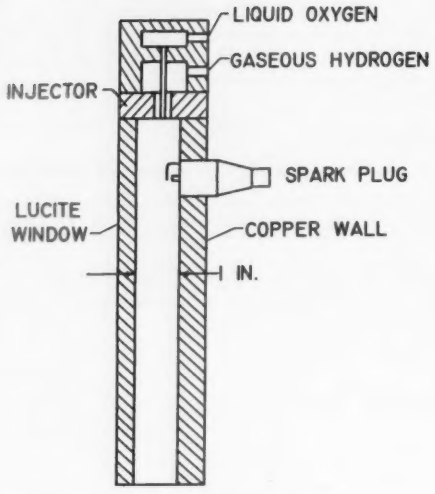

b: Side view

Figs. 1 Two-dimensional engine

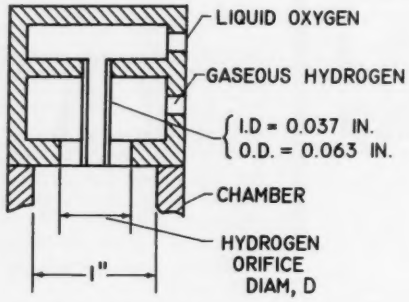

Fig. 2 Injector detail

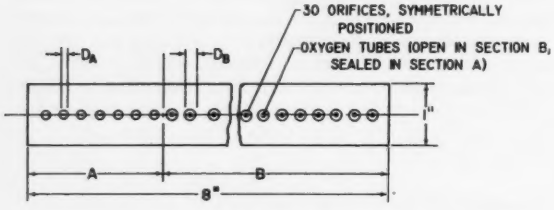

Fig. 3 Injector face plate

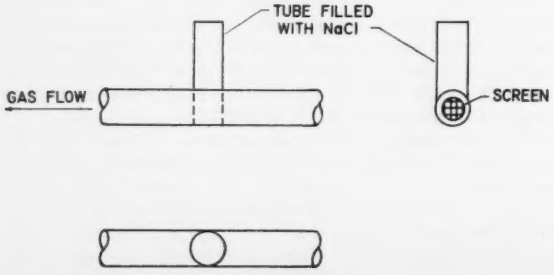

Fig. 4 NaCl seeder

Apparatus and Procedure

Engine Description

The tests were conducted in a nominal 100-lb thrust hydrogen-liquid oxygen combustor having a solid uncooled, one-piece copper chamber and nozzle (Figs. 1). The chamber was 8-in. wide, 1-in. thick and 14-in. long, with a full-length Lucite observation window on one side.

The injector (Figs. 2 and 3) contained two sections, labeled A and B. Gaseous hydrogen, seeded with finely divided NaCl dust (5–10 μ diameter), was injected into section A. The seeding device is shown in Fig. 4. Liquid oxygen and gaseous hydrogen without NaCl were injected into section B. The ability of these particles to follow gas flow is illustrated in Fig. 5. The curves were calculated by using the method of (16), p. 17, assuming the gas viscosity to be 6.48×10^{-4} poise and the salt density 2.16 gm per cm^3. If the turbulent motion is assumed to be sinusoidal with an amplitude of about 1 in. and $\sqrt{\overline{v^2}}$ (360 in. per sec) is assumed to be the maximum velocity, the particles should be small enough to follow a frequency of about 50 cps. From Fig. 5 it may be seen that particles in the range of 5 to 10 μ in diameter will follow this vibration with good fidelity.

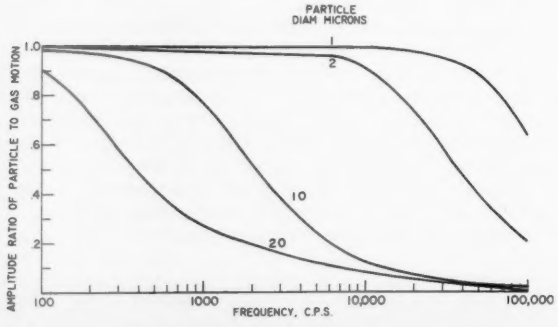

Fig. 5 Fidelity of tracer particles

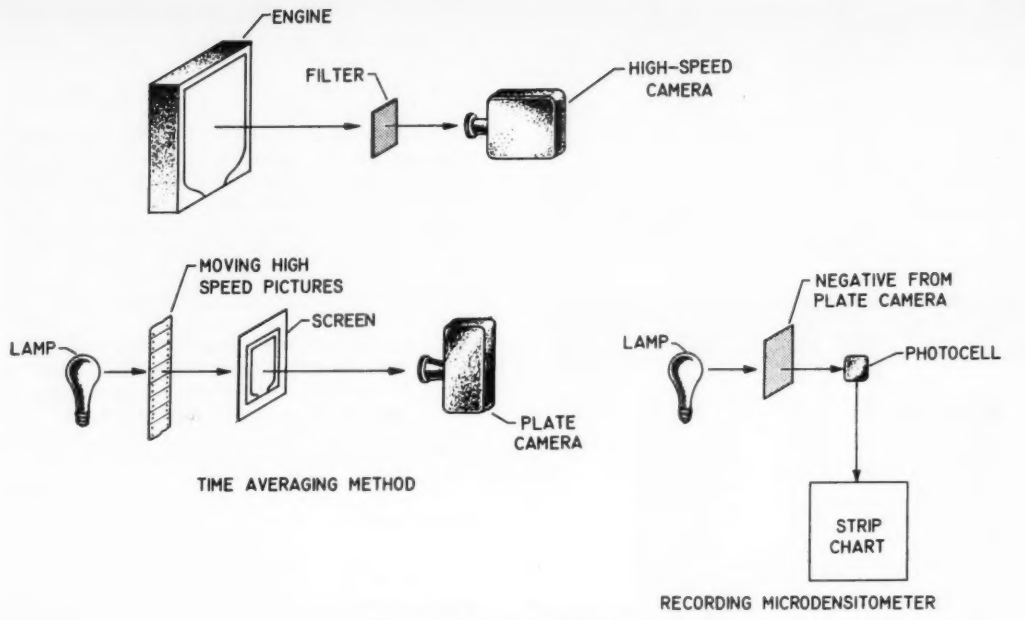

Fig. 6 Photographic procedure

The injector was designed so that the velocity ratio of hydrogen gas in section A to that in section B could be varied. Also the oxidant-fuel ratio of the mixture in section B and the lengths of sections A and B were varied. These variables are listed in Tables 1 and 2. This was accomplished by changing the sizes of the hydrogen orifices with a set of interchangeable face plates illustrated in Fig. 3. The overall oxidant-fuel ratio and total flow rate were held constant at 3.2 and 0.65 lb per sec, respectively. The chamber pressure was approximately 100 psia for all runs.

The injector was of the concentric-tube type, having a single row of uniformly spaced orifices with oxygen tubes in the center. The same tubes were used for all runs, those in section A plugged with removable pins.

Table 1 Injector dimensions

Run	Section A (hydrogen only) length, in.	D_A, in.	Section B (hydrogen + oxygen) length, in.	D_B, in.
31	4	0.1250	4	0.1250
37	3	0.1299	5	0.1285
58	3	0.1204	5	0.1406
60	3	0.1507	5	0.1094
61	4	0.1160	4	0.1405

Table 2 Operating conditions

Run	Local, F	Hydrogen velocity ratio (sect. A/sect. B)
31	6.46	1.0
37	5.66	1.0
58	4.71	0.402
60	9.30	2.47
61	5.50	0.605

The hydrogen gas, which originated from a single upstream source, was divided into two branches, the one to section A containing a source of NaCl dust. A check valve was used to prevent any dust from entering section B.

The combustion was recorded with a high speed Fastax camera run at about 3900 frames per sec. The camera was fitted with a narrow bandwidth (20 Å) interference-type filter, which blocked off all background light from the hydrogen-oxygen combustion and passed only the sodium-*d* frequency.

Data Reduction and Results

The light patterns on the high speed pictures were time averaged by running the film through a film viewer while taking a time exposure of the viewer screen with a 5 × 7-in. plate camera as shown schematically in Fig. 6. A Leeds and Northrup recording microdensitometer was used to measure the light transmission of the time averaged negative along lines parallel to the injector face at 2, 3, 4, 5 and 7 in. downstream.

Examples of typical high speed frames, a time averaged negative and a densitometer trace are shown in Fig. 7. The interpretation of the densitometer trace is explained in the following section and is shown schematically in Fig. 8. The lateral distance r from the axis of the light streak to points of known film densities was scaled from the densitometer chart and is shown as a function of chamber length in Fig. 9. In order to compensate for the base density, or "fog level" of the high speed film, the distance labeled "base density" on Figs. 7 and 8 was subtracted from the transmission curve.

The experimental jet spreading (Fig. 9) indicates that the jet wake is not triangular. Therefore, the tangent of the angle of spread for a given concentration level, which is used to determine the intensity of turbulence, varies with downstream distance. Because of this variation, the spread was measured in two ways: r/x and dr/dx. Values of r/x were calculated directly from the data points, whereas dr/dx was measured graphically from curves drawn through the points.

The intensity of turbulence in percentage units was calculated using the following equation (derived in the next section)

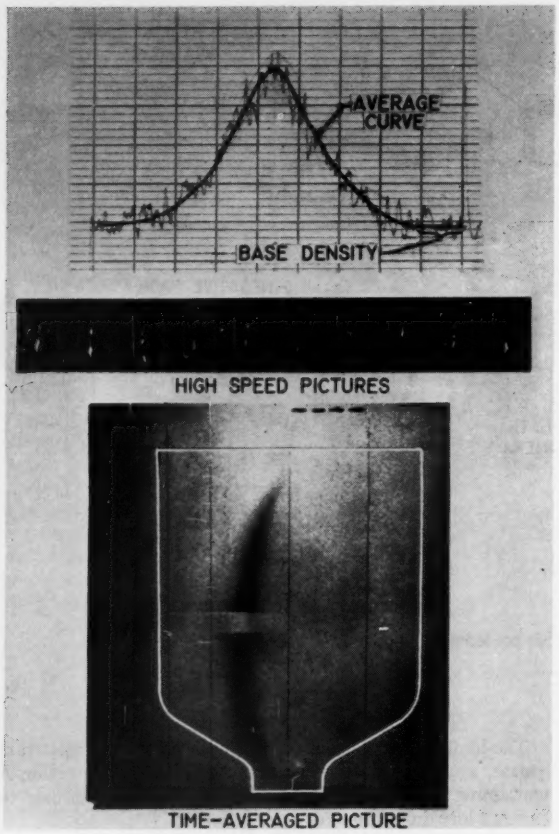

Fig. 7 Typical samples of high speed film, time averaged exposure and densitometer chart

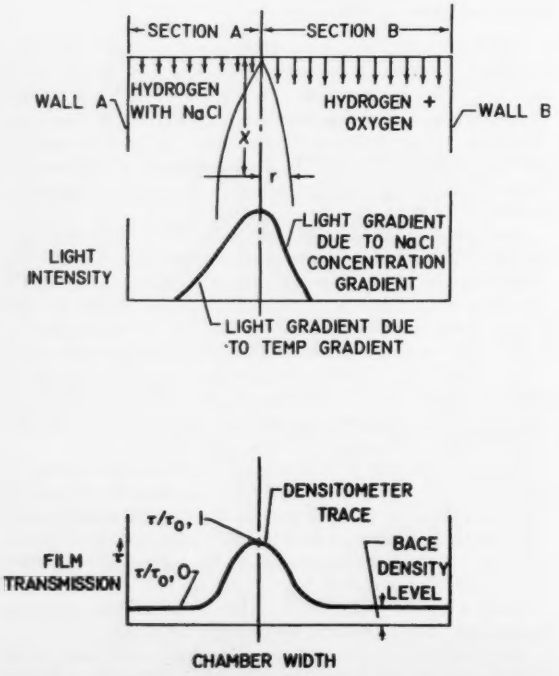

Fig. 8 Relationship of light intensity to densitometer curve

$$T = 70.7(r/x)/\sqrt{-\ln C/C_0}$$

or

$$T = 70.7(dr/dx)/\sqrt{-\ln C/C_0}$$

The relationship of the ratio C/C_0 to the photographic density is explained in the Appendix. The experimental intensity of turbulence thus calculated is shown in Figs. 10 and 11. The changes in oxidant-fuel ratio of propellants in section B, lengths of sections A and B, and hydrogen injection velocities seemed to have little effect on the intensity of turbulence. However, it appeared that an increase of the velocity ratio of the two gas streams did tend to increase the level of turbulence intensity.

The experimental turbulent velocity profiles (Fig. 12) were obtained by multiplying the assumed mean stream gas velocity profile by the intensity of turbulence profiles. It was assumed that the gas velocity profile was linear, with terminal points of 840 and 6000 in. per sec at the injector and nozzle entrance, respectively.

Discussion

The streak of light observed in the engine resulted from the mixing of a cold gas stream containing tracer particles with a hot gas containing no tracer. The decrease of light in the direction normal to the streak toward wall B therefore was a result of a decrease in the tracer concentration, whereas the decrease of light in the opposite direction was primarily a result of a temperature decrease. If the brightest portion of the light streak is assumed to be the edge of a plane indicating the demarcation of temperature and concentration gradients, the light intensity profiles from wall A to wall B may then be used to determine temperature and concentration gradients, as shown in Fig. 8. The intersection of this plane with the injector face may therefore be considered to be an imaginary line source of diffusion.

The concentration equation for a substance diffusing from a line source is [(20), p. 68, Eq. 161]

$$C = \frac{W\sqrt{v^2}}{\sqrt{4\pi\omega}\,U^2L}\exp\left(-\frac{r^2}{4\omega}\right) \qquad [1]$$

When written in the form of a concentration profile in a plane perpendicular to the mean stream flow at any given down-

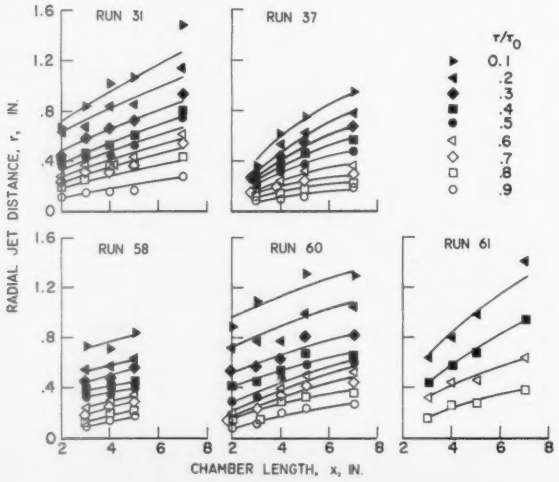

Fig. 9 Experimental jet spreading

stream distance, the equation becomes

$$C/C_0 = \exp(-r^2/4\omega) \quad [2]$$

If the Lagrangian correlation coefficient [(20), p. 60] is approximately 1.0 (which holds for the short residence times of gases in a rocket combustor), and if the turbulent field is assumed to be homogeneous ($\sqrt{\overline{v_{z,0}^2}} = \sqrt{\overline{v_{z,t}^2}}$), the spreading coefficient ω becomes (5),

$$\omega = \frac{x^2T^2}{2 \times 10^4} + \frac{xd}{U} \quad [3]$$

In Equation [3] the first term is the contribution due to turbulent diffusion and the second is that due to molecular diffusion. Using this simplified expression for the spreading coefficient, the equation for the concentration profile at some downstream position becomes

$$\frac{C}{C_0} = \exp\left[\frac{r^2}{4(x^2T^2/2 \times 10^4) + xd/U}\right] \quad [4]$$

By solving Equation [4] for T, it is found that

$$T = 100\sqrt{\frac{2}{x^2}\left[\frac{r^2}{-4\ln(C/C_0)} - \frac{xd}{U}\right]} \quad [5]$$

For probable values of r, C/C_0, x and U, the value of the term xd/U is negligible in comparison with the value of $r^2/-4 \times \ln(C/C_0)$; the coefficient of molecular diffusion is calculated using the method of (9) for a temperature and pressure approximating that of a rocket combustor. Therefore, the molecular diffusion term may be neglected, and the intensity of turbulence calculated from the equation

$$T = \frac{70.7(r/x)}{\sqrt{-\ln(C/C_0)}} \quad [6]$$

As seen in Fig. 9, however, for a given value of C/C_0, r is nonlinear with respect to x. Therefore, the intensity of turbulence was also calculated using the equation

$$T = \frac{70.7(dr/dx)}{\sqrt{-\ln(C/C_0)}} \quad [7]$$

The value of dr/dx was determined graphically at various downstream stations using the curves shown in Fig. 9. Values of intensity of turbulence calculated directly from measured values of r/x using Equation [6] are shown in Fig. 10, and those calculated from Equation [7] are shown in Fig. 11. The curves on Figs. 10 and 11 represent the mean values using all points.

The intensity of turbulence obtained by the use of Equation [6] could be considered a value averaged from the injector to the downstream station of measurement, whereas that obtained by the use of Equation [7] may be considered a local value, with the diffusion originating at or near the downstream station. A comparison of Figs. 10 and 11 shows that the results are not the same, but are, however, of the same order of magnitude. Although the second method may be preferable from a theoretical viewpoint, its practicality may be somewhat questionable because of the extreme sensitivity of the results to the slopes of the curves drawn through the data points and also because of the exact manner in which these curves are constructed.

If there is no variation of turbulence in the r direction, there should be no variation of the measured intensity of turbulence with film transmission τ/τ_0. However, as shown in Figs. 10 and 11 there is, for some runs, a trend of the measured intensity of turbulence with film transmission. Moreover, the trend for some runs is different in Fig. 11 than in Fig. 10. The trend of measured intensity of turbulence with film transmission may be a result of the assumption that the curve of film response to light exposure is linear. However, for extremes of light intensity the curve levels off, approaching the base density of the film for zero light intensity and almost complete opaqueness for very bright light. This effect was partly compensated for by subtracting the base density from all measurements of the time averaged transmission. However, the reversal of some data points in Figs. 10 and 11 cannot be explained.

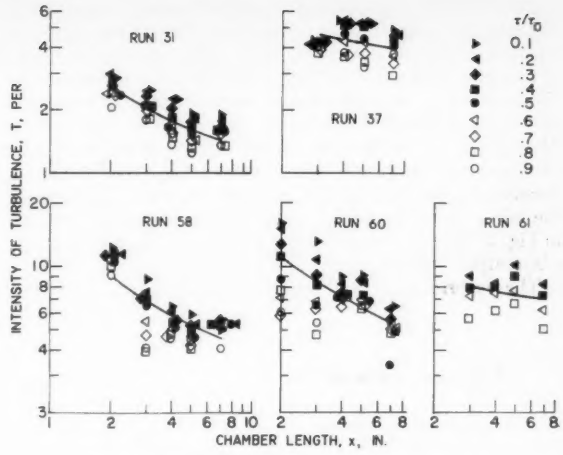

Fig. 10 Intensity of turbulence based on r/x

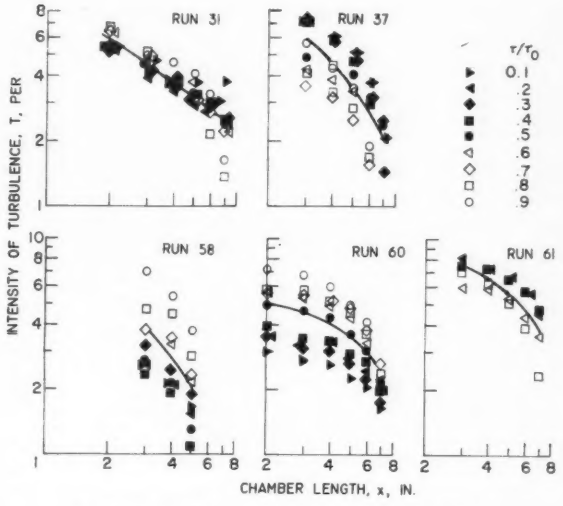

Fig. 11 Intensity of turbulence based on dr/dx

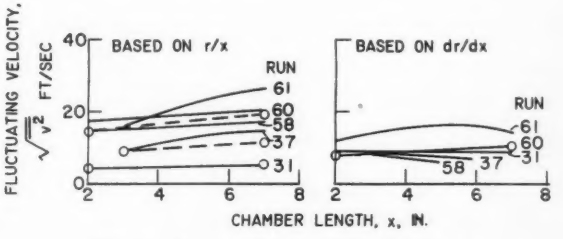

Fig. 12 Experimental fluctuating velocity

The theoretical variation of lateral fluctuating velocity with downstream distance in a contracting stream owing to acceleration effects is discussed in (3), p. 68, and that owing to acceleration with decay in (15). Flow in a rocket combustor also accelerates, but here the acceleration results from heat and mass addition rather than from stream contraction. Theoretical curves from these two references together with the experimental results are shown in Fig. 13, where the downstream fluctuating velocities are expressed as ratios of the initial upstream values. The experimental values shown in Fig. 13 were calculated from values of T obtained from the r/x analysis and the assumed mean stream velocity profile.

The experimental results appeared to follow the trend of the curve for an accelerating stream with decaying turbulence. For purposes of comparison, the experimental data nearest the injector face were normalized to this curve. The similarity of the trend of the experimental results to the slope of this curve seems to indicate that the decay of turbulence in a rocket combustor is approximately that which is predicted for turbulence in an accelerating flow of cold gases. The results of run 31, which had relatively little spread, are shown separately in the top portion of Fig. 13; the results of all runs are shown in the bottom portion of Fig. 13. A similar analysis using the values of T obtained from dr/dx was attempted, but the results showed a comparatively wide spread, which may have been a result of the extreme sensitivity of the results to the slope of the curves drawn through the original data points.

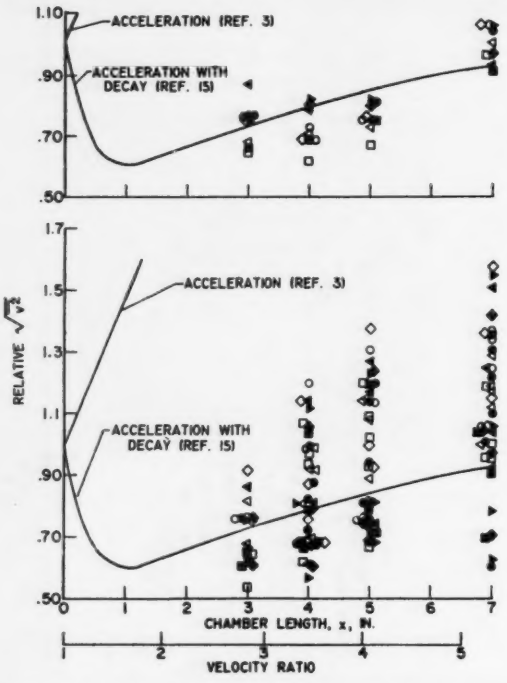

Fig. 13 Comparison of theoretical and experimental lateral fluctuation velocities

Among possible sources of error involved in this technique are the application of a line source model to a finite jet source, overlapping of the temperature and concentration effects on light intensity, wall effects, and variations in the photographic process. The use of a large, cool, hydrogen jet may have produced flow conditions that are atypical of normal rocket engine combustion conditions.

Future work using this method might be done with a continuous point source rather than a large cold jet, in order to approach more closely both the turbulent theory and typical rocket combustor conditions. That method would also eliminate large temperature and concentration gradients in the lateral direction. If an instantaneous point source could be devised, information about the longitudinal fluctuating velocity may be determined by studying the distortions of the puffs of material released from the instantaneous point source.

Summary of Results

Experimental measurements of intensity of turbulence in a two-dimensional rocket engine, using a photographic technique gave the following results:

1 The intensity of turbulence decreased with chamber length and averaged about 10 per cent near the injector and about 5 per cent near the nozzle.

2 The variation of lateral fluctuating turbulent velocity with downstream distance agreed with theoretical results for decaying turbulence in an accelerating cold gas stream.

3 Changes of various design parameters appeared to have little, if any, influence on the intensity of turbulence.

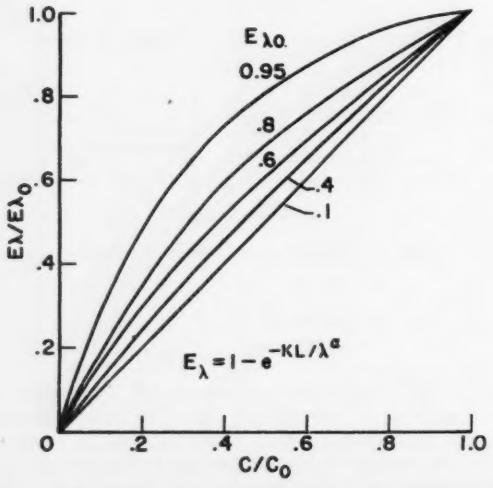

Fig. 14 Emissivity ratios vs. concentration ratios for various axial emissivities

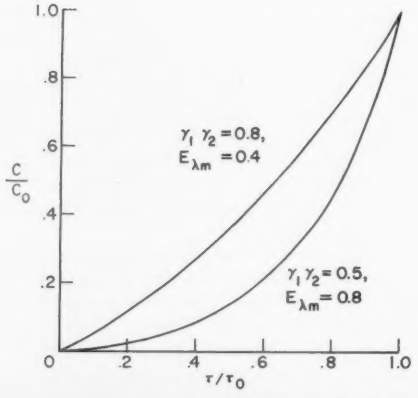

Fig. 15 Concentration ratios vs. light intensity from film ratios for various film gammas and engine light emissivities

Appendix: Relation of Tracer Concentration to Film Density

Relation of Light Intensity to NaCl Concentration

In (10) it is shown that monochromatic emissivity of luminous particles in a hot gas may be expressed by the equation

$$E_\lambda = 1 - e^{-KL/a} \qquad [A\text{-}1]$$

where

E_λ = monochromatic emissivity, dimensionless
KL = particle concentration factor, including concentration, path length and absorption coefficient
α = constant, assumed equal to 1.2
λ = monochromatic wave length, Å

For a given temperature, path length and light frequency, the emissivity, and therefore the light intensity, will depend only upon the concentration of the luminous particles. Therefore, concentration gradients of luminous particles in a gas of uniform temperature may be determined from light intensity gradients. The decrease of light, however, from an initial concentration will depend somewhat upon the maximum, or original, emissivity. The relation of changes in light intensity (expressed as a fraction of an initial intensity) to concentration gradients (also expressed as a fraction) is shown in Fig. 14, with initial emissivities as a parameter. It is shown in (7), however, that the emissivity for sodium particles in a rocket engine is likely to range from about 0.4 to 0.6.

Relation of Light Transmission of Film to Intensity of Exposure

Using the following approximate relation, known as the Hurter and Driffield curve

$$I_l/I_t = \log_{10} aI^\gamma$$

the relation between the intensity of exposure and light transmission of a photographic negative becomes

$$\frac{\tau}{\tau_0} = \left(\frac{I}{I_0}\right)^{\gamma_1\gamma_2}$$

where γ_1 in this case would refer to the high speed film and γ_2 to the time averaged negative. This equation was used to relate light intensity gradients in the combustion to light transmission gradients on the time averaged exposure.

Fig. 15 shows how the light transmission of the time averaged plate varies with tracer concentration for the largest expected variations in film development and emissivities. This figure was used to convert the film transmission profiles obtained from the recording microdensitometer into concentration profiles.

Nomenclature

a = constant in film exposure equation, (meter-candle-sec)$^{-\gamma}$
C = concentration of diffusing gas, lb/in.^{3}
d = molecular diffusion coefficient, in.^{2}/sec
I = light intensity, meter-candle-sec
L = scale of turbulence, in.
r = lateral distance from plane where concentration is C_0 to point where concentration has decreased to C, in.
T = turbulence intensity, $100\sqrt{\bar{v^2}}/U$, per cent
U = mean stream gas velocity in x direction, in./sec
$\sqrt{\bar{v^2}}$ = rms of lateral turbulent velocity fluctuation in the r direction, in./sec
W = source strength, lb/sec
x = downstream distance (chamber length), in.
γ = photographic film and development factor, dimensionless
τ = light transmission of film, dimensionless
ω = spreading factor, in.^{2}

Subscripts

l = light intensity of lamp behind film, meter-candle-sec
t = intensity of light transmitted by film, meter-candle-sec
0 = initial value, i.e., value on plane extending downstream from line source
1 = high speed film
2 = time averaged film

References

1 Agoston, G. A., "Development and Appraisal of a Photographic Technique for Rocket-Motor-Combustion Study," Jet Prop. Lab., CIT, Pasadena, Rep. no. 25-1, Jan. 1954.

2 Altseimer, J. H., "Photographic Techniques Applied to Combustion Studies—Two-Dimensional Transparent Thrust Chamber," JOURNAL OF THE AMERICAN ROCKET SOCIETY, vol. 22, no. 2, March-April, 1952, pp. 86–91.

3 Batchelor, G. K., "Homogeneous Turbulence," The Syndics of the Cambridge Univ. Press, London, England, 1953.

4 Bellman, D. R., Humphrey, J. C. and Male, T., "Photographic Investigation of Combustion in a Two-Dimensional Transparent Rocket Engine," NACA Rep. 1134, 1953.

5 Bittker, D. A., "An Analytical Study of Turbulent and Molecular Mixing in Rocket Combustion," NACA TN 4321, 1958.

6 Dryden, H. L., Schubauer, G. B., Mock, W. C., Jr. and Skramstad, H. K., "Measurements of Intensity and Scale of Wind-Tunnel Turbulence and Their Relation to the Critical Reynolds Number of Spheres," NACA Rep. 581, 1937.

7 Heidman, M. F. and Priem, R. J., "A Modified Sodium Line Reversal Technique for the Measurements of Combustion Temperatures in Rocket Engines," JOURNAL OF THE AMERICAN ROCKET SOCIETY, vol. 23, July–Aug. 1953, pp. 248–253.

8 Hett, J. H. and Gilstein, J. B., "Optical Studies of Rocket Combustion," Final Summary Rep., Res. Div., New York Univ., Jan. 1954, Contract DA-30-069-Ord-1025.

9 Hirshfelder, J. E., Curtiss, C. F. and Bird, R. B., "Molecular Theory of Gases and Liquids," John Wiley & Sons, Inc., N. Y., 1954, p. 539.

10 Hottel, H. C. and Broughton, F. P., "Determination of True Temperature and Total Radiation from Luminous Gas Flames," *Ind. Engng. Chem., Anal. Ed.*, vol. 4, no. 1, 1932, pp. 166–175.

11 Keagy, W. R. and Ellis, H. H., "The Application of the Schlieren Method to the Quantitative Measurement of Mixing Gases in Jets," in "Third Symposium on Combustion and Flame Explosion Phenomena," The Williams & Wilkins Co., Baltimore, Md., 1949, pp. 667–674.

12 Khramstov, V. A., "Investigation of Pressure Effect on the Parameters of Turbulence and on Turbulent Burning," in "Seventh Symposium (International) on Combustion," Butterworths Sci. Pub., London, 1958, pp. 609–614.

13 Kovásznay, L. S. G. and Clauser, F. H., "Investigation of Turbulence," Dept. Aeronautics, The Johns Hopkins Univ., Silver Spring, Md., Feb 1949, Contract NOrd 8036.

14 Prudnikov, A. G., "Flame Turbulence," in "Seventh Symposium (International) on Combustion," Butterworths Sci. Pub., London, 1958, pp. 575–582.

15 Ribner, H. S. and Tucker, M., "Spectrum of Turbulence in a Contracting Stream," NACA Rep. 1113, 1953.

16 Rosensweig, R. E. and Jensen, W. P., "Measurement and Characterization of Turbulent Mixing," Dept. of Chem. Engng., Fuels Res. Lab., MIT, Rep. no. 1, March 1958, Contract no. DA-19-020-ORD-4549.

17 Ross, C. C., "Scaling of Liquid Fuel Rocket Combustion Chambers," in "AGARD Selected Combustion Problems II—Transport Phenomena; Ignition, Altitude Behavior and Scaling of Aeroengines," Butterworths Sci. Pub., London, 1956, pp. 444–456.

18 Schubauer, G. B., "A Turbulence Indicator Utilizing the Diffusion of Heat," NACA Rep. 524, 1935.

19 Schuh, H. and Winter, K. G., "Investigation of the Turbulence Characteristics of an Experimental Low-Turbulence Wind Tunnel," NOLR 1136, Symposium on Turbulence, U. S. Naval Ordnance Lab., July 1949.

20 Scull, W. E. and Mickelsen, R., "Flow and Mixing Processes in Combustion Chambers," in "Basic Considerations in the Combustion of Hydrocarbon Fuels with Air," NACA Rep. 1300, chap. 2, 1957.

21 Towle, W. L. and Sherwood, T. K., "Eddy Diffusion—Mass Transfer in the Central Portion of a Turbulent Air Stream," *Ind. Engng. Chem.*, vol. 31, April 1939, pp. 457–462.

Prediction of Composition Limits for Detonation of Hydrogen-Oxygen-Diluent Mixtures

RICHARD W. PATCH[1]

United Aircraft Corp.
East Hartford, Conn.

Two different methods of predicting Chapman-Jouguet detonation limits in hydrogen-oxygen-diluent mixtures are presented for a model of the detonation wave comprising a shock wave followed by an ignition delay region and a combustion region. In the first method, a constant ignition-temperature criterion for the gas behind the shock wave is employed to correlate experimental data; in the second method explosion limits determined from chain branching considerations are employed. Various degrees of rotational and vibrational relaxation behind the shock in the ignition delay region are assumed for both methods to obtain three sets of temperature and pressure conditions behind the shock wave. Both methods are employed to predict detonation limits for various mixtures for which experimentally determined values are available in the literature. It is shown that the constant temperature criterion computed for a gas having complete rotational relaxation but no vibrational relaxation provides the best statistical correlation with experimental values obtained from the literature.

A GASEOUS detonation is a combustion wave which propagates with a supersonic velocity relative to the unreacted mixture. A detonation wave will not propagate unless conditions at some point in the wave are such that the fuel and oxidizer will react at an essentially spontaneous rate; for a given mixture, detonation will occur only within prescribed composition limits, which are generally different from the flammability limits of the mixture. Methods of predicting composition limits for detonation waves are required in the design of hypersonic ramjet engines in which combustion is accomplished by means of standing detonation waves (1,2),[2] and in determining the safety of exhaust systems for test equipment or the safety of industrial processes which involve the flow of detonable gases. Two different methods of predicting detonation limits have been employed in previous studies. One of these is based on the assumption that detonation occurs when a specified temperature is reached downstream of the shock wave which precedes the combustion wave (3), whereas the other is based on the application of explosion criteria to establish the conditions which would result in detonation (4). In these studies the effects of rotational and vibrational relaxation of the gas on the detonation limits were not considered, even though these effects would be expected to influence the limits predicted by either the one-temperature or the explosion criterion.

A detonation wave can be assumed to consist of a normal shock followed by a region of combustion, as postulated by von Neumann (5), and the normal shock may itself be divided into several regions according to the degree of thermodynamic relaxation, as shown in Fig. 1. (The temperatures shown in this figure and used throughout this paper are translational temperatures.) The rotational relaxation time is less than the vibrational relaxation time, but it is uncertain whether ignition will occur at T_2, T_3 or T_4. Which temperature should be used to predict the detonation limits is therefore uncertain. In the analysis presented herein, detonation limits predicted by the constant temperature criterion and the explosion criterion will be evaluated by assuming various degrees of relaxation behind the shock wave.

The analysis is limited to Chapman-Jouguet detonations (in which the Mach number of the combustion products is unity, relative to the wave front), and to the range of pressures and shock tube or flame tube diameters in which detonation limits are independent of pressure and tube size

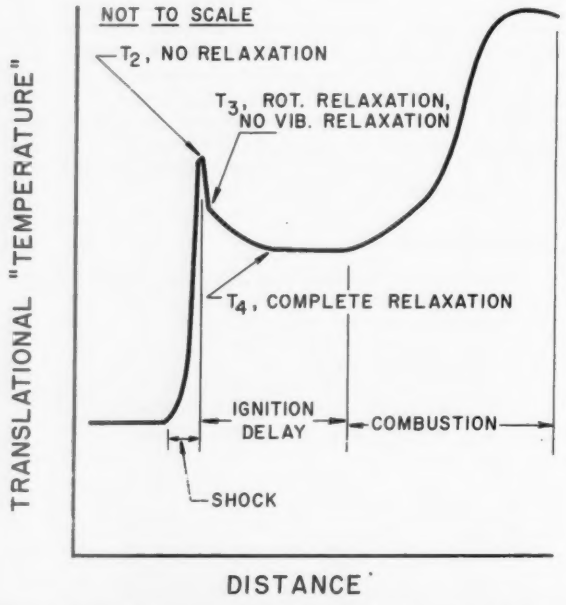

Fig. 1 Detonation wave structure, showing various possible degrees of relaxation between translational energy and the internal degrees of freedom

Presented at the ARS 14th Annual Meeting, Washington, D. C., Nov. 16–20, 1959.

[1] Research Engineer, Chemical Kinetics Group, Propulsion Section, Research Labs. Member ARS.

[2] Numbers in parentheses indicate References at end of paper.

Table 1 C_p for various degrees of thermodynamic relaxation

Molecule	No relax.	Rot. relax.; no vib. relax.	Complete relax.
Monatomic	5/2 R	5/2 R	5/2 R
Diatomic	5/2 R	7/2 R	variable

(pressures above 0.7 atm in tubes of 1-in. diameter or larger). A steady-state analysis is used, because essentially the same detonation limits are obtained experimentally whether a shock tube or a flame tube is employed.

Limits by the Constant Temperature Criterion

The constant temperature criterion (3) is based on the assumption that detonation limits are determined solely by the temperature behind the normal shock. Even if there is not complete equilibrium between the degrees of freedom, this is a reasonable approximation because kinetic energy tends to be more important in promoting bimolecular reactions than energy in internal degrees of freedom, with the possible exception of dissociations (6,7). To evaluate this criterion it is necessary to compute the temperatures T_2, T_3 and T_4 (see Fig. 1) corresponding to the various degrees of relaxation. To determine these temperatures, the theoretical detonation propagation velocities for hydrogen-oxygen-diluent mixtures at a given initial temperature and pressure were computed on an IBM 704 machine by solving the continuity, energy, momentum and state equations assuming chemical equilibrium behind the wave. The downstream Mach number of 1.0 required for a Chapman-Jouguet detonation was based on a frozen-composition speed of sound. Once the propagation velocity was known, the continuity, energy, momentum and state equations were again applied to determine conditions corresponding to the various degrees of relaxation, states 2, 3 and 4, prior to combustion. The energy equation was written as follows

$$\frac{V_1^2 - V_n^2}{2J} = \frac{C_{p,n}(T_n - T_1)}{W} \qquad [1]$$

where n may be 2, 3 or 4. The C_p's correspond to the degrees of thermodynamic relaxation at states 2, 3 and 4, as shown in Table 1. The C_p used in the case of state 4 was a mean value over the temperature range.

Lean and rich detonation limits determined experimentally for a number of mixtures and reported by Gordon and others (3) and by Breton (8) are reproduced in Table 2. In reading limits from these papers, a spinning detonation was considered a valid detonation, despite the lower-than-theoretical detonation velocity frequently observed for spinning detonations. The limits were, in general, not determined to an accuracy of better than 1 per cent hydrogen, but for the purposes of this study all hydrogen mole fractions are carried to four digits to allow the composition of other components of the mixtures to be correctly represented. It should be noted that mixtures D, E and G are hydrogen and air.

Values were calculated for T_2, T_3 and T_4 (see Fig. 1) for each of the mixtures given in Table 2, and the results are presented in Table 3. The standard deviation for each assumed degree of thermodynamic relaxation is relatively small and about the same magnitude for all three cases. The least standard deviation was obtained assuming rotational relaxation but no vibrational relaxation (T_3, Fig. 1). The calculated temperature values are slightly higher than the values which would be measured experimentally, because the theoretical propagation velocities used in the temperature calculations were generally slightly higher than experimental values (8–11). To be consistent, it was necessary to use theoretical propagation velocities in the calculations because all the experimental propagation velocities at the detonation limits were not available in (3).

In order to predict detonation limits, the problem was formulated in the opposite manner: A necessary temperature for ignition and an appropriate degree of relaxation were assumed and the composition which yields a detonation velocity just sufficient to produce this temperature was calculated. Assuming that 1314 K with rotational relaxation but no vibrational relaxation is the appropriate criterion for detonation (see Table 3), the fractions of hydrogen in column 3 of Table 4 were obtained. In the rows B and C the ratio of hydrogen to oxygen was stoichiometric, and the amount of diluent varied in the course of calculating the limits, whereas in the rows D, E and G the amount of hydrogen was varied while maintaining the same oxygen-nitrogen ratio (i.e., that of air). Mixtures A and F involve only two species.

The difference between the calculated values in column 3 and experimental values in column 2 was computed for lean mixtures by the following expression

$$\delta = (X_{H_2,\ \text{calculated}} - X_{H_2,\ \text{experimental}})/X_{H_2,\ \text{experimental}} \qquad [2]$$

and for rich mixtures by

$$\delta = (X_{O_2,\ \text{calculated}} - X_{O_2,\ \text{experimental}})/X_{O_2,\ \text{experimental}} \qquad [3]$$

These values are given in column 4. The average difference was only 13 per cent.

Limits by the Explosion Criterion

A theory resulting in a criterion for predicting the explosion limits of hydrogen mixtures (based on studies conducted in spherical constant volume bombs) has been developed by Lewis and von Elbe (12), and an application of this theory to the prediction of detonation limits has been carried out by Belles (4). The explosion criterion can be written mathematically as

$$\frac{2k_{II}}{k_{IV,\ H_2}} = [M] \sum_j X_j \eta_j \qquad [4]$$

Table 2 Hydrogen-oxygen-diluent mixtures at the detonation limits (experimental)

Mixture designation	X_{H_2}	X_{O_2}	X_{N_2}	X_A	X_{He}	Condition	Pressure P_1, atm	Reference
A	0.1500	0.8500	...	...	...	lean	1.00	8
B	0.0550	0.0275	...	0.9175	...	lean	1.25	3
C	0.0650	0.0325	...	...	0.9025	lean	1.80	3
D	0.1450	0.1796	0.6754	...	...	lean	0.70	3
E	0.1830	0.1716	0.6454	...	...	lean	1.00	8
F	0.9350	0.0650	...	...	...	rich	2.00	3
G	0.5890	0.0863	0.3247	...	...	rich	1.00	8

Note: All experiments were carried out at approximately room temperature (298 K).

Table 3 Calculated temperatures after shock for mixtures at the experimental detonation limits

Mixture designation (see Table 2)	Temperature T_2, deg K	Temperature T_3, deg K	Temperature T_4, deg K
A	1512	1207	1116
B	1380	1347	1340
C	1525	1480	1469
D	1528	1214	1157
E	1728	1365	1289
F	1524	1212	1187
G	1744	1376	1323
Average	1563	1314	1269
Standard deviation	129	106	123

where the rate constants k_{II} and k_{IV} apply to the reactions

$$H + O_2 \xrightarrow{k_{II}} OH + O \qquad II$$

$$H + O_2 + M \xrightarrow{k_{IV}} HO_2 + M \qquad IV$$

The right-hand side of Equation [4] represents an effective third-body concentration, in which the third body M may be any molecule. η_{H_2} is, by definition, equal to 1, and the rate constant $k_{IV,\,H_2}$ is the constant for hydrogen as a third body. The summation corrects for the fact that different third bodies have different collision diameters, and that triple collisions with certain molecules as third bodies are more or less effective in producing reaction than triple collisions with hydrogen as the third body. The following expression obtained from Equation [4] applies below the explosion limit

$$\frac{2k_{II}}{k_{IV,\,H_2}} < [M]\sum_j X_i\eta_i \qquad [5]$$

whereas above the explosion limit

$$\frac{2k_{II}}{k_{IV,\,H_2}} > [M]\sum_j X_i\eta_i \qquad [6]$$

Application of the explosion criterion to the prediction of detonation limits has been covered thoroughly by Belles (4), who gives two methods. In the present paper the method described by Belles [(4) under "Limits Due to Decaying Detonation Waves"] is used with two refinements: Dissociation is considered in calculating the detonation Mach number, and various degrees of relaxation are considered in calculating the critical Mach number.

Calculated detonation limits based on the explosion criterion are given in columns 5 and 7 of Table 4. Third-body efficiencies and reaction rate coefficients for the calculation were obtained from Lewis and von Elbe (12). The differences between the calculated values in columns 5 and 7 and the experimental values in column 2 are given in columns 6 and 8, respectively, where δ was computed from Equations [2 and 3].

Comparison of Limit Criteria

The constant temperature criterion used in column 3 of Table 4 gives significantly better results than the explosion criterion used in columns 5 and 7, as can be seen by comparing the average differences at the bottom of columns 4, 6 and 8. Except in column 6, no systematic error is evident either in the algebraic signs of the δ's in a given column or by comparing the δ's for lean and rich limits in a given column. The consistently negative differences in column 6 would be expected if the assumed degree of relaxation between translational energy and the internal degrees of freedom was insufficient. Limits based on the explosion criterion are not tabulated for complete relaxation between translational energy and the internal degrees of freedom; however, a few calculations were made which showed that the differences increased to even higher values than those given in column 8.

The criterion which best correlates the available experimental data is evidently the constant temperature criterion with rotational relaxation but no vibrational relaxation.

Discussion of Results

It does not appear that the large differences between theoretical and experimental values obtained using the explosion criterion can be explained by slight inaccuracies in the reaction rate data used. An explanation of the failure of the explosion criterion to predict detonation limits accurately can be obtained by examining the reactions occurring in the ignition delay period. These reactions include:

$H_2 + O_2 \rightarrow OH + OH + 20.12$ kcal	$E = 70$ kcal	I
$OH + H_2 \rightarrow H_2O + H - 15.77$ kcal	$E = 2.5$ kcal	I
$H + O_2 \rightarrow OH + O + 17.13$ kcal	$E = 17.5$ kcal	II
$O + H_2 \rightarrow OH + H + 2.99$ kcal	$E = 6$ kcal	III
$H + O_2 + M \rightarrow HO_2 + M - 47$ kcal	"E" $= -4$ kcal	IV

The heats of reaction (a negative value indicates an exothermic reaction) given in the foregoing were computed from Penner (13) and Minkoff (14), and the activation energies were obtained from Duff (15) and Schott and Kinsey (16).

Reactions I through IV have been generally accepted (12). The initiation of reactions I through IV requires an initial production of free radicals; therefore an initiation reaction is

Table 4 Calculated detonation limits based on two criteria

Mixture designation (see Table 2)	Experimental X_{H_2}	Constant temperature criterion; rotational relaxation but no vibrational relaxation $T_3 = 1314$ K X_{H_2}	δ, %	Explosion criterion; no rotational or vibrational relaxation X_{H_2}	δ, %	Explosion criterion; rotational relaxation but no vibrational relaxation X_{H_2}	δ, %
A	0.150	0.178	19	0.118	−21	0.210	40
B	0.055	0.053	− 4	0.046	−16	0.048	−13
C	0.065	0.053	−18	0.059	− 9	0.062	− 5
D	0.145	0.168	16	0.104	−28	0.181	25
E	0.183	0.169	− 8	0.116	−37	0.206	13
F	0.935	0.924	17	0.959	−37	0.840	146
G	0.589	0.626	− 8	0.698	−27	0.490	24
Average difference			$\frac{\Sigma\lvert\delta\rvert}{7} = 13\%$		$\frac{\Sigma\lvert\delta\rvert}{7} = 25\%$		$\frac{\Sigma\lvert\delta\rvert}{7} = 38\%$

required. In bomb experiments (12,17), surface reaction is assumed to provide initiation, but such reactions could not provide initiation in the case of detonation waves because the waves are so thin. Semenov (18) attributed homogeneous initiation to reaction i.

For the explosion criterion to be valid, reactions I and III must be assumed to be very fast compared to reactions II and IV (12) and HO_2 must not react to produce active free radicals (O, OH or H) to any great extent. Such conditions are met in bomb experiments at about 750 K and pressures somewhat below 1 atm, but at higher pressures Equation [4] is not valid in most bombs and would be expected to be in error in detonation waves where the pressure may be of the order of 10 atm and the temperature before ignition may be of the order 1300 K or higher. The explosion criterion would not be expected to apply to a detonation wave because HO_2 reacts by mechanisms such as

$$HO_2 + H_2 \rightarrow H_2O_2 + H + 15.17\ \text{kcal} \quad E = 24\ \text{kcal} \qquad \text{V}$$
$$HO_2 + H_2 \rightarrow H_2O + OH - 52.8\ \text{kcal} \qquad \text{VI}$$

The reverse of reaction IV need not be considered owing to its high activation energy.

In the explosion criterion, the only chain breaker is reaction IV. If reaction V or VI is included, then reaction IV is no longer a chain breaker because the active free radical consumed in reaction IV is regenerated by reaction V or VI. If it is assumed that reactions I and III are fast compared to the other reactions (12), that temperature changes may be neglected and that $[H_2]$, $[O_2]$ and $[M]\sum_j X_j\eta_j$ are practically constant, it is possible to solve for the hydrogen atom concentration as a function of the time after shock passage as shown

$$[H] = \frac{k_i[H_2]}{k_{II}}\left\{(1-\Lambda)\exp\left[(\Omega-\Psi)\frac{\tau}{2}\right] + \Lambda\exp\left[(\Omega+\Psi)\frac{\tau}{2}\right] - 1\right\} \quad [7]$$

where

$$\Omega = 2k_{II}[O_2] - k_V[H_2] - k_{IV,\,H_2}[O_2][M]\sum_j X_j\eta_j - k_{VI}[H_2] \quad [8]$$

$$\Psi = \{\Omega^2 + 8k_{II}(k_V + k_{VI})[H_2][O_2]\}^{1/2} \quad [9]$$

$$\Lambda = \{4k_{II}[O_2] - \Omega + \Psi\}/2\Psi \quad [10]$$

The assumptions given should hold quite well in the ignition delay period. From Equation [7] it can be shown that H increases continuously with time and that the value at any time is proportional to k_i. In addition, reaction i has the highest activation energy of any of the reactions, so it is likely to be a controlling reaction.

Experimental ignition delays for hydrogen-oxygen-diluent mixtures are shown in Fig. 2. Schott and Kinsey (16) indicated that the delay was inversely proportional to oxygen concentration for the range of temperature investigated, so the data of (16) have been adjusted to the partial pressure of oxygen in a stoichiometric hydrogen-air mixture at 1-atm total pressure. The upper branch of the ignition delay curve has a slope corresponding to about 90 kcal per mole, which is close to the estimated activation energy of reaction i of 70 kcal per mole. It therefore appears that reaction i is the controlling reaction on the upper branch of the ignition delay curve, whereas reaction II is the controlling reaction on the lower branch (16). On the upper branch reaction i is important in producing OH radicals only in the early stages of the ignition delay period, and thereafter the chain branching mechanism assumes control. Nevertheless, the concentration of free radicals at any time in the ignition delay period depends strongly on both the rate of reaction i during the early stages and the rate of reaction II during later stages.

The ignition temperatures in Table 3 are the same for both

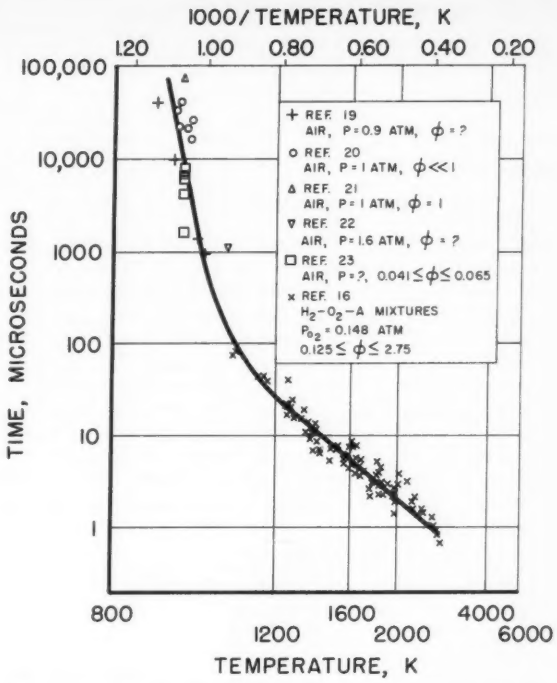

Fig. 2 Experimental ignition delays for hydrogen-oxygen-diluent mixtures

the lean and rich limits. This characteristic would be expected if both H_2 and O_2 participated in the rate-controlling reaction, which indeed is the case for reaction i. Consequently, it appears that reaction i is the controlling reaction for detonation limits, despite the fact that the knee of the ignition delay curve (Fig. 2) occurs at about 1100 K, whereas Table 3 gives 1314 K for the ignition temperature. This discrepancy is probably a result of the use of theoretical detonation velocities in the calculation of T_3 instead of the lower experimental velocities. The inhibition of detonation by small quantities of water vapor (3) indicates that reaction IV also has some rate-controlling influence, since water is believed to be a very efficient third body in reaction IV (12).

The assumption of rotational relaxation but no vibrational relaxation in the ignition delay period must also be considered in evaluating the constant temperature criterion. Rotational relaxation is attained in 300 collisions or less, so it is reasonable to assume complete relaxation between rotational and translational energy. However, vibrational relaxation is slower and therefore requires detailed analysis.

A hydrogen-air mixture consists largely of three gases (hydrogen, nitrogen and oxygen), each of which has a vibrational relaxation time which is a function of temperature, pressure and the composition of the mixture. The process of vibrational excitation may be represented classically, as shown in Fig. 3.

Collisions sometimes change the energy of vibration of molecule B-B and sometimes do not. Particle "A" may be any molecule. The dependence of the vibrational relaxation times on pressure may be eliminated by considering the average number of molecular collisions necessary to relax a molecule or by referring all times to a standard pressure such as 1 atm. Relation [11] was derived (24) in part from the Schrödinger wave equation and applies only where B-B is a diatomic molecule. It can be used to compute the number

of collisions necessary for vibrational relaxation

$$Z_b = \frac{135(W_a + 2W_b)^2}{W_a^2 W_b \bar{\nu}\bar{\sigma}^2}\left(\frac{T}{\theta'}\right)^{1/6} \times \exp\left[1.5\left(\frac{\theta'}{T}\right)^{1/3} - \frac{0.72\bar{\nu}}{T} - \frac{\epsilon}{KT}\right] \quad [11]$$

where

$$\theta' = 11.02 \times 10^{-3}\bar{\nu}^2\bar{\sigma}^2 W_a W_b/(W_a + 2W_b)$$

and Z_b is the average number of collisions for relaxation of molecule B-B. The number of collisions may be converted to relaxation time by use of relations in Kennard's book (25). Equation [11] correlates the experimental data for pure oxygen and pure nitrogen (26) quite well. Curves for pure oxygen and pure nitrogen are presented in Fig. 4. Calculations show that for a stoichiometric hydrogen-air mixture, the vibrational relaxation of hydrogen should be quite rapid and the vibrational relaxation of oxygen and nitrogen less rapid. The latter should depend almost entirely on the amount of hydrogen present, as was partly substantiated by experiments in which additions of hydrogen to pure oxygen reduced the relaxation time of the oxygen drastically (24). The results of calculations of the vibrational relaxation times for oxygen and nitrogen in a stoichiometric hydrogen-air mixture are presented in Fig. 4. These data should be viewed with reservations because, at 288 K, Equation [11] yields vibrational relaxation times, for additions of hydrogen to oxygen or for the somewhat similar case of additions of helium to chlorine, that are more than an order of magnitude lower than the experimental values (24). The accuracy of Equation [11] at higher temperatures under such conditions apparently has not been investigated.

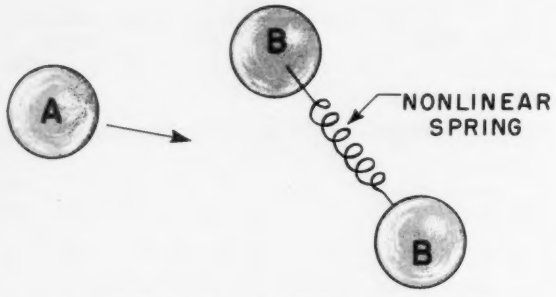

Fig. 3 Classical model for vibrational relaxation

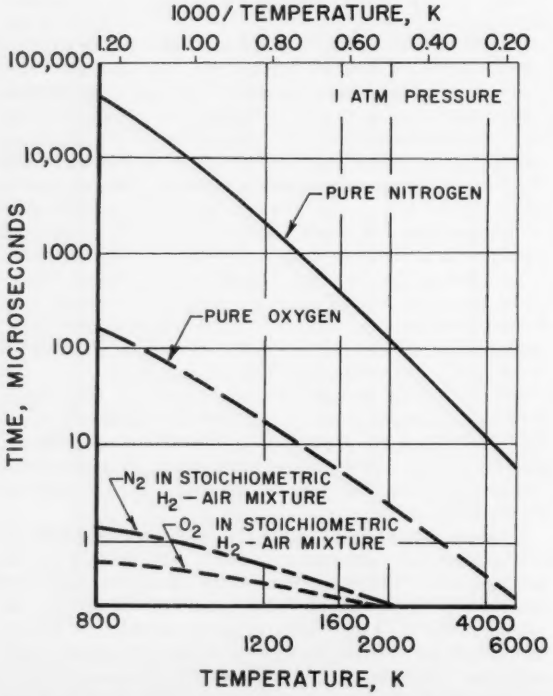

Fig. 4 Calculated vibrational relaxation times for N_2 and O_2

Comparing Figs. 2 and 4 and considering that Equation [11] gives answers that are probably too low for mixtures, it is evident that the vibrational relaxation times and ignition delays are not far different. Density measurements in detonation waves (27) indicated that vibrational relaxation was not achieved. On the other hand, using dilute mixtures of hydrogen and oxygen in argon, Schott and Kinsey (16) explained their observed ignition delays by assuming that in certain runs the ignition delay was long compared with the time for vibrational relaxation of oxygen, whereas in other runs it was short.

It appears that the question of ignition delay relative to vibrational relaxation warrants further experimental investigation. Additional experimental data would also be valuable in further substantiating the constant temperature criterion.

Conclusions

1 The composition limits for detonation of hydrogen-oxygen-diluent mixtures can be predicted by assuming that ignition occurs when the temperature downstream of the shock wave portion of the detonation wave exceeds a critical value. In making these predictions the detonation wave must be considered to consist of a shock wave followed by a combustion wave.

2 In hydrogen-oxygen-diluent mixtures initially near standard room temperature and pressure, detonation will occur when the temperature behind the shock wave equals or exceeds 1314 K. This temperature should be computed with the assumption that rotational relaxation occurs but that vibrational relaxation does not.

3 The composition limits for detonation of hydrogen-oxygen-diluent mixtures cannot be predicted as accurately by the explosion criterion as by the one-temperature criterion. The average differences between experimentally measured limits and those predicted by the explosion criterion are approximately twice as great as the differences obtained with the one-temperature criterion.

Nomenclature

b = conversion factor, 1.0133 dynes per atm cm²
C_p = average molar specific heat at constant pressure, based on the appropriate degree of relaxation, $C_p = \sum_j X_j C_{p,j}$ cal per mole K
E = activation energy, kcal per mole
J = conversion factor, 4.184×10^7 dyne cm per cal
k = reaction rate constant, cm³ per mole sec for reactions i, I, II, III, V and VI; cm⁶ per mole² sec for reaction IV
K = Boltzmann constant, erg per K
M = any third body
P = absolute static pressure, atm
R = universal gas constant, cm³ atm per mole K
T = absolute translational temperature, K
V = propagation velocity of a Chapman-Jouguet detonation wave, cm per sec
W = average molecular weight, $W = \sum_j X_j W_j$ gm per mole
X = mole or volume fraction of a species in a mixture, dimensionless
Z_b = average number of collisions for vibrational relaxation of B-B, dimensionless

δ = difference between computed and experimental composition limits, dimensionless
ϵ = Lennard-Jones interaction potential for "A" and B-B, ergs
η = third-body efficiency of a species relative to the third-body efficiency of hydrogen, dimensionless
θ' = vibrational energy parameter of molecule B-B, K
Λ = a function of k_{II}, $[O_2]$, Ω and Ψ, dimensionless
$\tilde{\nu}$ = fundamental wave number of vibration of molecule B-B, cm^{-1}
ρ = density, gm per cm^3
$\bar{\sigma}$ = bimolecular collision distance between "A" and B-B, Å
$\sum_j$ = operator indicating summation of subsequent quantity over all species
τ = time, sec (except as noted)
ϕ = equivalence ratio (ratio of fuel mass to stoichiometric fuel mass for given oxidizer mass), dimensionless
Ψ = a function of Ω, k_{II} k_V, k_{VI}, $[H_2]$ and $[O_2]$, sec^{-1}
Ω = a function of k_{II}, $[O_2]$, k_V, k_{VI}, $[H_2]$, k_{IV,H_2}, $[M]$, η_j and X_j, sec^{-1}
[ ] = concentration of included species, mole per cm^3

Subscripts

a = particle "A"
A = argon
b = atom "B"
He = helium
H_2 = molecular hydrogen
i = reaction i
j = species j
n = degree of relaxation (2, 3 or 4)
N_2 = molecular nitrogen
O_2 = molecular oxygen
1 = upstream of shock or detonation
2 = downstream of shock; no rotational or vibrational relaxation
3 = downstream of shock; rotational relaxation, but no vibrational relaxation
4 = downstream of shock; complete relaxation between translation, vibration and rotation
II = reaction II
IV = reaction IV
V = reaction V
VI = reaction VI

References

1 Dunlap, R., Brehm, R. L. and Nicholls, J. A., "A Preliminary Study of the Application of Steady-State Detonative Combustion to a Reaction Engine," JET PROPULSION, vol. 28, no. 7, 1958, pp. 451–456.

2 Weber, R. J. and MacKay, J. S., "An Analysis of Ramjet Engines Using Supersonic Combustion," NACA TN 4386, 1958.

3 Gordon, W. E., Mooradian, A. J. and Harper, S. A., "Limit and Spin Effects in Hydrogen-Oxygen Detonations," presented at the Seventh Symposium on Combustion, Oxford, Eng., 1958.

4 Belles, F. E., "Detonability and Chemical Kinetics: Prediction of Limits of Detonability of Hydrogen," presented at the Seventh Symposium on Combustion, Oxford, Eng., 1958.

5 von Neumann, J., OSRD Rep. no. 549, Ballistic Research Lab., file no. X-122, 1942.

6 Moelwyn-Hughes, E. A., "Physical Chemistry," Pergamon Press, N. Y., 1957, pp. 1112–1114.

7 Wall, F. T., Hiller, L. A., Jr. and Mazur, J., "Statistical Computation of Reaction Probabilities," *J. Chem. Phys.*, vol. 29, no. 2, 1958, pp. 255–263.

8 Breton, M. J., "Recherches sur la Détonation des Mélanges Gazeux," *Ann. Office National Combustibles Liquides*, vol. 11, 1936, pp. 487–548.

9 Morrision, R. B., "A Shock Tube Investigation of Detonative Combustion," Engineering Research Institute, University of Michigan, Ann Arbor, 1955.

10 Dixon, H. B., "The Rate of Explosion in Gases," *Philosophical Trans. Royal Soc. London*, vol. A184, 1893, p. 97.

11 Wendlandt, R., "Die Detonationsgrenze in explosiven Gasgemischen," *Zeitschrift fur Physikalische Chemie*, vol. 116, 1925, pp. 227–260.

12 Lewis, B. and von Elbe, G., "Combustion, Flames and Explosions of Gases," Academic Press, Inc., N. Y., 1951, chap. 2.

13 Penner, S. S., "Chemistry Problems in Jet Propulsion," Pergamon Press, N. Y., 1957, chap. 6.

14 Minkoff, G. J., "Some Recent Developments Concerning Free Radicals," *Combustion and Flame*, vol. 2, no. 2, 1958, pp. 193–207.

15 Duff, R. E., "Calculation of Reaction Profiles Behind Steady-State Shock Waves; I. Application to Detonation Waves," *J. Chem. Phys.*, vol. 28, no. 6, 1958, pp. 1193–1197.

16 Schott, G. L. and Kinsey, J. L., "Kinetic Studies of Hydroxyl Radicals in Shock Waves. II. Induction Times in the Hydrogen-Oxygen Reaction," *J. Chem. Phys.*, vol. 29, no. 5, 1958, pp. 1177–1182.

17 Patrick, C. R. and Robb, J. C., "The Initiation Step in the Thermal Hydrogen and Oxygen Reaction," Trans. Faraday Soc., vol. 51, 1955, pp. 1697–1703.

18 Semenov, N., "On the Constants of the Reactions $H + O_2 = OH + O$ and $H_2 + O_2 = 2\ OH$," *Acta Physicochimica U.R.S.S.*, vol. 20, no. 3, 1945, pp. 291–302.

19 Mullins, B. P., "Ignition Delay Measurements on Gas Turbine Fuels by the N.G.T.E. Method," NATO, AGARD AG 5/P2, 1952.

20 Swigart, R. J., "A Study of the Kinetics of the Hydrogen-Oxygen Reaction in a New Flow Reactor," Aeron. Engng. Lab., Rep. no. 432, Princeton Univ., Princeton, 1958.

21 Anagnostou, E., Brokaw, R. S. and Butler, J. N., "Effect of Concentration on Ignition Delays for Various Fuel-Oxygen-Nitrogen Mixtures at Elevated Temperatures," NACA TN 3887, 1956.

22 Bazhenova, T. V. and Soloukhin, R. I., "Gas Ignition Behind the Shock Wave," presented at the Seventh Symposium on Combustion, Oxford, Eng., 1958.

23 Fouré, C., "Stationary Flames in Cylindrical Flow of Homogeneous Hydrogen-Air Mixtures," *Recherche Aeron.*, no. 42, 1954, pp. 33–37.

24 Herzfeld, K. F., "Relaxation Phenomena in Gases," in "Thermodynamics and Physics of Matter," ed. by F. D. Rossini, High Speed Aerodynamics and Jet Propulsion Series, vol. 1, Princeton Univ. Press, Princeton, 1955.

25 Kennard, E. H., "Kinetic Theory of Gases," McGraw-Hill Book Co., Inc., N. Y., 1938, chap. 3.

26 Blackman, V., "Vibrational Relaxation in Oxygen and Nitrogen," *J. Fluid Mech.*, vol. 1, part 1, 1956, pp. 61–85.

27 Kistiakowsky, G. B. and Kydd, P. H., "Gaseous Detonations. IX. A Study of the Reaction Zone by Gas Density Measurements," *J. Chem. Phys.*, vol. 25, no. 4, 1956, pp. 824–835.

Calibrations of the Card-Gap Test[1]

MELVIN A. COOK[2]
University of Utah
Salt Lake City, Utah

LEX L. UDY[3]
Intermountain Research
and Engineering Co., Inc.
Salt Lake City, Utah

The shock waves generated by the standard and some modified donors of the card-gap test and propagated into water through the plastic cards were observed in water by a backlighted aquarium method using streak camera photography. The measured initial shock velocity V_w in water was plotted against the number of cards n and converted by means of shock pressure-velocity calibration data for water to $p_w(n)$ curves. The standard tetryl donor initiated with the recommended Special Engineer Corps electric blasting cap exhibited erratic, low-order detonation; high-order detonation was achieved, however, by doubling the length of the tetryl booster. A 38-gm (3.8-cm diameter, 2.0-cm long) cast 50/50 pentolite donor of higher detonation pressure detonated uniformly high order with the Special Engineer electric blasting cap, thus providing a much broader shock pressure coverage with the same card-gap system and a smaller charge. Pressure calibration measurements were also carried out using low density TNT. The aquarium method is shown not only to provide valuable calibration data for the card-gap test, but also to reveal important information on donor initiation, velocity transients and detonation pressures of donors for the card-gap test.

SENSITIVENESS tests have long been employed for characterizing "high" or detonating explosives. In such tests one usually observes the limiting gap for detonations in a receptor shocked by a hot gas wave from a donor charge ("air-gap sensitiveness") or by the shock wave transmitted from a donor charge through a condensed inert medium. Conventional nitroglycerine (NG) dynamite, air-gap sensitiveness tests include the "half cartridge" and the "whole cartridge" tests. In the half cartridge test a 1.25 × 4-in. donor is separated a distance S_1 from a similar receptor, both charges being cut from the same 1.25 × 8-in. cartridge and wrapped in paper with the cut ends facing over the air gap (1).[4] In the whole cartridge test a 1.25 × 8-in. whole cartridge donor is wrapped in a paper tube with a similar 1.25 × 8-in. receptor with the preformed or machined (shotgun) end crimps of the cartridges facing each other over the gap. To insure consistent performance, it has been conventional to measure sensitiveness of dynamites as the maximum distance for five successive detonations.

Modified air-gap sensitiveness tests came into existence with the introduction of *blasting agents*, i.e., commercial explosives which are not cap sensitive but require boosters to detonate them. In these tests, charge diameters were increased sometimes to as high as 10 in. to overcome the critical diameter limitation. Moreover, air-gap sensitiveness results, measured as the *minimum* air gap for consistent failures as a function of charge size, provide important data regarding safe spacings between charges, e.g., in a quarry operation [see (1) p. 142].

In the military field, the sensitiveness tests was modified in a different direction. Instead of air, some inert condensed medium was used to separate the donor and receptor, and, since critical diameters are generally relatively small for most military explosives, sensitiveness measurements were carried out only in small diameter charges sometimes using heavy confinement. In addition, probability theory criteria were applied to the detonation-failure results of the sensitiveness test using the Bruceton "up and down" technique (2–6), and instead of measuring the maximum gap for five consistent detonations or the minimum gap for five consistent failures, the 50/50 detonation-failure criterion was employed. In the Bruceton up and down technique one first establishes the approximate gap S_1 at which both detonations and failures of the receptor are encountered, and then increases the distance S_1 one increment each time a detonation occurs and decreases it one increment each time a failure occurs, carrying out a total of 20 shots. Results are then plotted to give the gap length corresponding to the 50/50 go/no go point.

The "card-gap" sensitiveness (7) test is currently a standard test for monopropellants and other military high explosives. In this test the donor charge is pressed tetryl.[5] The gap consists of plastic cards each of 0.25-mm thickness, and the receptor is used in a 2.54-cm ID metal tube lined on the end against the cards either with Teflon or a metal shield. The donor charge is detonated with a special Army Engineer Corps electric blasting cap (SEC-EB cap). The sensitiveness, determined by the up and down method, is expressed as the number n^* of cards for 50 per cent detonations and 50 per cent failures, the asterisk indicating this "sensitiveness limit."

Modified sensitiveness methods similar to the card-gap test have been used in fundamental investigations not only to elucidate the mechanism of the card-gap test, but also (8–14) to study the mechanism of initiation and the transition from deflagration to detonation (DDT). In these tests the gap

Received April 5, 1960.
[1] This work was sponsored by the Air Research and Development Command, USAF, under Air Reduction Co., Inc., Contract no. AF-33(616)5732 monitored by the Air Force Flight Test Center, Edwards Air Force Base, Calif. The investigation was carried out with the facilities made available by Intermountain Research and Engineering Co., Inc., Salt Lake City, Utah. This paper is an essential portion of the doctorate thesis submitted to the University of Utah by Lex L. Udy.
[2] Director, Institute of Metals and Explosives Research.
[3] Research Physicist.
[4] Numbers in parentheses indicate References at end of paper.
[5] The tetryl pellets used in the investigations were obtained from Picatinny Arsenal. They were from standard manufacture according to specifications for the standard card-gap test (7). They weighed 50.7 ± 1.5 gm each and measured 4.14 cm (d) × 2.54 cm (L); d = diameter, L = length.

Table 1 Donor charges and measured and theoretical V_s ($n = 0$) and p_w ($n = 0$) data

Code	ρ_1, gm/cc	d, cm	L, cm	Cap	Booster	V_w ($n = 0$), km/sec meas.	V_w ($n = 0$), km/sec ideal	p_w ($n = 0$), k.atm meas.	p_s Eq. [3]	p_2 theory
Tetryl series 1	1.5	4.14	2.54	SEC-EB	none	4.6	5.45	71	99	175
Tetryl series 2	1.5	4.14	5.08	SEC-EB	none	5.4		115	172	
Tetryl series 3	1.5	4.14	2.54	#6	*	5.4		115	172	
Tetryl series 4	1.5	4.14	7.62	SEC-EB	none	5.4		115	172	
Pentolite series 1	1.65	3.81	2.0	†	none	4.66	5.60	74	108	218
Pentolite series 2	1.65	3.81	2.0	SEC-EB	none	5.60		138	220	
Pentolite series 3	1.65	3.81	4.0	SEC-EB	none	5.60		138	220	
Pentolite series 4	1.65	3.81	2.0	‡	none	5.22		100	162	
Pentolite series 5	1.65	3.81	2.0	#6	**	5.56		135	215	
TNT series 1	0.87	3.81	2.0	SEC-EB	none	≈2.6	3.85	≈14	≈12	42
TNT series 2	0.87	3.81	5.0	SEC-EB	none	3.42		29	31	
TNT series 3	0.87	3.81	5.0	SEC-EB	**	3.60		34	37	

d = diameter, L = length; V_w ($n = 0$) and p_w ($n = 0$) are the initial velocity and pressure of the shock in the aquarium for zero cards; p_s is the peak pressure in the front of the detonation wave, and p_2 the computed ideal detonation pressure described by hydrodynamic theory.

† 350-mg PETN base charge at $\rho_1 \doteq 1.0$ gm per cc.

‡ 2.0-gm PETN base charge at $\rho_1 \doteq 1.0$ gm per cc.

* 38-gm, 3.8 cm (d) × 2.0 cm (L) cast 50/50 pentolite booster.

** 10-gm pressed tetryl booster.

material consisted of glass, steel, aluminum, brass or other inert solid materials.

There has long been a need for calibration of the shock strengths developed in the card-gap and other sensitiveness tests in order to provide means of correlating the simple go/no go results with more fundamental experimental and theoretical data. For example, by high speed photographic methods one may measure not only the gap thickness at the sensitiveness limit S_1*, or 50/50 detonation-failure point, but also the distance S_2 into the receptor where the detonation wave forms, the time τ between entrance of the shock into the receptor and the formation of detonation, and the relationships between these quantities and the gap thickness S_1, not only at the sensitiveness limit S_1* but also at $S_1/S_1^* < 1.0$. Moreover, complicated wave interactions and predetonation reactions in the receptor have also been observed directly. An "aquarium method" was used, which was developed by Cook, Keyes and Ursenbach (15) to make possible the determination of the peak pressure in the shock waves transmitted from high explosives into various transparent media. This method has already been applied in calibrating the glass plate sensitiveness test (13). It is similar to that developed earlier by Holton[6] except that the present method is based on the observed $p(V)$ curve for water, and obtained by measuring the free surface velocity V_f as a function of shock velocity V at water-free surfaces for shocks of different strengths, whereas the method of Holton was based on an assumed equation of state from which the particle velocity needed to obtain $p(V)$ for water was computed. The need for similar calibrations of the card-gap test prompted the present investigation to determine the initial pressure p_w in the shocks delivered by the donor charge through the card gaps and into the receptor charge as a function of n.

Experimental Methods

The aquarium method for measuring the shock pressure emerging from the (donor card gap) shock generator is illustrated in Fig. 1 showing a cross-sectional view through the axis of the donor card-gap system and perpendicular to the slit plane of the streak camera; the vertical dotted line is the region of focus of the slit of the camera. Two types of backlighting systems were used, one an exploding wire system (Fig. 1 top), and the other a high explosive flashbomb method (Fig. 1 bottom). The exploding wire system will be preferred in many laboratories owing to charge size limitations imposed by congestion. The plastic cards comprising the card gap were fastened to the donor charge in lieu of the usual receptor cup for the present shock calibration studies by means of wooden strips and rubber bands.

Charges were fired with SEC-EB caps except as indicated in Table 1; the donor charge and the flashbomb were fired simultaneously in these tests, since ample luminosity was available to illuminate the shock wave all during its propagation through the aquarium.

The $p(V)$ calibration curves employed in this study were those measured by Cook, Keyes and Ursenbach (15). The streak camera records of the shots were reduced by special mirror techniques. Photographs of the charge and a typical streak camera record are shown in Figs. 2. The initial shock velocity in water V_w could be determined with an accuracy of better than ±2.5 per cent corresponding to better than ±100 m per sec in the measured velocity V_w. Since the same accuracy applied to the measured $p(V)$ calibration curves, the measured initial shock pressures could be measured with an accuracy of better than ±6 per cent by the aquarium method.

Experimental Results

Fig. 3 shows the curve of initial shock velocity V_w against card number n obtained with the standard pressed tetryl donors using zero to 100 cards (tetryl series 1). The scatter of points was larger than expected from the known reproducibility of the aquarium method indicating a basic donor deficiency in the standard tetryl donor system. Moreover, the observed initial shock velocity of 4.6 km per sec for zero cards was much lower than the value expected if the tetryl were to detonate at its full high-order detonation velocity. Indeed, this donor exhibited primarily only low-order detonation when initiated with the SEC-EB cap. Actually, this was anticipated from information obtained earlier regarding low-order detonation and velocity transients in tetryl (8,16).

[6] An aquarium method differing from the one used here only in the method of establishing the $p(V)$ calibration curve for water was first described by William C. Holton in a classified Naval Ordnance Laboratory report, NavOrd 3968, 1 December 1954.

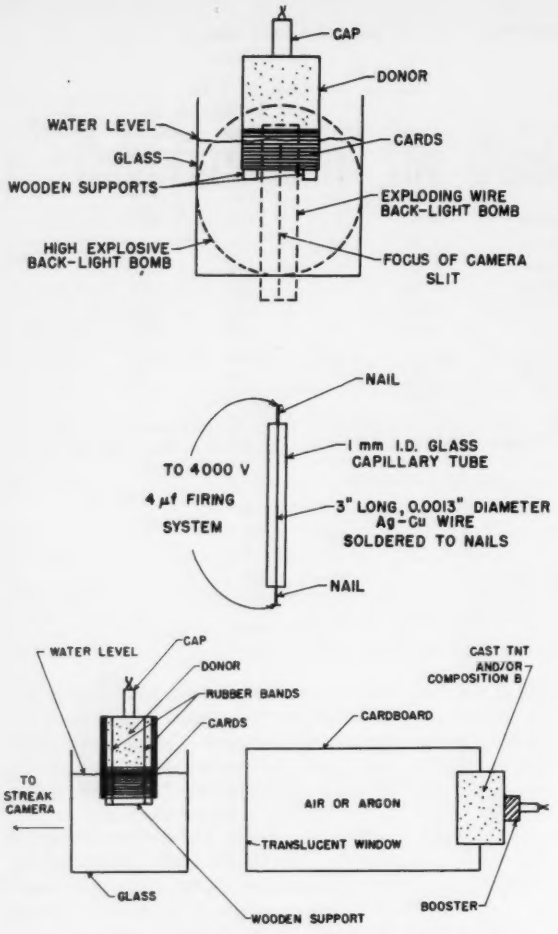

Fig. 1 Aquarium method for calibration of card-gap test

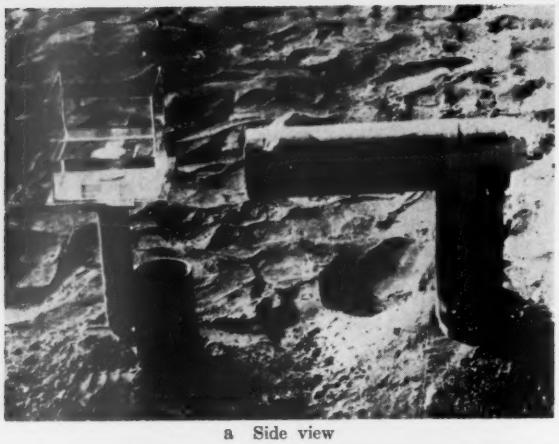

a Side view

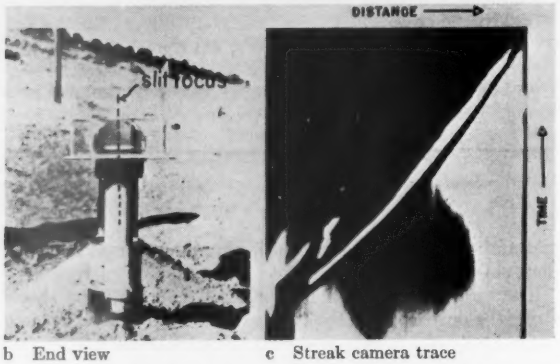

b End view c Streak camera trace

Figs. 2 Photographs of setup and typical trace in water $p(V)$ calibrations and shock pressure measurements in donor card-gap system

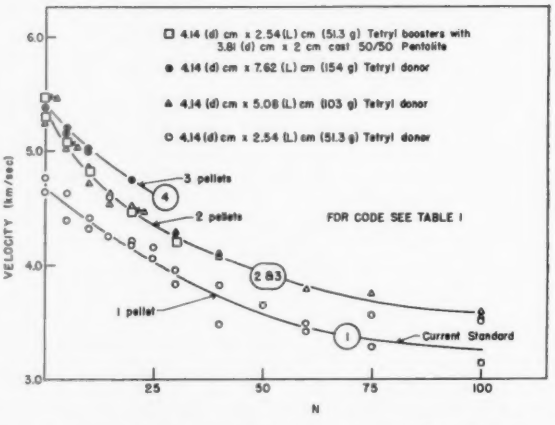
4.14 (d) cm x 2.54 (L) cm (51.3 g) Tetryl boosters with 3.81 (d) cm x 2 cm cast 50/50 Pentolite
4.14 (d) cm x 7.62 (L) cm (154 g) Tetryl donor
4.14 (d) cm x 5.08 (L) cm (103 g) Tetryl donor
4.14 (d) cm x 2.54 (L) cm (51.3 g) Tetryl donor
3 pellets
2 pellets
FOR CODE SEE TABLE I
2 83
1 pellet
Current Standard
VELOCITY (km/sec)
N
6.0
5.0
4.0
3.0
25
50
75
100

Fig. 3 Initial shock velocity in water vs. number of cards n for tetryl card-gap donor systems

The irreproducibility and low-order detonation of the standard donor system of the card-gap test thus seem to discredit the reliability of this donor system. However, the facts that the standard tetryl donor undergoes low-order detonation nearly all of the time with SEC-EB caps, and that a relatively large number of shots are used in the up and down method to establish n^* for a given receptor, permitting anomalous fluctuations to be smoothed out, justify its use. On the other hand, anomalies encountered in this test may possibly be attributed to occasional high-order detonation and fluctuations in performance of the standard donor system as brought out by these studies by the aquarium method.

Additional series of measurements were carried out with the pressed tetryl donor to determine under what conditions tetryl does develop reproducible high-order detonation. In tetryl series 2 (Fig. 3) the length of the tetryl pellet was doubled by using two standard pellets end to end. Note that V_w for zero cards was 5.4 km per sec in this case and that the $V_w(n)$ curve was appreciably above and more uniform over its entire range than with the standard donor charge. To show experimentally that $V_w(n = 0)$ corresponded in tetryl series 2 to high-order detonation, two additional series were run in one of which (tetryl series 3) the standard tetryl donor was detonated with a 38-gm cast 50/50 pentolite booster, and in the other (tetryl series 4) the tetryl length was increased to 7.62 cm by using three pellets end to end. Note that in both cases V_w $(n = 0)$ was the same as in tetryl series 2, confirming that all the modified donors developed high-order detonation of the same velocity. The 38-gm [3.8 cm $(d) \times 2.0$ cm (L)] cast 50/50 pentolite booster had been formulated in a previous study[7] as the card-gap donor to give the same 50/50 go/no go card number n^* for nitromethane (NM) as the receptor as with the standard 51-gm tetryl donor. It is therefore not surprising that the two curves for tetryl series 2 and tetryl series 3 were identical. On the other hand, as expected, the longer (L = 7.62 cm) pressed tetryl donor, although it generated a shock wave of the same initial velocity and pressure at $n = 0$ as that in tetryl series 2 and tetryl series 3,

[7] Tests carried out by Intermountain Research and Engineering Co., Inc., for Commercial Solvents Corp., Terra Haute, Ind.

generated shocks of higher strength for $n > 0$. This shows the influence of charge length on total end impulse; although the shock from the 7.62-cm pellet had the same initial pressure as that from the 5.08 pellet it decayed more slowly, owing to its greater total impulse.

To extend the range of available shock pressures in the card-gap test and also to evaluate a better, more reliable donor charge, cast 50/50 pentolite donor systems described in Table 1 were also investigated with the results shown in the top three curves of Fig. 4. Note the close similarity of the tetryl series 1 and the pentolite series 1 curves, showing that the latter charge, detonated with the 350-mg, low density PETN ($\rho_1 \approx 1.0$) base charge, actually matched quite closely the standard one. But the aquarium method showed that this donor also detonated low-order and irreproducibly with the 350-mg exploding wire cap. Assuming that this was due to the use of an excessively weak cap, two series (not shown in Fig. 4) were run with the 38-gm [3.8 cm (d) × 2.0 cm (L)] pentolite donor (see Table 1). In one, the charge in the exploding wire cap was increased from 0.35 to 2.0 gm. This resulted in an increase in V_w ($n = 0$) from 4.7 to 5.1 km per sec, still, however, somewhat below the hydrodynamic value of 5.6 ± 0.05 km per sec. In the next series a 10-gm tetryl pellet was used to detonate the donor yielding the expected value of V_w ($n = 0$) corresponding to ideal detonation within experimental error. This expected value was based on a detonation pressure of 218 kb computed by the inverse method described in (8) and the $\alpha(v)$ equation of state.

Although it was considered desirable to be able to use weaker caps with the pentolite booster to avoid the need for obtaining the SEC-EB caps, this was not possible with the 38-gm pentolite booster. Tests were therefore repeated with the cast 50/50 pentolite donor detonated with the SEC-EB caps with the results shown in Fig. 4, pentolite series 2. Note that V_w ($n = 0$) was in good agreement with the theoretical value in this case, showing the advantages of the strong detonator. The $V_w(n)$ curve of series 2 for pentolite fell rapidly with increasing n owing to the small size and therefore small end impulse of the 38-gm donor. But the $V_w(n)$ curve was considerably higher than that obtained with the same donor and a weaker cap, and with the larger standard tetryl donor and the strong SEC-EB cap. This result is of particular interest, because it shows that the pentolite donor is appreciably better than the tetryl donor not only because it undergoes high-order detonation with the SEC-EB cap in a smaller charge, whereas the larger standard tetryl donor showed low-order detonation under the same conditions, but also because it permits a pressure range coverage more than twice as great as with the standard donor.[8]

Pentolite series 3, Fig. 4, was obtained using two 38-gm [3.8 cm (d) × 4.0 cm (L)] pentolite donor charges detonated with the SEC-EB caps. Note the excellent correlation of $V_w(n)$ results with the pentolite series 2 curve as well as the results obtained with a 10-gm tetryl booster for the pentolite donor at $n = 0$. The V_w ($n = 0$) results for the pentolite series 2, 3 and 4 also agreed with similar results obtained with much larger 5 × 30-cm cast 50/50 pentolite charges (13). These results show that the detonation of the 38-gm cast pentolite donor with the SEC-EB caps is not only high-order and reproducible, but also that it is the ideal hydrodynamic one, since ideal detonation may be defined experimentally as detonation at a pressure level that does not increase when the charge size (length and diameter) is increased.

Shown also in Fig. 4 are three series of results obtained with 3.8-cm (diam), loose, low density ($\rho_1 = 0.87$ gm per cc), fine TNT using in all three series the SEC-EB caps. With the short (2 cm), 20-gm TNT donor, $V_w(n)$ results were extremely erratic, and V_w ($n = 0$) values were far below the expected ideal ones (TNT series 1). By increasing the donor

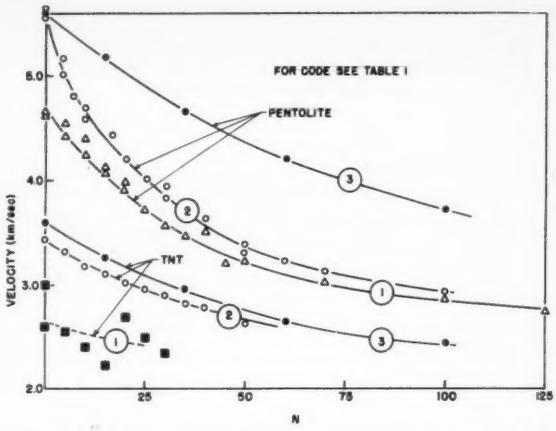

Fig. 4 Initial shock velocity in water vs. n for fine TNT and cast 50/50 pentolite card-gap donor systems

length to 5.0 cm (and charge size to 50 gm) a smooth $V_w(n)$ curve (TNT series 2) was obtained, although $V_w(n = 0)$ was still somewhat below the expected value based on the computed detonation pressure given in (8). Therefore, a third series (TNT series 3) was carried out with the 3.8 cm (d) × 5.0 cm (L) TNT donor detonated with a 10-gm tetryl pellet. Although $V_w(n = 0)$ was somewhat higher, it was still below the value computed for ideal detonation of low density TNT. The excellent reproducibility of the low density, fine TNT $V_w(n)$ curve (TNT series 2), however, shows that this donor should be a very useful one for studying the most sensitive explosives that initiate at very low shock pressures, permitting one to use a small number of cards and thereby increase the sensitivity of the card-gap test for the more sensitive receptor charges.

Discussion of Results

The following *impedance mismatch* equation relates the pressures in the shock wave on each side of an interface between two (sufficiently thick) media (8,13,17)

$$p_i = p_t[(\rho V)_t + (\rho V)_i]/2(\rho V)_t \qquad [1]$$

where

i = incident medium
t = transmission medium
V = shock velocity
(ρV) = impedance

In the card-gap test the impedance $(\rho V)_i$ pertains either to the card system ($n > 0$) or to the donor itself ($n = 0$), and is here designated $(\rho V)_c$ for the card system and $\rho_1 D$ (D = detonation velocity) for the donor, using $(\rho V)_w$ for the impedance of water. Thus, for the card-gap test one may write

$$p_w[(\rho V)_w + (\rho V)_c]/2(\rho V)_w = p_c \qquad (n > 0) \qquad [2]$$

$$p_w[(\rho V)_w + (\rho_1 D)]/2(\rho V)_w = p_e \qquad (n = 0) \qquad [3]$$

it being understood that all quantities here pertain to values at the interface between the cards or explosive and the aquarium. To apply Equations [2 and 3] one must thus know p_w, V_w and V_e or D; all other quantities are known. V_w is measured directly in the aquarium method. D data for the systems given here are known, and for others are easily obtained by the streak camera method or by the pin-oscillograph method. The determination of V_c is more difficult, but can be made by the streak camera by measuring the times of the shock entrance into and exit from the card gap, making measurements in small increments in gap length, e.g., by in-

[8] The cast pentolite donors are available commercially from Intermountain Research and Engineering Co., Inc.

Table 2 Some approximate average velocity $\bar{V}_c$ data for shocks in card gap. 3.8 cm (d) × 4.0 cm (L) cast 50/50 pentolite donor—SEC-EB cap

n	Transit time, μsec	$\bar{V}_c$	V_c*	V_c/V_w
5	0.22	5.70	5.70	1.05
10	0.45	5.55	5.45	1.03
15	0.68	5.50	5.25	1.01
20	0.93	5.40	4.80	0.96
30	1.53	4.90	4.10	0.86
40	2.15	4.65	4.00	0.88
50	2.80	4.45	3.85	0.88

* From $\Delta S/\Delta t$ data.

creasing the gap a single card at a time. Unfortunately, this has not yet been done accurately although a number of average shock velocity measurements ($\bar{V}_c$) were made in the pentolite series 3 permitting one to estimate $(\rho V)_c/(\rho V)_w$ with fair reliability (Table 2).

In supplying free surface and shock velocity data one uses the equation

$$p \doteq \rho_1 V U \qquad [4]$$

where

ρ_1 = initial density of the medium
U = particle velocity and equal to $V_f/2$

Results obtained at Institute of Metals and Explosives Research by this method for V and V_f are presented in Fig. 5 and provide the necessary $p(V)$ calibration for water over the required range of pressures for application to the card-gap test.

Application of the $p(V)$ data of (13) permit the $V_w(n)$ curves of Figs. 3 and 4 to be converted to the desired $p_w(n)$ curves of Figs. 5 and 6, thereby providing direct calibrations of the various donor card-gap systems in terms of the actual initial pressure of the shock waves from these shock-generator systems as they enter the aquarium. However, it is desirable in applying these results to know also the initial shock pressures in a receptor. To accomplish this one must also know $(\rho V)_r$, the initial shock impedance of the receptor. This can also be measured by the streak camera by backlighting through the receptor (if it is transparent), since detonation occurs only after a time τ and at a distance S_2 into the charge, or by immersion of the entire assembly into an aquarium (if it is opaque). Then the initial shock pressure p_r in the receptor may be computed from the equation

$$p_r = \frac{p_w\,[1 + (\rho V)_c/(\rho V)_w]}{1 + (\rho V)_c/(\rho V)_r} \qquad [5]$$

Since p_r/p_w is somewhat insensitive to $(\rho V)_c$ in the first place and $(\rho V)_c/(\rho V)_w$ does not deviate a great deal from unity anyway, in the shock pressure range of interest here Equation [5] may be approximated as

$$p_r \doteq \frac{2p_w}{1 + (\rho V)_w/(\rho V)_r} \qquad [6]$$

Significant results were obtained by the application of Equation [3] and measured $p_w(n = 0)$ and $V_w(n = 0)$ data in determining the peak pressure in the detonation wave of the donor itself. Note from the results in Table 1 that the measured pressures p_e for the explosive agreed closely with the calculated ideal detonation pressures p_2 whenever conditions were such as to cause ideal detonation; otherwise they were lower. This method for measuring the peak pressure in the detonation wave is not complicated by mass motion of the medium as in measurements of free surface velocity with thin plates and massive charges (18) because the aquarium may be made sufficiently massive so that no such mass motion occurs. The absence of a pressure *spike* is therefore noteworthy (19); the aquarium method seems to provide evidence that $p_e/p_2 \leq 1.0$ in all cases, p_e/p_2 being unity (within the accuracy of ±6 per cent of the aquarium method) for ideal detonation and less than unity for non-ideal detonation [see also (13)]. The basis used here for deciding whether or not the detonation was ideal was the experimental one mentioned, namely that for ideal detonation, detonationary increase in charge size (length or diameter) did not change the initial shock velocity in water.

It is of interest in studying the mechanism of the card-gap test to consider how p_r data determined by the aquarium method may be used to obtain fundamental information on the basic explosive sensitivity parameters. Besides Q, these are the enthalpy of activation $\Delta H^{\ddagger}$ and the entropy of activation $\Delta S^{\ddagger}$; the influence of initial temperature T_r on the rate of reaction and the time lag t' to explosion following shocking of the liquid are known largely in terms of these basic parameters. That is, impact sensitivity has been shown to involve basically adiabatic thermal decomposition (8,20). The shock heating of a liquid by the donor card-gap system brings the explosive initially to the temperature T_r given by

$$T_r = (p_e + p_1)(v_1 - v_e)/2\bar{C} + T_1 \qquad [7]$$

This equation is based simply on the fact that the shock energy is $1/2(p_e + p_1)(v_1 - v_e)$, and the temperature increase is the shock energy per average heat capacity. Using the average compressibility $\bar{\beta}$ and average heat capacity $\bar{C}$, one then obtains from Equation [7] and the definition of compressibility

$$T_r = p_r^2 v_1 \bar{\beta}/2\bar{C} \qquad [8]$$

neglecting p, and taking $\beta p v_1 = v_1 - v_e$. (Eq. [7] may, however, be applied directly once the ratio U/V $(=1 - v_2/v_1)$

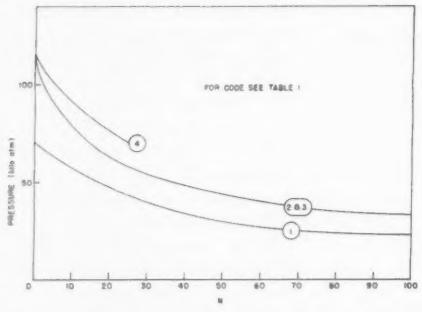

Fig. 5 Initial (water) shock pressure vs. n for tetryl card-gap donor systems

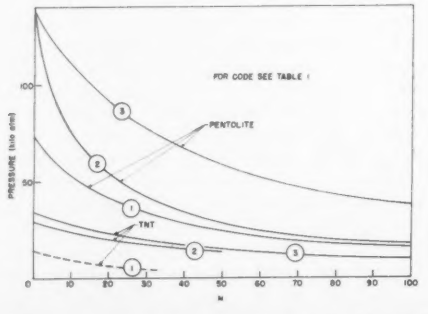

Fig. 6 Initial (water) shock pressure vs. n for fine TNT and cast 50/50 pentolite card-gap donor systems

is known. In this case $\bar{C}$ may also be obtained directly, since the equation of state is then also known.) Explosion should result by exothermic chemical reactions beginning at the temperature T_r and finally reaching the explosion level at the time t' given by (8).

$$\log t' = A/T_r + B \quad [9]$$

where

$$A = \Delta H^{\ddagger}/2.3\,R \quad [10]$$

and

$$B = \log_{10} Ch e^{-\Delta S^{\ddagger}/R} R T_r/Qkf\,\Delta H^{\ddagger} \quad [11]$$

where h and k are Planck's and Boltzmann's constants, and f is a function expressing the order of the decomposition reaction. The initial temperature T_r in the receptor should, in general, be considerably higher in the card-gap test for $n \leq n^*$ than the initial (hot spot) temperatures developed in the usual impact test. This results in much shorter initiation time lag. Although in these considerations it is tacitly assumed that the same adiabatic thermal decomposition laws apply in the card-gap test as in the conventional impact tests, still it will be of considerable interest in connection with the theory of the card-gap test to determine by means of the aquarium method whether the initial T_r (or p_r) alone is the important factor or whether total initial impulse must also be considered.

Acknowledgments

The authors express their appreciation to Dr. F. R. Balcar, G. A. Mead and J. Helck, Air Reduction Co., for valuable discussions and suggestions, and to A. Bauer, graduate student, University of Utah, and M. G. Cook, Intermountain Research and Engineering Co. for assistance in obtaining streak camera records and reducing the data presented in this article.

References

1 "Blasters' Handbook," E. I. du Pont de Nemours, Co., Wilmington, Del., 1958, 14 ed., p. 53.

2 Mood, A. M., "Introduction to the Theory of Statistics," McGraw-Hill Book Co., Inc., N. Y., 1950.

3 Dixon, W. J. and Massey, F. J., "Introduction to Statistical Analysis," McGraw-Hill Book Co., Inc., N. Y., 1951.

4 Office of Scientific Research and Development, Rep. 4040 (AMP Rep. no. 101.R), "Statistical Analysis for a New Procedure in Sensitivity Experiments," Statistical Research Group, Princeton University, Applied Mathematics Panel, July 1944.

5 Dixon, W. J. and Mood, A. M., "A Method for Obtaining and Analyzing Sensitivity Data," *J. Amer. Statistical Assoc.*, vol. 43, 1948, p. 109.

6 Grant, R. L. and Van Dolah, R. W., "Application of Statistics to Explosives Testing," Fourth Annual Symposium on Mining Research," University of Missouri, School of Mines and Metallurgy, Rolla, Mo., Nov. 13–15, 1958.

7 ARS Committee on Monopropellant Methods, Recommended Test no. 1, "Card-Gap Test for Shock Sensitivity of Liquid Monopropellants," American Rocket Society, New York, July 1955.

8 Cook, M. A., "The Science of High Explosives," Reinhold Publishing Corp., N. Y., 1958.

9 Cashia, C. P. and Whitbread, E. G., "The Initiation of Explosives by Shock," Proc. Roy. Soc., vol. A246, no. 1245, 1948, pp. 268–273.

10 Lampson, C. W. and Eichelberger, R. J., "Sympathetic Detonation and Initiation by Impact," Proc. Roy. Soc., vol. A246, no. 1245, 1948, pp. 274–281.

11 Cook, M. A., Pack, D. H. and Gey, W. A., "Deflagration to Detonation Transition," Proc. Roy. Soc., vol. A246, no. 1245, 1948, pp. 281–283; *also* "Seventh Symposium (International) on Combustion," Butterworth's Scientific Publications, London, 1959, pp. 820–836.

12 Cook, M. A., Pack, D. H., Cosner, L. N. and Gey, W. A., "Instrumented Card-Gap or SPHF-Plate Test," *J. Appl. Phys.*, vol. 30, no. 10, Oct. 1959, pp. 1579–1584.

13 Cook, M. A., Pack, D. H. and McEwan, W. S., "Promotion of Shock Initiation of Detonation by Metallic Surfaces," Trans. Faraday Soc., vol. 56, no. 451, Part 7, July 1960, pp. 1028–1038.

14 Clay, R. B., Cook, M. A., Keyes, R. T. and Shupe, O. K., "Trapped Detonation Initiation Waves," paper presented at the Honolulu meeting of American Physical Society, Aug. 1959.

15 Cook, M. A., Keyes, R. T. and Ursenbach, W. O., "Measurements of Detonation, Shock and Impact Pressures," paper presented at Third ONR Symposium on Detonation, Princeton University, Sept. 27, 1960.

16 Jones, A. and Mitchell, D., "Spread of Detonation in High Explosives," *Nature*, vol. 161, no. 4081, 1948, p. 98.

17 Walsh, J. M. and Christian, R. H., "The Equation of State of Metals from Shock Wave Measurements," *Phys. Rev.*, vol. 97, no. 6, 1955, p. 1544.

18 Cook, M. A., "Note on the Theory of the 'Free Surface Velocity Method'," Discussion of the Faraday Society, Glasgow, Sept. 1956.

19 Cook, M. A., Filler, A. S. and Keyes, R. T., "Mechanism of Detonation," Trans. Faraday Soc., vol. 52, no. 399, Part 3, 1956, p. 369

20 Bowden, F. P. and Yoffe, A. D., "Fast Reactions in Solids," Academic Press, Inc., N. Y., 1958.

Experimental Results With a Collinear Electrode Plasma Accelerator and a Comparison With Ion Accelerators

W. L. STARR[1] and
S. W. KASH[2]

Lockheed Aircraft Corp.
Sunnyvale, Calif.

A collinear electrode plasma accelerator using either plasma derived from an exploding wire or from electrode erosion has been in operation for some time. Maximum particle velocities approaching 10^7 cm per sec and impulses of 2×10^3 dyne·sec have been achieved. Effective specific impulses, computed from measured impulse and propellant mass, greater than 2000 sec have been obtained for the exploding wire measurements. For certain conditions of operation, the efficiency is greater than 30 per cent. Efficiencies of 50 per cent or more should be possible. The practicality of deriving the plasma by electrode erosion is demonstrated, and effective specific impulses of about 6000 sec are indicated.

SEVERAL ways have been suggested for the electromagnetic acceleration of ionized material for propulsive purposes. Two ways which seem most promising at present and are receiving the most attention are ion drive and plasma drive. Because these devices differ in some important aspects and because of the still limited amount of critical experimental data, it is difficult to conclude with certainty which type of device will ultimately prove to be superior. It is not unlikely that each type will be useful for some particular application.

In an ion drive device, positive ions, quite likely produced by surface ionization, are accelerated by static electric fields. Electrons or negative ions (1)[3] must be added to the accelerated positive ion beam to provide overall charge neutrality and maintain proper functioning of the accelerator.

In a plasma drive device, neutral plasma is accelerated by rapidly varying magnetic fields. These fields may result from large currents developed in a plasma discharge by externally applied voltages. The plasma itself can be produced by the action of the discharge.

Ion accelerators are conceptually simpler than plasma accelerators, and considerable experience with ion and electron guns exists. Possibly because of these reasons the ion drive device has received the greater attention. However, ion accelerators designed for terrestrial purposes are not particularly satisfactory for space application, and considerable effort will be required to develop an ion accelerator suitable for space propulsion. Considerable effort is also required for the development of a suitable plasma accelerator. Nevertheless, plasma drive offers several distinct advantages over ion drive, which conceivably could lead to the development of an earlier operating plasma device. For a detailed discussion on the comparison of ion and plasma propulsion see (2).

Because of the relative complexity of the interaction of magnetic fields and plasma and the resulting variety of plasma accelerator configurations, experiments are needed to determine the design of suitable plasma drive devices. The Plasma Physics Department of Lockheed's Missiles and Space Division has been engaged for a considerable time in experiments involving plasma acceleration (3–5), and measurements are being made with several different plasma accelerators. The results of impulse measurements with one of these accelerators are presented in this paper.

Presented at the ARS 14th Annual Meeting, Washington, D. C., Nov. 16–20, 1959.

[1] Research Scientist, Plasma Physics Dept., Missiles and Space Div.

[2] Manager, Plasma Physics Dept., Missiles and Space Div.

[3] Numbers in parentheses indicate References at end of paper.

Description of the Apparatus

Fig. 1 presents a schematic of the collinear electrode plasma accelerator. In essence the device consists of a pair of collinear discharge electrodes connected to a low inductance, high energy capacitor. The leads between the condenser and the electrodes are arranged to keep the inductance of the discharge circuit as low as possible and also to orient the direction of the discharge forces.

In operation, the region around the electrodes is evacuated and the condenser is charged to a high voltage. A discharge is initiated by the introduction of plasma between the electrodes. The plasma in the discharge is then accelerated by the magnetic fields produced by the large current in the discharge and the nearby circuit elements. The magnetic field of the opposing current in the lead paralleling the discharge provides the direction and principal force for the acceleration of the plasma. Additional acceleration is provided through ohmic heating; however, this is more or less omni-directed, and decreases in importance as the plasma is heated in the discharge.

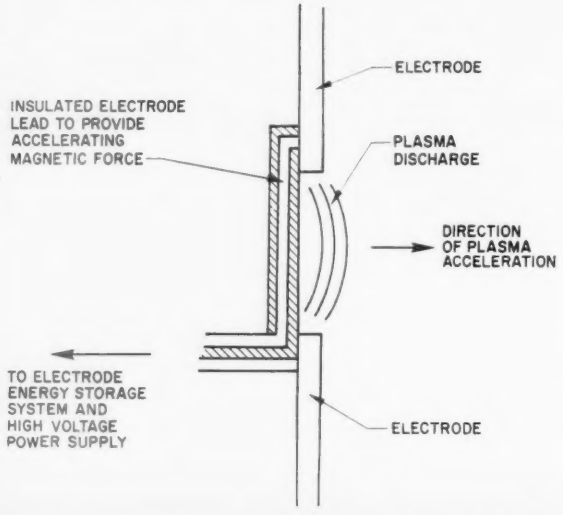
ELECTRODE
INSULATED ELECTRODE LEAD TO PROVIDE ACCELERATING MAGNETIC FORCE
PLASMA DISCHARGE
DIRECTION OF PLASMA ACCELERATION
TO ELECTRODE ENERGY STORAGE SYSTEM AND HIGH VOLTAGE POWER SUPPLY
ELECTRODE

Fig. 1 Schematic diagram of the collinear electrode plasma accelerator

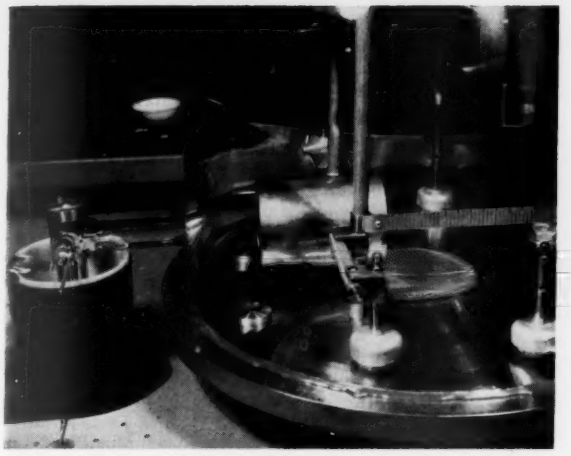

Fig. 2 Laboratory model of the collinear electrode accelerator. The electrode tube is sealed into the evacuated bell jar housing the ballistic pendulum

For one set of measurements the plasma for the discharge was produced by exploding a fine wire mounted between the electrodes at right angles to the plane of the discharge circuit. In a second set of measurements to be discussed later, the discharge was initiated by the introduction of a minute amount of gas between the electrodes, the major portion of the plasma supplied by the electrodes themselves.

Figs. 2 and 3 are pictures of the equipment employed for the exploding wire measurements. To facilitate replacement of the wire the electrode assembly was mounted outside an evacuated bell jar, directed to fire into a ballistic pendulum inside the bell jar. The electrodes were connected to a 1.1-μf, 30-kv condenser located directly beneath. The vaporization of the fine wire was accomplished by discharging a 3-kv capacitor through it. The ballistic pendulum consisted of a sheet copper cylinder, weighing 47 gm, open at one end and supported by four 22.5-cm long fine wires. It provided a sensitivity of about 310 dyne·sec per cm of horizontal travel. The electrodes were $\frac{1}{4}$ in. in diameter and were spaced about 5 cm apart. The distance between the lead to the upper electrode and the electrode gap was about 1 cm. Additional details are given in (3).

Measurements With the Exploding Wire System

A number of firings were made with different material and different diameter wires, and impulses of about 1000 dyne·sec per firing were measured. Maximum plasma velocities of about 8×10^6 cm per sec were measured by an electronic camera. It soon became apparent from photographs of the discharge (see Figs. 4 and 5) and from the deposit of material on the floor of the bell jar, that a considerable amount of ejected material was lost to the ballistic pendulum. A new pendulum curved and tapered in the form of a light trap was built and installed; see Fig. 6. In addition, the distance between the electrodes and the pendulum was shortened from about 10 to 3.5 cm.

Impulse measurements made with the apparatus described, mass of the wire vaporized and the specific impulse determined from the impulse and wire mass are shown in Table 1. It is important to note that the values listed for the specific impulse are not those determined by a streak camera or photomultipliers. Although such measurements have also been made, they record the fastest luminous plasma particles, and usually give velocities between 5 and 10 cm per microsec.

The last column in Table 1 presents the efficiency obtained by comparing the kinetic energy of the ejected plasma with the initial energy stored in the main condenser. The kinetic

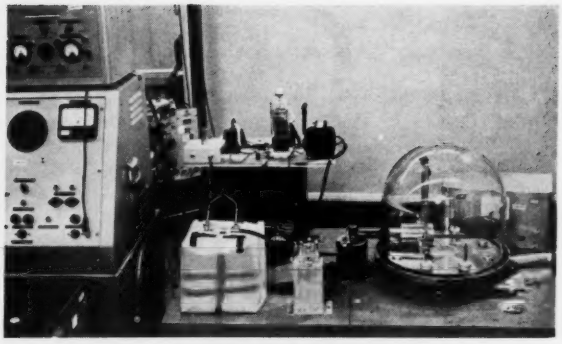

Fig. 3 Main components of the experimental system

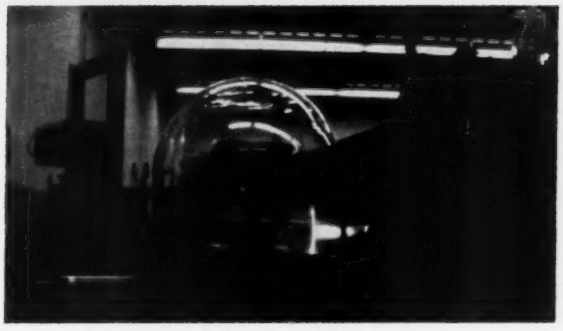

Fig. 4 Time-integrated picture showing plasma impinging on the pendulum

Fig. 5 Time-integrated picture of the accelerated plasma with the pendulum removed

Table 1 Results of impulse measurements

Wire size	Measured impulse,[a] dyne·sec	Mass of wire, mg	Effective specific impulse, sec	Efficiency, per cent
1 mil platinum	1380	0.90	1530	21
5 mil Nichrome	1620	6.4	260	4
1 mil tungsten	1800	0.83	2210	39
2 mil tungsten	1750	3.3	540	9
5 mil Nichrome	1750	6.4	279	5

[a] For the first two measurements the electrodes were about 10 cm from the pendulum; for the latter three measurements the distance was reduced to about 4 cm.

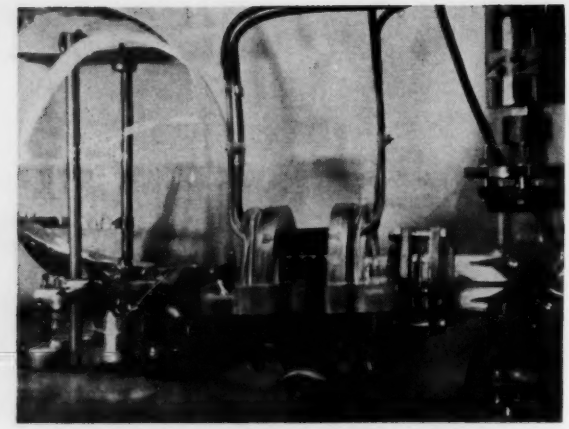

Fig. 6 "Light trap" ballistic pendulum used for impulse measurements. (The equipment in front of the pendulum is part of another experiment)

energy was computed from the mass of the wire and the average velocity. This is somewhat on the conservative side, since the square of the average velocity is less than the average of the square. As can be seen, the smaller size wires yield greater specific impulses and greater efficiency.

To determine how much, if any, of the impulse imparted to the ballistic pendulum resulted from an interaction of the magnetic fields of the discharge and induced currents in the pendulum, a glass plate was inserted in front of the pendulum and the system was fired. No motion was produced in the pendulum. After several firings a fair amount of material was deposited on the glass plate, but at the same time considerable glass was eroded, so that after six firings the plate weighed about 1 mg less than it did initially. There is some uncertainty about how much of the mass is accelerated in a single firing. Weighings of material deposited in the pendulum were about 1 mg more than the weight of the vaporized wire, which would indicate a somewhat lower plasma velocity and energy conversion efficiency. The additional mass is a result in part of material eroded off the glass tube between the electrodes and the bell jar, and in part of material sputtered off the electrodes. This extra mass is in part compensated for by the loss to the ballistic pendulum of mass deposited out on the connecting glass tube. The latter loss transfers momentum to the glass and probably decreases the measured values of the impulse. This is certainly indicated by the smaller values for the impulse obtained when the electrodes were further from the pendulum.

Joule heating undoubtedly contributes somewhat to the impulse, although the amount is difficult to determine. The resistance of a plasma decreases rapidly with temperature, and ohmic heating quickly becomes less effective. A check was made of the impulse produced by the vaporization of the propellant wire itself, that is, without any energy in the main condenser. The resulting impulse was less than 10 per cent of that with the voltage applied to the electrodes.

If one looks end on at the collinear electrode plasma accelerator the area is about 15 cm^2, so that the impulse per unit area per firing is of the order of 100 dyne·sec per cm^2. Thus, when fired once per second it produces a per-unit-area thrust equivalent to that of a 2000-v ion gun with about a 2-mm interelectrode spacing (1). At a firing rate of only once per second the accelerator used in this experiment produces a thrust equivalent to about 700 2000-v Pierce-type ion guns.

Measurements With the Expendable Electrode System

Experiments with ion guns and gaseous discharge (6,7) have demonstrated the seriousness of the problem of erosion. It is to be expected that plasma drive devices will also suffer from the effects of erosion, and experiments have been planned for the determination of these effects. For certain plasma drive designs erosion can be structurally almost as serious as for the ion drive case, although secondary effects, such as the coating of insulating supports, can probably be avoided.

An important feature of the plasma drive device described in this paper is the possibility it offers utilizing the erosion to provide the plasma propellant. With this in mind a modification of the collinear electrode plasma accelerator has been built, and measurements with it made. In the modified system the exploding wire used to generate the plasma was eliminated, and instead the discharge was triggered by the introduction of a small amount of gas through one of the electrodes. Argon gas was stored in a small annular chamber in a piston mounted over the upper electrode. The reciprocating action of the piston admitted the argon through a 3-mm diameter inlet hole in the upper electrode. The volume of the annular chamber was 0.3 cm^3, and the amount of gas released was controlled by varying the pressure in the main argon supply.

The impulse measurements obtained are shown in Tables 2 and 3. Table 2 shows the effect on the impulse of varying the amount of argon admitted. For small amounts of triggering gas the impulse is independent of the amount of gas introduced. As little as 6 μgm of gas was sufficient to trigger the discharge. Since this represents only a few per cent of the amount of gas ejected during the discharge, the propellant is provided almost entirely by material obtained from the nickel electrodes. The gas was admitted somewhat slowly into the discharge region, and quite likely the main discharge phenomena was over before all of it had escaped. If the gas had been admitted more rapidly, an even smaller amount would have been sufficient. There was no measurable impulse when the gas was introduced without the capacitor being charged. In other studies (8), triggering mechanisms employing plasma injection have been utilized.

Since the mass of the material eroded is proportional to the number and the energy of the particles incident on the electrodes, the total propellant mass is proportional to the time integral of the product of the voltage and current. Now, the impulse is the time integral of the force, and the force varies as the square of the current. The instantaneous current and voltage can be expressed as products of the initial voltage and functions involving time and the circuit parameters only.

Table 2 Variation of impulse with mass of triggering gas

Condenser voltage, kv	Mass of gas, μgm	Measured impulse, dyne·sec
30	5.9	640
30	59	640
30	295	700

Table 3 Variation of impulse with voltage and energy of the electrical storage condenser

Condenser voltage V, kv	Measured impulse I, dyne·sec	I/V^2 (arbitrary units)	CV^2/I, cm/sec
15	160	0.711	15.5×10^6
20	320	0.800	13.8
25	416	0.655	16.8
32	832	0.812	13.5
35	960	0.783	14.0

Thus, both the total mass eroded and the impulse are proportional to the square of the initial voltage. Hence the effective velocity, which is defined as the ratio of the impulse to the total mass, is a constant independent of the voltage. The velocity can be varied by changing the electrode material or altering the electrode geometry. The thrust itself can be changed by varying the voltage and/or the firing rate.

The experimental results as presented in the third column of Table 3 do in fact show that the impulse is proportional to the square of the initial voltage. It should also be noted that since the stored energy is also proportional to the square of the initial voltage, the efficiency of the system is also independent of the voltage. Column four of Table 3 gives the effective plasma velocity for an efficiency of 100 per cent. For an assumed efficiency of 40 per cent the effective velocity is 6×10^6 cm per sec. Higher efficiencies should be possible by improved design. Velocities above 10^7 cm per sec should also be achievable by additional improvements of the equipment.

For the 35-kv firing and a velocity of 6×10^6 cm per sec, the propellant mass eroded from the nickel electrodes is about 160 μgm. With less than 6 μgm of gas needed to trigger the discharge, over 96 per cent of the propellant is provided by the electrodes.

The experiments have demonstrated the feasibility of utilizing metal-derived plasmas in pulsed accelerators. Present experiments in which all of the mass is derived by erosion are producing plasma accelerators capable of firing at relatively rapid rates for many hours and yielding thrusts of about 200 dynes per accelerator. These experiments are limited by equipment auxiliary to the accelerator; higher thrusts are certainly possible. Deriving the plasma from expendable electrodes has obvious advantages.

The authors wish to express their appreciation to G. Brooks for his assistance in conducting these experiments.

References

1 Gilleo, M. A. and Kash, S. W., "Propulsion by Composite Beams of Negative and Positive Ions," ARS preprint 1157-60, May 1960.
2 Kash, S. W., "A Comparison of Ion and Plasma Propulsion," Proc. IRE, vol. 47 April 1960, pp. 458–465.
3 Starr, W. L., "A Propulsive Device Using an Exploding Wire Plasma Accelerator," in "Exploding Wires," Plenum Press, Inc., N. Y., 1959, pp. 365–373.
4 Kash, S. W., "Experiments at Lockheed Missile Systems Division," in "Magnetohydrodynamics," Stanford University Press, 1957, pp. 92–98.
5 Kash, S. W., Gauger, J., Starr, W. L. and Vali, V., "Velocity Measurements in Magnetically Driven Shock Tubes," in "Plasma in a Magnetic Field," Stanford University Press, 1958, pp. 99–109.
6 Massey, H. S. W. and Burhop, E. H. S., "Electronic and Ionic Impact Phenomena," Oxford Press, London, 1952, pp. 578–594.
7 Naiditch, S., "Experimental Ion Sources for Propulsion," ARS preprint 883-59, June 1959.
8 Starr, W. L. and Naff, J. T., "Acceleration of Metal Derived Plasmas," in "Plasma Acceleration," Stanford University Press, 1960, pp. 47–59.

Dissociation Effects Upon Compressible Turbulent Boundary Layer Skin Friction and Heat Transfer

WILLIAM H. DORRANCE[1]

Convair Div.,
General Dynamics Corp.
San Diego, Calif.

The equations for skin friction and heat transfer associated with a dissociating, compressible, turbulent boundary layer are derived from the appropriate boundary layer equations making a minimum number of assumptions. The equations of momentum, energy, conservation of mass and species and state are briefly derived taking proper account of terms contributed by turbulent fluctuations. A sublayer-turbulent layer model is assumed in order to obtain the heat transfer coefficient to skin friction coefficient ratio for Lewis number not equal to 1. The conditions under which dissociation equilibrium concentrations apply, on one hand, or diffusion controlled concentrations apply, on the other hand, are examined, and it is shown that the use of diffusion controlled concentrations are quite appropriate for calculating skin friction coefficient for most cases of interest. The diffusion controlled concentration profile is then used in combination with the energy and state equations and the Kármán momentum integral to obtain skin friction coefficients for a flat plate. Prandtl number and Lewis number are assumed equal to 1 in this latter calculation only. It is shown that the skin friction coefficients obtained are in excellent agreement with recent measurements by Coles and Matting, Chapman, Nyholm and Thomas. Agreement with the heat transfer measurements of Rose, Probstein and Adams with dissociation present is also shown. Curves of local skin friction coefficient are presented for local Mach numbers from zero to 4 and degrees of dissociation at the surface or in the external stream of from zero to complete dissociation. The equations for calculating local heat transfer rates are given.

Presented at the ARS Semi-Annual Meeting, Los Angeles, Calif., May 9–12, 1960.
[1] Senior Staff Scientist, Scientific Research Laboratory. Member ARS.

IN RECENT years the problem of convective and diffusive heat transfer from a hot dissociating boundary layer to a cooler surface has received considerable attention with particular reference to design problems attendant upon hypervelocity atmospheric re-entry vehicles. As might be anticipated, the laminar boundary layer heat transfer theory has received most exhaustive treatment despite the fact that under several circumstances of direct concern to designers a turbulent boundary layer is more likely to prevail. Since a rigorous theory for the turbulent boundary layer without dissociation present is yet to be presented, there is no reason to suppose the turbulent boundary layer would lend itself to exact analysis when the complicating effects of gas dissociation are present.

The heat transfer from a dissociating laminar boundary layer to a cool surface may be said to be fairly well understood. Fay and Riddell (1),[2] Lees (2) and Kemp (3) et al., among others, have brought out the effects of dissociation, and various departures from equilibrium dissociation, of the boundary layer gas upon the classical laminar boundary heat transfer equations. At this time it appears that the principal uncertainty in applying the results of these authors lies in the accuracy of the calculated values of the transport coefficients of gases at the high temperatures of interest (4, 5).

Until the present paper, no attempt to calculate heat transfer from a dissociating turbulent boundary layer to a cool surface proceeding from first principles has been presented. Van Driest (6) presented an analysis of the nondissociating compressible turbulent boundary layer over a flat plate which is included within the framework of the present theory when $P = 1$, no dissociation occurs, and certain approximations not used herein are incorporated in the present work. Hidalgo (7), using a plausible assumption relating density to enthalpy through the boundary layer, modified Van Driest's formula to account for the effects of dissociation upon Van Driest's skin friction equation for the case where the boundary layer is assumed to be in dissociation equilibrium. Lees (8), proceeding from Prandtl's modification of Reynolds analogy, developed an expression for turbulent boundary layer convective heat transfer for Lewis numbers other than and including unity but with heat transfer coefficient undetermined. Rose (9) et al. developed essentially the same expression as Lees (8) for the dissociated turbulent boundary layer heat transfer, and with some valuable experimental data were able to empirically establish an assumed expression for heat transfer coefficient. In none of these analyses were heat transfer and skin friction equations developed starting from the appropriate boundary layer equations proceeding through their integration with a minimum of assumptions and qualifications.

The appearance recently of several careful direct measurements of skin friction and heat transfer at supersonic Mach numbers (10–14) and the state of affairs sketched in the previous paragraph led the author to consider approaching the calculation of skin friction and heat transfer from a dissociating compressible turbulent boundary layer to a flat plate, proceeding step by step from the appropriate boundary layer equations. As in the past, it was found that several simplifying assumptions had to be made. The expressions for skin friction and heat transfer finally derived are found to agree with the experimental data remarkably well, possibly better than does any alternative formulation. Because the theory and experiment do agree well, calculations of local skin friction coefficient were performed, using a 704 computer, for a wide range of Mach numbers, Reynolds numbers, heat transfer and dissociation conditions, and the results are presented herein.

[2] Numbers in parentheses indicate References at end of paper.

Development of Theory

The equations of change and state for the flow of a compressible dissociating turbulent boundary layer over a flat plate will be derived first. The case of the flat plate was chosen because of its geometric simplicity, the wealth of experimental data available for comparison and because of its probable direct applicability to surfaces over which a turbulent boundary layer is apt to be flowing (wing surfaces and near-cylindrical surfaces). With appropriate modifications the results can also be used with conical surfaces and, probably, with most surfaces of moderate curvature and pressure gradient. Throughout the development that follows the following assumptions will apply:

1 The geometry being treated is that of two-dimensional flow over a flat plate.

2 The boundary layer equations of motion apply and the flow is in a steady state.

3 The dissociating gas is assumed to be a mixture of perfect gases. For simplicity air will be approximated as a mixture of one species of atoms and one species of molecules.

4 The gas stream external to the boundary layer is in dissociation equilibrium.

Assumptions 1 and 2 are commonly accepted formalities. Assumption 3 has already been used successfully by Fay and Riddell (1) and Lees (2) in treating the laminar boundary layer, and by Hansen (5) and Scala and Baulknight (15) in computing thermodynamic and transport properties of high temperature air in equilibrium. Assumption 4 can be shown to be reasonable for the high temperatures and high densities in the external streams of interest to us here (16). Further assumptions will be made and, where possible, justified as the analysis proceeds.

Equations of Change and State

The appropriate equations for the problem at hand can be developed from the equations already developed in treating the laminar boundary layer. See for example, (1) or (8). These equations are:

Equation of state

$$p = \sum_i p_i \qquad [1a]$$

$$p_i = \rho_i (k/m_i) T \qquad [1b]$$

Continuity of species

$$\rho u \frac{\partial c_i}{\partial x} + \rho v \frac{\partial c_i}{\partial y} = -\frac{\partial (\rho c_i V_{i,y})}{\partial y} + \rho \frac{\partial c_i}{\partial t} \qquad [2a]$$

where, from Fick's Law and by adopting assumption 3[3]

$$\rho c_i V_{i,y} = -\rho D_{12} (\partial c_i / \partial y) \qquad [2b]$$

$$c_i = (\rho_i / \rho) \qquad i = 1, 2 \qquad [2c]$$

Thermal diffusion is neglected at the temperatures of interest herein, a reasonable assumption as was shown by Lees (8).

Continuity of mass

$$\frac{\partial \rho u}{\partial x} + \frac{\partial \rho v}{\partial y} = 0 \qquad [3]$$

Conservation of momentum

$$\rho u \frac{\partial u}{\partial x} + \rho v \frac{\partial u}{\partial y} = \frac{\partial}{\partial y} (\tau) \qquad [4a]$$

where

$$\tau = \mu (\partial u / \partial y) \qquad [4b]$$

$$dp = 0 \qquad [4c]$$

[3] The term $\rho \, \partial c_i / \partial t$ (later $\rho \, \partial \alpha / \partial t$) is the rate of production of species i owing to chemical reactions occurring upon collisions between atoms or molecules and molecules. It is *not* the Eulerian increase in mass per unit time.

A contribution to shear stress owing to the product of orthogonal diffusion fluxes can be shown to be of the order of R_e^{-1} relative to the remaining term in Equation [4b], and can reasonably be neglected as can the contribution of diffusion fluxes in the energy equation for the same reason.

Conservation of energy

$$\rho u \frac{\partial H}{\partial x} + \rho v \frac{\partial H}{\partial y} = \frac{\partial}{\partial y}\left[\left(\frac{\mu}{P}\frac{\partial H}{\partial y}\right) + \mu\left(1 - \frac{1}{P}\right)\frac{1}{2}\frac{\partial u^2}{\partial y}\right] + \frac{\partial}{\partial y}\left[\left(\frac{1}{L} - 1\right)\sum_i \rho_i V_{i,y} h_i\right] \quad [5]$$

and $H = h + u^2/2$ where

$$h = \sum_i c_i h_i \quad [6a]$$

$$h_i = \int_0^T c_{p_i} dT + h_i^\circ \quad [6b]$$

This completes our boundary layer equations for the flow of a reacting gas over a flat plate.

The development of the turbulent boundary layer equations proceeds in the familiar fashion. Assume each independent variable in the above equations is the sum of a mean value and a fluctuating value (primed)

$$Q = \bar{Q} + Q' \qquad \frac{1}{t}\int_0^t Q'dt \equiv 0 \qquad \frac{1}{t}\int_0^t Q dt \equiv \bar{Q}$$

then, introduce

$$\begin{aligned} u &= \bar{u} + u' \\ \rho u &= \overline{\rho u} + (\rho u)' \\ \rho v &= \overline{\rho v} + (\rho v)' \\ h &= \bar{h} + h' \\ c_i &= \bar{c}_i + c_i' \\ h_i &= \bar{h}_i + h_i' \end{aligned}$$

into the foregoing equations (first combined in order to put all dependent variables under differentiation), perform the time averaging operation indicated, and drop the lesser terms in the inequalities given in the following from the resulting differential equations when the larger quantities appear with them in the equations. This latter step is consistent with the concept of a thin turbulent boundary layer

If, in addition we adopt assumption 3 stated earlier, we have

$$\sum_i c_i = c_1 + c_2 = 1 = \alpha + (1 - \alpha) \quad [7]$$

and from this point on $\alpha = c_1$ denotes the atomic species, and $(1 - \alpha) = c_2$ denotes the molecular species. Therefore, from Equation [2b]

$$\rho_1 V_{1,y} = -\rho D_{12}\frac{\partial c_1}{\partial y} = -\rho D_{12}\frac{\partial \alpha}{\partial y} \quad [8a]$$

$$\rho_2 V_{2,y} = -\rho D_{12}\frac{\partial c_2}{\partial y} = \rho D_{12}\frac{\partial \alpha}{\partial y} \quad [8b]$$

and if, also, we introduce the turbulent eddy viscosity, conductivity and diffusion coefficients as

$$\epsilon(x, y) = \frac{\overline{-(\rho v)'u'}}{\partial \bar{u}/\partial y} \quad [9]$$

$$\kappa(x, y) = \frac{\overline{-(\rho v)'h_i'}}{\partial \bar{T}/\partial y} \quad [10]$$

$$D_T(x, y) = \frac{\overline{-(\rho v)'c_i'}}{\bar{\rho}(\partial \bar{c}_i/\partial y)} \quad [11]$$

and if we define a (frozen mixture) specific heat as

$$\bar{c}_p = \sum_i \bar{c}_i c_{p_i} = \bar{\alpha} c_{p_1} + (1 - \bar{\alpha}) c_{p_2} \quad [12]$$

which with Equations [6a, 7 and 12] can be combined to give

$$\frac{d\bar{T}}{dy} = \frac{1}{\bar{c}_p}\left[\frac{\partial \bar{h}}{\partial y} - (\bar{h}_1 - \bar{h}_2)\frac{\partial \bar{\alpha}}{\partial y}\right] \quad [13]$$

Then all of the foregoing can be used to arrive at the turbulent boundary layer equations. These are

$$\overline{\rho u}\frac{\partial \bar{\alpha}}{\partial x} + \overline{\rho v}\frac{\partial \bar{\alpha}}{\partial y} = \frac{\partial}{\partial y}\left[\bar{\rho}(D_{12} + D_T)\frac{\partial \bar{\alpha}}{\partial y}\right] + \bar{\rho}\frac{\partial \bar{\alpha}}{\partial t} \quad [14]$$

$$\frac{\partial \overline{\rho u}}{\partial x} + \frac{\partial \overline{\rho v}}{\partial y} = 0 \quad [15]$$

$$\overline{\rho u}\frac{\partial \bar{u}}{\partial x} + \overline{\rho v}\frac{\partial \bar{u}}{\partial y} = \frac{\partial}{\partial y}\left[(\mu + \epsilon)\frac{\partial \bar{u}}{\partial y}\right] \quad [16]$$

and

$$\overline{\rho u}\frac{\partial \bar{h}}{\partial x} + \overline{\rho v}\frac{\partial \bar{h}}{\partial y} = \frac{\partial}{\partial y}\left[\left(\frac{\mu}{P} + \frac{\epsilon}{P_T}\right)\frac{\partial \bar{h}}{\partial y}\right] + \frac{\partial}{\partial y}\left\{\left[\frac{\mu}{P}(L - 1) + \frac{\epsilon}{P_T}(L_T - 1)\right](\bar{h}_1 - \bar{h}_2)\frac{\partial \bar{\alpha}}{\partial y}\right\} + (\mu + \epsilon)\left(\frac{\partial \bar{u}}{\partial y}\right)^2 \quad [17]$$

if

$$\bar{H} = \bar{h} + \bar{u}^2/2 \quad [18]$$

Equations [15, 16 and 17] can be combined to yield

$$\overline{\rho u}\frac{\partial \bar{H}}{\partial x} + \overline{\rho v}\frac{\partial \bar{H}}{\partial y} = \frac{\partial}{\partial y}\left[\left(\frac{\mu}{P} + \frac{\epsilon}{P_T}\right)\frac{\partial \bar{H}}{\partial y}\right] + \frac{\partial}{\partial y}\left\{\left[\frac{k}{\bar{c}_p}(L - 1) + \frac{\kappa}{\bar{c}_p}(L_T - 1)\right](\bar{h}_1 - \bar{h}_2)\frac{\partial \bar{\alpha}}{\partial y}\right\} + \frac{\partial}{\partial y}\left\{\left[\mu\left(1 - \frac{1}{P}\right) + \epsilon\left(1 - \frac{1}{P_T}\right)\right]\frac{1}{2}\frac{\partial \bar{u}^2}{\partial y}\right\} \quad [19]$$

$$\left|\overline{\rho u}\,\bar{u}\right| \gg \left|\overline{(\rho u)'u'}\right|$$
$$\left|\overline{\rho u}\,\bar{h}\right| \gg \left|\overline{(\rho u)'h'}\right|$$
$$\left|\overline{\rho u}\,\bar{c}_i\right| \gg \left|\overline{(\rho u)'c_i'}\right|$$
$$\left|\overline{\rho_i V_{i,y}}\,\bar{h}_i\right| \gg \left|\overline{(\rho_i V_{i,y})'h_i'}\right|$$
$$\left|\frac{\partial \bar{u}}{\partial y}\right| \gg \left|\frac{\partial \bar{u}}{\partial x}\right|$$
$$\left|\bar{c}_i\,\overline{(\rho v)'h_i'}\right|;\ \left|\bar{h}_i\,\overline{(\rho v)'c_i'}\right| \gg \left|\overline{c_i'h_i'(\rho v)'}\right|$$

It is immediately apparent that if $L = L_T = P = P_T \equiv 1$, then $\bar{H} = a\bar{u} + b$ from Equations [16 and 19], if surface enthalpy and free stream total enthalpy are such that $H \equiv H(u)$. This requires a constant wall temperature, for example.

Heat Transfer Coefficient and Recovery Factor

Recent measurements of hypersonic turbulent boundary

layer velocity profiles by Hill (14) indicate that the laminar sublayer-turbulent outer layer structure of the turbulent boundary layer persists in nondissociated compressible turbulent boundary layers up to Mach numbers of 8 to 10. Rubesin (17) has made use of this model of the structure of the turbulent boundary layer in the past to derive useful expressions for the recovery factor and a relation between skin friction and heat transfer coefficients for compressible, nondissociating, turbulent boundary layers. A procedure analogous to that used by Rubesin will be used here to develop similar expressions applicable when the boundary layer is dissociating.

To proceed, write Equation [19] as

$$\overline{\rho u}\frac{\partial \bar{H}}{\partial x} + \overline{\rho v}\frac{\partial \bar{H}}{\partial y} = \frac{\partial G}{\partial y} \qquad [20]$$

where, with the help of Equation [18]

$$G = \left(\frac{\mu}{P} + \frac{\epsilon}{P_T}\right)\frac{\partial \bar{h}}{\partial y} + \left[\frac{k}{c_p}(L-1) + \frac{\kappa}{c_p}(L_T - 1)\right] \times (\bar{h}_1 - \bar{h}_2)\frac{\partial \bar{\alpha}}{\partial y} + (\mu + \epsilon)\bar{u}\frac{\partial \bar{u}}{\partial y} \qquad [21]$$

$$G_w = -\dot{q}_w \qquad [22]$$

as can be found using Equation [21] with Equations [2b, 7 and 13].

Now the ratio of Equation [20] to [16] can be written

$$\frac{\overline{\rho u}\,(\partial \bar{H}/\partial x) + \overline{\rho v}\,(\partial \bar{H}/\partial y)}{\overline{\rho u}\,(\partial \bar{u}/\partial x) + \overline{\rho v}\,(\partial \bar{u}/\partial y)} = \frac{\partial G}{\partial \tau} \qquad [23]$$

where

$$\tau = (\mu + \epsilon)(\partial \bar{u}/\partial y) \qquad [24]$$

If it is assumed that $\bar{H} = a\bar{u} + b$, as it is when $P = P_T = L = L_T = 1$, then

$$\partial G/\partial \tau = a \qquad G = a\tau + c \qquad [25]$$

Now $G = G_w$ when $\tau = \tau_w$, and $G = 0$ when $\tau = 0$, hence

$$\frac{G}{\tau} = \frac{G_w}{\tau_w} = \frac{-\dot{q}_w}{\tau_w} = \frac{c_H}{c_f/2}\frac{(h_r - h_w)}{u_e} \qquad [26]$$

since, by definition

$$-\dot{q}_w = c_H \rho_e u_e (h_r - h_w) \qquad [27]$$

$$\tau_w = \frac{c_f}{2}\rho_e u_e^2 \qquad [28]$$

combining Equation [26] with Equations [21 and 24] we arrive at a differential equation relating h and α to u

$$\frac{c_H}{c_f/2} = \frac{u_e}{h_r - h_w}\left\{\left[\frac{\left(\frac{\mu}{P} + \frac{\epsilon}{P_T}\right)}{\mu + \epsilon}\right]\frac{dh}{du} + u + \left[\frac{\frac{k}{c_p}(L-1) + \frac{\kappa}{c_p}(L_T - 1)}{\mu + \epsilon}\right](h_1 - h_2)\frac{d\alpha}{du}\right\} \qquad [29]$$

From this point on the bars are omitted over the dependent variables, since when they appear, the dependent variables will be mean values.

Now it is assumed that in the laminar sublayer molecular viscosity and thermal conductivity predominate and thus

$$\epsilon \ll \mu \qquad \kappa \ll k$$

and in the turbulent layer

$$\epsilon \gg \mu \qquad \kappa \gg k$$

These assumptions are supported by the experimental evidence that, except for a narrow region (sometimes called the "buffer layer") between the two layers, these assumptions can be used, in conjunction with assumptions as to the magnitude of ϵ, to describe the turbulent boundary layer velocity and temperature profiles, at least at low speeds.

Thus for the sublayer Equation [29] becomes

$$\frac{c_H}{c_f/2} = \frac{u_e}{h_r - h_w}\left[\frac{1}{P}\frac{dh}{du} + \frac{1}{P}(L-1)(h_1 - h_2)\frac{d\alpha}{du} + u\right] \qquad [30]$$

and, in the turbulent outer layer Equation [29] becomes

$$\frac{c_H}{c_f/2} = \frac{u_e}{h_r - h_w}\left[\frac{1}{P_T}\frac{dh}{du} + \frac{1}{P_T}(L_T - 1)(h_1 - h_2)\frac{d\alpha}{du} + u\right] \qquad [31]$$

Integrate Equation [30] from the surface ($u = 0$) to the interface between the two layers ($u = u_L$) and integrate Equation [31] from the interface ($u = u_L$) to the outer edge of the boundary layer ($u = u_e$), solve for h_L in the resulting expressions and equate them. Solve the resulting algebraic equation for $c_H/(c_f/2)$. There results

$$\frac{c_H}{c_f/2} = \left[P_T + (P - P_T)\frac{u_L}{u_e}\right]^{-1}\left[1 + \frac{F(h_1^0 - h_2^0)}{h_r - h_w}\right] \qquad [32a]$$

where

$$F = [(L-1) - (L_T - 1)](\alpha_L - \alpha_w) + (L_T - 1)(\alpha_e - \alpha_w) \qquad [32b]$$

$$r = P_T + (P - P_T)(u_L/u_e)^2 \qquad [33]$$

$$h_1 - h_2 \cong h_1^0 - h_2^0 = \text{constant} \qquad [34]$$

Here h_1^0 and h_2^0 are the heats of formation of the atoms and molecules per unit mass at some reference temperature. Equation [34] has implicit in it the one approximation that the differences in enthalpy of the atoms and molecules at any temperature of interest to us is largely in the heat of formation of the atoms, which far overshadows the difference resulting from the fact that the molecules have more degrees of freedom for internal energy storage than do the atoms. Substitution of numerical values into the exact expressions for enthalpy of a mixture of atoms and diatomic molecules will substantiate this assumption.

Equations [32a and 33] can be simplified still further when the following approximations are adopted

$$\epsilon = \kappa/c_p = \rho D_T \quad \text{or} \quad P_T = L_T = 1 \qquad [35a]$$

$$1 + (P-1)\frac{u_L}{u_e} \cong P^{u_L/u_e} \cong P^{2/3} = \left(\frac{c_f/2}{c_H}\right)_0 \qquad [35b]$$

$$r = 1 - (1-P)(u_L/u_e)^2 \cong P^{1/3} \qquad [35c]$$

$$(L-1)(u_L/u_e) \cong L^{u_L/u_e} - 1 \cong L^{2/3} - 1 \qquad [35d]$$

$$\alpha_L - \alpha_w \cong (\alpha_e - \alpha_w)(u_L/u_e) \qquad [35e]$$

When Equations [35] are used with Equations [32a] there results

$$\frac{c_H}{c_f/2} = P^{-2/3}\left[1 + (L^{2/3} - 1)\frac{h_D}{(h_r - h_w)}\right] \qquad [36]$$

with Equation [35c]

$$r = (2/u_e^2)(h_r - h_e) \cong P^{1/3} \qquad [37]$$

$$h_D = (\alpha_e - \alpha_w)(h_1^0 - h_2^0) \qquad [38]$$

Equation [36] relates heat transfer coefficient to skin fric-

tion coefficient for a dissociating compressible boundary layer. Its derivation proceeds logically from the boundary layer equations under the assumptions stated.

Equation [35a] is a direct consequence of the original Reynolds analogy for turbulent shear flow. The justification for using this assumption in the present case rests on its successful application to turbulent shear flows in the past. It is difficult to see where the introduction of the additional complication of dissociation suggests that a change in the analogy is called for.

Equations [35b, 35c and 35d] are related and can be justified once the values for the velocity ratio at the edge of the sublayer u_L/u_e are known. In general $0.1 \leq u_L/u_e \leq 0.8$ with most values near $\frac{2}{3}$. An expression given by Rubesin (17), based upon examination of nondissociating compressible turbulent boundary layer velocity profiles, can be used for order of magnitude estimates in the present case. This is

$$\frac{u_L}{u_e} = 11.5\sqrt{\frac{c_f}{2}\frac{T_w}{T_e}} \qquad [39]$$

For example, if $R_e = 10^6$, $T_w/T_e = 2.0$ and $M_e = 2$ using Fig. 4 (to be discussed later), we obtain $u_L/u_e = 0.56$.

For Prandtl numbers near 1, Equations [35b and 35c] and hence [35d] are excellent approximations providing that $u_L/u_e \cong 0.3$ to 0.75. If u_L/u_e is outside this range, the more exact expressions can be used with Equation [36]. Note that this development fixes the exponent on Lewis number at $\frac{2}{3}$ consistent with the acceptance of $P^{1/3}$ as an approximation for the recovery factor. The exponent on Lewis number (and analogously the exponent on P in Eq. [35b]) will vary with u_L/u_e and with L. For example, if L varies between 1.2 and 1.8 and u_L/u_e varies between 0.2 and 0.8 the exponent on L in Equation [35d] varies from $\frac{1}{3}$ to about $\frac{4}{5}$. The point to be made here is that the chosen exponent on L is a representative one and that if a value other than $\frac{2}{3}$ is appropriate in Equation [35d] then the exponents on P in Equations [35b and 35c] should also change from $\frac{2}{3}$ and $\frac{1}{3}$, respectively, if the value of u_L/u_e is the reason for the change in exponent on L.

Equation [35e] is exactly correct, as will be demonstrated later (see Eq. [48]) for the case of a frozen boundary layer wherein the distribution of atoms and molecules is determined by diffusion. It is a reasonable first approximation for the case of equilibrium dissociation throughout the boundary layer as an inspection of an example calculation shown later in Fig. 7 will show.

It remains now to develop an expression for skin friction coefficient for the dissociating, compressible, turbulent boundary layer.

Skin Friction Coefficient

An expression for local skin friction coefficient can be derived by substituting velocity and density profiles determined by solving boundary layer equations [14, 16 and 17] into the well-known Kármán momentum integral

$$c_f = 2(d\theta/dx) \qquad [40a]$$

where

$$\theta = \frac{\rho_w}{\rho_e}\int_0^1 \frac{\rho}{\rho_w} z(1-z)\left(\frac{dz}{dy}\right)^{-1} dz \qquad [40b]$$

$$z = u/u_e \qquad [40c]$$

Expressions are now required for $(dz/dy)(z)$ and $(\rho/\rho_w)(z)$. These are obtained from solving the equations of state and conservation of species, momentum and energy.

From Equation [16] it can be shown that

$$\left(\frac{\partial \tau}{\partial y}\right)_w = \left(\frac{\partial^2 \tau}{\partial y^2}\right)_w \equiv 0$$

whence

$$\tau = \tau_w + O\left(\frac{\partial^3 \tau\, y^3}{\partial y^3\, 3!}\right)$$

and thus $\tau = \tau_w$ is a reasonable first approximation throughout a large region of the boundary layer. Therefore, following Prandtl's original mixing length concepts we write

$$\tau = \tau_w = \epsilon\frac{du}{dy} = \rho K^2 y^2\left(\frac{du}{dy}\right)^2 \qquad [41]$$

for the turbulent outer layer. If we define

$$E = K\left(\frac{\rho_e}{\rho_w}\frac{c_f}{2}\right)^{-1/2} \qquad [42]$$

Equation [41] can be integrated to obtain

$$\frac{1}{K}\log_e\left[\frac{\rho_w}{\mu_w}\left(\frac{\tau_w}{\rho_w}\right)^{1/2} y\right] + \phi(0) = \frac{1}{K} I_1 \qquad [43a]$$

where

$$I_1 = E\int_0^z \left(\frac{\rho}{\rho_w}\right)^{1/2} d\xi \qquad [43b]$$

and the constant of integration is determined by the fact that Equation [43a] becomes the "law of the wall" (18) given as Equation [43c] when $M_e = 0$ and $T = T_w = T_e$

$$u\left(\frac{\tau_w}{\rho_w}\right)^{-1/2} = \phi(0) + \frac{1}{K}\log_e\left[\frac{\rho_w}{\mu_w}\left(\frac{\tau_w}{\rho_w}\right)^{1/2} y\right] \qquad [43c]$$

also, since

$$\frac{dI_1}{dz} = E\left(\frac{\rho}{\rho_w}\right)^{1/2} \qquad [44]$$

then, from Equations [43a and 44]

$$\frac{dy}{dz} = \frac{E^2 \exp[-K\phi(0)]}{K(\rho_w u_e/\mu_w)}\exp(I_1)\left(\frac{\rho}{\rho_w}\right)^{1/2} \qquad [45]$$

This is the desired expression for use in Equation [40b].

In order to obtain an equation for ρ/ρ_w we must obtain equations for concentration and temperature as a function of velocity through the boundary layer. Equations [14 and 16] are used to obtain an expression for concentration of atoms through the boundary layer as follows.

Let us assume $\alpha = \alpha(u)$, and determine the conditions under which this is so, using Equations [14 and 16]. Substitute $\alpha = \alpha(u)$ into Equation [14]. We obtain

$$\left(\overline{\rho u}\frac{\partial u}{\partial x} + \overline{\rho v}\frac{\partial u}{\partial y}\right)\frac{\partial \alpha}{\partial u} = \frac{\partial}{\partial y}\left[\rho(D_{12}+D_T)\frac{\partial u}{\partial y}\right]\frac{\partial \alpha}{\partial u} + \rho(D_{12}+D_T)\left(\frac{\partial u}{\partial y}\right)^2\frac{\partial^2 \alpha}{\partial u} + \rho\frac{\partial \alpha}{\partial t} \qquad [46]$$

Combining Equations [16 and 46] we find that if $\rho D_{12} = \mu$ and $\rho D_T = \epsilon$, our condition for $\alpha = \alpha(u)$ becomes

$$\frac{\partial^2 \alpha}{\partial u^2} + \frac{\rho(\mu+\epsilon)}{\tau^2}\frac{\partial \alpha}{\partial t} = 0 \qquad [47]$$

since, in general, $\partial\alpha/\partial u \neq \infty$. It is thus apparent that in the general case the relation between the concentration of atoms α and the velocity through the boundary layer u depends upon the shear stress distribution τ, the viscosities μ and ϵ, and the rate at which atoms are created by the dissociation process. If the denominator of the second term in Equation [47] is much larger than the numerator, diffusion predominates in determining the atom concentration through the boundary layer. If $\partial\alpha/\partial t = 0$ then, of course, diffusion exactly determines the concentration profile (called "frozen flow"). If the second term in Equation [47] is much larger

than the first, then the flow is essentially in equilibrium and Equation [47] is not needed to determine the local equilibrium which would then be determined wholly by the external stream static pressure and the velocity and temperature distribution through the boundary layer.

We assume the "frozen flow" or wholly diffusion determined concentration profile through the boundary layer applies and will justify this assumption later. From Equation [47]

$$d^2\alpha/du^2 = 0$$

whence, since $\alpha = \alpha_w$ when[4] $u = 0$ and $\alpha = \alpha_e$ when $u = u_e$, we obtain

$$\alpha = \alpha_w + (\alpha_e - \alpha_w)(u/u_e) \qquad [48]$$

The temperature distribution as a function of velocity is determined as follows. From Equations [16 and 17], assuming $L = L_T = P = P_T = 1$ and $h = h(u)$, using Equations [16 and 17] in a manner analogous to the way Equations [14 and 16] were used to obtain $\alpha(u)$, we obtain

$$d^2h/du^2 = -1 \qquad [49]$$

if $dh/du \neq \infty$, as is generally true. Since $h = h_w$ when $u = 0$, and $h = h_e$ when $u = u_e$ then

$$h + \frac{u^2}{2} = h_w + \left(h_e - h_w + \frac{u_e^2}{2}\right)\frac{u}{u_e} \qquad [50]$$

or

$$H = h_w + (H_e - h_w)(u/u_e)$$

where, from Equations [6a, 6b and 7]

$$h = \alpha\left[\int (c_{p_1} - c_{p_2})dT + (h_1^0 - h_2^0)\right] + \int c_{p_2}dT + h_2^0 \qquad [51]$$

Now assume the atoms possess the translational degrees of freedom only, and the molecules the translational and rotational degrees of freedom, neglecting the vibrational energy as being secondary at the temperatures of interest to us. Then

$$c_{p_1} = 2.5(k/m_1) \qquad [52a]$$
$$c_{p_2} = 3.5(k/m_2) \qquad [52b]$$
$$h_1^0 = D_1/m_2 \qquad [52c]$$
$$h_2^0 = 0 \qquad [52d]$$
$$2m_1 = m_2 \qquad [52e]$$

whence, from Equations [51 and 52]

$$h = (3.5 + 1.5\alpha)\frac{k}{2m_1}T + \alpha\left(\frac{D_1}{2m_1}\right) \qquad [53]$$

Similarly, from Equations [1a, 1b, 4c, 7 and 52e] we obtain

$$p = p_e = \rho(k/2m_1)T(1 + \alpha) \qquad [54]$$

whence

$$\frac{\rho}{\rho_w} = \frac{(1 + \alpha_w)T_w}{(1 + \alpha)T} = \frac{T_w}{T_e}\left(\frac{1 + \alpha_w}{1 + \alpha}\right)\left(\frac{T}{T_e}\right)^{-1} \qquad [55]$$

The relation between T and u is obtained from Equations [48, 50 and 53]

$$\frac{T}{T_e} = \left(\frac{7 + 3\alpha_w}{7 + 3\alpha}\right)\left(\frac{T_w}{T_e}\right) + \left[\left(\frac{7 + 3\alpha_e}{7 + 3\alpha}\right) - \left(\frac{7 + 3\alpha_w}{7 + 3\alpha}\right)\left(\frac{T_w}{T_e}\right)\right]\left(\frac{u}{u_e}\right) + \left(\frac{u}{u_e}\right)\left(1 - \frac{u}{u_e}\right)\left(\frac{1.4\,M_e^2}{7 + 3\alpha}\right) \qquad [56]$$

[4] In essence, the assumption implied in arriving at Equation [48] is that the atom concentration determined by infinite reaction rate constants in the layer (equilibrium concentrations) with a catalytic wall can be approximated by the concentrations for zero reaction rate constants in the layer and an infinite reaction rate constant at the surface. See (21) for an elaboration of this point.

where by definition for our purposes

$$M_e^2 = u_e^2[1.4(k/2M_1)T_e]^{-1} \qquad [57]$$

when $\alpha = \alpha_e = \alpha_w = 0$ Equation [56] becomes the familiar Crocco relation

$$\frac{T}{T_e} = \frac{T_w}{T_e} + \left(1 - \frac{T_w}{T_e}\right)\left(\frac{u}{u_e}\right) + \left(\frac{u}{u_e}\right)\left(1 - \frac{u}{u_e}\right)(0.2\,M_e^2)$$

as it should for $\gamma = 1.4$ (diatomic molecules).

Our skin friction law now can be derived using Equations [40, 43b, 45, 48, 55 and 56]

$$R_e c_f = 0.389(T_w/T_e)^{0.76}I_2 \qquad [58]$$

where

$$I_1 = E\int_0^z \left(\frac{\rho}{\rho_w}\right)^{1/2} d\xi$$

$$E = 0.557\left[\left(\frac{T_w}{T_e}\right)c_f\left(\frac{1 + \alpha_w}{1 + \alpha_e}\right)\right]^{-1/2} \qquad [59]$$

$$I_2 = E^2\int_0^1 \left(\frac{\rho}{\rho_w}\right)^{3/2}(z - z^2)\exp(I_1)dz \qquad [60]$$

$$\frac{\rho}{\rho_w} = \frac{T_w}{T_e}\left(\frac{1 + \alpha_w}{1 + \alpha}\right)\left(\frac{T}{T_e}\right)^{-1}$$

T/T_e is given by Equation [56], and α is given by Equation [48]. The constants $\phi(0)$ and K were chosen as 6.53 and 0.393, respectively, in order that Equation [58] fit the experimental measurements of local skin friction coefficient at $M_e = 0$.

In obtaining Equation [58] it is assumed that

$$\int_0^x c_f dx = c_f x$$

for large x on the left-hand side of Equation [58]. This is a reasonable approximation for large x appropriate to the values for turbulent flow, particularly since the approximation is made before the empirical constants are determined by fitting the measured values of c_f at $M_e = 0$ and $T_w = T_e = T$.

The function $\mu \propto T^{0.76}$ was used in arriving at Equation [58]. This dependency of viscosity on temperature is in good accord with the findings of Bauer and Zlotnick (4) for high temperature air mixtures and by Scala and Baulknight (15) for mixtures of O_2 and O and N_2 and N.

Equation [58] will reduce to Equation [37] in the paper by Dorrance and Dore (19) when dissociation and mass transfer are zero, and it will reduce to Equation [66] of Van Driest when a series expansion of the integral I_2 in Equation [60] is resorted to. However, Equation [58], because it retains terms neglected in Van Driest's treatment, is more accurate at supersonic Mach numbers and moderate values of T_w/T_e as a comparison with experiment will demonstrate.

Equation [58] was solved for c_f for a variety of combinations of R_e, M_e, T_w/T_e, α_w and α_e using a 704 computer to perform the tedious numerical integrations and iterations involved. In preparing to present the results it became apparent that since five parameters of c_f were involved, any method of reducing the number of plots necessary would be a contribution. Fortunately, this was made possible by expanding all expressions appearing in the integrals I_1 and I_2 involved in determining c_f into series in powers of α_w and α_e. Retaining only first-order terms it was found that

$$\frac{c_f}{c_{f_0}} = f\left(\frac{1 + \alpha_e}{1 + \alpha_w}\right)^{1/7} - g$$

where f and g are weakly varying functions of R_e, T_w/T_e and M_e near 2.0 and 1.0, respectively, and c_{f_0} is c_f evaluated at the proper value of M_e, T_w/T_e and R_e but *with dissociation equal to zero*, i.e., $\alpha_w = \alpha_e = \alpha = 0$ in Equations [55 and 56].

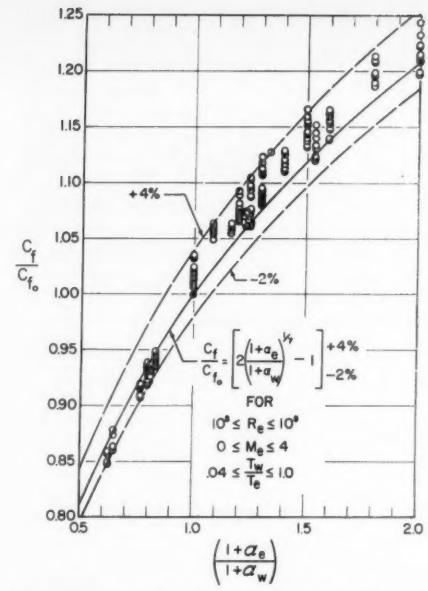

Fig. 1 Correlation curve for c_f/c_{f_0} given by Equation [61] compared with results given by numerical integration of Equation [58] for c_f and c_{f_0}

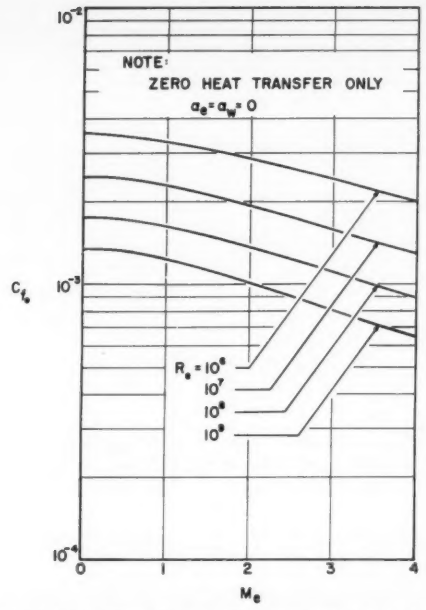

Fig. 2 Zero heat transfer and zero dissociation local turbulent boundary layer skin friction coefficient c_{f_0} vs. local stream Mach number M_e

Plotting the results showed that

$$\frac{c_f}{c_{f_0}} = \left[2.0\left(\frac{1+\alpha_e}{1+\alpha_w}\right)^{1/7} - 1\right] + 4\% - 2\% \qquad [61]$$

for *all cases considered*. Fig. 1 presents the results of correlating the calculations according to Equation [61].

Equation [61] or the plot in Fig. 1 indicates several interesting features regarding the effects of dissociation upon local skin friction coefficient. First, it appears that c_f is affected ± 22 per cent or less by dissociation in all cases. That is, c_f can be calculated as c_{f_0}, the value corresponding to the Mach number and temperatures present but with no dissociation, and the error involved will be within 22 per cent of the value of c_{f_0}. Secondly, Equation [61] or Fig. 1 indicates that the effect of using a noncatalytic wall ($\alpha_w \neq 0$) would be to reduce the skin friction coefficient under the value it would have if $\alpha_w = 0$. This reduction could amount to as much as 22 per cent for the case where $\alpha_e = 1$ and $\alpha_w = 1$ over the case where $\alpha_e = 1$ and $\alpha_w = 0$.

Plots of c_{f_0} were prepared as functions of R_e, M_e and T_w/T_e and are presented as Figs. 2, 3, 4, 5 and 6. Our calculations are now complete.

Equation for Local Heat Transfer

All of the results of the foregoing calculations can now be combined into the final equation for local heat transfer rate. From Equations [27, 36 and 61] we have

$$-\dot{q}_w = \rho_e u_e P^{-2/3}(h_r - h_w)\frac{c_{f_0}}{2}\left[2\left(\frac{1+\alpha_w}{1+\alpha_e}\right)^{1/7} - 1\right]\times \left[1 + (L^{2/3} - 1)\frac{h_D}{(h_r - h_w)}\right] \qquad [62]$$

where

$$h_r = h_e + r(u_e^2/2) \qquad [63]$$

$$r = P^{1/3}$$

$$h_D = (\alpha_e - \alpha_w)(D_1/2m_1) \qquad [64]$$

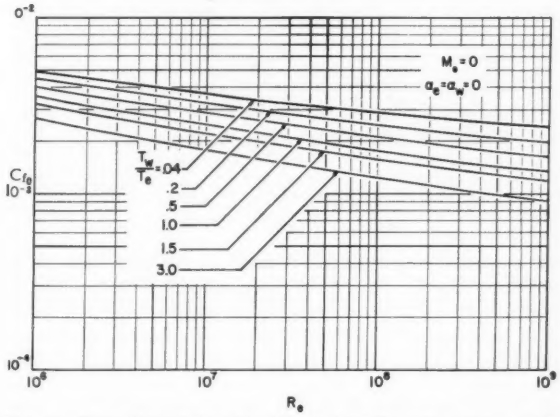

Fig. 3 Zero dissociation local turbulent boundary layer skin friction coefficient c_{f_0} vs. local stream Reynolds number R_e for a variety of temperature ratios and a local stream Mach number $M_e = 0$

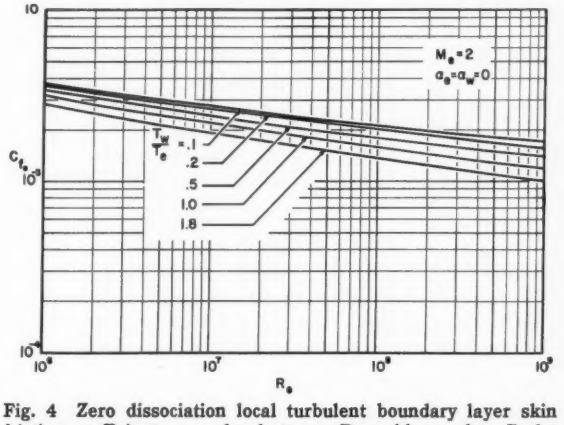

Fig. 4 Zero dissociation local turbulent boundary layer skin friction coefficient c_{f_0} vs. local stream Reynolds number R_e for a variety of temperature ratios and a local stream Mach number $M_e = 2$

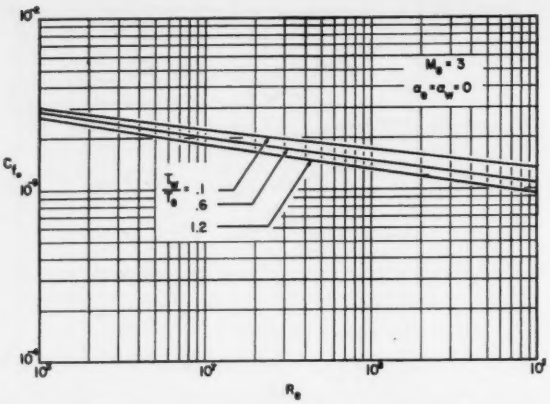

Fig. 5 Zero dissociation local turbulent boundary layer skin friction coefficient c_{f_0} vs. local stream Reynolds number R_e for a variety of temperature ratios and a local stream Mach number $M_e = 3$

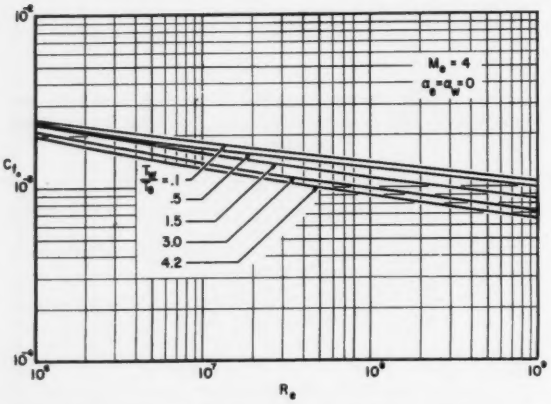

Fig. 6 Zero dissociation local turbulent boundary layer skin friction coefficient c_{f_0} vs. local stream Reynolds number R_e for a variety of temperature ratios and a local stream Mach number $M_e = 4$

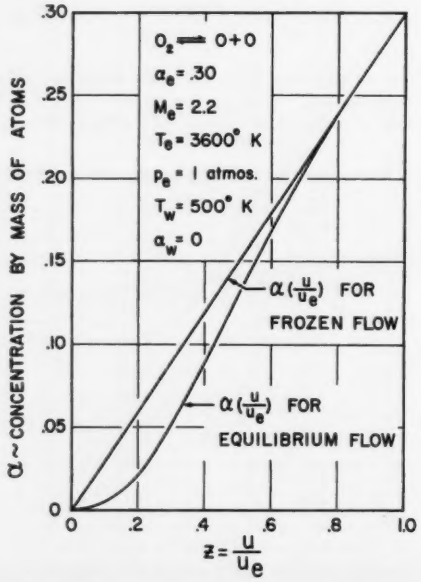

Fig. 7 The distribution of atom concentration through a dissociated turbulent boundary for a boundary layer in dissociation equilibrium and for a frozen boundary layer

h_D as defined by Equation [64] is strictly exact for a mixture of atoms and diatomic molecules of one species. For a mixture of two species, such as N_2, N, O_2 and O such as for air, for example

$$h_D = (\alpha_e - \alpha_w)\frac{\sum_{i=O,N}\left[(c_i)_e - (c_i)_w\right]\frac{D_i}{2m_i}}{\sum_{i=O,N}\left[(c_i)_e - (c_i)_w\right]} \qquad [65]$$

where α, as before, is the fraction by mass of the gas in the atomic state.

Discussion of Assumptions Used

With respect to the assumption of using the frozen flow concentration of atoms across the boundary layer, some conclusions can be drawn by considering Fig. 7. Fig. 7 presents the diffusion controlled distribution of atoms across a boundary layer for a typical set of external and surface conditions, i.e., $p_e = 1$ atm, $\alpha_e = 0.3$, $T_e = 3600$ K, $\alpha_w = 0$, $T_w = 500$ K. Also shown is the equilibrium distribution of atoms, assuming the rate of formation of atoms is far in excess of the rate at which they diffuse across the streamlines. In this latter case the same external stream and surface conditions were assumed for a pure oxygen layer for simplicity's sake. Equation [56] was used with equilibrium constant given in (20) to determine the equilibrium concentration of atoms through the layer. Surely the intermediate case of finite reaction rates will fall between the two curves shown on Fig. 7. Surely also the use of Equation [48] to determine the atom concentration is reasonable, since it is a great improvement over assuming α is some constant value throughout the boundary layer. The calculation procedure for the equilibrium case is indicated briefly here as: Solving Equation [56] which gives $T = T(\alpha, u/u_e)$ simultaneously with the equilibrium constant equation which gives $\alpha = \alpha(T)$ at each value of u/u_e, i.e.

$$K_p(T) = \frac{1 - \alpha^2}{\alpha^2}\frac{1}{4p_e} \qquad [66]$$

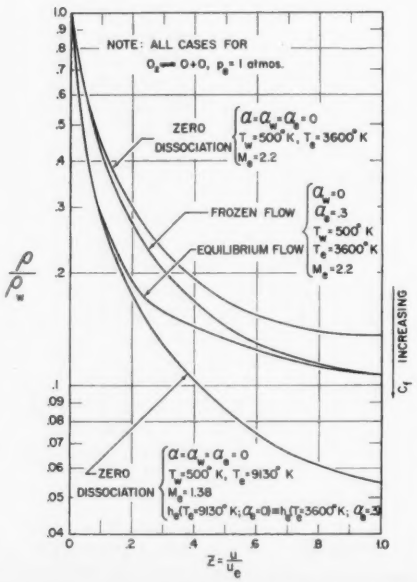
NOTE: ALL CASES FOR
$O_2 \rightleftharpoons O+O$, p_e = 1 atmos.
ZERO DISSOCIATION
$\alpha = \alpha_w = \alpha_e = 0$
T_w = 500° K, T_e = 3600° K
M_e = 2.2
FROZEN FLOW
EQUILIBRIUM FLOW
α_w = 0
α_e = .3
T_w = 500° K
T_e = 3600° K
M_e = 2.2
$\frac{\rho}{\rho_w}$
C_f INCREASING
$\alpha = \alpha_w = \alpha_e = 0$
T_w = 500° K, T_e = 9130° K
M_e = 1.38
$Z = \frac{u}{u_e}$

Fig. 8 Several density variations through a dissociated turbulent boundary layer

where K_p is given in (20) for oxygen and nitrogen dissociation, for example.

The concentration profiles given in Fig. 7 can be used in conjunction with Equation [55] to obtain values of ρ/ρ_w through the boundary layer. It is this ratio which directly appears in the momentum integral, Equation [43b]. Fig. 8 presents four curves of ρ/ρ_w vs. u/u_e. The upper curve is calculated using Equations [55 and 56] assuming $\alpha = \alpha_w = \alpha_e = 0$. It corresponds, then, to c_{f_0}. The next curve down is that appropriate to the frozen equilibrium flow case calculated using Equations [48, 55 and 56]. The next lowest curve is that calculated for equilibrium flow using Equations [55, 56 and 66]. The lowest curve is that calculated for the special case where the enthalpy and velocity at the wall and the edge of the boundary layer are equal to the dissociated values. This last case corresponds to the curve assumed when c_f is evaluated as c_{f_0} when the velocity and enthalpy at the edge of the boundary layer and at the wall are assumed as the same as when dissociation takes place. It is clear, in view of the fact that most cases of interest will fall between the frozen flow and dissociation equilibrium flow curves, that use of the frozen flow case for simplicity's sake is probably a reasonable simplification. It is further clear that calculations based on the assumption that c_f can be determined from values of c_{f_0} for nondissociating flow but with the same surface enthalpy and the same free stream enthalpy and velocity will not be as accurate as are the present calculations.

Comparisons With Experiment

As with any theory, the proof of validity rests on comparison with experimental results as well as with its internal consistency. The present analysis yields results which compare remarkably well with experiment as will be seen.

Fig. 9 shows the comparison of c_{f_0} as calculated using the present theory with measurements of Schultz-Grunow (22), Kempf (23), Coles (10, 11) and Matting et al. (12) for the case of zero heat transfer and no dissociation. The agreement between experiment and theory for these cases is quite remarkable.

When heat transfer occurs the agreement between experiment and theory is less precise but acceptable in view of the uncertainties in taking measurements with heat transfer present. Fig. 10 presents the comparison with measurements of Winkler (13) wherein the agreement between theory and experiment is shown to become poorer as heat transfer increases (T_w/T_e decreases) but is within +20 per cent, −5 per cent in all cases.

There are little data available for heat transfer from turbulent boundary layers under high stagnation enthalpy conditions where dissociation is apt to occur. Data measured using a shock tube were reported by Rose et al. (9) and are used here for comparision with Equation [62] slightly rearranged to give

$$\frac{N}{P} = c_H R_e = R_e \frac{c_{f_0}}{2} P^{-2/3} \left[2 \left(\frac{1 + \alpha_e}{1 + \alpha_w} \right)^{1/7} - 1 \right] \times \left[1 + (L^{2/3} - 1) \frac{h_D}{h_r - h_w} \right] \quad [67]$$

where c_{f_0} is interpolated using Figs. 3, 4 and 5, and the values of α_e, α_w, h_D, h_r and h_w were calculated appropriate to the experimental or estimated values given in (9). P was assumed equal to 0.72, and L equal to 1.40—reasonable values for these temperatures as the calculations of (4 and 5) show.

In Fig. 11 Equation [67] is compared with the data of (9). Although the data scatter about the line obtained using Equation [67], the agreement is satisfactory. Note that in all cases there was considerable heat transfer, and in some cases some dissociation present ($0.14 \geq T_w/T_e \geq 0.04$; $0 \leq \alpha_e \leq 0.27$).

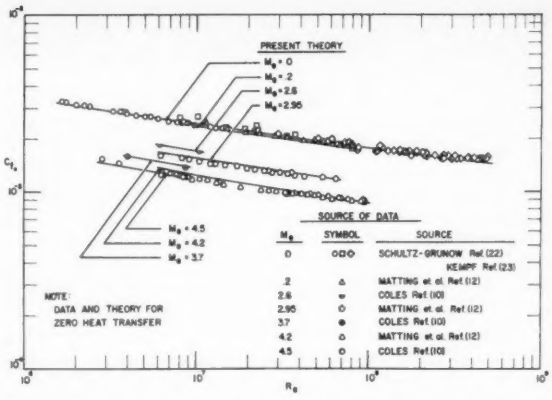

Fig. 9 A comparison of the theoretical nondissociated zero heat transfer local skin friction coefficient c_{f_0} given in Equation [58] with measured values of nondissociated zero heat transfer local skin friction coefficient c_{f_0}. Data from (10, 11, 12, 22 and 23)

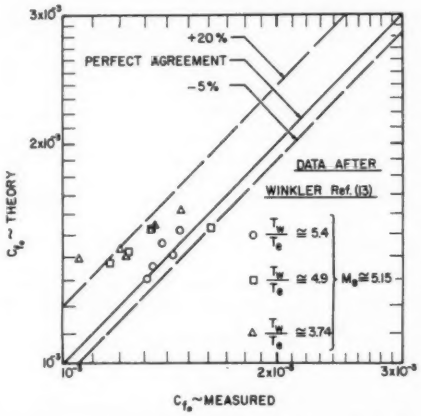

Fig. 10 A comparison of the theoretical nondissociated skin friction coefficient c_{f_0} with measured values of nondissociated local skin friction coefficient c_{f_0}. Data from Winkler (13)

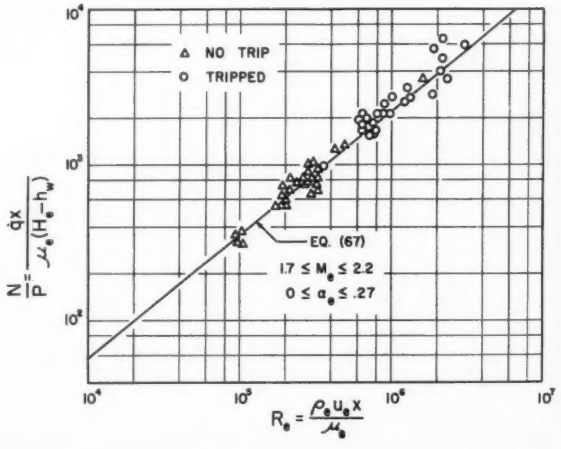

Fig. 11 A comparison of the theoretical heat transfer coefficient parameter given by Equation [67] with measured values under conditions of high heat transfer and low or zero dissociation. Data from (9)

Conclusions

The following conclusions seem justified as a result of the work described in this paper:

1 Flat plate dissociating compressible turbulent boundary layer local skin friction coefficients calculated using the theory of this report agree very well with measured values under zero heat transfer and zero dissociation conditions and with decreasing accuracy as heat transfer is increased, although data are sparse in the latter case.

2 An equation for local heat transfer from a dissociating compressible turbulent boundary layer is derived which agrees well with measurements under strong heat transfer and low or zero dissociated boundary layer conditions.

3 The analysis from which are developed both the skin friction and heat transfer coefficient equations is internally self-consistent and stems from solutions with justifiable approximations of the appropriate turbulent boundary layer equations.

Nomenclature

c_i = fraction by mass of species i
c_f = local skin friction coefficient, see Equation [28]
c_H = local heat transfer coefficient, see Equation [27]
c_{pi} = specific heat of species i
c_p = frozen mixture specific heat, see Equation [12]
D_i = energy of dissociation per molecule
D_T = turbulent diffusion coefficient, see Equation [11]
D_{12} = bimolecular diffusion coefficient
E = see Equation [42]
G = see Equation [21]
H = total enthalpy $= h + u^2/2$
h = enthalpy per unit mass
h_D = dissociation enthalpy per unit mass, see Equation [64]
h_i = enthalpy per unit mass of species i, see Equation [6b]
h_i^0 = heat of formation of species i per unit mass
K = mixing length proportionality constant, see Equation [41]
k = thermal conductivity, also Boltzmann's constant, see Equation [1b]
K_p = equilibrium constant
L = $\bar{\rho}D_{12}\overline{c_p}/k$ = Lewis number
L_T = $\bar{\rho}D_T\overline{c_p}/\kappa$ = turbulent Lewis number
M_e = Mach number of external flow
m_i = molecular mass of species i
N = $c_H R_x P$, Nusselt's number
p = $\Sigma_i p_i$, pressure
p_i = partial pressure of species i
P = $\overline{c_p}\mu/k$, Prandtl number
P_T = $c_p\epsilon/\kappa$, turbulent Prandtl number
q = heat transfer rate per unit area
r = recovery factor, see Equation [63]
R_e = $\rho_e u_e x/\mu_e$, Reynolds number
t = time
T = temperature
u, v = x and y components of velocity
$V_{i,x}, V_{i,y}$ = mass diffusion velocity in x and y directions
x, y = coordinates parallel to and perpendicular to flat plate surface
z = u/u_s
α = c_i, fraction by mass of atoms
γ = ratio of specific heats
ϵ = turbulent viscosity coefficient, see Equation [9]
θ = momentum thickness, see Equation [40b]
κ = turbulent conductivity coefficient, see Equation [10]
μ = viscosity coefficient
ρ = density
τ = shear stress
$\phi(0)$ = intercept in velocity distribution Equation [43c]

Subscripts

D = dissociation
e = external to boundary layer
i = denotes species i
L = value at edge of laminar sublayer
0 = value when no dissociation occurs
r = value when $q_w = 0$
T = turbulent value
w = value at the surface, $y = 0$

References

1 Fay, J. A. and Riddell, F. R., "Theory of Stagnation Point Heat Transfer in Dissociated Air," *J. Aeron. Sci.*, vol. 25, no. 2, Feb. 1958, pp. 73–85.

2 Lees, L., "Laminar Heat Transfer Over Blunt-Nosed Bodies at Hypersonic Flight Speeds," JET PROPULSION, vol. 26, no. 4, April 1956, pp. 259–269.

3 Kemp, N. H., Rose, P. H., and Detra, R. W., "Laminar Heat Transfer Around Blunt Bodies in Dissociated Air," *J. Aero/Space Sci.*, vol. 26, no. 7, July 1959, pp. 421–430.

4 Bauer, E. and Zlotnick, M., "Transport Coefficients of Air to 8000 K," ARS JOURNAL, vol. 29, no. 10, Oct. 1959, pp. 721–728.

5 Hansen, C. F., "Approximations for the Thermodynamic and Transport Properties of High Temperature Air," NACA Technical Note 4150, March 1958.

6 Van Driest, E. R., "Turbulent Boundary Layer in Compressible Fluids," *J. Aeron. Sci.*, vol. 18, no. 3, March 1951, pp. 145–160.

7 Hidalgo, H., "On the Application of Van Driest's Method to a Highly Cooled Partially Dissociated Turbulent Boundary Layer," JET PROPULSION, vol. 28, no. 7, July 1958, pp. 487–488.

8 Lees, L., "Convective Heat Transfer With Mass Addition and Chemical Reactions," in "Combustion and Propulsion, Third Agard Colloquium," Pergamon Press, N. Y., 1959.

9 Rose, P. H., Probstein, R. F. and Adams, M. C., "Turbulent Heat Transfer Through a Highly Cooled, Partially Dissociated Boundary Layer," *J. Aero/Space Sci.*, vol. 25, no. 12, Dec. 1958, pp. 751–760.

10 Coles, D., "Measurements of Turbulent Friction on a Smooth Flat Plate in Supersonic Flow," *J. Aeron. Sci.*, vol. 21, no. 7, July 1954, pp. 433–448.

11 Coles, D., "Measurements in the Boundary Layer on a Smooth Flat Plate in Supersonic Flow. III. Measurements in a Flat-Plate Boundary Layer at the Jet Propulsion Laboratory," Jet Propulsion Laboratory, California Institute of Technology Rep. no. 20–71, June 1, 1953.

12 Matting, F. W., Chapman, D. R., Nyholm, J. R. and Thomas, A. G., "Turbulent Skin Friction at High Mach Numbers and Reynolds Numbers," in "Proceedings of the 1959 Heat Transfer and Fluid Mechanics Institute," Stanford University Press, 1959, pp. 80–93.

13 Winkler, E. M., "Investigation of Flat Plate Hypersonic Turbulent Boundary Layers With Heat Transfer," ARS preprint no. 856–59, 1959.

14 Hill, F. K., "Turbulent Boundary Layer Measurements at Mach Numbers from 8 to 10," *Phys. Fluids*, vol. 2, no. 6, Nov.-Dec. 1959, pp. 668–680.

15 Scala, S. M. and Baulknight, C. W., "Transport and Thermodynamic Properties in a Hypersonic Boundary Layer. Part 1 Properties of Pure Species," ARS JOURNAL, vol. 29, no. 1, Jan. 1959, pp. 39-45

16 Hansen, C. F. and Heims, S. B., "A Review of the Thermodynamic, Transport, and Chemical Reaction Rate Properties of High Temperature Air," NACA TN 4859, July 1958.

17 Rubesin, M. W., "A Modified Reynolds Analogy for the Compressible Turbulent Boundary Layer on a Flat Plate," NACA TN 2917, March 1953.

18 Coles, D., "Measurements in the Boundary Layer on a Smooth Flat Plate in Supersonic Flow. I. The Problem of the Turbulent Boundary Layer," California Institute of Technology, Jet Propulsion Laboratory Rep. 20-69, June 1, 1953.

19 Dorrance, W. H. and Dore, F. J., "The Effect of Mass Transfer on the Compressible Turbulent Boundary-Layer Skin Friction and Heat Transfer," *J. Aeron. Sci.*, vol. 21, no. 6, June 1954, pp. 404–410.

20 Alpher, R. A. and Greyber, H. D., "Calculation of Shock Hugoniots and Related Quantities for Nitrogen and Oxygen," General Electric Research Laboratory Rep. no. 58-RL-1915, April 1958.

21 Goulard, R., "On Catalytic Recombination Rates in Hypersonic Stagnation Heat Transfer," JET PROPULSION, vol. 28, no. 11, Nov. 1958, pp. 737–745.

22 Schultz-Grunow, F., "New Frictional Resistance Law for Smooth Plates," NACA TM 986, 1941.

23 Kempf, von G., "Wietere Reibungsergebnisse an ebenen glatten und rauhen Flachen," *Hydrodynamische Probleme des Schiffsantriebs*, vol. 1, 1932, pp. 74–82.

Measured Pressure Distribution and Local Heat Transfer Rates for Flow Over Concave Hemispheres

J. C. Y. KOH[1] and
J. P. HARTNETT[2]

University of Minnesota
Minneapolis, Minn.

The use of parachutes for recovery of equipment from very high velocity vehicles, such as missiles, has directed attention to the need for aerodynamic and heat transfer information associated with such high drag bodies. With this application in mind, a solid concave hemisphere, positioned in a subsonic flow, was studied. Plexiglas models were placed in water and in air streams, and by using straightforward flow visualization techniques it was determined that the flow in the cup was, in essence, a separate flow region. Quantitative measurements were made of the pressure distribution and local heat transfer rate over a Reynolds number range of 6000 to 89,000. The pressure on the inner surface of the hemisphere was found to be equal to the total pressure from the stagnation point to an angle of 75 deg, dropping somewhat at greater angles. The heat transfer was found to increase monotonically from the stagnation point to the edge. The overall dimensionless heat transfer may be given in the form $Nu_D/(Re_D)^{1/2} = 0.42$.

RECENT interest in the use of parachutes for the recovery of equipment from high speed vehicles has directed attention to the aerodynamics and heat transfer of extremely high drag bodies. At the time the present study of heat transfer to parachutes was initiated, only limited aerodynamic information was available, and no pertinent heat transfer information was found in the open literature. [Recently, information on the pressure distribution about a hemisphere with 20 per cent porosity (1)[3] and heat transfer data for a fist-type parachute (2) has become available.] To obtain preliminary estimates of the time-temperature history of descending parachutes, the porosity was neglected and the convective heat transfer coefficients were estimated for an upstream facing hemisphere. The convective coefficient on the rear surface was assumed to be the same as on the rear surface of a sphere. For the front surface of the hemisphere, the potential flow solution of Schiffman and Spencer (3) yielded the velocity and pressure distribution, which, in turn, was used to determine the local convective heat transfer performance. The velocity and heat transfer results are shown in Fig. 1 and compared with established values for flow over the front side of a sphere; surprisingly, the predicted velocity and heat transfer coefficient distribution for the front face of the hemisphere is very similar to the distribution on the front face of a sphere. However, the validity of these results was brought sharply into question when preliminary pressure distribution measurements using a solid hemisphere gave markedly different behavior. As a consequence, a rather detailed aerodynamic and heat transfer investigation using concave hemispheres was initiated.

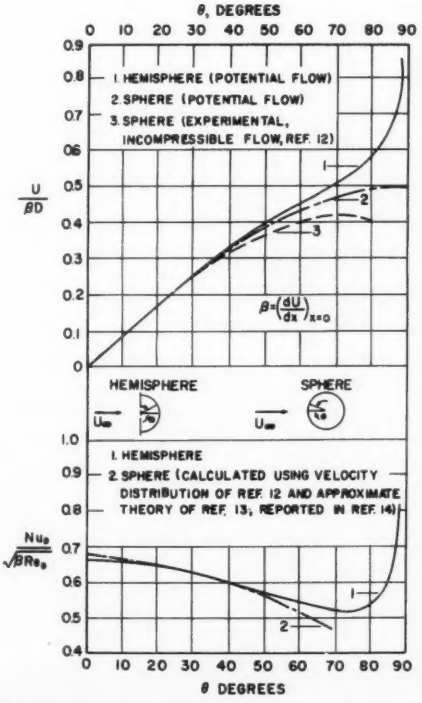
θ, DEGREES
0 10 20 30 40 50 60 70 80 90
1. HEMISPHERE (POTENTIAL FLOW)
2. SPHERE (POTENTIAL FLOW)
3. SPHERE (EXPERIMENTAL, INCOMPRESSIBLE FLOW, REF. 12)
U/βD
β=(dU/dx)x=0
HEMISPHERE
SPHERE
1. HEMISPHERE
2. SPHERE (CALCULATED USING VELOCITY DISTRIBUTION OF REF. 12 AND APPROXIMATE THEORY OF REF. 13, REPORTED IN REF. 14)
Nuθ/√βReθ
θ DEGREES

Fig. 1 Distribution of velocity and Nusselt number for flow over hemisphere based on potential flow

Presented at the ARS Semi-Annual Meeting, Los Angeles, Calif., May 9–12, 1960.

[1] Present address, Boeing Airplane Co., Seattle, Wash.

[2] Professor of Mechanical Engineering. Member ARS.

[3] Numbers in parentheses indicate References at end of paper.

Description of Investigation

Pressure Distribution Measurement and Flow Visualization Study

A $2\frac{13}{16}$-in. diameter finished copper hemisphere with static pressure taps located at 15-deg intervals from the center (i.e., $\theta = 0$, 15, 30 deg, etc.) was placed in a subsonic wind tunnel to measure the pressure distribution. Preliminary measurements showed that the pressure inside the concave hemisphere was essentially equal to the total pressure and, accordingly, is markedly different from the calculated result (4) based on the potential flow assumption. To gain additional insight into the mechanics of the flow, a Plexiglas model (see Figs. 7 and 8) was placed in a water stream and an air stream for flow observation. Aluminum powder and cigar smoke were introduced into the water and air streams, respectively, to make the flow visible. The schematic diagram for the air flow visualization study is shown in Fig. 2. In addition to the qualitative flow visualization information, the free stream turbulence level and the magnitude of the flow fluctuations inside the hemisphere cup were also measured using standard hot-wire equipment.

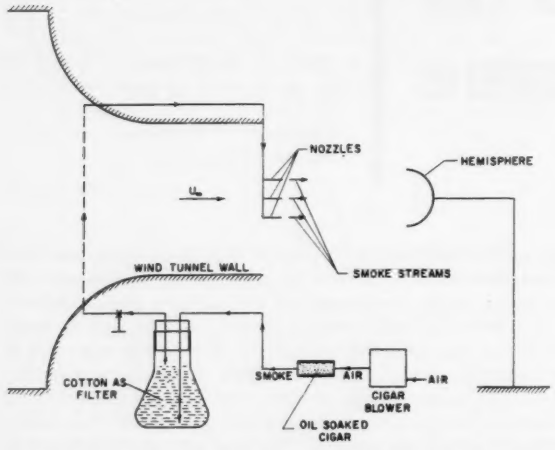

Fig. 2 Schematic diagram for flow visualization study of air flow over the hemisphere

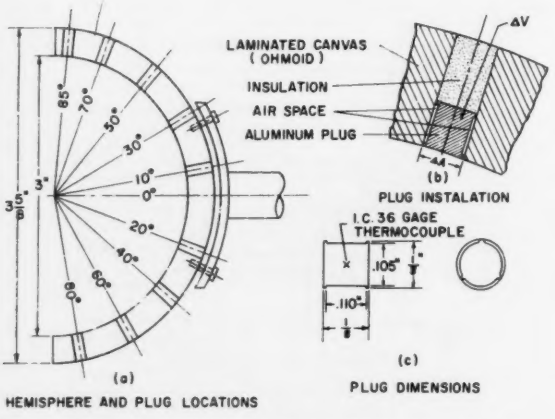

Fig. 3 Hemisphere and aluminum plugs for heat transfer measurement

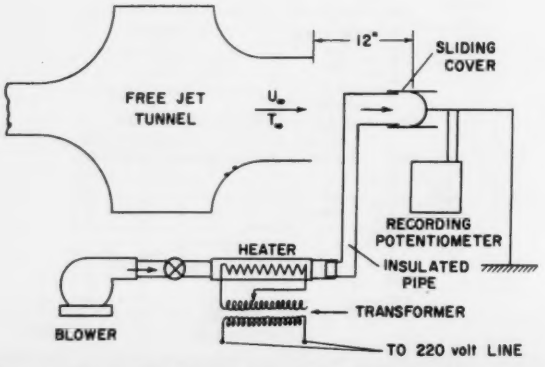

Fig. 4 Schematic diagram for heat transfer measurement

Local Heat Transfer Measurement

The heat transfer model was a 3-in. diameter hemisphere made of laminated canvas with aluminum plugs inserted at the locations indicated in Fig. 3 to provide the local heat transfer measurement. A transient method was used wherein the model was heated to an elevated temperature and then positioned in the air stream. The recorded temperature-time history of the aluminum plugs allowed the determination of the local convective heat transfer coefficient. Aluminum was chosen as the material for the plugs because of its low emissivity (0.04) and high conductivity (approximately 100 Btu/hr-ft F). The heat capacity of the aluminum was measured as 0.23 Btu/lb F (4). Iron constantan thermocouple wires, 36 gage, were used to measure the temperature of the aluminum plugs and of the free stream air. The thermocouple leads were connected to a 24-point thermocouple switch which, in turn, was connected to a Leeds and Northrup Speedomax Recording Potentiometer. Heat transfer measurements were accomplished in two different wind tunnels, a free jet tunnel with velocities up to 8 fps and a closed circuit wind tunnel with velocities up to 150 fps.

Fig. 4 shows a schematic diagram for the heat transfer measurement using the free jet wind tunnel. The concave hemisphere was set normal to the air stream and 12 in. from the tunnel exit. The hemisphere was initially enclosed by the pipe insulation material, and the hot air was introduced. The temperatures of the plugs were checked constantly by the Speedomax Recording Potentiometer. When the temperature of the hemisphere was approximately 140 F and the maximum temperature difference among the plugs was ± 0.5 F, the cover was removed and the hot air pipe was swung aside exposing the hemisphere to the air stream. The resulting temperature decay of one of the aluminum plugs was recorded. This procedure was repeated until the temperature histories of all the plugs were recorded. In principle, the same procedure was used with the model in the closed circuit wind tunnel.

To determine the local convective heat transfer coefficient from the recorded temperature-time history, a heat balance was written for the aluminum plug; see Fig. 3. If this small aluminum element is exposed to an air stream, and if there is a temperature difference between this element and the surrounding air, then heat exchange by conduction, convection and radiation will take place until an equilibrium temperature between the element and its surrounding is reached. If the plug is insulated except at the front face, and if the radiative heat transfer is negligibly small in comparison to the convective heat transfer,[4] then the rate of change of energy capacity must be balanced by the heat transfer by convection

$$-Wc(dT/d\theta) = h\Delta A(T - T_\infty)$$

or

$$h = \frac{Wc}{(\Delta A)(T - T_\infty)}\left(-\frac{dT}{d\theta}\right) \qquad [1]$$

[4] The radiation was negligible in the present program owing to the low emissivity of the aluminum and the low temperature level of the investigation.

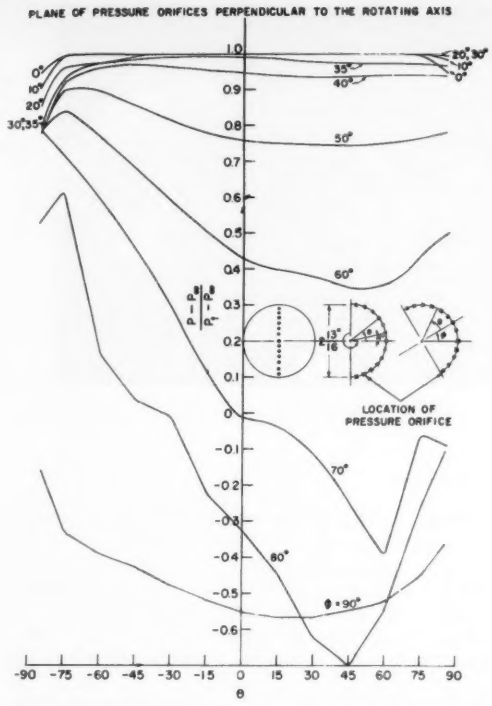

Fig. 5 Pressure distribution of a concave hemisphere at different angles of attack—plane of pressure orifices perpendicular to the axis of rotation

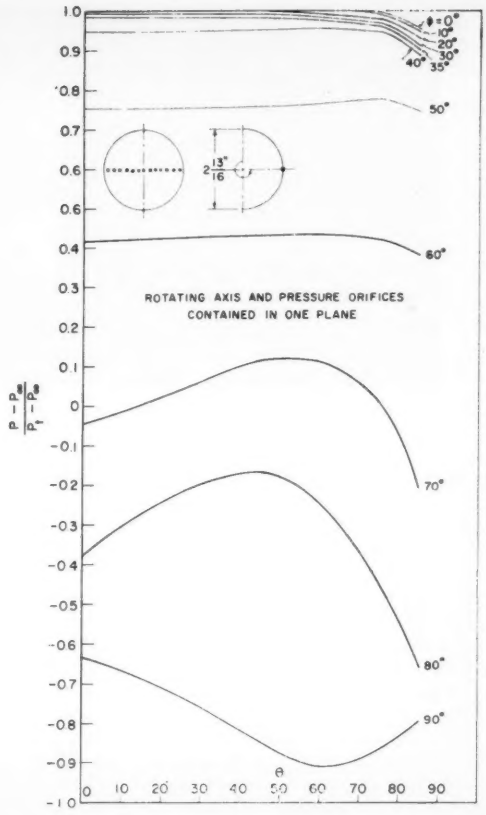

Fig. 6 Pressure distribution of a concave hemisphere at different angles of attack—axis of rotation and pressure orifices contained in one plane

The boundary condition is $T = T_0$ at $t = 0$.

If the temperature difference between the free stream and the surface of the object is small, the heat transfer coefficient can be taken as constant. In this case, Equation [1] together with its boundary condition, can be integrated to give

$$h = \frac{Wc}{(\Delta A)t} \log_e \frac{T_0 - T_\infty}{T - T_\infty} \qquad [2]$$

Hence, if the temperature history is recorded, the heat transfer coefficient can be calculated by either Equation [1] or [2].

Results and Discussion

Pressure Distribution Measurement and Flow Visualization Study

The results of measurement of the pressure distribution for flow over the concave hemisphere at different angles of attack are shown in Figs. 5 and 6. Fig. 5 shows the pressure distribution when the plane of the pressure orifices is normal to the supporting axis about which the hemisphere was rotated to obtain an angle of attack. Fig. 6 shows the pressure distribution when the orifices and the supporting axis are contained in one plane. For flow normal to the hemisphere mouth (zero angle of attack), it can be seen from these figures that the static pressure on the concave hemisphere is equal to the total pressure up to an angle of 75 deg from the stagnation point. This means that there is practically no flow near and parallel to the surface of the hemisphere except near the edge.

The streamline patterns for the flow of air and water over the concave hemisphere are presented in Figs. 7 (water) and 8a (air). These two figures show essentially the same flow picture whether the fluid in motion is air or water, and there appears to be very little flow into the concave hemisphere. In fact, placing a flat disk across the mouth of the hemisphere, thereby presenting a solid hemisphere to the oncoming

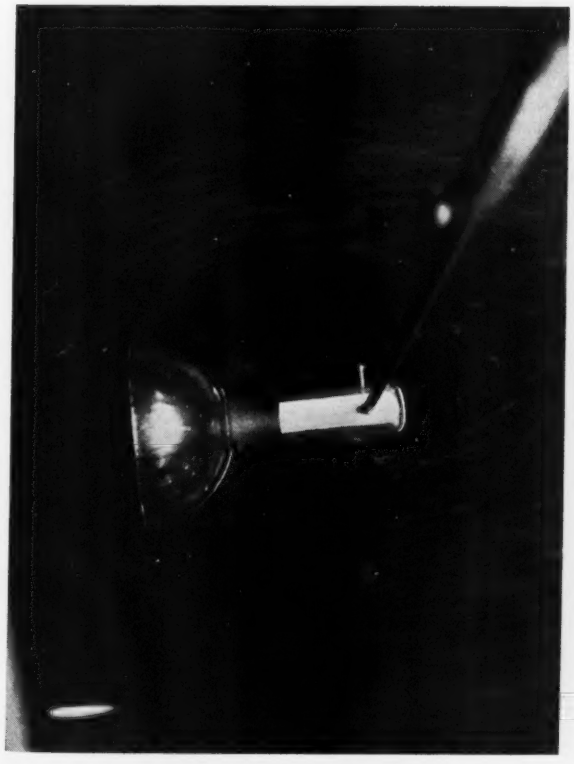

Fig. 7 Water flow over hemisphere

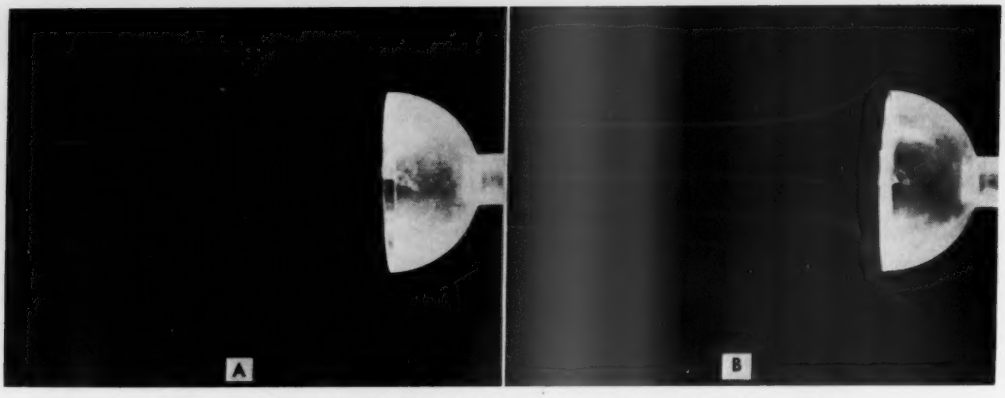

Figs. 8 Air flow over hemisphere: (a) concave hemisphere; (b) solid hemisphere

flow, did not markedly influence the streamline pattern, as can be seen by comparing Fig. 8a for the open hemisphere and Fig. 8b for the solid hemisphere.

For the open hemisphere a hot wire was inserted into the cup and indicated that the flow in this region was quite unstable and could be considered a rather unusual type of separated flow. It certainly cannot be described by the potential flow solution cited in the introduction, and it is suggested that the fluid is unable to overcome the sharp turn at the lip which would require an extremely high velocity—accordingly, a rotational flow pattern develops. Owing to this complicated flow behavior, it is not possible to calculate the heat transfer on the concave side of the hemisphere. Consequently, the heat transfer distribution was determined experimentally.

Local Heat Transfer Measurement

The heat transfer measurements were performed in both a free jet wind tunnel and a closed subsonic wind tunnel. The Reynolds number based on the inside diameter of the hemisphere ranged from 5.9×10^3 to 8.86×10^4. The local Nusselt number based on the inside diameter and free stream velocity is shown in Fig. 9, where it may be seen that the measurements from the free jet tunnel agree well with those from the closed wind tunnel. Since the data have been successfully represented by a simple curve covering a wide range of Reynolds number, it is clear that this method of presentation eliminates, or at least minimizes, any Reynolds number effect. Notice that, except for the dip at about 60 deg, the measured heat transfer coefficient on the concave hemisphere increases from the stagnation point to the tip as contrasted with the incorrect potential flow distribution in Fig. 1 which decreases as the distance from the stagnation point increases.

Noting that the free stream turbulence level of the free jet is 0.7 per cent (4), whereas the closed wind tunnel has a low turbulence level of 0.1 per cent (5), it can be stated that the free stream turbulence level does not have a significant effect on heat transfer from this geometry.[5] Based on the best fitted curve, the average Nusselt number divided by the square root of Reynolds number for flow over the concave hemisphere is found to be 0.42.

It is interesting to compare the heat transfer of a concave hemisphere to that of a disk normal to the air stream. Based on the projected area of the hemisphere, the value of $Nu_D/(Re_D)^{0.5}$ would be 0.84, since the surface area of a hemisphere is twice that of the disk with equal diameter. This value is only 13 per cent lower than the heat transfer from a circular disk as reported by Sogin (11).

[5] A noticeable effect of free stream turbulence level on heat transfer from other geometries has been reported in (6 to 10).

Conclusions

In the light of the present investigation, the following conclusions may be drawn:

1 Owing to the sharp turns of the lips and the viscosity of the fluid, the flow over concave hemisphere is unstable and rotational. Consequently, the potential flow for this geometry does not describe the physically real flow. The flow fluctuations inside the hemisphere cup are random and irregular.

2 For zero angle of attack, the pressure inside a concave hemisphere is equal to the total pressure from the stagnation point to an angle of 75 deg. The pressure drops near the edge of the hemisphere.

3 The heat transfer from the hemisphere increases from the stagnation point to the edge. Over a range of Reynolds number from 5.9×10^3 to 8.86×10^4, the overall dimensionless heat transfer $Nu_D/(Re_D)^{1/2}$ is 0.42. Based on the projected area, the value of $Nu_D/(Re_D)^{1/2}$ is 0.84, which is 13 per cent lower than the heat transfer from a circular disk.

4 The free stream turbulence level does not have a significant effect on heat transfer from a concave hemisphere.

Acknowledgments

Special appreciation is extended to the Mechanical Engineering Shops for building all the testing apparatus. The authors also acknowledge the help of S. H. Lin in drafting the final graphs and figures.

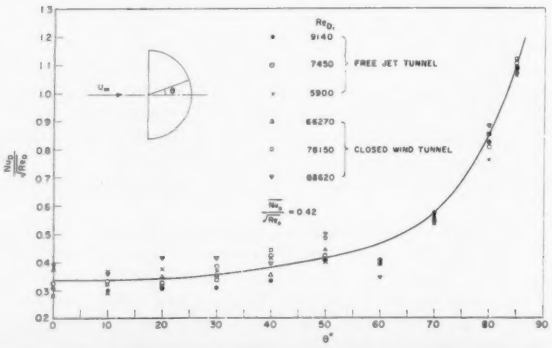

Fig. 9 Heat transfer from concave hemisphere

Nomenclature

ΔA = area
c = specific heat
D = diameter
h = heat transfer coefficient
k = thermal conductivity
Nu_D = Nusselt number, $Nu_D = hD/k$
p = static pressure
p_t = total pressure, $p_t = p_\infty + (\rho/2)U_\infty^2$
Re_D = Reynolds number, $Re_D = U_\infty D/\nu$
t = time
T = temperature
T_∞ = free stream temperature
U = velocity at the outer edge of the boundary layer
U_∞ = uniform free stream velocity
W = mass
ρ = density
μ = absolute viscosity
ν = kinematic viscosity, $\nu = \mu/\rho$

References

1 Heinrich, H. G., Ballinger, J. G. and Grant, J. J., "Temperature of Parachutes in Supersonic Flow (Part B, Flow Studies)," Progress Rep. no. 718, Dept. of Aero. Engng., No. 5188, University of Minnesota, Aug. 15, 1957.

2 Schoeck, P. A., Hool, J. N. and Eckert, E. R. C., "Experimental Studies for Determining Heat Transfer on the Ribbons of Fist Type Parachutes," Heat Transfer Laboratory Technical Rep. no. 24, University of Minnesota, Sept. 1959.

3 Schiffman, M. and Spencer, D. C., "The Flow of an Ideal Incompressible Fluid About a Lens," *Quarterly J. Mech. Appl. Math.*, vol. 5, no. 270, 1957.

4 Koh, J. C. Y., "Experimental Investigation of the Pressure Distribution and Heat Transfer for Flow over Concave Hemispheres and Cylindrical Cups," Ph.D. Thesis, University of Minnesota, Oct. 1959.

5 Eichhorn, R., "Reduction of Turbulence in a Low-Speed Wind Tunnel," M.S. Thesis, University of Minnesota, Oct. 1955.

6 Giedt, W., "Effect of Turbulence Level of Incident Air Stream on Local Heat Transfer and Skin Friction on a Cylinder," *J. Aeron. Sci.*, vol. 18, no. 11, 1951.

7 Kestin, J. and Maeder, P., "Influence of Turbulence on Transfer of Heat from Cylinders," NACA TN 4018, 1957.

8 Seban, R. A., "The Influence of Free Stream Turbulence on the Local Heat Transfer from Cylinders," ASME Paper no. 58-H-152-G, 1958.

9 Sato, K. and Sage, B. N., "Thermal Transfer in Turbulent Gas Stream-Effect of Turbulence on the Macroscopic Transport from Spheres," ASME Paper no. 57-A-20, 1957.

10 Sugawara, S., Sato, T., Komatsu, H. and Osaka, H., "The Effect of Free-Stream Turbulence on Heat Transfer from a Flat Plate," NACA TM 1441, 1958.

11 Sogin, H. H., "Sublimation from Disks to Air Stream Flowing Normal to Their Surfaces," Trans. ASME, vol. 80, 1958, p. 61.

12 Fage, A., "Experiments on a Sphere at Critical Reynolds Number," Aeronautical Research Council, Reports and Memoranda (Great Britain), no. 1766, 1937.

13 Drake, R. M., Jr., "Calculation Method for Three-Dimensional Rotationally Symmetrical Laminar Boundary Layers with Arbitrary Free Stream Velocity and Arbitrary Wall Temperature Variation," *J. Aeron. Sci.*, vol. 20, 1953, p. 309.

14 Korobkin, I. and Gruenwald, K. H., "Investigation of Local Laminar Heat Transfer on a Hemisphere for Supersonic Mach Numbers at Low Rate of Heat Flux," *J. Aeron. Sci.*, vol. 24, 1957, p. 188.

Technical Notes

Differentiating Gas Jet for Space Attitude Control

ROBERT S. GAYLORD[1]

Space Technology Laboratories, Inc., Los Angeles, Calif.

A COMMON problem arising in any automatic control system is the one of insuring adequate damping for the dynamic system under control. The concept of "positive damping" may be generalized to include any function of the velocity of a controlled variable which causes the velocity of this controlled variable to approach zero (1).[2] Of course, in any real system "zero" means that some threshold or dead band or other typically nonlinear region has been reached. These nonlinearities may result in a steady-state "hunting" or limit cycle operation of the control system. Frequently this limit cycle operation is either not noticed or not important in the everyday use of the automatic control system. However, for various space applications, for example satellites of long duration, system nonlinearities become dominant considerations (2). See Fig. 1 for a simple block diagram of a typical satellite attitude control system. Such a satellite attitude control system is frequently designed to operate in a limit cycle which is as conservative of energy consumption as possible. The magnitude of the velocity in the limit cycle corresponds to momentum which needs to be removed each complete period of the limit cycle. This wastes a great deal of energy stored in the satellite (stored gas in the case of a jet control system). What is needed to reduce these velocities is anticipation or measurement of the velocity.

Usually, a derivative of the controlled variable is obtained either by a lead network in the control system or by an in-

Received July 14, 1960.

[1] Member of the Technical Staff. Member ARS.

[2] Numbers in parentheses indicate References at end of paper.

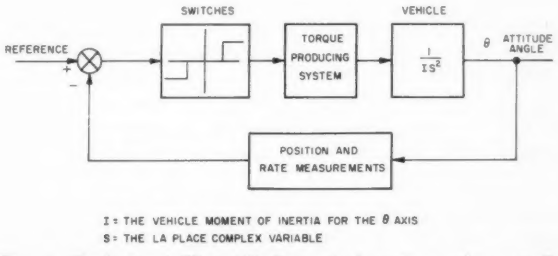

Fig. 1 Typical satellite attitude control system using on-off control of torque

EDITOR'S NOTE: The Technical Notes and Technical Comments sections of ARS JOURNAL are open to short manuscripts describing new developments or offering comments on papers previously published. Such manuscripts are usually published without editorial review within a few months of the date of receipt. Requirements as to style are the same as for regular contributions (see masthead page).

ertial velocity measuring device, such as a rate gyro. Unfortunately, by neither of these methods can one measure the velocity at rates low enough to be used for long duration satellite applications.

This note is concerned with a technique of reducing limit cycle velocities below those which can be ordinarily measured by the control system. The device used is a "differentiating gas jet" and may be used alone or in conjunction with reaction wheel controls (3,4). To better understand the problem, examine the simple phase-plane diagram of Fig. 2 which shows trajectories for control systems with and without rate measurement. Notice that the system which switches on the control torque as a function of position only (vertical switching lines) returns to the initial state (I.C.) of the system. In fact, the system does so repeatedly in a stable oscillation (called a limit cycle) until all the control energy has been expended. The dotted trajectory corresponds to a rate measuring system, which has diagonal switching lines, and is shown to converge. The slope of the diagonal switching lines is equal to the negative of the ratio of position control gain to rate measurement gain for the control system. For very low values of attitude rate the rate measuring device may contain a deadband region or other inaccuracies, and the switching lines then essentially become vertical. For cases where these threshold rates are still too great to be tolerated, one searches for new techniques of handling the convergence problem. It is the purpose of this note to present such a technique.

To demonstrate the operation of the proposed gas jet system, suppose the jet thrust (hence torque) is a function of time as shown in Fig. 3. We see that whenever a switching occurs, we receive a high pulse of torque followed by a period of constant low torque which will be switched off when the control dead zone is reached for negative velocities. See Fig. 4 for the phase-plane diagram.

The thrust function is very easy to obtain. A possible mechanization is shown in the schematic of Fig. 5. When the jet control valve is opened, the calibrated volume discharges at the manifold pressure, and hence the thrust peaks. The flow restrictor then allows a small steady flow (at a pressure drop) until the valve is closed by the autopilot. The chamber is then recharged from the manifold and is ready for the next positive cycle to occur. Through the proper adjustment of discharge time constant and restrictor sizing, a variety of torque shapes is possible. Notice that a fast opening, slow closing solenoid valve may be used as the nozzle control valve.

In this note the effects of hysteresis and pure delay are not discussed, for the sake of brevity. It is felt that the arguments are still valid even when reasonable values of hysteresis and pure delay are present in the system.

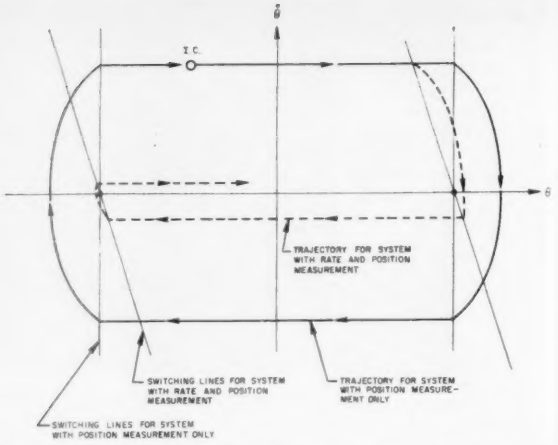
I.C.
TRAJECTORY FOR SYSTEM WITH RATE AND POSITION MEASUREMENT
SWITCHING LINES FOR SYSTEM WITH RATE AND POSITION MEASUREMENT
TRAJECTORY FOR SYSTEM WITH POSITION MEASUREMENT ONLY
SWITCHING LINES FOR SYSTEM WITH POSITION MEASUREMENT ONLY

Fig. 2 Simplified phase-plane diagram for two attitude control schemes, one with rate measurement and one without

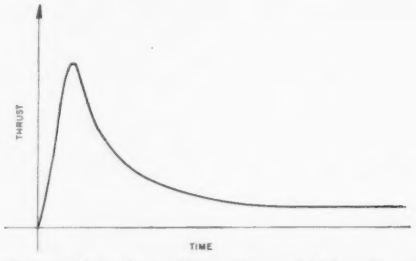

Fig. 3 Theoretical thrust-time characteristics for the differentiating gas jet

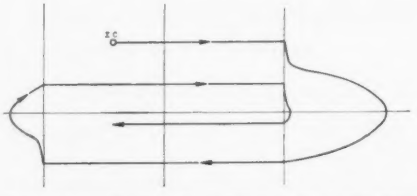

Fig. 4 Phase-plane diagram for control system with differentiating gas jet as torque producing device

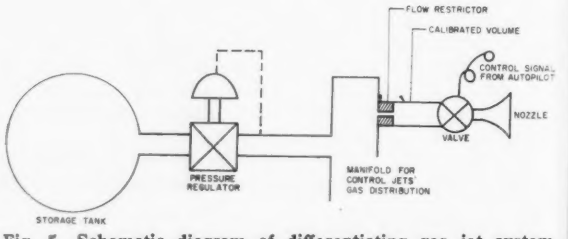

Fig. 5 Schematic diagram of differentiating gas jet system

Acknowledgments

The author wishes to express his appreciation to B. Siegel and Dr. H. A. Lassen of Space Technology Laboratories, Inc. Without their stimulating discussions the differentiating gas jet concept could not have been created.

References

1 Pipes, L. A., "Applied Mathematics for Engineers and Physicists," McGraw-Hill Book Co., Inc., N. Y., 2nd ed., 1958, chap. 22, pp. 656–715.

2 Pistner, J. S., "On-off Control System for Attitude Stabilization of a Space Vehicle," ARS JOURNAL, vol. 29, no. 4, April 1959, p. 283.

3 Haeussermann, W., "An Attitude Control System for Space Vehicles," ARS JOURNAL, vol. 29, no. 3, March 1959, p. 203.

4 Froelich, R. W. and Patapoff, H., "Reaction Wheel Attitude Control for Space Vehicles," IRE National Automatic Control Conference, Dallas, Texas, Nov. 4–6, 1959.

Instrument for Measuring Total Incident Radiant Heat Transfer to a Jet Engine Surface[1]

R. E. WALKER[2] and S. E. GRENLESKI Jr.[3]

Applied Physics Laboratory,
The Johns Hopkins University, Silver Spring, Md.

RADIANT heat transfer is a problem of increasing importance in high performance rocket and jet propulsion systems. Although the basic principles of radiant heat transfer are well established (1)[4] and considerable background on material properties in the infrared region has appeared in the literature (2), the problem of computing radiant heat transfer to critical points in a high performance jet engine is a most formidable one, and the results often give "order-of-magnitude" values for net heat transfer. The ambiguity in such calculations may include the point between safe operation for a component or thermal failure of that component.

In order to avoid these theoretical errors, the authors have designed an instrument that is simple in construction and operation and can be used on large-scale experiments where the radiant heat transfer is high (of the order of 1 cal/sec/cm²). The instrument is robust enough to withstand the severe mechanical and pneumatic forces normally encountered in ramjet engine combustion chambers where it has been successfully tested.

This instrument, shown in cross section in Fig. 1, measures the total radiation *incident* upon an orifice from a half-space (2π solid angle). The orifice is made flush with the engine wall and is shaped so that all of the radiation that enters the orifice either passes directly to a blackened receiver or is reflected off polished gold-plated surfaces to the receiver. Construction is almost entirely of copper parts with the exceptions noted in Fig. 1. Copper is used to insure the best thermal uniformity possible, and because it forms a convenient thermojunction with the constantan alloy used as part of a differential thermocouple. The radiation receiver is a thin, soot-blackened copper disk (0.50-in. diameter × 0.015-in. thick) attached to the tubular constantan support (0.125-in. O.D. × 0.010-in. wall). The orifice size and tubular support dimensions are selected so that the differential thermocouple output (the copper base-constantan support forms the cold junction and the copper disk constant support forms the hot junction), which is proportional to the incident radiant energy, can conveniently be monitored on a 0–5 or 0–10 mv recording potentiometer. Because of the large amount of radiant energy, it is unnecessary to operate the sensing element in a vacuum, since the primary loss of heat is by conduction through the solid support elements and not by convection. The soot-blackened receiver temperature seldom exceeds 100 C above the base temperature.

Two mechanisms are provided for cooling the instrument. First, cold water is circulated through an annular cavity in the main body near the orifice where the instrument is in good thermal contact with the hot engine wall, and second, pressurized air is bled through the annular space between the window tube which houses the receiver and the main body of the instrument and is exhausted through the conical orifice into the combustion chamber. This airflow serves to keep the hot engine combustion gases from damaging the instrument (in particular, the reflecting surfaces and window) and does not permit the hot gases to influence the sensitive differential thermocouple. A window is required so that the coolant airflow will not impinge directly on the receiver, and must be a material that is transparent through the infrared. Although better materials are probably available, sapphire was selected because it was commercially available in thin disks[5] and is transparent out to about 6 μ wave length. The window ($\frac{5}{8}$-in. diameter × 1-mm thick) was mounted by spinning a retaining cap onto the tube surrounding the radiation receiver and then sealed with a coat of Glyptal varnish. A small hole which opens to the cooling air annulus is drilled through the protecting tube below the hot junction, to equilibrate the pressure differential across the window.

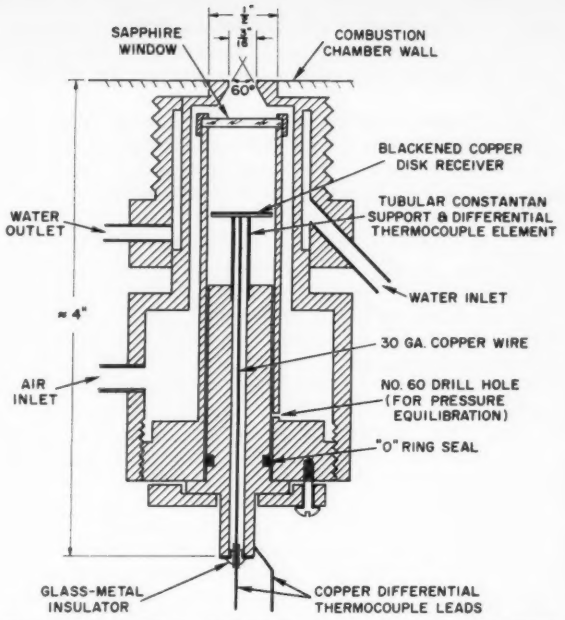

Fig. 1 Cross section of radiation meter. All parts are copper unless otherwise noted; internal surfaces are polished and gold-plated

The main body is threaded (1 in. NPT[6]) so that it can be conveniently attached and sealed to an engine wall which has been prepared by having a section of pipe nipple welded to it and then by having a hole to receive the orifice boss of the instrument drilled (coaxially). When the radiation instrument is not being used, the hole in the engine wall can be plugged with an appropriate fitting.

The receiver assembly and its tubular housing are sealed and threaded into the main body to allow for adjustment of the gap between the window and the orifice plate. In this way, a gap can be left for coolant air, whereas the incident radiation from all forward angles (180 deg) can be trapped and reflected to the receiver. Unless this gap is properly adjusted, radiation from a particular angle will be lost. All permanently assembled parts are hard (silver) soldered.

The instrument is easily calibrated with a black body made of a length of steel pipe capped on both ends and heated in a muffle furnace. A hole for the instrument was provided at one end, and, when necessary, vernier heating elements were added near the ends of the pipe to permit a uniform black-body temperature to be obtained. When calibrations are made in this manner, only a small amount of coolant air flow is required. A typical calibration curve is shown in Fig. 2, where the instrument output is plotted against the mean black-body absolute temperature raised to the fourth

Received July 5, 1960.
[1] This work was sponsored by Bureau of Ordnance, U. S. Navy, under contract NOrd 7386.
[2] Research Physicist.
[3] Research Engineer.
[4] Numbers in parentheses indicate References at end of paper.
[5] Our window materials were supplied by Linde Co., a division of Union Carbide Co.
[6] National Pipe Thread.

power. The calibration curve is essentially a straight line; however, a slight curvature can be expected at these temperatures because of the cutoff wave length for the sapphire window.

The instrument has been used successfully for measuring radiant heat transfer in research ramjet engines and full-scale ramjet engines. With a combustion chamber pressure of about 2 atm, the instrument performed satisfactorily for instrument airflows of the order of 7000 cm³ per sec and coolant water flows of about 3 gm per sec. During running periods the airflow was changed by about a factor of 2 with no significant change in the instrument output, indicating that the receiver was well isolated from and independent of the coolant. Experience indicates there is a minimum air flow that will assure keeping the cooled internal surfaces free from cracked-fuel deposits.

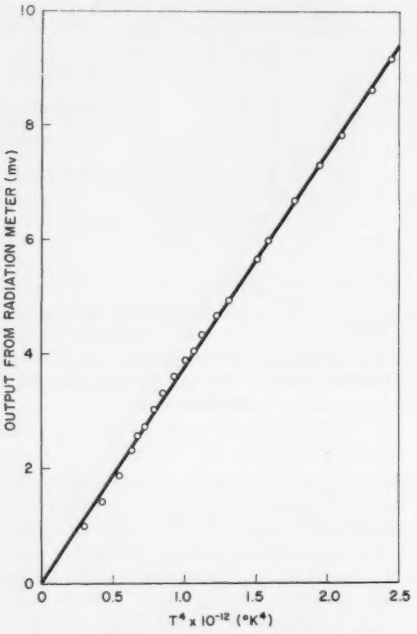

Fig. 2 Calibration of a radiation meter

The instrument has shown to be reliable (provided caution is exercised in the air and water coolant flows) by giving reproducible calibrations before and after use. It contains no moving parts that can be a problem in its abnormal environment, and the shielding of the unique differential thermocouple is adequate to permit very good zero stability (no zero drift has ever been experienced). The massive receiver, unfortunately, has a long time constant (about 30 sec) that does not permit measurement of rapidly varying radiant heat transfer—a more delicate receiver would be necessary if more rapid response were desirable.

A miniaturized model (about half the size of the one shown in Fig. 1) has been built and is presently being tested. In this model the orifice is about one half of the original size, whereas the sensitivity has been kept about the same by notching the constantan support in such a manner as to increase the effective length and decrease the cross-sectional area of the support tube. The blackened receiver has been placed closer to the sapphire window to avoid unnecessary reflections.

Acknowledgments

The authors would like to express their thanks to Drs. W. H. Avery and G. L. Dugger for their discussions and support while developing this instrument. We should also like to thank the several engineering personnel who helped in the tests, and, in particular, N. deHaas who helped considerably in preliminary laboratory examinations.

References

1 Jacob, M., "Heat Transfer," John Wiley & Sons, Inc., N. Y., 1949.

2 Crowley, D. E., "Emittance and Reflectance in the Infra Red, an Annotated Bibliography," IRIA 2389-15-S, The University of Michigan, Willow Run Laboratories, Ann Arbor, Mich., 1959.

Heat Transfer Gage for Use in Highly Ionized Gases[1]

RICHARD W. ZIEMER[2]

Space Technology Laboratories, Inc., Los Angeles, Calif.

A DIFFICULT problem in studies of high temperature hypersonic aerodynamics has been that of obtaining laboratory heat transfer measurements in the presence of highly ionized gases. Conventional metallic film resistance thermometers are precluded because of shunting and charge pickup by the electrically conducting gas in contact with it. To overcome this difficulty, thin electrically insulating coatings of silicon monoxide have been applied over the gage. This technique has been successful at low ionization levels. However, with highly ionized gases, much thicker insulation is required. Unfortunately, the increased thickness of insulation seriously decreases gage responsivity. The situation is made even more difficult if the gage is to be used in conjunction with an electromagnetic shock tube because of the very short duration of "steady-state" conditions, and because of induced electrical noise from the high voltage discharges.

Received June 10, 1960.

[1] Prepared for the Air Force Ballistic Missile Division Headquarters Air Research and Development Command under Contract AF 04(647)-309, magnetoaerodynamic research.

[2] Presently Senior Scientist, Astro Sciences, Norair Div., Northrop Corp., Hawthorne, Calif. Member ARS.

One solution of the problem is to use a wire resistance gage instead of the thin metal film. A wire of small radius, when used as both the test body *and* the resistance element, offers several advantages over the flat film gage. The wire has a small radius, and, since the heat transfer rate per unit area varies as $r^{-1/2}$, high rates result. Also there is no substrate to act as a heat sink, as in the case of the film. Both of these effects increase gage response permitting the use of the necessary thicker insulation.

In order to achieve maximum response of the wire gage, the rate of temperature rise ΔT should be as large as possible. The average rate of temperature rise of the wire is given by

$$\Delta T = Q/c_p m$$

where m is the mass of the wire per unit length. The heat transfer rate to the wire per unit length is

$$Q \approx 2\int_0^{\theta=\pi/2} r\, q(\theta) d\theta = (\text{constant})\, q_0 r$$

in which θ is the polar angle measured from the forward stagnation point. Since

$$m = \rho \pi r^2$$

it is seen that

$$\Delta T \sim r^{-3/2}$$

Thus, for high gage response per unit length, the wire radius should be small.

The operating principle of a resistance thermometer is well known. The circuit normally consists of a constant current loop, containing the resistance element in series with a large constant resistance. The wire resistance is determined by simply measuring the potential drop across the element.

The variation of the wire resistance with temperature is given by the linear relation

$$R = R_0[1 + \alpha(T - T_0)]$$

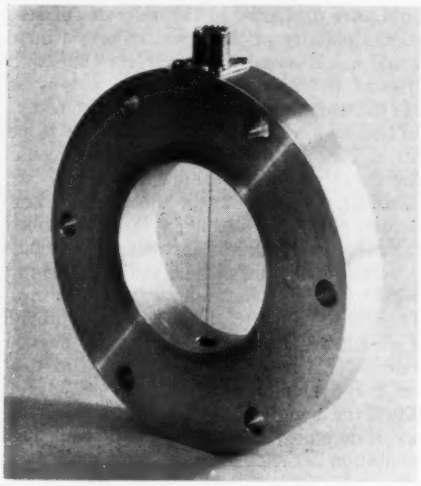

Fig. 1 **Resistance wire heat transfer gage assembly**

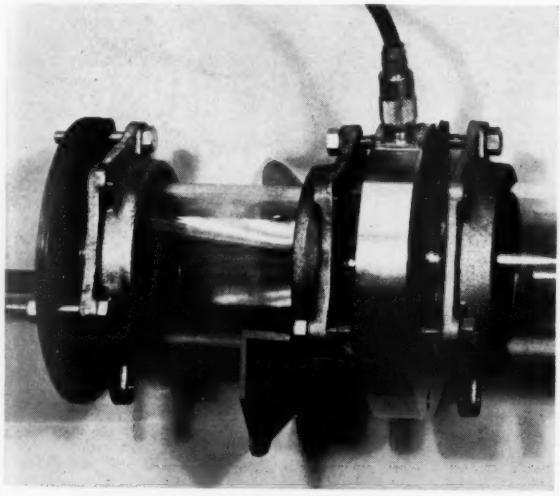

Fig. 2 **Heat transfer gage assembly installed in 3-in. diameter electromagnetic shock tube**

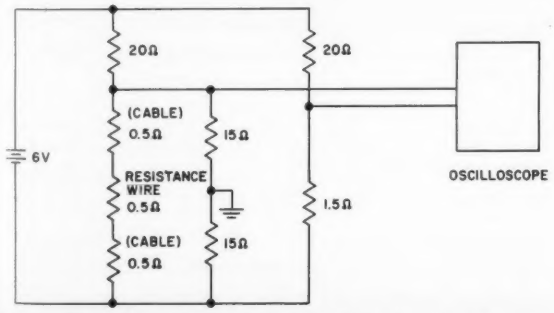

Fig. 3 **Floating bridge measuring circuit for heat transfer gage**

where

α = temperature coefficient of resistance
R_0 = wire resistance at some reference temperature T_0

The temperature of the resistance element is expressed in terms of the measured voltage drop E as

$$T = \frac{R - R_0}{\alpha R_0} + T_0 = \frac{E - E_0}{\alpha R_0 I_0} + T_0$$

Thus, the temperature is determined directly from the measured change in potential across the wire.

The gage was designed to be used in a 3-in. ID electromagnetic shock tube, as shown in Figs. 1 and 2. The flange supporting the wire is bolted between sections of the shock tube pipe. The flange contains a spring-loaded hook which suspends the resistance wire diametrically across the passage. The wire doubles back parallel to itself, to expose a double length of wire to the flow, thereby doubling the signal output. The spacing is six wire diameters, sufficient to eliminate aerodynamic interference and yet small enough to minimize magnetic induction in the circuit. The electrical connection between the resistance element and double conductor cable is shielded from electromagnetic pickup by the flange, and the cable connector is vacuum sealed.

For the resistance wire, AWG 40-gage copper magnet wire with Single Formvar insulation was chosen, since it was the smallest diameter wire with single insulation readily available. The wire diameter is 0.0031 in., and the wall thickness of the electrical insulation is 0.0002 in. The temperature coefficient of resistance of the copper is 0.0022 per deg F.

Experience with instrumentation circuits used with the electromagnetic shock tube has shown that floating circuits are necessary to minimize the effects of severe ground float accompanying the high voltage discharge. The floating bridge circuit shown in Fig. 3 was used. The balanced bridge allows a d-c differential amplifier to be used, which has a better rejection ratio than an a-c unit. The two 15-ohm leakage resistors reduce the float of the circuit without appreciably affecting the measured signal.

The heat gage device was tested in the 3-in. electromagnetic shock tube. The wire was located 16.5 in. from the downstream edge of the ring electrode. The shock tube was operated with air at an initial pressure of 50 μ. The driving energy was supplied by 9 μf of capacitance charged to 25 kv. (Details and operation of the electromagnetic shock tube are described elsewhere.[3]) At these conditions, a shock wave of Mach 30 is generated, causing air to flow over the wire at a static temperature of 9000°K and a velocity of 31,000 fps, with a steady flow duration of about 25 μsec.

The gage current was 232 milliamps, and the resistance of the wire at room temperature was 0.5 ohm. The voltage drop across the wire was measured with a 545 Tektronix oscilloscope with a 53/54 D-differential preamplifier. The scope trace was triggered by the triggering pulse to the shock tube.

The observed signal of the voltage across the wire is shown in Fig. 4. The sweep speed was 50 μsec per cm with an amplifier gain of 10 mv per cm. The trace shows the 10-μsec delay from the initial triggering pulse until the shock tube fires. When the high voltage capacitors discharge, severe noise pickup is observed and continues until about 55 μsec. The shock wave arrives at the wire at 45 μsec (as determined from a simultaneous rotating mirror camera photograph), and the wire is subsequently heated by the high velocity and high temperature gases. At about 80 μsec the rate of temperature rise decreases, until at 160 μsec the wave reflected from the end of the tube arrives at the wire. The small rise in temperature (resistance) after this may be a result of

[3] Ziemer, R. W., "Electromagnetic Shock Tubes," presented at Third Biennial Gas Dynamics Symposium, Evanston, Ill., Aug. 24–26, 1959; ARS preprint 906–59.

equilibration of the temperature distribution in the wire and insulation or continued heating by the essentially stagnant but hot gases.

The rate of temperature rise as determined from the slope of the curve, was 2.02 F per μsec. This corresponds to a total heat transfer rate to the wire of approximately 21,000 Btu per ft^2 sec, based on frontal area. Heat transfer measurements were made at only one initial pressure, although no problem is anticipated in operating at other free stream conditions.

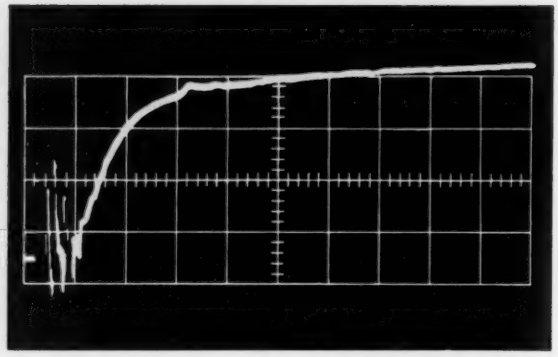

Fig. 4 Output signal of gage for shock tube initial pressure of 50 μ and shock Mach number of 30. Free stream temperature and velocity are 9000 K and 31,000 fps. Sweep speed is 50 μsec per cm, and gain is 10 mv per cm

To determine the validity of the observed signal as a true resistance measurement rather than an induced voltage signal, the trace was observed at slower sweep speeds. It was found that after reaching a maximum resistance at about 500 μsec, the signal remained constant until about 100 millisec, at which time it decayed exponentially, returning to the original resistance after a total of about 5 sec. Such response must have been a result of thermal effects, since any induced voltages would have dissipated in the order of milliseconds. In addition, the polarity of the signal indicated increasing resistance and was reversed with reversal of battery polarity.

The use of the insulated resistance wire is admittedly limited to the transverse circular cylinder geometry, and only the total surface integrated heat transfer rate is measurable. In addition, because of the small diameter, conditions approaching the slip flow regime are encountered, except at the higher densities obtainable in the shock tube. For example, at the density of the free stream gas in the described test, the molecular mean free path was approximately 0.002 in., which is of the same order of magnitude as the 0.0035-in. diameter of the wire. (The Reynolds number based on wire diameter was estimated to be 0.9.) However, it also provides an important advantage, since the heat gage may be used to study heat transfer phenomena of ionized gases in the slip flow regime of fluid dynamics.

In spite of the definite limitations of the insulated resistance wire gage, it does provide a simple tool for some heat transfer experimentation in the presence of highly ionized gases.

Optimum Radiant Straight Fin With Exponential Sides

IRVING GRANET[1] and WILLIAM McILROY[2]

Republic Aviation Corp., Farmingdale, N. Y.

SEVERAL recent papers (1,2)[3] have emphasized the fact that radiation is the only mode of heat rejection in space. For a propulsion system operating in a space environment, it is readily apparent that the largest single component (and the heaviest) will be the space radiator. Therefore, the reduction of the weight of such a radiator per unit of heat rejected becomes a prime objective for the designer. As in conventional units, the proper use of fins can lead to savings in weight. This conclusion is true even when the only mode of heat transfer is by radiation.

In order to solve such a problem, i.e., of a fin radiating to space, several assumptions will be made (3):

1 The fin material is isotropic.
2 The fin radiates to a vacuum space which is at an assumed temperature of absolute zero.
3 The temperature at the base of the fin is constant.
4 There are no heat sources or heat sinks in the fin.
5 The heat flow is steady-state, i.e., time-independent.
6 The thermal conductivity of the fin is constant.
7 The heat transferred through the outermost edge of the fin is negligible compared with that passing from the fin through its sides.
8 The fin and base are integral, i.e., the bond resistance is zero.
9 Heat is assumed to flow along the axis of symmetry only.
10 The heat transfer is considered to be one dimensional.

On the basis of the foregoing assumptions it is possible to formulate the problem in the following manner by considering Fig. 1. The sides of the fin will have the following assumed exponential form

$$y = me^{-nx} \qquad [1a]$$

where

$y = w$ at $x = 0$

$y = h$ at $x = L$

Therefore

$$y = we^{-nx} \qquad [1b]$$

In this fin, w is specified but h is not.

The Fourier equation for one-dimensional steady-state heat transfer is

$$q = -KA(dT/dx) \qquad [2a]$$

which for this case is

$$q = -K2y(dT/dx) \qquad [2b]$$

The rate of change of heat flow with respect to distance which equals the heat flow out, in steady state, is

$$\frac{dq}{dx} = \left(\frac{d}{dx}\right)\left(-K2y\frac{dT}{dx}\right) = Q \qquad [3]$$

Received July 29, 1960.
[1] Associate Scientist, Plasma Propulsion Laboratory.
[2] Scientist, Plasma Propulsion Laboratory.
[3] Numbers in parentheses indicate References at end of paper.

On the basis of the listed assumptions and denoting the emissivity and angle factors by F_e and F_A, respectively, Equation [3] can be written in the form

$$-K\frac{dT}{dx}\,2\frac{dy}{dx} - 2yK\frac{d^2T}{dx^2} = 2F_AF_e\sigma T^4\frac{dS}{dx} \qquad [4]$$

Rearranging Equation [4] and simplifying yields

$$\frac{d^2T}{dx^2} + \frac{dT}{dx}\frac{(dy/dx)}{y} + F_AF_e\sigma T^4\frac{(dS/dx)}{y} = 0 \qquad [5]$$

where y is given by Equations [1].

Equation [5] is highly nonlinear, and the only method of solving for the temperature distribution is to program it for a computer such as the IBM 704. Such a procedure was used in (4 and 5), and solutions for temperature distribution for two specific cases are presented in these papers. From the temperature distribution the heat flow can readily be evaluated.

While the foregoing procedure is general and can be made to yield the desired results, it does so in a roundabout manner. The designer needs to know the amount of heat the fin can dissipate, not its temperature distribution. A procedure has therefore been devised which yields the heat dissipation in closed mathematical form. This procedure is applied to the case of the optimum fin, i.e., maximum heat rejection per unit volume of fin, and can be extended to any fin shape. For the "exponential" fin the results are extremely interesting. The quantity to be optimized is

$$\frac{Q}{V} = \frac{\int_0^L 2\sigma yF_AF_eT^4dS}{\int_0^L 2we^{-nx}dx} \qquad [6]$$

In general, F_A and T are unknown functions of y. Keeping these terms under the integral and denoting the integral by I where

$$I \equiv \int_0^L yF_AT^4dS \qquad [7]$$

Equation [6] becomes

$$\frac{Q}{V} = \frac{2\sigma F_eI}{2(w/n)(1 - e^{-nL})} \qquad [8]$$

In order to optimize Q/V it is necessary that the derivative of Q/V with respect to the variable (in this case n) be equated to zero.

$$\frac{d}{dn}\left(\frac{Q}{V}\right) = 0 = \frac{d}{dn}\left[\frac{\sigma F_eIn}{w(1 - e^{-nL})}\right] \qquad [9]$$

Performing the differentiation and grouping terms, one finds the following relation

$$\frac{dI}{I} = dn\left(\frac{Le^{-nL}}{1 - e^{-nL}} - \frac{1}{n}\right) \qquad [10]$$

By changing variable, integrating and simplifying

$$I = \frac{I_0(1 - e^{-nL})}{nL} \qquad [11]$$

The remarkable consequence of Equation [11] is the fact that the unknown integral I is explicitly defined and such items as F_A do not enter the evaluation of the maximum heat transfer for this type of fin. Replacing [11] in [8] yields this result

$$\left(\frac{Q}{V}\right)_{max} = \frac{\sigma F_eI_0[(1 - e^{-nL})/nL]}{(w/n)(1 - e^{-nL})} = \frac{\sigma F_eI_0}{wL} \qquad [12]$$

Once again this yields the unique and even surprising result that the optimum Q/V is a simple function.

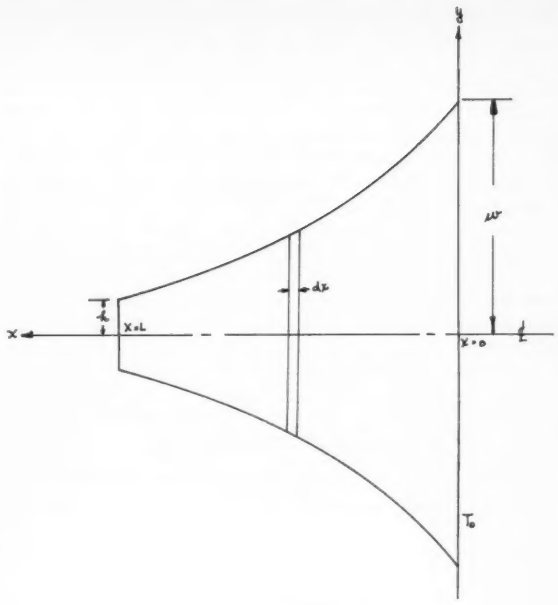

Fig. 1 Fin configuration

Equation [12] can be derived in an alternate and more elegant manner as follows.

From Equation [9] it is evident that the derivative of a function can only be zero if the function is a constant with respect to the argument. Therefore $(Q/V)_{max}$ is a constant, independent of n. Thus $(Q/V)_{max}$ can be evaluated by simply placing n equal to zero in Equation [8] and noting that

$$\lim_{n\to 0}[(1 - e^{-nL})/n] = L$$

This procedure yields Equation [12]. Thus I_0 is to be understood to correspond to a fin with n equal to zero in Equation [1b].

To evaluate I_0 in Equations [11 and 12] still remains. Two limiting cases are available for this purpose. The first is the case of $n = 0$. For this case y equals w and the fin degenerates to a rectangular fin radiating to space. This is exactly the case solved by Chambers and Somers (4), and I_0 is thus evaluated directly from their paper. The second condition is when $L = 0$. This resolves itself into a flat plate of width $2w$ at T_0 radiating to space. This, of course, is the value of I_0 corresponding to the limiting solution Chambers and Somers have plotted. Therefore, I_0 can be identified as being identical to the solution for a square fin radiating to space under the same imposed assumptions as used herein.

The value of the exponent n (corresponding to the optimum condition) can readily be evaluated from a heat balance. If it is known that a certain amount of heat is to be transferred, then

$$Q = 2F_e\sigma I = [2F_e\sigma I_0(1 - e^{-nL})]/nL \qquad [13]$$

and n is determined.

A further observation regarding these solutions can be made. The exponential fin volume is $(2w/n)(1 - e^{-nL})$, and the volume of a rectangular fin is just $(2w/L)$. Therefore the fin volume divided by a rectangular fin volume is $(1 - e^{-nL})/nL$, but this is identically equal to I/I_0. Therefore

$$\frac{I}{I_0} = \frac{\text{volume of exponential fin}}{\text{volume of rectangular fin}} \qquad [14]$$

It can be demonstrated that the procedure outlined herein

can be used for shapes composed of several exponentials, i.e.

$$y = A_1 e^{-n_1 x} + A_2 e^{-n_2 x} + \ldots \quad [15]$$

In other words, by a simple approximation almost any shape of fin can be solved easily. This technique may also be applied to other fins of nonexponential shape, where y is *any* function of x, without using the exponential approximation. In such a case the resulting expressions are not simple but the procedure is still valid. It is also equally evident that this procedure applies to convection heat transfer as well as radiant heat transfer. If there is a longitudinal temperature gradient along the fin as might be found in a heat exchanger, methods already developed can be applied directly (6) once the shape is determined by the methods outlined in this paper.

Nomenclature

S = surface area per unit fin length
e = 2.718+...
F_A = geometric factor (view factor)
F_e = emissivity factor
h = half height of fin at $x = L$
I_0, I = integrals defined in the text
K = conductivity of fin—constant
L = length of fin
m, n = shape constants
q = total heat flow along fin per unit length of fin
Q = heat removed per unit length of fin
V = volume per unit length
w = half height of fin at $x = 0$
x = any position along fin
σ = Stefan-Boltzmann constant
A = heat flow area per unit length of fin

References

1 Sutherland, G. S., "Recent Advances in Space Propulsion," ARS JOURNAL, vol. 29, no. 10, Oct. 1959, pp. 698–705.
2 Bussard, R. W. and De Lauer, R. D., "Nuclear Rocket Propulsion," McGraw-Hill Book Co., N. Y., 1958.
3 Kern, D. Q., "Process Heat Transfer," McGraw-Hill Book Co., N. Y., 1950.
4 Chambers, R. L., and Somers, E. V., "Radiation Fin Efficiency for One-Dimensional Heat Flow in a Circular Fin," ASME paper 59-HT-8.
5 Nilson, E. N. and Curry, R., "The Minimum-Weight Straight Fins of Triangular Profile Radiating to Space," *J. Aero/Space Sci.*, vol. 27, no. 2, Feb. 1960, pp. 146–147.
6 Granet, I., "Heat Transfer Performance Curves," *Chem. Engng.*, vol. 62, March 1955, pp. 187–190.

Shock Tunnel Experimental Techniques for Force and Moment and Surface Flow Direction Measurements[1]

W. R. WARREN,[2] E. M. KAEGI[3] and R. E. GEIGER[4]

General Electric Co., Philadelphia, Pa.

RECENTLY, two relatively new measurement techniques have been found to be useful in shock tunnel experimental studies. The purpose of this note is to describe these techniques as they have been employed in the General Electric MSVD shock tunnel. Detailed descriptions of the facility and its performance can be found in (1 and 2).[5]

Fig. 1 is a schematic representation of the method that has been used to obtain lift, drag and pitching moment data for hypersonic vehicle shapes over an approximate Mach number range of 12 to 18. A light-weight (cast Isofoam, generally weighing from 1 to 5 gm) model is suspended in the shock tunnel test section on thin (0.5–1.5 mils) nylon strands. The strands break at the beginning of the test flow, and the model flies freely under the influence of the aerodynamic forces it experiences. For the current three component studies, the model is flown horizontally, i.e., with the force vector in the horizontal plane. A 26,000 frame per sec camera (Beckman Whitley Dynafax) is used to record the model motions. A direct reading of the film, upon which a stationary grid is also imaged, provides trajectory information from which force data are deduced.

To minimize the variation of forces during a run, the model center of gravity is adjusted in an attempt to locate it at the aerodynamic center of the body (actually at a point lying on the line of motion of the resultant aerodynamic force). The c.g. location is obtained by a preferential hollowing out of the model; the pitch moment of inertia is then measured. Models are generally destroyed during test runs; however, for most shapes of interest, their cost is low, and their preparation time is short. In practice, the objective of no model rotation, or pitch, is difficult to obtain; however, a small amount of rotation can be accepted since its effects on lift, drag and pitching moment can be estimated satisfactorily (3,4). It has been found that only a small percentage of the runs made with this technique are not acceptable. Since the model velocity during a typical test period reaches only the order of 1 per cent of the

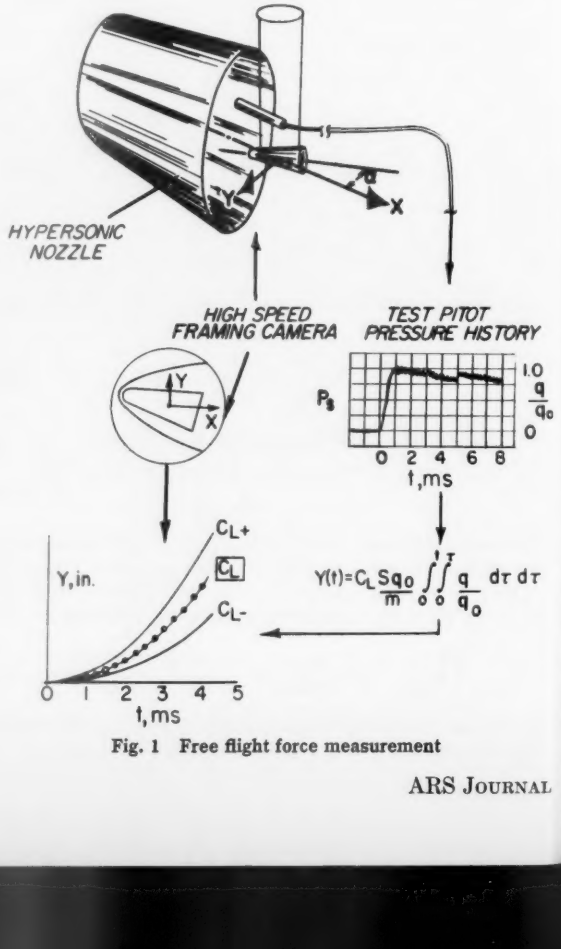

Fig. 1 Free flight force measurement

Received Aug. 19, 1960.
[1] This work was supported by the Air Force Ballistic Missile Division under Contract AF 04(647)269.

[2] Manager, Aerothermodynamics, Space Sciences Lab., Missile and Space Vehicle Dept. Member ARS.
[3] Aerodynamicist, Space Sciences Lab., Missile and Space Vehicle Dept.
[4] Hypersonics Specialist, Space Sciences Lab., Missile and Space Vehicle Dept.
[5] Numbers in parentheses indicate References at end of paper.

free stream velocity, it is assumed that dynamic effects can be neglected.

The following data reduction technique is used to eliminate the need for double differentiation of the model trajectory data. A pitot pressure probe, located in the test section, measures model stagnation pressure during the quasi-steady test flow time (see Fig. 1). The free stream dynamic pressure q is then calculated from the normal hypersonic relationships, and it is assumed that the q/q_0 history is similar to the p_s history. If it is assumed that the force coefficients are constant throughout the run [variations with angle of attack are discussed in (3)], a trajectory relationship can be established, as shown in Fig. 1, which requires simply a double integration of the q/q_0 history. A family of curves for various constant coefficient values (in this case C_L) can be constructed and compared with the observed motion. The best match then gives the actual force coefficient (Fig. 2). Fig. 3 illustrates the results obtained from this procedure on a lifting body over a wide angle of attack range.

To our knowledge, personnel of the Naval Ordnance Laboratory, Silver Springs, Md., were the first to use freely flying models in shock tunnel flows (5). It is our understanding that the present method, which is suitable for the determination of static aerodynamic coefficients only, employs an approach different from that used at NOL.

The second shock tunnel experimental technique involves the generation of oil streak patterns on the surface of bodies subjected to the test flow. Such data are useful in heat transfer studies and in developing an understanding of complex three-dimensional flows. Typical results obtained with this technique are shown in Figs. 4. Just prior to a test run, thin layers of SAE 30 weight oil mixed with a finely divided molybdenum disulfide powder are painted in rings around the models. Apparently, the impulse given to the oil during the short duration test time is of sufficient magnitude both to impart the proper flow direction to the mixture and to appreciably thin the layer so that it is unaffected by the later shock tunnel flow processes (after initial test period). To date, conclusions drawn from observations of the resultant flow patterns have been in qualitative agreement with those generated by other measurements; thus, it is believed that the validity of the technique is reasonably well established.

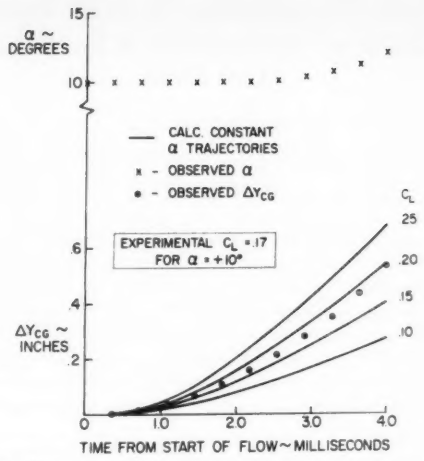

Fig. 2 Trajectory matching scheme for lift (and drag) coefficient determination

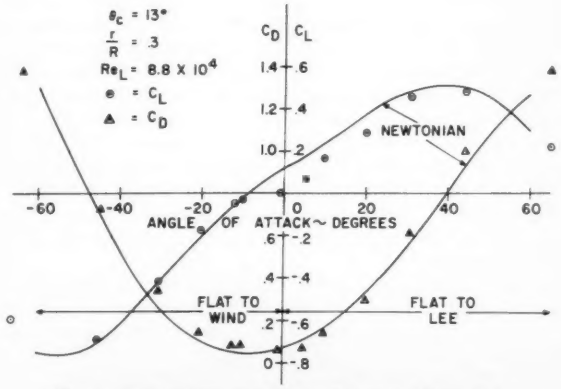

Fig. 3 Half sphere-cone lift and drag at Mach 17.5

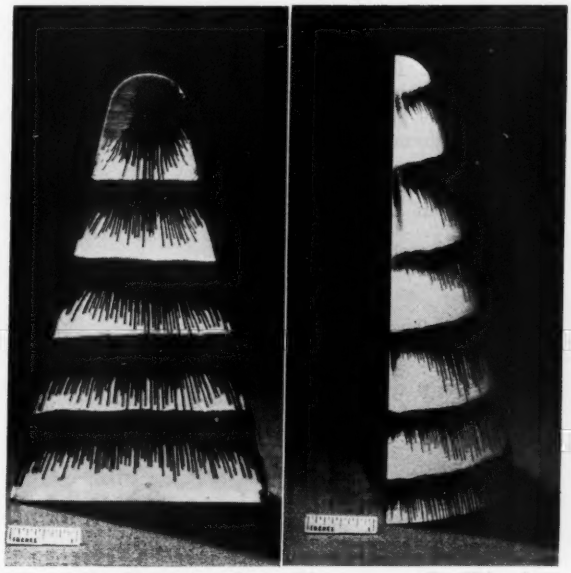

(a) $\alpha = 0°$. Flat surface view, flat surface parallel to free stream direction

(b) $\alpha = -15°$. Side view, flat surface to windward

Figs. 4 Oil streak patterns on half sphere-cone body, Mach 12.4 $\theta_c = 13°$, $r/R = 0.3$

Nomenclature

- m = mass of model
- p_s = test section pitot pressure
- q = free stream dynamic pressure
- r = model nose radius
- t = time
- C_D = drag coefficient
- C_L = lift coefficient
- R = model base radius
- Re_L = Reynolds number based on model length
- S = reference area (flat surface in Fig. 3)
- X = displacement in drag direction
- Y = displacement in lift direction
- α = angle of attack
- θ_c = cone half angle
- τ = dummy variable

References

1 Warren, W. R., "Laboratory Experimental Studies in Re-Entry Aerothermodynamics," GE MSVD TIS Rep. no. R59SD362, May 1959. Proc. 10th Int. Astronautics Cong., Sept. 1959, London, England.

2 Vitale, A. J., Kaegi, E. M., Diaconis, N. S. and Warren, W. R., "Results From Aerodynamic Studies of Blunt Bodies in Hypersonic Flows of Partially Dissociated Air," Proc. 1960 Heat Transfer and Fluid Mechanics Inst., June 1958, Berkeley, Calif.

3 Kaegi, E. M., Malczynski, J. R. and Warren, W. R., "The Measurement of Aerodynamic Forces in Shock Tunnel Test Flows," GE MSVD TIS Rep. no. R60SD339, March 1960.

4 Geiger, R. E., "Experimental Lift and Drag of a Series of Glide Configurations at Mach Numbers 12.4 and 17.5," IAS Paper no. 60-92, presented at the IAS National Summer Meeting, June 1960, Los Angeles, Calif.

5 Seigal, A. E, "Millisecond Measurement of Forces and Moments in Hypersonic Flow," NOLR 1238, May 1959.

Thrust Termination in Solid Rocket Motors—Evaluation of Ballistic Test Data

SHERWIN KALT[1]

Lockheed Aircraft Corp., Missiles and Space Div., Sunnyvale, Calif.

This paper investigates the interpretation of the chamber pressure measurement as an indication of the time of full opening of a thrust termination system in a solid rocket motor. Quasi steady-state equations are used to derive the expected pressure-time history for any assumed open thrust termination port area. The same approach is used to derive equations showing the relation between a measured pressure-time curve and the effective port area open at any time.

THRUST termination systems in solid rocket motors are generally designed to deliver a specified negative thrust level (or ratio of reverse to forward thrust) within a few millisec after termination signal. The most direct method of verifying proper termination is the measurement of thrust in a static test of the rocket motor. However, especially in the case of large motors, it is difficult to measure thrust with response rapid enough to evaluate the ballistics of reversal. Chamber pressure measurements, on the other hand, may be made with considerably better dynamic response. This paper, therefore, summarizes analytical methods which may be used to determine ballistic parameters from chamber pressure measurements. The response time obtained will, then, be limited by the natural frequency of the gases in the combustion chamber.

Fig. 1 is a sketch of a solid rocket motor after opening of n thrust reverser ports. The following derivation will indicate the expected change in chamber pressure with time after an assumed reversal port area A_r is opened.

Gas flow rate out of the motor can be expressed as

$$W_{out} = C_{WR}PA_r + C_{wt}PA_t \quad [1]$$

where

W_{out} = gas flow rate out of motor
C_{WR} = mass flow coefficient of combustion products through reversers
C_{wt} = mass flow coefficient of combustion products through nozzle
P = chamber pressure
A_r = area of reverser ports open
A_t = nozzle throat area

The mass flow coefficient is defined as

$$C_W = W_{out}/PA_t \quad [2]$$

For isentropic flow of a perfect gas (1)[2]

$$C_W = \frac{W_{out}}{PA_t} = \sqrt{\frac{kg}{RT}\left(\frac{2}{k+1}\right)^{(k+1)/(k-1)}} \quad [3]$$

where

k = ratio of specific heats
g = gravity constant
R = gas constant per unit weight
T = chamber, or stagnation, temperature

Equation [3] applies for sonic flow and is otherwise independent of conditions outside the throat. From the above equation, it can be seen that the mass flow coefficient is primarily a function of combustion gas properties, and therefore in most cases it may be assumed that $C_{WR} = C_{wt}$. Equation [1] becomes, then

$$W_{out} = C_WP(A_t + A_r) \quad [4]$$

where C_W is the mass flow coefficient for combustion products.

The rate of generation of propellant combustion products can be expressed as

$$W_G = A_b\rho_paP^n \quad [5]$$

where

W_G = rate of gas generation
A_b = total exposed propellant burning surface at time t
ρ_p = solid propellant density
a, n = empirical constants determined for the propellant from the burning rate equation: Burning rate $= aP^n$

Conservation of mass, applied in conjunction with Equations [4 and 5], leads to the following expression

$$dW = [A_b\rho_paP^n - C_WP(A_t + A_r)]dt \quad [6]$$

where W = weight of propellant gases in rocket chamber at time t.

Assuming that the perfect gas law applies, and that changes in the chamber free volume are negligible in the time interval considered

$$dP = (RT/V)dW \quad [7]$$

where V = chamber free volume (volume occupied by combustion products).

Substituting in Equation [7] for dW as defined in Equation [6]

$$dP = (RT/V)[A_b\rho_paP^n - C_WP(A_t + A_r)]dt \quad [8]$$

Integration of Equation [8] yields

$$t - t_i = \frac{V}{-RTC_W(A_r + A_t)(n-1)} \times \ln\left\{(P/P_i)^{n-1}\left[\frac{A_b(RT/V)\rho_paP_i^{n-1} - (RT/V)C_W(A_r + A_t)}{A_b(RT/V)\rho_paP^{n-1} - (RT/V)C_W(A_r + A_t)}\right]\right\} \quad [9]$$

where

P_i = chamber pressure at time of reverser port opening
t_i = time of reverser port opening

Equation [9] may be simplified by introducing another expression for the mass flow coefficient. It is assumed, here, that numerically the same value can be used for C_W during

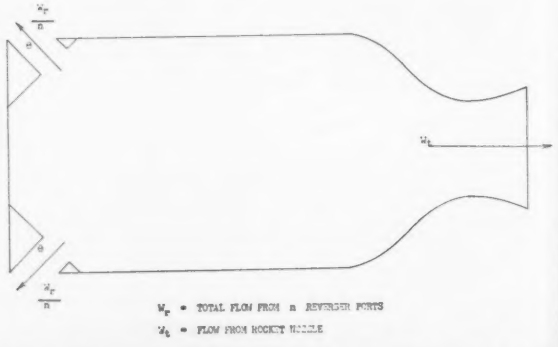

Fig. 1 Schematic representation of solid rocket motor after opening of thrust termination ports

Received Aug. 4, 1960.
[1] Senior Research Engineer, Propulsion Department.
[2] Numbers in parentheses indicate References at end of paper.

transients as under steady-state conditions, and as indicated by Equation [3], C_W is relatively constant with chamber pressure. For conveni nce, C_W is expressed in terms of steady-state conditions before the termination ports open, when $P = P_i$. For these conditions

$$W_{out} = C_W P_i A_t = W_G = A_b \rho_p a P_i^n \qquad [10]$$

Therefore

$$C_W = A_b \rho_p a / A_t P_i^{1-n} \qquad [11]$$

Substituting Equation [11] for C_W in Equation [9]

$$\frac{V}{RTC_W(A_t + A_r)(1 - n)} \ln \frac{1 - [A_t/(A_t + A_r)]}{(P/P_i)^{1-n} - [A_t/(A_t + A_r)]} = t - t_i \qquad [12]$$

Chamber pressure will tend to approach a lower value determined by the denominator of the second term in Equation [12], or

$$\left(\frac{P}{P_i}\right)^{1-n} = \frac{A_t}{A_t + A_r} \qquad [13]$$

A predicted curve of chamber pressure, as a function of time after termination port ejection, can be determined from Equation [12] for different assumed values of port area A_r. Fig. 2 is a graph of the relations between the dimensionless parameters $(P/P_i)^{1-n}$ and $(RT/V)C_W(A_t + A_r)(1 - n)(t - t_i)$ for different values of $A_t/(A_t + A_r)$, based on Equation [12].

It is possible to present the above equations in a form convenient for direct analysis of test data rather than for prediction. Equation [8] may be rearranged as follows

$$A_r + A_t = \frac{A_b \rho_p a P^{n-1}}{C_W} - \frac{V}{RTC_W} \frac{dP/P}{dt} \qquad [14]$$

Substitution of Equation [11] and further rearrangement gives

$$\frac{A_r}{A_t} = \left[\left(\frac{P_i}{P}\right)^{1-n} - 1\right] - \frac{V}{A_t RTC_W} \frac{1}{P} \frac{dP}{dt} \qquad [15]$$

which can be expressed in terms of thrust as

$$\frac{F_R}{F_t} = \frac{C_{FR} \cos \theta}{C_{Ft}} \frac{A_r}{A_t} \qquad [16]$$

where

F_R = reverse thrust
F_t = forward thrust
C_{FR}, C_{Ft} = reverse and forward thrust coefficients
θ = effective angle of action of thrust reversers relative to the longitudinal axis

In some cases, the burning rate of a propellant may be expressed in terms of a_1 and n_1 within the range of pressures P_i to P_1, and in terms of a_2 and n_2 within the range P_1 to P_2. In these cases, when applying Equations [12 and 15] in the range P_1 to P_2, the value n_2 is used; in addition, P_{ia} (the apparent initial steady-state chamber pressure which would have existed if the constants a_2 and n_2 had applied through the range P_{ia} to P_2) is used in place of P_i. The value of P_{ia} may be derived from Equation [11], assuming the mass flow coefficient is constant over the range of pressures involved. This gives

$$P_{ia}^{1-n_2} = \left(\frac{a_2}{a_1}\right) P_i^{1-n_1} \qquad [17]$$

Chamber pressure variation with time will be unaffected by ambient pressure for all cases where sonic flow is established in the exhaust. When subsonic flow exists, the above equations do not apply without the use of proper mass flow coefficients for subsonic flow. This condition will exist initially during ejection of thrust reverser port covers. However, the time required for establishing sonic flow will generally be less than 1 millisec, and may be estimated from (2). During this short transient condition, it is not expected that a quasi steady-state analysis as made in the preceding paragraphs would give a good approximation regardless of the choice of mass flow coefficient.

Following is an example of the calculation of reverser port opening using the methods discussed previously.

A solid rocket is thrust terminated at a chamber pressure of 500 psia. The nozzle throat area of the rocket is 150 in.^{2}. The motor uses eight reverser ports, each with a total area when open of 40 in.^{2}. Combustion products in the chamber have a stagnation temperature of 4500 R, ratio of specific heats of 1.25, and molecular weight of 25. The mass flow coefficient has been determined to be 0.0074 lb-mass per lb-force sec. The burning rate equation for the propellant is $r = 0.03P^{0.3}$ in. per sec for a pressure range of 300 to 1200 psia, and $r = 0.04P^{0.25}$ in. per sec for a pressure range of 50 to 300 psia. The chamber free volume is 400,000 in.^{3}. Fig. 3 shows a pressure measurement taken during thrust termination. It is necessary to calculate reverser port opening during termination.

Equation [15] can be applied to calculate reverser port area at any time after termination signal. For example, at 31 millisec after termination signal, chamber pressure 460 psia. The slope of the pressure-time curve is −2340 psi per sec. The other constants employed in Equation [15], presented in

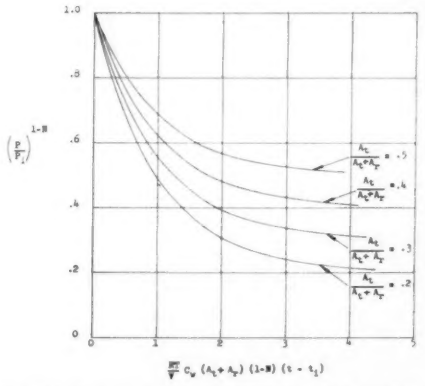

Fig. 2 Graphical representation of Equation [12], relating chamber pressure to time after thrust termination

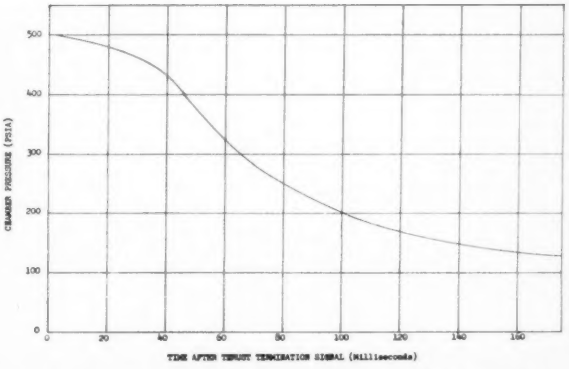

Fig. 3 Example of a measured chamber pressure curve after thrust termination signal

a consistent set of units, are

P_i = 500 psia
n = 0.3
V = 231.5 ft³
A_t = 1.042 ft²
R = 1546/25 = 61.84 ft-lbf per lbm deg R
T = 4500 R
C_W = 0.0074 lbm per lbf sec

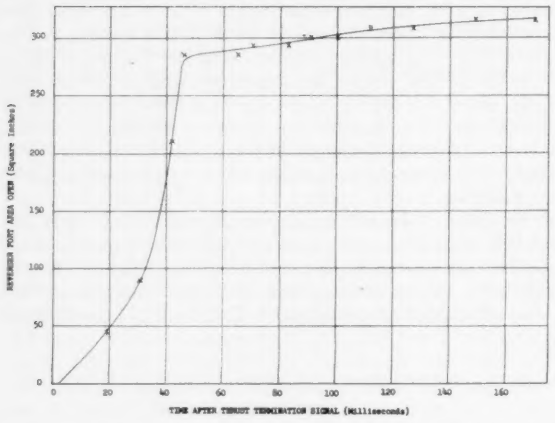

Fig. 4 Thrust reverser port area open, calculated from pressure curve in Fig. 3

Substituting in Equation [15]

$$\frac{A_r}{A_t} = \left[\left(\frac{500}{460}\right)^{1-0.3} - 1\right] - \frac{231.5}{1.042 \times 61.84 \times 4500 \times 0.0074} \times \frac{1}{460}(-2340)$$

$$\frac{A_r}{A_t} = 0.06 + 0.000234 \times 2340 = 0.06 + 0.55 = 0.61$$

$$A_r = 0.61 \times 150 = 91.5 \text{ in.}^2$$

When the chamber pressure falls below 300 psia, the burning rate exponent $n = 0.25$ is substituted instead of $n = 0.3$. In this case, P_{ta} must be substituted for P_i, as defined in Equation [17]

$$P_{ta}^{1-0.25} = (0.04/0.03)(500)^{1-0.3} = 104$$
$$P_{ta} = 494 \text{ psia}$$

With these substitutions in Equation [15], the method is applied as outlined above, and will result in the curve of reverser port area presented in Fig. 4. Examination of this curve leads to the conclusion that effective opening of the thrust reverser ports was not reached until approximately 45 millisec after signal, with full opening reached after 160 millisec.

Acknowledgment

The author would like to express his appreciation to Mr. G. Ladd for his assistance in preparing graphs and making calculations.

References

1 Shapiro, A. H., "The Dynamics and Thermodynamics of Compressible Fluid Flow," The Ronald Press Co., N. Y., 1953, vol. I, p. 85.
2 *Ibid.*, vol. II, figs. 24 and 26, p. 983.

Comparison of Theoretical and Experimental Film Thickness

A. E. DUKLER[1]

University of Houston, Houston, Texas

IN A RECENT PAPER (1)[2] the author analyzed the mechanics and heat transfer in film flow. As part of this development the thickness of a liquid film in concurrent flow with a gas was predicted theoretically. These results, which were obtained by computer solution of the differential equations, were presented graphically. No comparison with experiment was made. Since that time a number of experimental film thickness studies have come to light which permit a testing of these theoretical results. This comparison and the ability to predict film thickness is of considerable importance to those concerned with film and transpiration cooling of propulsion and re-entry vehicles.

Fig. 1 shows the comparison of experiment and theory. The ordinate of this graph is the dimensionless film group introduced by Nusselt (2). The abscissa is the gas phase Reynolds number. Each curve is characterized by a value of the dimensionless group β defined as

$$\beta = D g_L^{1/3} \rho_L^{2/3} (dP/dL)_f / 4\mu_L^{2/3}$$

where

D = tube diameter
g_L = gravitational acceleration
ρ_L = liquid density
μ_L = liquid viscosity
$(dP/dL)_f$ = frictional pressure gradient in the direction of gas flow

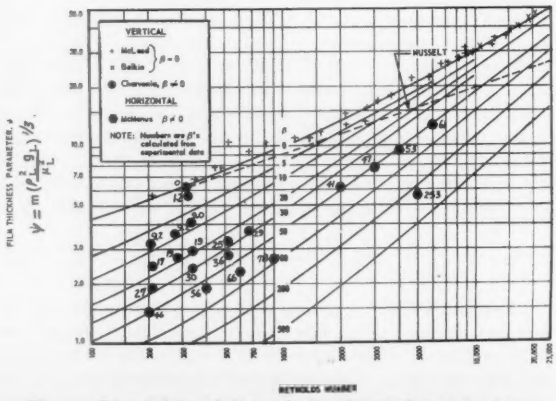

Fig. 1 Comparison of theoretical and experimental values

Received July 27, 1960.

[1] Associate Professor, Dept. of Chemical Engineering.
[2] Numbers in parentheses indicate References at end of paper.

Note that $\beta = 0$ corresponds to zero interfacial shear. The lines represent the result from theory and were determined without the use of experimental data.

Results of four investigators (3–6) are shown as points on the graph. Data of McLeod (3) and Belkin (4) were obtained at zero interfacial shear in connection with mass transfer studies in films. Charvonia (5) reported his results from the Purdue Jet Propulsion Laboratory where he was concerned with film cooling studies. McManus' studies (6), carried out at Cornell for Army Ordnance, were on horizontal tubes with the liquid in annular flow. Experimental data for each point were used to calculate ψ and Re and these values were plotted on the graph. The experimental value of β was then calculated and noted next to the point. The suitability of the theory can be judged by comparing the experimental values of β with those predicted from the curves for the corresponding values of ψ and Re. Good agreement is obtained over the range of Reynolds numbers and β's for which data are available.

References

1 Dukler, A. E., "Fluid Mechanics and Heat Transfer in Vertical Falling Film Systems," *Chem. Engrg. Progress*, Symposium Series, vol. 56 no. 30, pp. 1–10, 1960.

2 Nusselt, W., "The Surface Condensation of Steam," *ZVDI*, vol. 60, pp. 541–569, 1916.

3 McLeod, A. A., "Liquid Turbulence in a Gas-Liquid Absorption System," Ph.D. thesis, Carnegie Inst. Technology, Pittsburgh, Pa., 1951.

4 Belkin, H. M., "Mass Transfer in Turbulent Liquid Films," Doctoral dissertation, Carnegie Inst. Technology, Pittsburgh, Pa., 1953.

5 Charvonia, D. A., "A Study of the Mean Thickness of the Liquid Film and the Characteristics of the Interfacial Surface in Annular, Two-Phase Flow in a Vertical Pipe," Interim Rep. 59-1, Contract N-onr-1100 (14), Jet Propulsion Center, Purdue Univ., Lafayette, Ind., May 1959.

6 McManus, H. N. Jr., "An Experimental Investigation of Liquid Distribution and Surface Character in Horizontal Annular Two-Phase Flow," Interim Rep. no. 1, OOR Project no. 2117 ,Oct. 1959.

Meteoritic Impact

DAVID B. BEARD[1]

Lockheed Aircraft Corp., Missiles and Space Div., Sunnyvale, Calif.

The impact of meteoroids on a space vehicle skin is examined from a consideration of the different physical processes by which energy transfer can occur. It is shown that only evaporation is significant, that erosion is negligible, and that puncture is less likely than previously thought by many authorities, the threshold thickness in centimeters being only 0.6 cm for one puncture per year per 100 m² of surface.

THE HAZARD from meteoritic impact to space vehicles divides into the two problems of surface erosion caused by dust particles, and puncture of tubes or other containers by rarer more massive material. Surface erosion is of consequence to thermal control since the radiation properties of the surface may change as a result of erosion. Puncture is of obvious consequence to the proper functioning of an airtight compartment housing live animals, or of liquid carrying tubes which are an integral part of the heat exchange system of a nuclear power supply, to cite only two of many examples.

The two problems are similar in that they involve hypervelocity impact at velocities far in excess of any presently attainable laboratory velocity. In general, two phenomena are responsible for changing the character of the physical process occurring at high velocities from that occurring at low velocity. Momentum effects, being linearly dependent on velocity, dominate low velocity experiments, whereas the quadratic dependence on velocity of the energy causes energy effects to dominate high velocity events. Secondly, at high velocity, target materials become more resistant to momentum effects, since the greater inertial stress of the target atoms dominate the common static stress of the target material at high rates of strain. Even at the maximum presently obtainable laboratory velocities, the shape of a crater bears no relation to the incident projectile momentum. Projectiles at glancing incidence merely cause smaller craters, since less energy is delivered to the target surface (1).[2]

Dust particles, having a diameter of about 10 μ and a density of 0.05 gm per cc, are impacted with a space vehicle at minimal meteoritic velocities of 11 km per sec as a result of their fall into Earth's gravitational field for low altitude vehicles. Because of their number they are the prime consideration as causes of surface erosion. Approximately 10^{-6} particles per cm² sec will be impacted with a space vehicle surface unshielded by Earth (2). Larger particles are less numerous; particle numbers depend inversely on the fourth power of the particle radius. The impulse from such a slight object is, in any case, quickly dissipated in a mono layer or two of target molecules, but the power delivered per unit surface area is impressive. 10^{11} atoms, each having an energy of 10 ev, bombard 10^{-6} cm² in 10^{-9} sec delivering an average power of 10^{28} ev per cm² sec. Thermal or statistical considerations determine the course of the event, and energy is transported or lost by evaporation many orders of magnitude more rapidly than by any other possible process.

Essentially, the surface is maintained at a temperature of about 10^5 K for times of the order of $10^{-9} - 10^{-8}$ sec. Since this temperature is well above the critical temperature of any conceivable target material, 10^{-9} sec is sufficient time to vaporize $10^{11} - 10^{12}$ molecules from the 10^{-6} cm² of target area. Since each molecule carries away several electron volts of kinetic and potential energy, the target area is left too cool to vaporize further material after the impact, and the heat is rapidly conducted into the target material, the upper layer of which fuses and re-solidifies.

No other physical process transports energy away from the target area during the duration of the impact, since radiation, thermal conduction and pressure waves may be easily shown to be too slow for any conceivable material. Less than 10 per cent of the energy can be radiated away in 10^{-9} sec and heat is not transmitted into the target faster than the progress of the vaporization. Thus a fairly accurate estimate of surface erosion may be made by equating the kinetic plus potential energy of the escaping target molecules to the incident dust particle energy. Roughly one or at most two molecules of Al_2O_3, for example, would be vaporized per incident dust particle atom. For micrometeorite average density of a few tenths gm per cc, a hemispherical hole of 5-μ radius would be formed. For a more likely density of a few hundredths gm per cc the crater would have an area of 10^{-6} cm² but a depth of only $\frac{1}{2}\mu$ since the depth of the crater would be linearly proportional to dust particle density but constant in area for all densities less than or equal to a few tenths gm per cc. Therefore the total fractional area eroded in one year will amount to $10^{-6} \times 3 \times 10^7 \times 10^{-6} = 3 \times 10^{-5}$.

More massive puncture-causing particles might partially "cap" the evaporative explosion on contact, during the early part of the impact. The vapor pressure at point of contact,

Received Aug. 8, 1960.

[1] Consultant, Gaseous Dynamics Dept.

[2] Numbers in parentheses indicate References at end of paper.

however, could be in excess of 10,000 or 100,000 atm if the vapor were completely confined. Plastic flow would occur, and fused material would be blown out around the meteor contact area. Even at relatively low laboratory velocities of 4 km per sec, a curtain of high velocity fused target material has been observed being ejected around the projectile contact area (3). Consequently more massive meteors will do relatively more damage than micrometeorites. Most of the energy will still go into evaporation of target and meteor material, but a significant fraction of the crater volume will result from the escape of fused material under pressure supplied by compressed and vaporized target material.

In general, as projectile velocity increases, a larger share of the energy goes into the inefficient process of evaporation rather than fusion. If ablation efficiency is defined as crater volume divided by projectile energy, then as projectile velocity increases there results the steady decline in ablation efficiency, which is an invariable characteristic of many diverse hypervelocity impact observations in the laboratory.

At meteoritic velocities in excess of 10 km per sec, it is likely that the crater volume will not exceed the hemispherical mass obtained by dividing the incident energy by the heat of vaporization of the target material by more than a factor of 2. The recoil momentum resulting from the loss of ejected target material is roughly comparable to the incident projectile momentum. The resulting shock wave will cause material to spall from the inner wall of the space vehicle surface. The depth of the hole may be estimated by the depth of the compressed or rarefied (on reflection) material in the shock wave, which is equal to the product of the speed of sound in the material times the duration of the impact r/v sec, where r is the particle radius and v is its velocity. If v is 30 km per sec this depth is only 1 per cent of the depth of the outer surface crater. We conclude that a good estimate of puncture may be obtained by taking the third root of twice the meteor energy divided by the mass of vaporized target atoms times the heat of vaporization of the target material.

The best and most recent survey of visual and photographic meteors (4) gives a meteoroid flux density of

$$N = 2.0 \times 10^{-5}\, m^{-1.34} \qquad [1]$$

where

N = number per m^2 per year
m = mass of the meteoroid, gm

From the discussion given in the previous paragraph, the depth of target penetration by a particle of kinetic energy $\frac{1}{2}mv^2$ is

$$t = [3(1/2)mv^2/\pi d_T H_T]^{1/3} \qquad [2]$$

where

m = mass of incident meteoroid
v = velocity of incident meteoroid
d_T = density of target material
H_T = heat of vaporization of target, ergs per gm

All quantities are expressed in cgs units. Taking 30 km per sec as a representative meteoroid velocity, and substituting Equation [1] for the mass in Equation [2] we find

$$t = 1.1 \times 10^3 (d_T H_T)^{-1/3} N^{-1/4} \qquad [3]$$

For aluminum this amounts to

$$t = 0.18 N^{-1/4}$$

Hence 0.6 cm of aluminum will suffer, at most, one puncture per year per 100 m^2, on the average. This is more than an order of magnitude less than Kornhauser's estimate (5) of puncture rate.

With reference to the calibration of satellite micrometeorite detector microphones [see (5)] the momentum of ablated target material increases the microphones' sensitivity to micrometeorites over lower velocity laboratory particles having equal momentum. On the other hand, micrometeorite velocities have been overestimated by a factor of 3 in interpreting the satellite measurements. Inferences from solar corona and zodical light measurements (2) reveal an interplanetary dust concentration several orders of magnitude too low to explain the observations, unless the dust gravitates and concentrates about Earth. In this case, the particle velocity cannot be greater than 10 km per sec, in conformity with telescopic and radar observations of the faintest meteors. The statement that the total visually estimated meteoritic mass is in agreement with satellite observations (6) is misleading since the most numerous, lightest particles may not be an appreciable fraction of the total meteoritic mass in the solar system. The assumed low momentum effects and high velocity balance so that the deduced particle mass is in agreement with solar corona observation inferences (2). It should be emphasized that the particle number observed by satellites cannot be reconciled with any calculated dust distributions (2,7,8) unless a thick blanket about Earth is inferred. Such a blanket can result only if the dust is approximately initially at rest with respect to Earth (2).

Acknowledgments

The author would like to express his thanks to Dr. D. Bershader and Dr. F. S. Johnson, Lockheed Missiles and Space Div., for their interest and enlightening discussion of this subject.

References

1 Anderson, G. C., Doran, D. G., Hempy, F. S. and Kells, M. C., "Cratering by High Velocity Microparticles," in "Proc. of Third Symposium on Hypervelocity Impact, Vol. I," Armour Research Foundation, Illinois Institute of Technology, Chicago, Ill., 1959, p. 45.

2 Beard, D. B., "Interplanetary Dust Distribution," *Astrophys. J.*, vol. 129, 1959, pp. 496–506.

3 Kineke, J. H., Jr., "An Experimental Study of Crater Formation in Lead," in "Proc. of Third Symposium on Hypervelocity Impact, Vol. 1," Armour Research Foundation, Illinois Institute of Technology, Chicago, Ill., 1959, p. 157.

4 Hawkins, G. S. and Upton, E. K. L., "The Influx Rate of Meteors in the Earth's Atmosphere," *Astrophys. J.*, vol. 128, 1958, p. 727.

5 Kornhauser, M., "Satellite Pressure Losses Caused by Meteoroid Impacts," ARS JOURNAL, vol. 30, 1960, p. 175.

6 Dubin, M., "Meteoritic Dust Measured from Explorer I," *Planet Space Sci.*, vol. 2, 1960, p. 121.

7 Allen, C. W., "The Spectrum of the Corona at the Eclipse of 1940 October 1," *Monthly Not. Roy. Astron. Soc.*, vol. 106, 1946, p. 137.

8 van de Hulst, H. C., "Zodiacal Light in the Solar Corona," *Astrophys. J.*, vol. 105, 1947, p. 471.

Formulation of the Optimum Rocket Trajectory

Y. C. SHEN[1]

Aerojet-General Corp., Azusa, Calif.

A RECENT paper, "Optimum Rocket Trajectory," by Dommasch and Barron (1,2)[2] has been a controversial issue since its publication. Miele (3), Leitmann (4) and Kelley (5) question the correctness of the Dommasch and Barron formulation. In reply, Dommasch (6,7) disagrees with their remarks. In the controversy not only is the specific problem treated by Dommasch and Barron debated, but also the basic principles of variational calculus involved. It is the purpose of this note to clarify some conflicting points in this specific problem; more detailed discussions will follow at a later date.

Controversial Problem

The problem is finding the optimum height of a rocket in planar motion where thrust and initial conditions are given. The governing equations, according to the original notation (1,2) of Dommasch and Barron, are essentially

$$\phi_1 = F \cos \alpha - m\dot{V}_a - mg \sin \gamma_1 = 0 \qquad [1]$$

$$\phi_2 = F \sin \alpha - mg \cos \gamma_1 + mV_a \left(\frac{V_a \cos \gamma_1}{h_a} - \dot{\gamma}_1 \right) = 0 \qquad [2]$$

with

$$\phi_3 = \dot{h}_a - V_a \sin \gamma_1 = 0 \qquad [3]$$

where

V_a = velocity
γ_1 = path angle
h_a = altitude measured from Earth center
α = angle between thrust line and velocity vector
g = $g_0(R_e/h_a)^2$
R_e = Earth radius
g_0 = acceleration of gravity at Earth surface

According to Dommasch and Barron, the problem is to extremize the integral

$$h_a(t_2) - h_a(t_1) = \int_{t_1}^{t_2} V_a \sin \gamma_1 \, dt \qquad [4]$$

subject to the conditions $\phi_1 = 0$ and $\phi_2 = 0$. But Miele, Leitmann and Kelley disagree with this formulation, stating that the correct formulation should have three subsidiary conditions, $\phi_1 = 0$, $\phi_2 = 0$ and $\phi_3 = 0$. In reply, Dommasch contends that the kinematic relation $\phi_3 = 0$ is already used to obtain integral [4], and that the double introduction can serve no purpose.

Dommasch and Barron would be right if h_a did not enter into $\phi_1 = 0$ and $\phi_2 = 0$. Since it does, $\phi_3 = 0$ must be included as a constraint. Furthermore, in order to avoid the claim of double introduction of $\phi_3 = 0$ into the formulation, one could formulate the problem as extremizing $h_a(t_2) - h_a(t_1)$ subject to $\phi_1 = 0$, $\phi_2 = 0$ and $\phi_3 = 0$, or equivalently, extremizing

$$h_a(t_2) - h_1(t_1) + \int_{t_1}^{t_2} (\lambda_1\phi_1 + \lambda_2\phi_2 + \lambda_3\phi_3)dt$$

The results should be essentially the same as those suggested by Miele, Leitmann and Kelley.

Pilot Example

Commenting on the paper of Dommasch and Barron, Miele (3) gives the following example, which he calls "pilot example": Optimize the height of a rocket flying in a two-dimensional plane with Earth considered to be flat. Neglecting induced drag with respect to zero-lift drag, Miele obtains the equation of motion

$$J_1 = \frac{\dot{V}}{g} + \sin \gamma - \frac{F(h) - D(h, V)}{mg} = 0 \qquad [5]$$

with

$$J_2 = \dot{h} - V \sin \gamma = 0 \qquad [6]$$

Miele formulates the problem of optimum height as extremizing

$$\int_{t_1}^{t_2} (V \sin \gamma + \lambda_1 J_1 + \lambda_2 J_2)dt \qquad [7]$$

and obtains

$$\cos \gamma = 0 \qquad [8]$$

$$\frac{\partial}{\partial V} \frac{(F - D)V}{mg} - \frac{V}{g} \frac{\partial}{\partial h} \frac{(F - D)V}{mg} = 0 \qquad [9]$$

This, he claims, is the right approach, whereas the approach of Dommasch and Barron, by Miele's interpretation, would lead to extremizing

$$\int_{t_1}^{t_2} (V \sin \gamma + \lambda_1 J_1)dt \qquad [10]$$

and the Euler equations

$$\cos \gamma = 0 \qquad [11]$$

$$\frac{\partial}{\partial V} \frac{(F - D)V}{mg} = 0 \qquad [12]$$

However, in reply, Dommasch (6) asserts that Miele's interpretation of their results is incorrect, as well as his physical reasoning for disregarding the equation of motion normal to the flight path. The proper approach, according to Dommasch, would be that of eliminating $\sin \gamma$ from Equations [5 and 6] and extremizing the integral

$$\int_{t_1}^{t_2} V \left(\frac{F - D}{mg} - \frac{\dot{V}}{g} \right) dt \qquad [13]$$

which, according to Dommasch, results in one Euler equation

$$-\frac{\dot{V}}{g} - \left(\frac{F - D}{mg} - \frac{\dot{V}}{g} \right) - V \frac{\partial}{\partial V} \frac{F - D}{mg} = 0 \qquad [14]$$

with

$$\frac{\partial}{\partial V} \frac{F - D}{mg} = \frac{1}{mg} \left(\frac{\partial F}{\partial V} + \frac{\partial F}{\partial h} \cdot \frac{\partial h}{\partial V} - \frac{\partial D}{DV} - \frac{\partial D}{\partial h} \cdot \frac{\partial h}{\partial V} \right) - \frac{\dot{m}(F - D)}{m^2 g} \qquad [15]$$

It is apparent that Equations [12 and 14] are essentially the same. However, in Equation [12], h is regarded as independent of V; in Equation [14], h is considered as a function of V, as shown in Equation [15]. (Note that there is error in Equation [15].) F is equal to $F(h)$ in Miele's formulation; F is equal to $F(h, V)$ in Dommasch's formulation.

Dommasch's reasoning here would again be valid if it were possible to find $h(V)$. However, there is a difference in his reasoning here and the reasoning in the original paper (1) where, neglecting $h_a = h_a(V, \gamma)$ in the formulation, no terms like $(\partial h_a/\partial V)$ and $(\partial h_a/\partial \gamma)$ enter into the Euler equations; here the term $(\partial h/\partial V)$ occurs in Equation [15]. However, since it is impossible to obtain explicitly $h = h(V)$, the correct formulation (8,9) should therefore be that of ex-

Received June 22, 1959.

[1] Research Aerodynamicist. Presently, Senior Scientist, Nor-air, Hawthorne, Calif.

[2] Numbers in parentheses indicate References at end of paper.

tremizing

$$h(t_2) - h(t_1) + \int_{t_1}^{t_2} \lambda(t) \left[\dot{h} - V \left(\frac{F - D}{mg} - \frac{\dot{V}}{g} \right) \right] dt$$

which leads to the Euler equation

$$\frac{F - D}{mg} + V \frac{\partial}{\partial V} \frac{F - D}{mg} - \frac{V^2}{g} \frac{\partial}{\partial h} \frac{F - D}{mg} = 0 \qquad [16]$$

which is essentially Equation [9]. [Note the absence of cos $\gamma = 0$, an exceptional case in variational calculus (10) and a physical improbability.]

Conclusion

A casual application of multiplier rule without sufficient realization of its intrinsic meaning and exceptions will result in an error; this may give a stationary solution without any physical meaning, or may lead to a completely wrong formulation.

References

1 Dommasch, D. O. and Barron, R. L., "Optimum Rocket Trajectory, Part I—Initial Value Variational Solutions," *Aero/Space Engng.*, vol. 19, no. 1, Jan. 1960, p. 46.

2 Dommasch, D. O. and Barron, R. L., "Optimum Rocket Trajectory, Part II—Generalized Boost Analysis," *Aero/Space Engng.*, vol. 19, no. 2, Feb. 1960, pp. 45–48.

3 Miele, A., in Letters to the Editor, *Aero/Space Engng.*, vol. 19, no. 3, March 1960, p. 4.

4 Leitmann, G., in Letters to the Editor, *Aero/Space Engng.*, vol. 19, no. 4, April 1960, p. 5.

5 Kelley, H. J., in Letters to the Editor, *Aero/Space Engng.*, vol. 19, no. 4, April 1960, p. 6.

6 Dommasch, D. O., in Letters to the Editor, *Aero/Space Engng.*, vol. 19, no. 3, March 1960, p. 36.

7 Dommasch, D. O., in Letters to the Editor, *Aero/Space Engng.*, vol. 19, no. 4, April 1960, p. 5.

8 Shen, Y. C., "Multiplier Rule in Calculus of Variation and Its Application to Optimum Performance of Rocket Vehicles," Aerojet-General TM-832, Azusa, Calif., Nov. 1959.

9 Shen, Y. C., "General Formulation of the Problem of Optimum Rocket Trajectories," Aerojet-General TM-833, Azusa, Calif., Nov. 1959.

10 Courant, R. and Hilbert, D., "Methods of Mathematical Physics," Interscience Publishers, Inc., N. Y., 1953.

Useful Correlation of Interior Ballistic Theory and Experimental Data[1]

HAROLD D. BLACK[2]

Applied Physics Laboratory, The Johns Hopkins University, Silver Spring, Md.

RAIMOND A. STRUBLE[3]

North Carolina State College, Raleigh, N. C.

CLEMMOW (1)[4] in 1928 showed that the theoretical maximum pressure in a gun utilizing neutral propellant geometry is proportional to

$$P_{max} = (B^2 M F^2 C^2 / 12 w^2 A^2 V)^{1/(3-2n)} \qquad [1]$$

wherein a consistent set of units is as follows:

P_{max} = maximum pressure (psi)
C = charge weight (lb)
M = mass of the projectile (slugs)
F = the so-called propellant "force" (ft lb/lb)
B = the burning rate constant, in./sec/(lb/in.^{2})^n
w = propellant web thickness (in.)
A = bore cross-sectional area (in.^{2})
V = initial chamber volume behind the projectile (in.^{3})

Recently (2) it has been shown that the theoretical maximum pressure in a gun utilizing ideally progressive propellant geometry is proportional to

$$P_{max} = (2CMF\ B^2/k\ w^2\ A^2)^{1/(2-2n)} \qquad [2]$$

wherein k is the ratio of specific heats of the powder gas.

Experimental correlation with Equation [2] has been obtained for a gun utilizing highly progressive powder geometry. The technique described here provides a useful design rationale which can be expected to apply equally well to Equation [1] for guns utilizing neutral propellant geometry.

Background of Analytical Study

In attempting to improve the performance of a light weight, high piezometric efficiency gun, we faced a familiar frustrating circumstance: A rigorous analytical model of the system was virtually impossible to wield; also, the number of variables was too large to permit a satisfactory experimental solution to the problem.

Compromising the analytical model led to extremely useful results. The analytical model settled on—albeit a drastically simplified one—contained the following assumptions:

1 Heat transfer from the propellant gas and pressure gradients in the propellant gas were neglected. In addition, bore friction, gun recoil and the rotational energy of the projectile were neglected.

2 The co-volume of the powder gas was assumed to equal the specific volume of the unburned powder so that the equation of state reduced to the perfect gas law.

3 The powder geometry was idealized to the point that the form function became

$$N/C = (1 - f)(1 + \theta f) \qquad [3]$$

wherein

N/C = ratio of the consumed propellant to the initial charge weight
f = normalized instantaneous web thickness
θ = form factor

($\theta = -1$ corresponds to an ideally progressive charge, i.e., a hollow cylinder of vanishingly small perforation burning only on the interior surface. $\theta = 0$ corresponds to a neutral geometry and $0 < \theta \leq 1$ corresponds to regressive propellant geometries.) Equation [3], which assumes the validity of Piobert's Law, is well known; see (3 and 4).

4 The burning rate law was taken to be

$$r = BP^n \qquad [4]$$

where $0 < n < 1$.

Equation [4] with $n < 1$ is infrequently used in the study of the interior ballistics of guns because of the nonlinearity it introduces. Exceptions to this are (1 and 2).

Experimental Correlation

At the onset, we were unable to produce any useful result from the set of equations other than an interesting limiting form for the pressure curves. This was obtained by noting that $\theta = -1$ and $dP = 0$ gave a *constant* pressure solution, i.e., for ideally progressive geometry, a theoretical 100 per cent piezometric efficiency solution exists. The magnitude of this constant pressure is given by Equation [2]. Since the practical case with which we were concerned more closely approximated a constant pressure solution than it did any other

Received July 22, 1960.

[1] The experimental portion of this investigation was carried out while the writers were staff members of Armour Research Foundation of the Illinois Institute of Technology, Chicago, Ill.

[2] Engineer. Member ARS.

[3] Professor of Mathematics.

[4] Numbers in parentheses indicate References at end of paper.

known ballistic solution,[5] we attempted the following experimental correlation.

For the 2.75-in. gun under study—a fixed projectile weight (9.0 lb) and M-2 single-perforation double-base propellant—a series of shots was fired with constant loading density.[6] This was achieved by increasing the chamber volume of the gun as the propellant weight was increased by simply positioning the projectile in the bore.[7] To abet uniform ignition of the powder, the projectile was restrained by a calibrated shot-start device which failed when the pressure reached 600 psi. The pressure range encompassed by the entire experiment was 4000 to 10,000 psi.

The pressure-time history in the gun chamber was sensed by a calibrated gage and was photographically recorded. To eliminate the variation of B and n with ambient temperature, all ammunition was temperature conditioned at 70 F for at least four hours before firing. At least three shots were fired for each data point. Utilizing the data thus obtained, the log P_{max} was plotted as a function of the quantity (log C/w^2) and least squares fitted by a straight line. The results are shown in Figs. 1 and 2. It should be noted that the existence of this straight line is predicted by Equation [2] and, moreover, according to this equation, the slope of these lines should be $1/(2-2n)$ where n is the burning rate exponent.[8] From the slopes of the three lines, we obtained

$$n_1 = 0.78 \qquad n_2 = 0.78 \qquad n_3 = 0.74$$

for the burning rate exponent. Weinstein and Pallingston (5) give the burning rate exponent at 70 F for M-2 propellant (from closed bomb tests) as $n = 0.77$. The experimental correlation with the theoretical result, Equation [2], appears to be excellent.

The success of this experimental correlation motivated the extensive analytical study reported in (2). It was found that for an ideally progressive charge ($\theta = -1$), the theoretical pressure curve is proportional to the quantity in Equation [2] and that the limiting form, as the initial volume V vanishes, results in the constant pressure solution discovered earlier.

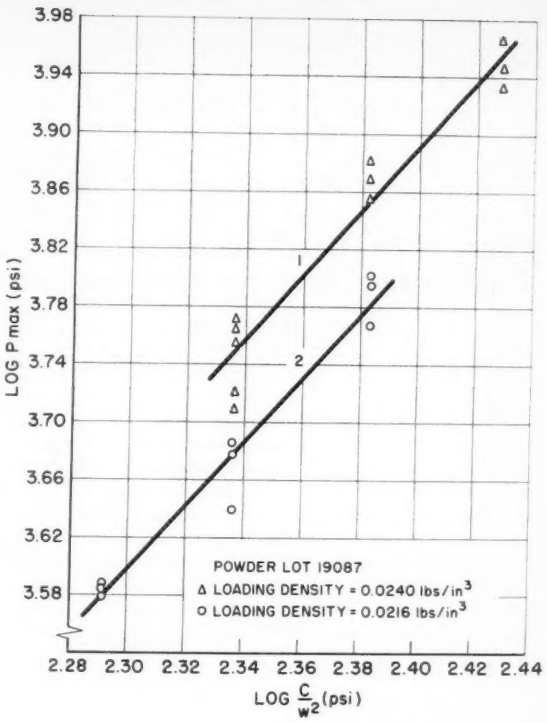

Fig. 1 Correlation of experimental data and Equation [2]

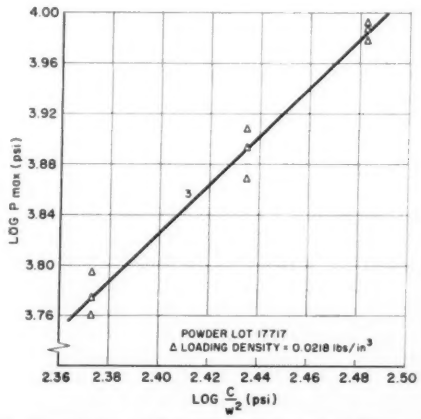

Fig. 2 Correlation of experimental data and Equation [2]

Discussion

Equation [2] has several interesting implications:

1 Since the exponent in Equation [2] approaches infinity as n approaches unity, the progressive charge gun is a very tricky device for n close to unity. Consequently, propellants having small values of n are highly desirable. In any case, theoretical results based upon a linear burning law, i.e., $n = 1$, will be unreliable.

2 During the experimental program it became apparent that P_{max} in this progressive charge geometry gun is more sensitive to ambient temperature changes than is the maximum pressure in a conventional (neutral propellant geometry) gun. This observation is explained by a comparison of the respective exponents in Equations [1 and 2], together with the fact (5) that n increases with ambient temperature from $n = 0.70$ at -70 F to $n = 0.81$ at 140 F.

3 A useful propellant quality control procedure is indicated: Slight variations in B resulting, say, from variations in the propellant composition, could be compensated for by slight changes in the web thickness. Specifically, rather than a propellant specification in which w, B and n are individually specified, only the two quantities B/w^2 and n are needed. During the latter stages of propellant processing, several small strands could be extruded, dried, and the burning rate constant (representative of the lot) measured. On the basis of this measurement and the concomitant specifications, the web thickness would be determined. However, ambient temperature effects cannot be compensated for in this way—only lot-to-lot variations in composition, mixing variables, etc.

4 Since Equation [2] is a limiting form based on rather restrictive assumptions, it is unsuitable for direct computation. We suggest that it be used as a basis of experimental correlation such as has been done here. A set of curves log (P_{max}) vs. log (C/w^2) for various loading densities provides a very useful design rationale for this system. A similar technique (note Equation [1]) should apply equally well to guns utilizing neutral propellant geometries.

[5] $\theta = -0.7$ was computed from the powder geometry. The piezometric efficiency on a number of preliminary shots was 60 to 80 per cent.

[6] The loading density is defined as the powder charge weight divided by the initial volume behind the projectile, i.e., C/V.

[7] The rifle barrel (one turn in 12 calibers) was preceded by a smooth bore section. The copper rotating bands on the projectiles were not pre-engraved.

[8] The reader might note the similarity of this procedure to that used in obtaining the familiar "P-K" curves for a rocket propellant configuration.

References

1 Clemmow, C. A., "A Theory of Internal Ballistics Based on a Pressure Index Law of Burning for Propellants," Phil. Trans. Royal Soc., London, vol. A 227, p. 345, 1928.

2 Struble, R. A., "A Study of the Interior Ballistic Equations," *Arch. Rational Mechanics and Analysis*, vol. 3, no. 5, 1959, pp. 397–416.

3 Corner, J., "Theory of the Interior Ballistics of Guns," John Wiley and Sons, Inc., N. Y., 1950, p. 31.

4 "Interior Ballistics," edited by F. R. W. Hunt, H. M. Stationery Office, London, 1951, p. 51.

5 Weinstein, M. and Pallingston, A. O., "Preliminary Study of M-2 and M-9 Propellants Between 137 F and −65 F," Picatinny Arsenal, Samuel Feltman Ammunition Labs., Rep. 2240, June 1956.

Effect of Electrical Augmentation on Nuclear Rocket Flight Performance

EDWIN R. BERRY[1]

Convair Div., General Dynamics Corp., Fort Worth, Texas

THE SPECIFIC impulse obtainable from a nuclear rocket using a working fluid heated directly by a reactor is limited by the maximum allowable temperature of the reactor core and structural materials. It has been suggested (1,2)[2] that this limitation could be circumvented by taking electrical power from the reactor and transmitting it to the working fluid leaving the reactor. This would raise the working fluid temperature above the reactor temperature and increase the specific impulse. The price paid for this higher specific impulse is the increased dead weight (and added complexity) of the electrical machinery. It is interesting, then, to determine the effect of such an electrical augmentation system on the flight performance of typical nuclear rocket booster vehicles, i.e., to ascertain whether or not the higher specific impulse is offset by the increased dead weight and consequent poorer mass ratio of the vehicle, and to compare the performance of augmented and unaugmented vehicles. It is the purpose of this note to present a specific example of such a comparison.

The heat produced by the reactor could be converted to electricity by several methods. One method would be to take the hot working fluid from the reactor, expand it through power turbines driving generators, and then reheat it in the reactor as proposed in (1). Many stages of power extraction and reheat could be used, and the amount of power extracted per unit mass flow of working fluid would be theoretically unlimited. Another method would be to use a closed cycle regenerative gas turbine, such as that described in (2). Still another method, possibly more attractive than turbomachinery, would be to use a direct heat-to-electrical power converter, such as a thermionic device, which might be built into the reactor core itself. A possible arrangement, suggested in (3), would be to build the converter elements around individual fuel rods and to use the working fluid as the anode (cold junction) coolant. Such a converter should be much lighter than a turbogenerator.

A schematic diagram of a hypothetical augmented nuclear rocket using thermionic converters is shown in Fig. 1. Liquid hydrogen working fluid enters the thrust chamber cooling jacket, regeneratively cools the thrust chamber, and then goes to the reactor. Here it cools the converter anodes until its temperature reaches the maximum allowable anode temperature, which must be held low enough to avoid excessive back emission of electrons from the anode to the cathode (hot junction). Such back emission can cause a serious deterioration in converter performance. After leaving the converter section of the reactor, the hydrogen is heated to as high a temperature as the reactor limitations will permit. It then passes into the thrust chamber, where the electrical energy taken from the reactor via the converters is transmitted to the working fluid by means of an arc discharge. After the final electrical heating, the working fluid is ejected through a conventional nozzle.

A general expression for the specific impulse of an electrically augmented nuclear rocket is

$$I_{sp} = 9.32\sqrt{h_r + h_a - h_e} \qquad [1]$$

where

I_{sp} = specific impulse, lbf-sec per lbm
h_r = working fluid enthalpy at reactor exit, cal per gm
h_a = electrical energy added to working fluid in the thrust chamber, cal per gm
h_e = working fluid enthalpy at nozzle exit, cal per gm

The thermionic converter acts as a heat engine, since a part of the reactor heat absorbed at the hot cathode is converted into electrical energy while the remainder is rejected to the working fluid at the cool anode. The relation between the electrical power delivered to the working fluid in the thrust chamber and the waste heat rejected by the converter is

$$h_a = [\eta_a \eta_c/(1 - \eta_c)]q \qquad [2]$$

where

η_a = arc efficiency
η_c = converter efficiency
q = converter heat rejected per unit mass of working fluid, cal per gm

The heat rejected q is the enthalpy rise of a unit mass of working fluid while passing over the converter anodes. This enthalpy rise is limited because the maximum anode temperature must be held low enough to avoid excessive back emission of electrons from the anode to the cathode. It appears that practical converters will operate with anode temperatures above 650 K (4). Converters have been operated with anode temperatures as high as 1700 K (5), but it seems unlikely that good converter performance would be obtained at such high temperatures. In any event this limitation on q limits h_a, the amount of electrical energy which can be delivered to a unit mass of working fluid in the thrust (arc) chamber, as shown by Equation [2].

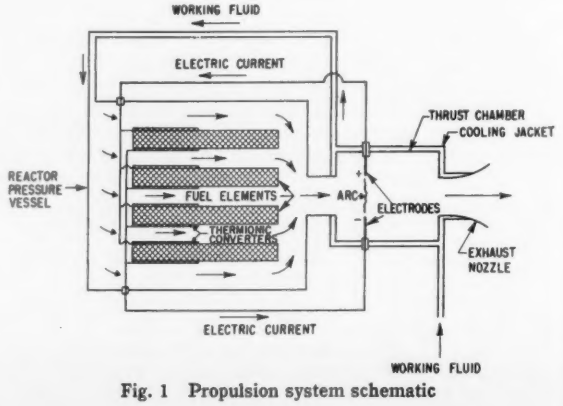

Fig. 1 Propulsion system schematic

Received Aug. 8, 1960.

[1] Senior Propulsion Engineer. Member ARS.

[2] Numbers in parentheses indicate References at end of paper.

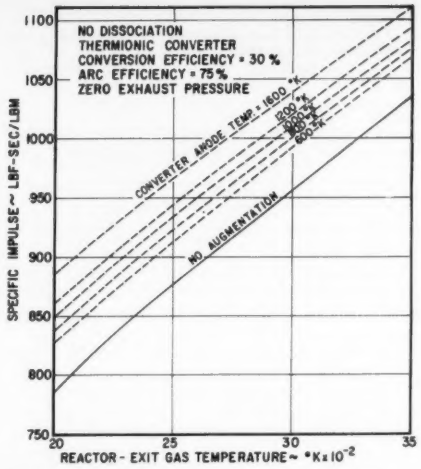

Fig. 2 **Hydrogen specific impulse with electrical augmentation**

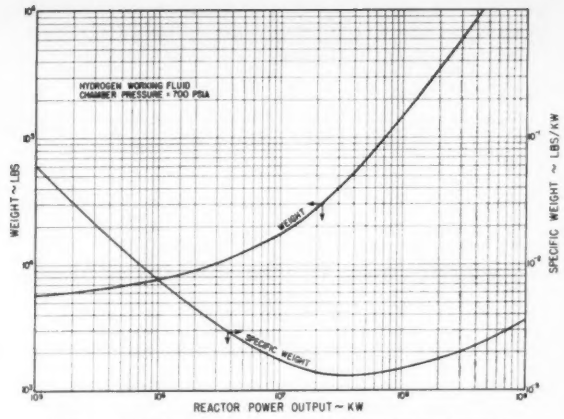

Fig. 3 **Weight of reactor, thrust chamber and nozzle**

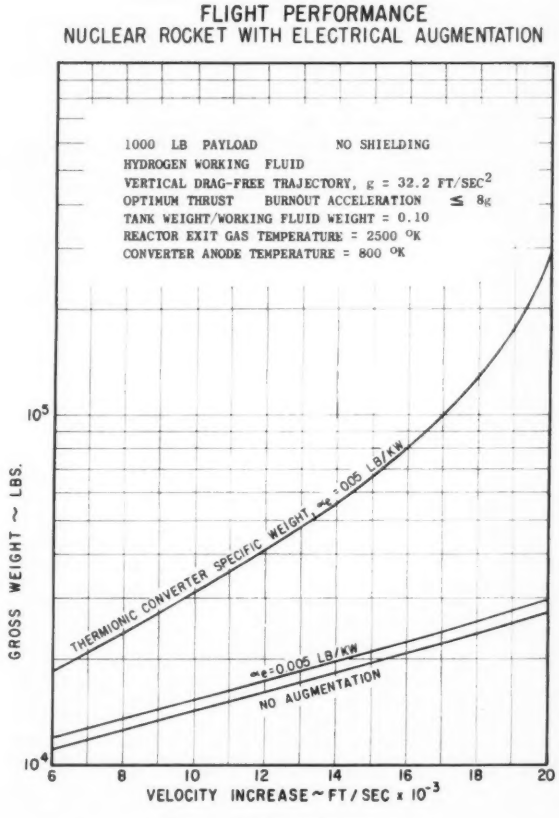
FLIGHT PERFORMANCE
NUCLEAR ROCKET WITH ELECTRICAL AUGMENTATION
1000 LB PAYLOAD NO SHIELDING
HYDROGEN WORKING FLUID
VERTICAL DRAG-FREE TRAJECTORY, g = 32.2 FT/SEC²
OPTIMUM THRUST BURNOUT ACCELERATION ≤ 8g
TANK WEIGHT/WORKING FLUID WEIGHT = 0.10
REACTOR EXIT GAS TEMPERATURE = 2500 °K
CONVERTER ANODE TEMPERATURE = 800 °K
THERMIONIC CONVERTER SPECIFIC WEIGHT, α = 0.005 LB/KW
α = 0.005 LB/KW
NO AUGMENTATION
GROSS WEIGHT ~ LBS.
VELOCITY INCREASE ~ FT/SEC x 10⁻³

Fig. 4 **Flight performance**

Specific impulse of both augmented and unaugmented rockets was calculated from Equations [1 and 2] for reactor exit gas temperatures from 2000 to 3500 K and converter anode maximum temperatures from 600 to 1600 K. The results are shown in Fig. 2. To simplify the calculations, it was assumed that no dissociation or ionization of the working fluid occurred and that the working fluid was completely expanded to a vacuum by the exhaust nozzle without condensation or freezing. The hydrogen entering the thrust chamber cooling jacket was assumed to be a saturated liquid at its boiling point. For the augmented rockets, converter and arc efficiencies were assumed to be 30 per cent (4) and 75 per cent (6), respectively.

Flight performance was calculated for a vertical, drag-free trajectory by the familiar equation

$$\Delta V = 32.2\, I_{sp} \ln (m_0/m_b) - \bar{g} t_b \qquad [3]$$

where

ΔV = vehicle velocity increase, ft per sec
m_0 = vehicle gross mass
m_b = vehicle mass at burnout
$\bar{g}$ = mean gravitational acceleration, ft per sec²
t_b = burning time, sec

In calculating flight performance, a reactor exit gas temperature of 2500 K and converter anode maximum temperature of 800 K were used, which, from Fig. 3, give specific impulses of 922 and 876 for the augmented and unaugmented cases, respectively. Other conditions and assumptions were as follows:

1000-lb payload.

Reactor, thrust chamber and nozzle weight from Fig. 3.

Tankage and structure weight = 10 per cent of working fluid weight.

Optimum thrust per weight ratio.

Burnout acceleration $\leq 8g$.

Thermionic converter specific weights of 0.05 and 0.005 lb per electrical kw, based on tungsten electrodes with a total thickness of 1 mm and power densities of about 100 and 1000 w per cm² of electrode area, respectively.

Average gravitational acceleration of 32.2 ft per sec².

No shielding.

The various assumptions correspond most closely to a booster rocket upper stage operating at very high altitude but within Earth's gravitational field.

Results of the performance calculations are summarized in Fig. 4, which shows the unaugmented rocket to have the lowest gross weight in all cases. While the assumptions made are arbitrary and approximate, they do not appear to penalize the augmented rocket, and reasonable changes in them should not significantly alter the results. Note that a higher converter anode temperature and/or efficiency would merely result in greater total augmentation, i.e., higher specific impulse but also higher converter total weight. Other working fluids, including lithium, lithium hydride, ammonia and water, were investigated with substantially the same results as were obtained for hydrogen. It appears, therefore, that unless heat-to-electrical power conversion equipment lighter than 0.005

lb per ekw can be developed, which seems unlikely, electrical augmentation will offer no advantages in flight performance for nuclear rocket boosters subject to Earth's gravity.

References

1 Goldsmith, M., "Augmentation of Nuclear Rocket Specific Impulse Through Mechanical-Electrical Means," ARS JOURNAL, vol. 29, no. 8, Aug. 1959, pp. 600–601.

2 Resler, E. L. and Rott, N., "On Rocket Propulsion with Nuclear Power," ARS preprint no. 1210-60, May 1960.

3 Wilson, V. C., "Electric Energy Sources and Conversion Techniques for Space Vehicles," IAS paper no. 60-31, Jan. 1960.

4 Wilson, V. C., "Conversion of Heat to Electricity by Thermionic Emission," *J. Appl. Phys.*, vol. 30, April 1959, pp. 475–481.

5 Grover, G. M., "Los Alamos Plasma Thermocouple," *Nucleonics*, vol. 17, July 1959, pp. 54–55.

6 Brogan, T. R., "Preliminary Evaluation of Helium as an Electric Arc-Heated Propellant," ARS JOURNAL, vol. 29, no. 9, Sept. 1959, pp. 662–663.

Nonequilibrium Ionization in a Shock Tunnel Flow[1]

ALAN Q. ESCHENROEDER[2] and JOHN W. DAIBER[3]

Cornell Aeronautical Laboratory, Buffalo, N. Y.

An approximate method for calculating nonequilibrium degrees of ionization in adiabatic quasi one-dimensional expanding flows is used for the case of weak interaction between the rate processes and the gasdynamic flow. Results are shown for air flow in a hypersonic shock tunnel nozzle, and the effects of nonequilibrium ionization on electromagnetic wave propagation are estimated for conditions at the tunnel test section.

IN HIGH energy flow studies concerned with electromagnetic phenomena, the processes of free electron production and recombination must be considered. For rapidly expanding flows, the rate of electron-ion recombination may be insufficient to maintain equilibrium ionization, and the electron mass concentration may become asymptotic to some frozen nonequilibrium value. The transition from equilibrium to frozen conditions is called "freezing" of the ionization. Although the electron densities may be significant for the purposes of electromagnetic studies, the energy stored in ionization is relatively so small for a broad range of stagnation conditions that the electron-ion reaction kinetics influence the flow very little. Consequently, the electron-ion rate problem and the gasdynamic problem may be solved separately. Hypersonic air flows and rocket exhaust flows are two examples of such cases. Smith (1)[4] analyzed the electron-ion recombination in an expanding gas with constant specific heat ratio, considering only three-body recombination processes. Bray and Wilson (2) discussed the nonequilibrium ionization in a wind tunnel nozzle for a monatomic "ideal ionizing gas." In the present work, a method is outlined for a real gas with parallel recombination processes. In order to illustrate the application of the method, an example is carried out for air flow in the 6-ft, Cornell Aeronautical Laboratory, hypersonic shock tunnel. Although the solutions are obtained for air, the method has broad application.

The shock tunnel for which the example is carried out has a two-dimensional first-stage nozzle designed for wave cancellation. Freezing of the ionization is predicted to occur in this nozzle, a portion of which is shown to scale in Fig. 1. A 10-deg turning section links the first-stage to the conical second-stage nozzle which expands the flow to the 6-ft test section. More detailed discussions regarding the design and application of this tunnel have been given by Hertzberg and Wittliff (3).

Before the rate processes are analyzed, the kinetics of electron-ion recombination must be examined. Detailed discussions of these kinetics are found in (4–6). According to the conventions of gaseous electronics, the recombination rate equation is always written for second-order kinetics regardless of the process; i.e.

$$-dn_e/dt = \alpha n_e n_+$$

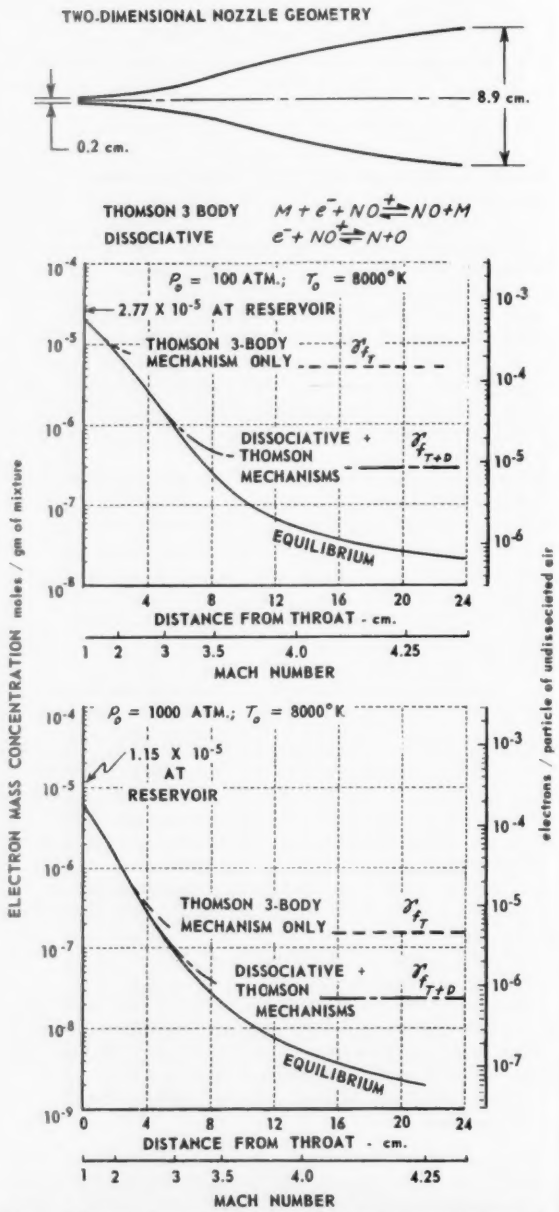
TWO-DIMENSIONAL NOZZLE GEOMETRY
8.9 cm.
0.2 cm.
THOMSON 3 BODY
DISSOCIATIVE
$M + e^- + NO^+ \rightleftharpoons NO + M$
$e^- + NO^+ \rightleftharpoons N + O$
P_0 = 100 ATM.; T_0 = 8000°K
2.77 X 10⁻⁵ AT RESERVOIR
THOMSON 3-BODY MECHANISM ONLY
DISSOCIATIVE + THOMSON MECHANISMS
EQUILIBRIUM
DISTANCE FROM THROAT - cm.
MACH NUMBER
P_0 = 1000 ATM.; T_0 = 8000°K
1.15 X 10⁻⁵ AT RESERVOIR
THOMSON 3-BODY MECHANISM ONLY
DISSOCIATIVE + THOMSON MECHANISMS
EQUILIBRIUM
DISTANCE FROM THROAT - cm.
MACH NUMBER
ELECTRON MASS CONCENTRATION moles / gm of mixture
electrons / particle of undissociated air

Fig. 1 Electron concentration profiles in first stage of hypersonic shock tunnel nozzle

Received July 28, 1960.

[1] This work was sponsored by the Rome Air Development Center of the Air Research and Development Command under Contract no. AF 30(602)-2267.

[2] Associate Aeronautical Engineer. Member ARS.

[3] Assistant Aeronautical Engineer.

[4] Numbers in parentheses indicate References at end of paper.

where

n_e = the number of electrons per unit volume
n_+ = the number of positive ions per unit volume
α = the rate coefficient

The main source of electrons in high temperature air is nitric oxide. It is assumed that two parallel reactions involving electrons and nitric oxide ions play the major roles. The first is the classical Thomson recombination which requires a third body M to carry away some of the excess energy. Residual internal excitation of the neutral NO also serves as an energy sink. The Thomson mechanism and its corresponding reverse reaction are

$$M + e^- + NO^+ \underset{}{\overset{\alpha_T}{\rightleftharpoons}} NO + M$$

α_T is the recombination rate coefficient appearing in the rate equation. The second and most important recombination path is dissociative recombination, a two-body reaction in which excess energy is absorbed by breaking the NO bond and by imparting kinetic energy to the resultant particles. This reaction and its reverse are

$$e^- + NO^+ \underset{}{\overset{\alpha_D}{\rightleftharpoons}} N + O$$

Radiative or dielectronic recombination (6) is also possible; however, the rate of this process is considerably less than those just discussed. Estimates made from classical theory (4) give an expression for the Thomson rate coefficient, and a formula (7) fitting experimental results is used to obtain the coefficient for dissociative recombination.

Weak-interaction approximate solutions of the electron conservation equation can be developed for the beginning and end of the electron freezing region. The analytical reasoning basically follows the approach of Hall and Russo (8). The beginning of the freezing region is characterized by small departures from equilibrium, and a linearized perturbation form of the electron conservation equation is employed. This same expression is subsequently applied formally to obtain the asymptotic frozen value of electron mass concentration γ_f. Free electron conditions throughout the expansion may be approximated by assuming $\gamma = \gamma_{eq}$ upstream from the station where $\gamma_{eq} = \gamma_f$ (called the freezing point), and by assuming $\gamma = \gamma_f$ for the remainder of the flow. Details of the analytical method will be described in a later paper.

For the independent gasdynamic solution of the air flow problem considered here, equilibrium flow results were obtained with an IBM-704 computer using a program based on an extension of the Brinkley method (9). In addition to giving the composition which satisfies conservation of mass and minimization of free energy, this program gives the pressure which results in the mixture entropy specified by the stagnation state. The Newton-Raphson iterated solution for composition and pressure at each value of static temperature is followed by computations of density, velocity, Mach number and area ratio. Mach numbers are based on equilibrium sound speed found from local values of $(dp/d\rho)^{1/2}$ along the isentropic path. The throat location is found by determining the maximum mass flux with a regressive numerical procedure. The application of the program to equilibrium air calculations includes the species $N_2, O_2, A, N, O, NO, N_2^+, O_2^+, N^+, O^+, O^-$, NO^+ and e^-. Composition vs. area ratio plots are shown in (10) for a wide range of stagnation conditions.

The following assumptions were made in estimating the electron densities in the tunnel test section. The nitric oxide ion concentration was considered to be equal to that of electrons, and only the reactions between these two species were considered as rate processes. Neutral species in the gas were assumed to be in chemical equilibrium. It was further assumed that the electron temperature always equals the translational gas temperature. As mentioned earlier, only the Thomson and dissociative recombinations were considered.

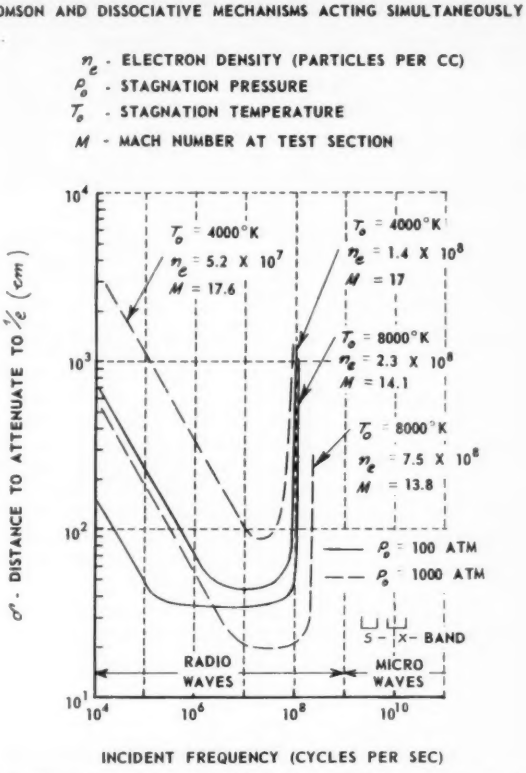
ELECTRON-ION RECOMBINATION IS ASSUMED TO OCCUR BY THE THOMSON AND DISSOCIATIVE MECHANISMS ACTING SIMULTANEOUSLY
η_e - ELECTRON DENSITY (PARTICLES PER CC)
ρ_0 - STAGNATION PRESSURE
T_0 - STAGNATION TEMPERATURE
M - MACH NUMBER AT TEST SECTION
T_0 = 4000°K
η_e = 5.2 X 10^7
M = 17.6
T_0 = 4000°K
η_e = 1.4 X 10^8
M = 17
T_0 = 8000°K
η_e = 2.3 X 10^8
M = 14.1
T_0 = 8000°K
η_e = 7.5 X 10^8
M = 13.8
ρ_0 = 100 ATM
ρ_0 = 1000 ATM
S - X - BAND
RADIO WAVES
MICRO WAVES
σ' - DISTANCE TO ATTENUATE TO 1/e (cm)
INCIDENT FREQUENCY (CYCLES PER SEC)

Fig. 2 Damping of transmitted electromagnetic wave in test section of the shock tunnel

These assumptions regarding electron interactions and chemical kinetics are provisional and must be investigated further.

The disappearance of free electrons in the first-stage nozzle of the 6-ft, Cornell Aeronautical Laboratory, hypersonic shock tunnel (see Fig. 1) was calculated for near equilibrium and for asymptotic frozen conditions. One set of calculations was done for the Thomson mechanism acting alone (T), and another set was done for the Thomson and dissociative mechanisms acting simultaneously ($T + D$). Fig. 1 shows the resultant electron mass concentration profiles for the particular nozzle geometry of interest. As should be expected, pressure influences the three-body mechanism more than it does the combined mechanism because three-body collision rate depends on density to a higher degree than the two-body rate. Exact integrations of the electron conservation equation would be required to fill in the central regions of the nonequilibrium profiles in Fig. 1.

The frozen electron densities in the hypersonic shock tunnel test section are shown on the electromagnetic wave attenuation curves in Fig. 2 for the stagnation conditions 4000 and 8000 K, 100 and 1000 atm. Since the fluid density is somewhat insensitive to chemical nonequilibrium (10), the equilibrium fluid densities from the machine-computed results were used.

The test section electron density is surprisingly insensitive to stagnation conditions over the range shown. Compensating effects of temperature and pressure are explainable by examining their influence on initial equilibrium ionization, rate processes and gas density. High temperature and low pressure result in high degrees of ionization and early freezing. On the other hand, low temperature and high pressure give

high gas density, hence the tendency toward uniformity in the electron density. The direct pressure effect on $(T + D)$ recombination is more significant at low temperatures than at high temperatures because of the more important role of three-body encounters at low temperatures. This is seen by comparing the expressions for α_T and α_D. Thus, at $T_0 = 4000$ K, the electron density at the test section for $p_0 = 100$ atm is actually greater than that for $p_0 = 1000$ atm.

Electromagnetic Wave Propagation in the Tunnel Test Section

The distance δ, required for electromagnetic waves to be attenuated to e^{-1} of their original amplitude, is generally a function of wave frequency, electron collision frequency and electron density (11). In Fig. 2, δ is plotted vs. wave frequency for four stagnation conditions in the Cornell Aeronautical Laboratory shock tunnel. The test section conditions are obtained by a further expansion of the flow, which has been frozen by the combined mechanisms. The free stream Mach number and electron particle densities at the test section are indicated on the curves. Effectively, complete transmission occurs at frequencies greater than the plasma frequency. Consequently, any microwave band with a frequency greater than the plasma attenuation frequencies and less than the rotational absorption band of the oxygen molecule starting approximately at 50 kmc per sec would be suitable for transmission (12) through the tunnel test section.

References

1 Smith, F. T., "On the Analysis of Recombination Reactions in an Expanding Gas Stream," Seventh Symposium (International) on Combustion, Butterworths Scientific Pub., London, 1959.

2 Bray, K. N. C. and Wilson, J. A., "A Preliminary Study of Ionic Recombination of Argon in Wind Tunnel Nozzles," Univ. of Southampton, Aeron. and Astron. Rep. no. 134, Feb. 1960.

3 Hertzberg, A. and Wittliff, C. E., "Studying Hypersonic Flight in the Shock Tunnel," Paper no. 60-67, presented at the IAS National Summer Meeting, June 28–July 1, 1960, Los Angeles, Calif.

4 Massey, H. S. W. and Burhop, E. H. S., "Electronic and Ionic Impact Phenomena," Oxford Univ. Press, 1952, London, England.

5 Loeb, L. B., "Basic Processes of Gaseous Electronics," Univ. of Calif. Press, Berkeley, Calif., 1955.

6 Calcote, H. F., "Relaxation Processes in a Plasma," Third Biennial Gas Dynamics Symposium, Northwestern Univ. Press, 1959, Evanston, Ill.

7 Teare, J. D., Hammerling, P. and Kivel, B., "Theory of the Shock Front. II. High-Temperature Reaction Rates," AVCO Res. Lab., Res. Note 133, June 1959.

8 Hall, J. G. and Russo, A. L., "Studies of Chemical Nonequilibrium in Hypersonic Nozzle Flows," Cornell Aeron. Lab., Rep. no. AD-1118-A-6, AFOSR TN 59-1090, Nov. 1959. To be published in Proc. Combustion Institute Meeting, Western States Section, Nov. 2–5, 1959, Los Angeles, Calif., Butterworths, London, England.

9 Brinkley, S. R., "Computational Methods in Combustion Calculations," in "Combustion Processes, Vol. II," pp. 64–98, Princeton Univ. Press, Princeton, N. J., 1956.

10 Boyer, D. W., Eschenroeder, A. Q. and Russo, A. L., "Approximate Solutions for Nonequilibrium Airflow in Hypersonic Nozzles," Cornell Aeronautical Lab. Rep. no. AD-1345-W-3; AEDC-TN 60-181, Aug. 1960.

11 Lin, S. C., "A Rough Estimate of the Attenuation of Telemetering Signals Through the Ionized Gas Envelope Around a Typical Re-Entry Missile," AVCO Res. Rep. 74, Feb. 1956.

12 White, J. R., "Communication During Re-Entry Blackout," ARS preprint 963-59, Nov. 1959.

Particle Impaction Efficiencies for Bodies in a Free Molecule Flow[1]

S. K. FRIEDLANDER[2]

The Johns Hopkins University, Baltimore, Md.

THE TESTING of nuclear weapons has resulted in the introduction of a considerable amount of fine radioactive debris into the stratosphere. The matter dispersed by the test explosions is of uncertain size distribution and radioactivity content. It has joined the particulates brought into the stratosphere from space and from the troposphere and, very likely, combined with them to some extent as a result of the Brownian motion. The continuing deposition of particulates on Earth's surface from their stratospheric reservoir is an important aspect of the fallout problem.

To predict the rates and time periods of the deposition process, it is necessary to obtain information on the size and radioactivity of the particulates in the stratosphere. Quite naturally, sampling by rocket has been proposed as a method for making such measurements at heights greater than 20 miles above which balloon sampling becomes impractical. Impaction on an exposed surface would be a particularly simple mechanism of removal. In a previous note (1),[3] the author considered particle impaction at high Mach numbers for air densities sufficiently great to permit the formation of a standing shock ("bow") wave at the forward stagnation point of the sphere. He was able to generalize the criteria for the impaction cutoff in subsonic flows and to apply them to the prediction of minimum collectible particle size in high Mach number flows. For a 1-in. sphere, these results should be applicable up to heights of about 50 miles; at this altitude, the mean free path approaches the sphere diameter, and the sphere ceases to "see" a continuum flow. At altitudes above about 60 miles, the mean free path becomes much greater than 1 in., and it is possible to approach the calculation of the impaction efficiency as a problem in free molecule flow.

When a body with characteristic length much less than the mean free path passes through a gas, the molecules reflected from its surface are not likely to collide with the incoming molecules. Hence each new set of molecules striking the body will, as an approximation, possess the Maxwellian distribution characteristic of the ambient gas. This is the basic assumption of the theory of free molecule flow (2,3). The radioactive particles generated by test explosions are probably the result both of disintegration and condensation processes. It is likely that the debris which remains in the stratosphere after injection ranges in size from molecules and molecular clusters to particles with diameters up to 0.1 to 1 μ. This material is in thermal equilibrium with the air molecules, and each size range will possess a characteristic Maxwellian velocity distribution. Particles and molecular clusters will have a less vigorous thermal (Brownian) motion than single molecules. The rate at which any class of particulates strikes the body can easily be calculated if it is assumed that the reflected air molecules do not collide with the incoming particulates and molecular clusters. In this case, the incoming particulates will possess the Maxwellian distribution characteristic of the ambient temperature.

Flux on an Elemental Area in a Free Molecule Flow

Consider an elemental area set at the origin of a Cartesian coordinate system in the yz plane normal to the x axis. Instead of moving the surface through gas, let the area remain fixed while the gas flows by with a mean velocity $\vec{U}$ and components U_x, U_y, U_z. The velocity distribution of the ith constituent (molecules, molecular clusters or small particles)

(*Continued on page 153*)

Received July 14, 1960.

[1] This work was carried out at The Johns Hopkins University under the sponsorship of Atomic Energy Commission Contract AT(30-1)-2165.

[2] Associate Professor, Dept. of Chemical Engineering.

[3] Numbers in parentheses indicate References at end of paper.